GEOCHRONOLOGY AND PETROGENETIC STUDIES OF ALAGBEDE GOLD DEPOSIT, SOUTHWESTERN NIGERIA

BY

AJADI, JIMOH

(14/27/PGE001)

A DISSERTATION SUBMITTED TO THE DEPARTMENT OF GEOLOGY AND MINERAL SCIENCES, KWARA STATE UNIVERSITY, MALETE NIGERIA,

IN PARTIAL FULFILLMENT OF THE REQUIREMENTS FOR THE AWARD OF DOCTOR OF PHILOSOPHY DEGREE (Ph.D) IN GEOLOGY

JUNE, 2018

ProQuest Number: 10930135

All rights reserved

INFORMATION TO ALL USERS
The quality of this reproduction is dependent upon the quality of the copy submitted.

In the unlikely event that the author did not send a complete manuscript
and there are missing pages, these will be noted. Also, if material had to be removed,
a note will indicate the deletion.



ProQuest 10930135

Published by ProQuest LLC (2018). Copyright of the Dissertation is held by the Author.

All rights reserved.
This work is protected against unauthorized copying under Title 17, United States Code
Microform Edition © ProQuest LLC.

ProQuest LLC.
789 East Eisenhower Parkway
P.O. Box 1346
Ann Arbor, MI 48106 – 1346

WE CERTIFY THAT THIS THESIS WAS PREPARED AND PRESENTED IN ACCORDANCE WITH THE GUIDELINES ON SUPERVISION OF Ph.D DISSERTATION AS PRESCRIBED BY THE KWARA STATE UNIVERSITY, MALETE, NIGERIA.

AUTHOR:	**AJADI, JIMOH**
MATRIC. NO.:	**14/27/PGE001**
DISSERTATION TITLE:	**GEOCHRONOLOGY AND PETROGENETIC STUDIES OF ALAGBEDE GOLD DEPOSIT, SOUTHWESTERN NIGERIA**
DEGREE:	**Ph.D GEOLOGY**
MAJOR FIELD:	**PETROLOGY, GEOCHEMISTRY AND GEOCHRONOLOGY**

Dr. Paulinus N. Nnabo ..... **26/07/2018** (Signature & Date)
Supervisor

Dr. Ifeanyi A. Oha ..... **26/07/2018** (Signature & Date)
Co-Supervisor

Dr. Olufemi Olaniyan ..... **26/07/2018** (Signature & Date)
Head of Department

Prof. Stephen Kayode Subair ..... **26/07/2018** (Signature & Date)
Dean of Postgraduate School

Prof. Samuel B. Olobaniyi ..... **26/07/2018** (Signature & Date)
External Examiner

COPYRIGHT DECLARATION

I, Jimoh Ajadi, solemnly declare that the manuscript of this dissertation titled, "Geochronology and Petrogenetic Studies of Alagbede Gold Deposit, Southwestern Nigeria" consist entirely of my research work under the scrutiny and guidance of my supervisors and that no part thereof has been published or presented for another degree elsewhere, except for the permissible citations from other authors whose sources have been duly referenced and acknowledged.

Declarant ……**Jimoh Ajadi**……..

Signature ………… Date ……**25/07/2018**……..

DEDICATION

This dissertation is dedicated to Almighty Allah (S.W.T) who is the giver of life and to my family.

ACKNOWLEDGEMENT

First and foremost, I would like to appreciate the invaluable contributions of my teacher, mentor and role model, Prof. S. S. Dada who actually motivated me to join academics and substantially supervised this Ph.D thesis before his exit from KWASU. His mentorship, guidance and constructive criticism constantly put me on my toes and spurred me to success. I am also grateful to my supervisors, Dr. Paulinus N. Nnabo and Dr. Ifeanyi A. Oha. Their acceptance to continue with the supervision of this thesis and their immense contributions made this Ph.D dissertation possible.

My appreciation also goes to the head of department of Chemical, Geological and Physical Sciences, Dr. Olufemi Olaniyan, the Provost and Deputy Provost, College of Pure and Applied Sciences, Prof. Adebayo Aina and Prof. Mohammed Siddiq Abubakar respectively as well as the College's postgraduate coordinator, Dr. Sunday Awe for their encouragement and supports. I wish to acknowledge my indebtedness in appreciation to the Vice Chancellor of the Kwara State University, Malete, Prof. Abdulrasheed Na'Allah and the Tertiary Education Trust Fund (Tetfund) for providing part of the funds for this work.

To Dr. Abdulrasaq A. Garba, the Director of the Department of Economic Geology, Nigerian Geological Survey Agency, Abuja I say a big thank you for his support towards the successful completion of this work. I appreciate all my friends who contributed in one way or the other to this course. Lastly, I would like to thank my family members especially my darling wife, Hajia A. S. Ajadi, who virtually became my study buddy, for her understanding, sacrifice and support without which this Ph.D dissertation would not have been successful.

AUTHOR'S PROFILE

The author is a geoscientist with over 20 years of professional practice involving research, consultancy services and teaching with a strong background in petrology, structural geology, geochemistry, mineral exploration and geochronology. He started his career with the Federal Ministry of Solid Minerals Development in 1996 and later rose to the position of Assistant Director in the Economic Geology Department of the Nigerian Geological Survey Agency (NGSA) in January 2013 before joining the Department of Geology and Mineral Sciences, Kwara State University Malete in February 2015 as a Research Associate I.

He obtained a B.Sc. and M.Sc. degree in geology (mineral exploration option) from the University of Ilorin in 1992 and 2009 respectively. His present PhD dissertation focuses on Isotope Geochemistry and Geochronology. He has attended over 15 professional trainings, both local and overseas, presented over 12 local and international conference papers with 8 technical/professional reports and 10 scholarly peer-reviewed publications in local and international journals. He is a member of many professional bodies including the Nigerian Mining & Geosciences Society (NMGS), Society of Economic Geologists (SEG) and Society for Geology Applied to Mineral Deposits (SGA).

ABSTRACT

Geological mapping around the gold-bearing main quartz vein of Alagbede area, located about 25km northeast of the Kwara State University, Malete shows that the Basement Complex rocks comprised the biotite-gneiss, migmatitic gneiss, quartzite, quartz-mica schist, talc-tremolite-actinolite schist, porphyroblastic granite, porphyritic granite, porphyritic diorite, alkali granite, granodiorite, alkali syenite, pegmatite/aplite and vein quartz. The AFM chemical classification diagrams for common volcanic rocks revealed that the Alagbede granites exhibit volcanic arc granites (VAG) origin based on the (Rb) vs Log (Y+Nb) discrimination diagrams for tectonic interpretation. Electron Probe Micro Analysis (EPMA) and ore microscopic work has shown that Alagbede gold occurs mainly as small inclusions or microfracture-fillings in pyrite, chalcopyrite and arsenopyrite in the deposit and this suggest that the gold mineralization is coeval with the precipitation of the sulfide phases. The abundances of light REE relative to that of the heavy REE in the host quartzitic and granitic rocks, the presence of negative Eu anomaly on the chondrite-normalized REE spider diagram and the major element fractionation pattern argued for a metamorphic source accompanied by magmatic differentiation of granitic magma as the possible source for the ore fluids for the gold mineralization at Alagbede, consistent with other orogenic vein-type gold deposits. A process of fractional crystallization in which the latent heat of crystallization provides sufficient thermal energy to consume the wall-rock, is hereby proposed as the fractionation model for the major element chemistry of the igneous rocks in Alagbede area. The U-Th-Pb on zircon was dated by in situ Laser Ablation ICP-MS which yielded upper intercept

crystallization ages with superimposed Pan African imprints for the gold mineralization. Alagbede gold deposit is hosted in the vein quartz (formed at 590±27 Ma) and fine grained syeno-granite (formed 596±28 Ma) that are sinistrally sheared by a NW-SE trending fault, linked to the transcurrent fault line of the Anka-Yauri-Iseyin schist belt. A Pan African age of 590±27 Ma is hereby proposed as the age of gold mineralization in Alagbede area.

TABLE OF CONTENTS **Page**

Title page i

Approval Page ii

Copyright Declaration iii

Dedication iv

Acknowledgements v

Author's Profile vi

Abstract vii

Table of Contents ix

List of Tables xv

List of Appendices xvi

List of Figures xvii

CHATPER 1

INTRODUCTION

1.1 General Statement 1

1.2 Location and Accessibility 4

1.3 Statement of Problems 6

1.4 Aim and Objectives 7

1.5 Research Justification/Expected Results 8

1.6 Physiographic Setting 8

1.6.1 Relief and Drainage 8

1.6.2 Climate and Vegetation 9

1.7 The People 10

CHAPTER 2

REVIEW OF LITERATURE

2.1 An Overview of the Geology of Nigeria 13

2.2 Precambrian Basement Complex 16

2.2.1 Migmatite-Gneiss Complex 17

2.2.2 The Schist Belt 18

2.2.3 Pan African Granitoid (Older Granite) 19

2.2.4 Undeformed Acid and Basic Dykes 21

2.2.5 Jurassic Anorogenic Younger Granite 21

2.3 The Cretaceous Tertiary Sedimentary Basins 22

2.4 Geology of the Basement Complex of Southwestern Nigeria 24

2.4.1 Metamorphism in the basement rocks of southwestern Nigeria 28

2.4.2 Geochronology of the basement rocks of southwestern Nigeria 29

2.5 History of Gold Exploration in Nigeria 29

2.5.1 Gold Exploration Techniques 31

2.5.2 Genetic Model 32

CHAPTER 3

MATERIALS AND METHODS

3.1 Methodology …… 36

3.2 Fieldwork …… 36

3.3 Laboratory Work …… 37

3.4 Geochemical Laboratory Instrumentation …… 38

3.4.1 Preparation of Fusion Disks for Major Element Analysis by XRF …… 38

3.4.2 Sample Dissolution for Trace Element Analysis by ICP-MC …… 41

3.5 Heavy Mineral Separation for U-Pb on Zircon Dating …… 42

3.5.1 Rock Crushing …… 42

3.5.2 Density Separation using a Wilfley Table …… 43

3.5.3 Density Separation using Heavy Liquids …… 46

3.5.4 Mineral Separation using Magnetic Susceptibility …… 47

3.6 Laser Ablation Technique …… 48

CHAPTER 4

LITHOLOGY, STRUCTURE AND GEOCHEMISTRY OF ROCKS IN ALAGBEDE AREA

4.1 Local Geology …… 51

4.1.1 Biotite Gneiss…… 54

4.1.2 Migmatitic Gneiss …… 59

4.1.3 Quartzite …… 66

4.1.4 Quartz-Mica Schist 72

4.1.5 Talc-tremolite-actinolite Schist 77

4.1.6 Gabbro 82

4.1.7 Porphyritic Granite 86

4.1.8 Porphyroblastic Granite 91

4.1.9 Porphyritic Quartz Diorite 95

4.1.10 Coarse-grained Granite 99

4.1.11 Granodiorite 104

4.1.12 Medium-grained biotite-hornblende Granite 109

4.1.13 Alkali Syenite 114

4.1.14 Pegmatite and Aplite 119

4.1.15 Vein Quartz 124

4.2 Structural Geology 130

4.2.1 Ductile Structure 130

4.2.2 Brittle Deformation 137

4.2.3 Structural Evolution 142

4.3 Metamorphic Geology 143

4.3.1 Metamorphic Mineral Assemblages and Grades 144

4.4 Economic Geology 146

4.4.1 Mineral Resources 146

4.4.2 Construction Materials 146

4.4.3 Hydrogeology 147

4.4.4 Geotourism Potentials 147

4.5 Geochemistry 149

4.5.1 Interpretation of Geochemical Data 149

4.6 Petrogenesis 161

4.6.1 Major Element Fractionation Pattern 161

4.6.2 REE Fractionation Pattern 161

4.6.3 Trace Element Geochemistry 169

4.6.4 Source Characteristics 169

CHAPTER 5

AGE OF GOLD MINERALIZATION IN ALAGBEDE AREA

5.1 Gold Exploration in Alagbede Area 173

5.2 Estimation of Ore Grade 174

5.3 Ore Microscopy 176

5.4 Mineralization Pattern 181

5.5 Geochronological Dating of Alagbede Gold Deposit 181

5.5.1 Mounting, Cutting and Polishing of Zircon Grains 182

5.5.2 Electron Microprobe Studies 182

5.5.3 Scanning Electron Microscope (SEM) – Cathodoluminiscence (CL) 183

5.5.4 Textural Classification of Zircons 186

5.5.5 Laser Ablation ICP-MS Data Treatment 194

5.5.6 U-Th-Pb Zircon Dating 196

5.6 Interpretation of Results 197

5.6.1 Alkali Granite 197

5.6.2 Porphyritic Granite 202

5.6.3 Syenite 202

5.6.4 Granodiorite 209

5.6.5 Pegmatite 209

5.6.6 Vein Quartz 216

5.6.7 Alkali Granite (Syeno-granite) 216

CHAPTER 6

DISCUSSION AND CONCLUSION

6.1 Discussion 222

6.2 Conclusion 226

6.3 Recommendations 228

References 230

Appendices 246

LIST OF TABLES **Page**

1. A modified sequence of events in the basement rocks 27

2. Magnetic susceptibilities of common minerals 50

3. Modal concentration of minerals in Biotite Gneiss 57

4. Modal concentration of minerals in migmatitic gneiss 63

5. Modal concentration of minerals in Quartzite 69

6. Modal composition of the Quartz-mica schist 75

7. Modal composition of the Talc-tremolite-actinolite schist 79

8. Modal composition of the Gabbro 83

9. Modal composition of the Porphyritic Granite 89

10. Modal composition of the Porphyroblastic Granite 93

11. Modal composition of the Porphyritic Diorite 97

12. Modal composition of the coarse-grained granite 102

13. Modal composition of the medium-grained granodiorite 107

14. Modal composition of the medium-grained Granite 112

15. Modal composition of the Alkaline Syenite 117

16. Modal composition of the Pegmatite/Aplite 122

17. Modal composition of the Vein Quartz 128

18. Gold concentration and ore grade in mineralized rocks of Alagbede area 175

LIST OF APPENDICES **Page**

1a. Geochemical data of some rock samples (samples 3 to 55) 246

1b. Geochemical data of some rock samples (samples 57 to 85) 248

2. U-Th-Pb Isotopic data for Alkali Granite 250

3. U-Th-Pb isotopic data for Porphyritic Granite 252

4. U-Th-Pb isotopic data for Syenite 255

5. U-Th-Pb isotopic data for Granodiorite 256

6. U-Th-Pb isotopic data for Pegmatite 258

7. U-Th-Pb isotopic data for vein quartz 261

8. U-Th-Pb isotopic data for Alkali Granite (Syeno-granite) 262

LIST OF FIGURES **Page**

1. Geological map of Nigeria showing major areas of gold mineralization ……..…….. 3

2. Geological map of the Hoggar–Aır–Nigeria province ……..... 5

3. Geological map of Northern African showing Precambrian rocks ……..... 5

4. A thick vegetation bordering an artificial lake on River Werufini 11

5. A farmland in the study area showing heaps of yam cultivation ……..…….. 11

6. Some youths on hunting expedition in the study area ……..…….. 12

7. Geological map of Nigeria showing the schist belts ……..…… 20

8. Simplified Geological map of Nigeria showing the schist belts on the eastern margin of the West African craton ……..…….. 35

9. Furnace used for Platinun crucibles and LOI crucibles ……..…….. 44

10. XRF machine at the EarthLab of the University of Witwatersrand ……..…… 44

11. (a) ESCO Lab Fume Hood (b) Microwave Acceleration Reaction System …….. 45

12. RESOlution and Perkin Elmer ICPMS machines at the EarthLab ……..…….. 45

13a. Geological map of Alagbede area, Northcentral Nigeria ……..... 52

13b. Geological cross-section of Alagbede area ……..…….. 53

14. Hand specimen sample of the biotite gneiss ……..…….. 56

15. A bouldery outcrop of a flaggy biotite gneiss ……..…….. 56

16a. Photomicrograph of biotite gneiss in thin section under PPL ……..…… 58

16b. Photomicrograph of biotite gneiss in thin section under XPL ……..…… 58

17. A section of an outcrop of ophthalmic migmatitic gneiss 61

18. A section of an outcrop of schollen migmatitic gneiss 61

19. A section of an outcrop of stromatic migmatite 62

20. Photomicrograph of the migmatitic gneiss under PPL & XPL 64

21. An outcrop of quartzite showing angular boulders and rubbles 68

22. A hand specimen sample of a milky white colored quartzite 68

23. A hand specimen sample of a mica-rich quartzite 69

24. Photomicrograph of the quartzites under PPL & XPL 70

25. A low-lying outcrop of the quartz-mica schist 74

26. Hand specimen samples of the quartz-mica schist 74

27. Photomicrograph of the quartz-mica schist under PPL & XPL 76

28. An outcrop of the talc-tremolite schist 78

29. A hand specimen sample of the talc-tremolite-actinolite schist 78

30. Photomicrograph of the talc-tremolite-actinolite schist (PPL & XPL) 80

31. Hand specimen samples of the gabbro 83

32. Photomicrograph of the gabbro under PPL & XPL 84

33. A hand specimen sample of the porphyritic granite 88

34. An outcrop of the coarse porphyritic granite 88

35. Photomicrograph of the porphyritic granite under PPL & XPL 90

36. A hand specimen sample of the porphyroblastic granite 93

37. Photomicrograph of the porphyroblastic granite under PPL & XPL 94

38. Hand specimen sample of the porphyritic diorite 97

39. Photomicrograph of the porphyritic diorite under PPL & XPL 98

40. A bare rock exposure of the coarse-grained granite 101

41. Hand specimen sample of the coarse-grained granite 100

42. Photomicrograph of the coarse-grained granite under PPL & XPL 103

43. An outcrop of the coarse-grained granodiorite 106

44. A hand specimen of the coarse-grained granodiorite 106

45. Photomicrograph of the granodiorite under PPL & XPL 108

46. A low ridge outcrop of the medium-grained granite 111

47. Hand specimen sample of the medium-grained granite 111

48. Photomicrograph of the medium-grained granite under PPL & XPL 113

49. A low ridge outcrop of the Alkali Syenite 116

50. Hand specimen sample of the Alkali Syenite 116

51. Photomicrograph of the alkali syenite under PPL & XPL 118

52. (a & b) Outcrop of granodiorite with pegmatite (c) Aplite specimen 121

53. Photomicrograph of the pegmatites under PPL & XPL 123

54. A section of an outcrop of the biotite gneiss with vein quartz 126

55. Satellite Imagery of the NE-SW trending gold-bearing quartz vein 126

56. Hand specimen of the vein quartz 127

57. Hand specimen of the gold-sulfide-bearing vein quartz 127

58. Photomicrograph of vein quartz under PPL & XPL 129

59. Plot of the pole to point on foliation planes in the gneisses 132

60. An outcrop of a migmatitic gneiss showing tight isoclinal folds 135

61. A section of a migmatitic gneiss outcrop showing ptygmatic fold 135

62. An outcrop of a migmatitic gneiss showing deformed basin structure 136

63. An outcrop of porphyroblastic granite showing ductile shears 136

64. An outcrop of granodiorite showing healed joints 139

65. Rosette diagram showing the trend of joints in granite 139

66. Rosette diagram of the trend of joints in the gneisses 140

67. Rosette diagram of the trend of joints in the schists 140

68. Rosette diagram of the trend of joints healed with vein quartz 141

69. Rosette diagram of the trend of joints healed with pegmatites & aplites 141

70. A hand-dug well and a manual borehole in Alagbede village 148

71. Binary plot for general classification of volcanic rocks of Alagbede 152

72. AFM diagram for chemical classification of common volcanic rocks1 152

73. AFM diagram for chemical classification of common volcanic rocks2 153

74. K_2O vs SiO_2 for general classification of volcanic rocks1 153

75. K_2O vs SiO_2 for general classification of volcanic rocks2 154

76. TAS discriminatory plot for volcanic rocks (LeBas et al., 1986) 154

77. TAS discriminatory plot for volcanic rocks (Cox-Bell-Pank, 1979) 155

78. TAS discriminatory plot for plutonic rocks (Cox-Bell-Pank, 1979) 155

79. Log (Nb) vs Log (Y) binary plot for granites (Pearce et. al, 1984) 156

80. Log (Ta) vs Log (Yb) binary plot for granites (Pearce et. Al, 1984) 156

81. Log (Rb) vs Log (Yb+Ta) binary plot for granites (Pearce et. al, 1984) 157

82. Log (Rb) vs Log (Y+Nb) binary plot for granites (Pearce et. al, 1984) 157

83. Ti vs Zr discriminatory diagram for basaltic rocks (Pearce Cann 1973) 158

84. Discriminatory plots of Th/Yb v Ta/\Yb for the basaltic rocks 158

85. Ti-Zr-Y ternary diagram for the basaltic rocks 159

86. Ti-Zr-Sr diagram for the basaltic rocks 159

87. Nb-Zr-Y diagram for the basaltic rocks 160

88. Th-Hf/3-Ta diagram for the basaltic rocks 160

89. Harker's (major element bivariate) diagrams for igneous rocks 164

90. Bivariate graph showing the degree of REE fractionations 166

91. Chondrite-normalized REE spider diagram for igneous rocks 167

92. Chondrite-normalized REE spider diagram for plutonic rocks 167

93. Chondrite-normalized REE spider diagram for volcanic rocks 168

94. Chondrite-normalized REE spider diagram for metasedimentary rocks 168

95. Chondrite-normalized spider diagram for igneous rocks 171

96. Chondrite-normalized spider diagram for plutonic rocks 171

97. Chondrite-normalized spider diagram for volcanic rocks 172

98. Chondrite-normalized spider diagram for metamorphic rocks 172

99. One of the artisanal exploratory pit for mining of gold in Alagbede 175

100. Occurrence of small free gold in syeno-granite 178

101. Microfracture-filling gold inclusions within the vein quartz 178

102. Blebs of arsenopyrite with gold inclusions within the vein quartz 179

103. Zoning of sulfide: pyrite-chalcopyrite-pyrrhotite assemblage 179

104. Sulfide mineralization within the vein quartz 180

105. Quorum Q300T ES for carbon-coating at the Univ. of Johannesburg 185

106. VEGA3 TESCAN for cathodoluminiscence imaging 185

107. Cathodoluminiscence images of zircons in alkali granite 190

108. Cathodoluminiscence images of zircons in porphyroblastic granite 191

109. Cathodoluminiscence images of zircons in Syenite 191

110. Cathodoluminiscence images of zircons in Granodiorite 191

111. Cathodoluminiscence images of zircons in Pegmatite 192

112. Cathodoluminiscence images of zircons in Vein Quartz 192

113. Cathodoluminiscence images of zircons in Syeno-granite 193

114. Weighted average age plot of 31 zircon grains from alkali granite 199

115. Weighted average age plot of 23 zircon grains from alkali granite 199

116. Weighted average age plot of 11 zircon grains in alkali granite 200

117. Probability frequency histogram for zircon ages in alkali granite 200

118. $^{206}Pb/^{238}U$ vs $^{207}Pb/^{235}U$ Concordia diagram for zircons in alkali granite 201

119. Weighted average age for plot of 15 zircon grains in porphyritic granite 204

120. Weighted average age for plot of 12 zircon grains in porphyritic granite 204

121. Weighted average age for plot of 24 zircon grains in porphyritic granite 205

122. Probability frequency histogram for zircon ages in porphyritic granite 205

123. $^{206}Pb/^{238}U$ vs $^{207}Pb/^{235}U$ Concordia diagram for zircons in OGp 206

124. Weighted average age plot of 10 zircon grains in syenite 206

125. Weighted average age plot of 8 zircon grains in syenite 207

126. Weighted average age plot of 10 zircon grains in syenite 207

127. Probability frequency histogram for zircon ages in syenite 208

128. $^{206}Pb/^{238}U$ versus $^{207}Pb/^{235}U$ Concordia diagram for zircons in syenite 208

129. Weighted average age plot of 6 zircon grains in granodiorite 211

130. Weighted average age plot of 42 zircon grains in granodiorite 211

131. Probability frequency histogram for zircon ages in granodiorite 212

132. $^{206}Pb/^{238}U$ vs $^{207}Pb/^{235}U$ Concordia diagram for zircons in granodiorite 212

133. Weighted average age plot of 71 zircon grains in pegmatite 213

134. Weighted average age plot of 13 zircon grains in pegmatite 213

135. Weighted average age plot of 13 zircon grains in pegmatite 214

136. Probability frequency histogram for zircon ages in pegmatite 214

137. $^{206}Pb/^{238}U$ vs $^{207}Pb/^{235}U$ Concordia diagram for zircons in pegmatite 215

138. Weighted average age plot of 7 zircon grains in vein quartz 218

139. Probability frequency histogram for zircon ages in vein quartz 218

140. $^{206}Pb/^{238}U$ vs $^{207}Pb/^{235}U$ Concordia diagram for zircons in vein quartz 219

141. Weighted average age plot of 24 zircon grains in syenogranite 219

142. Probability frequency histogram for zircon ages in syenogranite 220

143. $^{206}Pb/^{204}Pb$ vs $^{238}U/^{204}Pb$ isochron plot for syenogranite 220

144. $^{206}Pb/^{238}U$ vs $^{207}Pb/^{235}U$ Concordia diagram for zircons in syeno-granite 221

CHAPTER 1

INTRODUCTION

1.1 General Statement

The role the field of geology and mineral exploration plays in human life is enormous. Consider a typical activities and morning routine of a human being. His digital alarm clock is made of plastic produced from petroleum, and its LED display is made of materials such as silica and aluminum. He brushes his teeth using a plastic toothbrush and a toothpaste containing silica as an abrasive and fluoride from the mineral fluorite. His bathroom mirror is made of glass derived from beach sand and coated with silver or aluminum to make it reflective while it hangs on a wall that is most likely made of gypsum wallboard. He travels to work in a car or on a bus or bicycle, all made of a mixture of metal, plastic, and rubber components. These resources and many others that he uses within the first few hours of the day have to be mined and processed by machinery made of iron in factories powered by electricity.

Geological field mapping is one of the most applied technique used to delineate the geology and identify mineral resources of an area, and is frequently complimented by other techniques such as remote sensing, geophysical survey, geomorphological study and geochemical survey. Geological mapping finds its expression in a systematic and general study of the natural and artificial exposures of rocks with the aim of determining their composition, origin, age, structural and thermotectonic history as well as the application of their occurrence on the topographic map. The use of gold as an ornament, money and dentistry as well as its rarity and value, which dated back

to antiquity, makes it a precious metal with the attendant ‘rush’ for its exploration and exploitation worldwide.

Investigations around Alagbede area located about 25km northeast of the Kwara State University, Malete in Moro LGA of Kwara State witnessed a beehive of artisanal miners’ activities who are wining gold from the main quartz vein in the area using crude method. Preliminary investigations around the main quartz vein in the area have indicated interesting gold mineralization within a fracture zone that lies along the transcurrent fault line (figures 1) of the Anka-Yauri-Iseyin schist belt. The fact that this mineralization has neither been reported in any literature nor any known systematic studies carried out on it and considering the fact that the country is presently in dire need of diversifying her monolithic economy from petroleum to other resources particularly the solid mineral sector, has provoked my research interest in this area with a view to unravel the genesis, extent and age of the gold mineralization as well as attract investment.

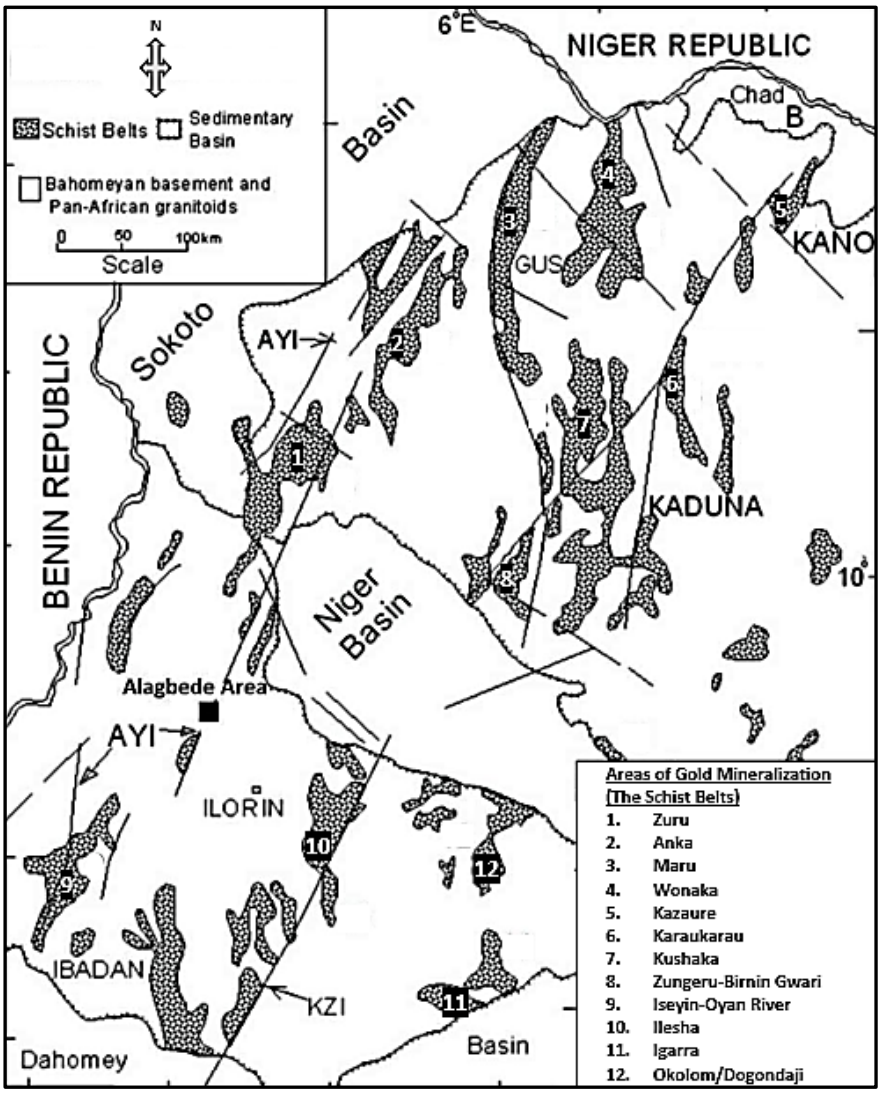


Fig. 1: Geological map of Nigeria showing major areas of gold mineralization and location of the study area (Modified after GSN 1994).

1.2 Location and Accessibility

The study area, located around Alagbede village, about 25km northeast of the Kwara State University, Malete in Moro LGA of Kwara State, covers the eastern part of 1:100,000 Igbetti sheet 201 and western part of 1:100,000 Share sheet 202. It is bounded by latitudes 8°42'N to 8°55'N and longitudes 4°20'E to 4°35'E, and extends for about 711 Km^2 in area. The area is underlain by rocks of the Basement Complex of Nigeria, which forms part of the Pan African mobile belt, situated east of the West African craton and the west of the Congo craton (figure 2 and 3). The area under investigation which includes the eastern half of the 1:50,000 Igbetti NE sheet 201 and the western half of the 1:50,000 Share NW sheet 202.

Accessibility in the study area is fairly good with the presence of some tarred and earth roads, in addition to numerous network of foot paths, animal tracks, etc that connects some of the major towns and villages with the remote farm settlements in the area. Accessibility to rock outcrops which are usually poorly exposed are, however, hindered due to the poor state of these earth roads which are sometimes inaccessible particularly during the raining season. Prominent settlements in the area includes *Malete, Elemere, Alagbede, Ejidongari, Yeregi, biala, Ajuba, Akbuyo, Olodan-Jagbe, Amukoko,* and *Jefe*.

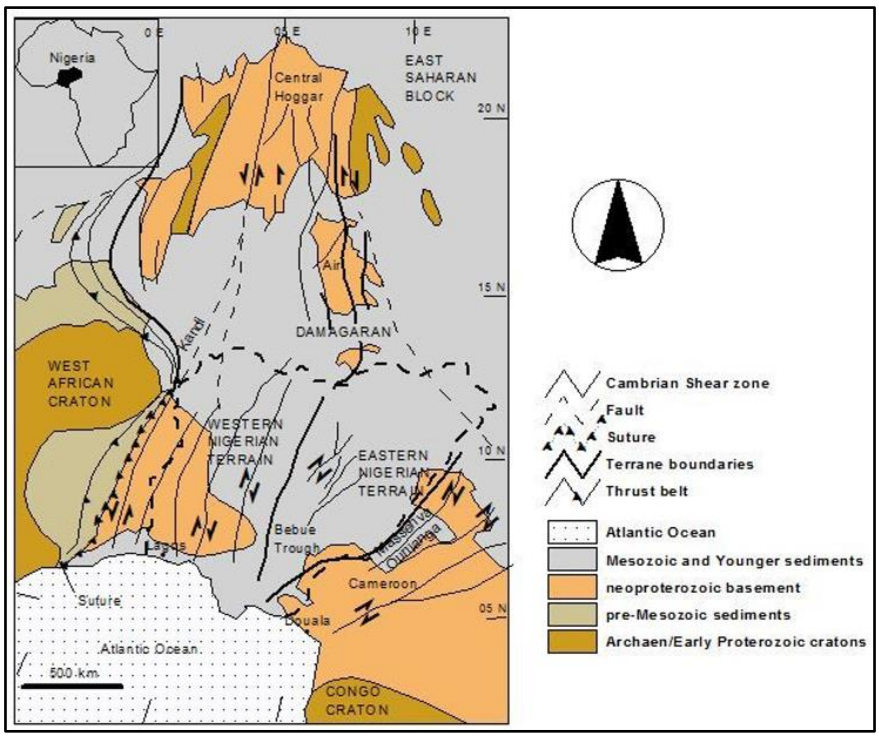


Figure 2: Geological map of the Hoggar–Aır–Nigeria province within the Late Proterozoic – Early Phanerozoic basement separating the West African and Congo cratons (After Ferre *et al*., 2002).

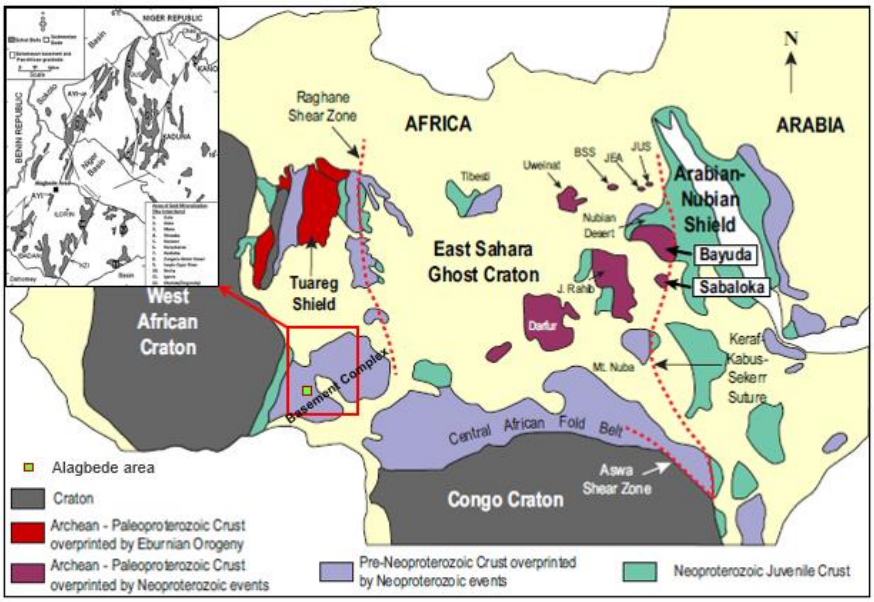


Figure 3: Generalized geological map of Northern Africa showing the age distribution of exposed Precambrian rock units (modified after Stern et al, 1984).

1.3 Statement of Problems

Available records revealed that several studies have been carried out on the Basement Complex of Nigeria by many researchers, providing detailed data and information on its lithological types and distribution as well as characteristics in terms of petrography, mineralogy, geochemistry, deformational episodes, structural association and petrogenetic affiliations of the various lithological units. Interestingly, some of the Basement Complex rocks are known to play host to several minerals of economic importance including industrial minerals such as clay, talc, feldspar, marble, iron ore and gemstones as well as some precious metals such as platinum and gold. Several previous studies have associated major primary gold deposit with the Schist belts which are particularly restricted to the western half of Nigeria. The following problems have, however, been identified which the present studies seek to unravel and proffer solutions:

i. There are no available records of systematic research work carried out on lithological characterization and the associated gold mineralization around Alagbede area;
ii. The geochemistry, petrogenesis and geochronological data on Alagbede area are largely unknown prior to the present study;
iii. Gold mineralization in Alagbede has neither been reported in any literature nor any known systematic studies carried out on it till date;
iv. Although many workers have carried out studies on the nature of gold mineralization, metallogeny, distribution, rock association and control, but not much information is

presently available on their specific age of mineralization and the specific geological events the gold mineralization was associated with.

1.4 Aim and Objectives

The primary aim of any geological field mapping exercise is ultimately to produce a geological map of the area mapped. This study attempts to analyze the various structural elements present on the rocks in the study area and tried to relate their occurrence to the geology of the area, with the objectives of understanding the structural history of the rocks and the deformational episodes that pervaded them in relation to the associated mineralization. In addition to the production of geological map, this work is also aimed at:

i. Determining the nature of the Alagbede gold occurrence; whether it is a mineralization or a deposit.
ii. Determining the pattern, extent, source, ore grade and age of mineralization;
iii. Determining the petrogenesis of associated rocks and geological history of the study area;
iv Formulating a genetic model for gold exploration in Alagbede area and other areas of similar geological setting;
v Establishing the geological event the gold mineralization is related to; in terms of its age (Eburnean or Pan-African) and its origin (syngenetic or epigenetic).
vi. Providing data and information on Nation's solid minerals.

1.5 Research Justification/Expected Results

The country is presently in dire need of diversifying her monolithic economy away from crude oil to include other areas such as tourism, agriculture and solid minerals. Any systematic study aimed at providing information on the Nation's solid mineral potentials is therefore a worthwhile venture towards achieving this objective. The present study around Alagbede gold deposit is therefore expected to proffer solutions to the stated research problems by making available scientific information on,

i. field relationship, distribution and petrological characteristics of rocks around the gold mineralization in Alagbede area;
ii. the geochemistry, petrogenesis and age of the gold mineralization in Alagbede;
iii. the specific control of mineralization, associated geological event as well as the ore grade for Alagbede gold deposit.

1.6 Physiographic Setting

1.6.1 Relief and Drainage

The study area is characterized by gently undulating topography, generally low lying and dotted with ridges and hills of various heights of bare rock exposures. The area is associated with moderate relief; while the highest elevation stands at 1,615ft above the sea level, corresponding to the top of *Oke Baba Hill* in the western part of the area, the lowest altitude lies below 750ft along *River Awun* in the northeastern region of the area. Most of the low-lying areas are either underlain by thick soil cover or ferruginized lateritic rocks.

Prominent rivers in the area, some of which are structurally controlled, include *Awun, Weru, Oloyin, Aremu, Afuniye, Laonu, Werufini, Kitifomi, Omidoyin* and *Ipabe*, most of which flow northeasterly and empty their loads into the bigger *Awun* river. A few of the streams and rivers are constrained by natural and artificial barrages, forming reservoir lakes (figure 4) that are used by the locals as their main source of water for laundry and domestic purposes.

1.6.2 Climate and Vegetation

The study area is under the influence of two major weather conditions, namely: the rainy season which commences in April and ends in September with its peak in July/August; and the dry season which starts in October and ends in March. The annual rainfall recorded ranges between 1250mm to 1500 mm while the annual temperature varies between 32-35^{o}C, with February to April being the hottest periods of the year. By February and March, the river channels are almost totally dry, providing easy access to rock outcrops exposed on dry river channels.

Tropical continental climate with high temperature and low rainfall (500-1000mm) gives rise to the type of vegetation found in the study area. The vegetation in the area is typified by Guinea savanna lying between the desert of the northern Nigeria and the tropical rainforest of the southern Nigeria. This is characterized by forested woodland savanna with trees contain few deciduous species. The vegetation is luxuriant in the rainy season with relatively scanty vegetation during the dry season when most plants shed their leaves and the grasses become dried up due to the fall in water table.

The Guinea savanna is characterized by scanty forest interspersed by small trees, parasites, climbers, epiphytes, shrubs and tall grasses with thick gallery forests occurring mainly along the stream paths (figure 5). The type of vegetation found in the study area include trees of average heights above the surrounding grasses of about 7m tall, comprising *Milicia exelsa* (Iroko), *Piptadeniastrum africanum* (Small leaf timber), *Astonia congensis* (Milk tree), *Eles genesis* (Palm tree), *Entandrophrama cilindricum* (Mahogany) and *Gmelina arborea* (Gmelina). Others include shear butter, Bamboo and locust bean trees. The thick vegetation is well developed in the northern part of the map making the area largely inaccessible except through the river channels.

1.7 The People, Occupation and Culture

Kwara state can best be described as a socio-cultural melting pot of all the three major ethnic groups in Nigeria namely the Yorubas, the Hausas and the Igbos. Ethnicity line around the study area is drawn along the Yorubas who constitute about 70% of the population and are the indigenous owners of the land and other ethnic groups including the Hausas, the Fulanis, and the Igbos. The main occupation of the people in the study area is farming, lumbering, mining and hunting by the Yorubas, trading and transport business by the Igbos and fishing, mining and cattle raring by the Hausas and Fulanis. The people are engaged in peasant farming which includes shifting and crop rotation on subsistence scale, where vegetable, yam (figure 6), cassava and cereals amongst others are the common agricultural produce. Young men often go for hunting during the dry season (figure 7). The main source of water for domestic purpose comes from the perennial rivers draining the area.

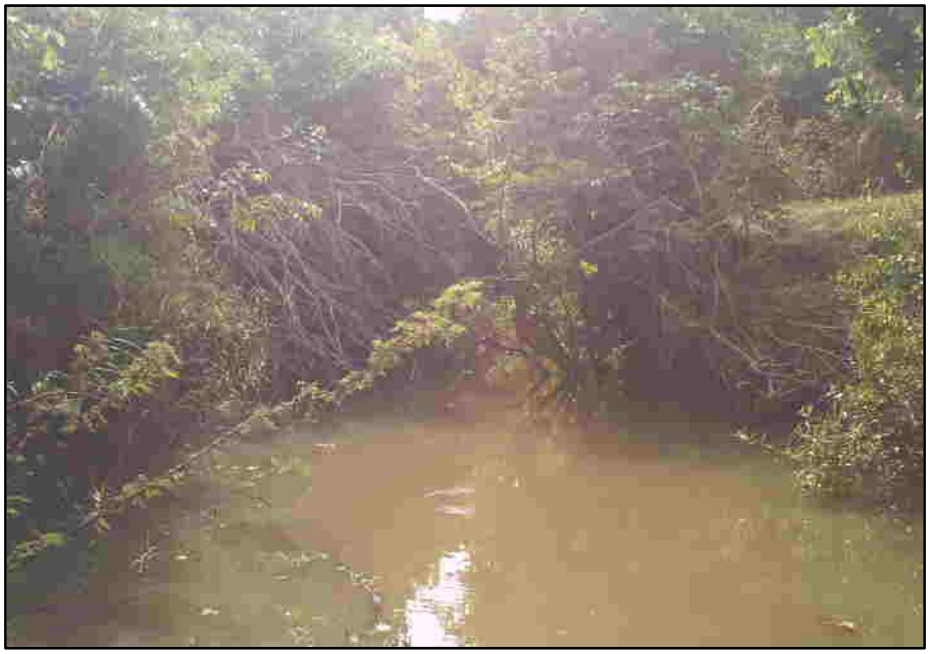


Figure 4: A thick vegetation bordering an artificial lake on River Werufini.



Figure 5: A farmland in the study area showing heaps of yam cultivation



Figure 6: Some locals on hunting expedition in the study area.

CHAPTER 2

REVIEW OF LITERATURE

2.1 An Overview of the Geology of Nigeria

Nigeria lies approximately between latitudes 4^{o}N and 15^{o}N and Longitudes 3^{o}E and 14^{o}E, within the Pan African mobile belt in between the West African and Congo cratons (figure 2 and 3). Oyawoye (1972), Cooray (1972), Elueze (1981), Caby (1981), Dada (1998, 1999) previously studied the general geology and geochronology of the basement rocks of Nigeria. On a regional scale, the geology is divided into two parts; the crystalline rocks and the sedimentary Basins. The geology of Nigeria is made up of three major litho-petrological components, namely, the Basement Complex (including Pan-African and older, i.e. Precambrian of ≥ +600 million years), the Younger Granites (Jurassic = 200 – 145 million years) and the Sedimentary Basins (Cretaceous to Recent, < 145 million years).

The crystalline rocks in Nigeria are distributed in a circular area in the north central, a triangular area in the west which runs into the Benin Republic, and a rectangular area broken into three parts by sedimentary rocks on the eastern border of Nigeria with Cameroun Republic. The Precambrian rocks of Nigeria, collectively known as the basement complex, occupy nearly half the total area of the country. The other half is covered by the Cretaceous and younger sedimentary rocks.

The Precambrian Basement complex of Nigeria has been extensively studied by various workers, providing substantial information covering its geology, geochemistry and geochronology. A review of previous literatures shows that the first major work carried out in the study area was by Oluyide

et. al, (1998), on the geology of Ilorin area with explanations on 1:250,000 series, sheet 50 (Ilorin) published in the Geological Survey of Nigeria bulletin 42. The work shows that Ilorin area is underlain almost entirely by rocks of the Basement Complex with minor patch of sandstone occurring in the extreme northeast around Share.

In the Ilorin sheet area, migmatite occurs in several varieties, depending on the criteria used to classify them. For convenience, a combination of structure and composition of the geometrical components is used to identify three groups which are lit-per-lit (stromatic) migmatites, porphyroblastic (ophthalmic) migmatites and agmatites. The lit-per-lit migmatite occur around Ilorin town and northwards, westwards, and southwards and are said to belong to the class of migmatites distinguished by Mehnert (1968) on the basis of structure as being stromatic or layered. The porphyroblastic migmatite occurrence is prominent at the east of Igbetti, where they give rise to topographic prominence, as well as in parts of Ilorin town and south of it, where they are terminated by a fault. The agmatite can be found in the southern part of Elerinjare near Idofian in the southeast occurring occasionally with other metamorphic rocks.

Egbuniwe (1982) regarded the areas covered by Ilorin sheet as a metamorphic terrain and considered the migmatite which underlain one-third of the sheet as the groundmass or country rock into which other rock types, especially the granites have been emplaced. Hockey et al, (1986) identified that the difficulty encountered in classifying the migmatite rocks appears to be quite persistent over the entire Basement Complex of Nigeria. According to Mehnert (1968), a migmatite is usually amenable to resolution into two lithologic/geometric elements; the palaeosome which

is the older pre-existing component which may be schist, gneiss or amphibolite and a narrow neosome which is the younger component often consisting of granite, aplite or pegmatite.

Spry (1969) defines granite gneiss as a massive homogeneous, leucocratic, granoblastic to porphyroblastic quartz feldspar or feldspar rock with separate parallel flakes of mica. The granite gneiss of Ilorin sheet are generally well exposed usually occurring as isolated domes and low ridges often strewn with boulders. A good example is the occurrence of the biotite-hornblende gneiss at the Sobi Hills, along the Shao-Ilorin road where the feldspars occur as pods or augen.

Previous work around Bode Saadu, about 30km northeast of the present study area and the headquarters of Moro Local Government Area of Kwara State, has shown that the basement complex rocks in the area comprise metaigneous and metasedimentary rocks which have been subjected to polyphase deformation and have subsequently been intruded by post-tectonic granite rocks (Okonkwo, 2001). The work of Okonkwo (1992) on the structural geology of the Basement complex rocks of Jebba area which lies at the northern margin of the Southwestern sector of the Basement complex of Nigeria shows that the area comprises of migmatitic gneisses, quartzites, quartz biotite schists and granite gneisses that have been intruded by undeformed Pan-African granite rocks.

Oyawoye (1965) recognized the following rock types as part of the Migmatite-Gneiss Complex including banded gneisses, augen gneisses and pegmatites. However, porphyroblastic gneiss occurs to the west of the granite body at Igbetti. The Migmatite-gneiss complexes of the Precambrian Basement Complex are Archean (Dada, 1989; Bruguier *et al*., 1994). Rahaman (1988)

grouped the rocks in this region as Migmatite-Gneiss Complex comprising largely of sedimentary series with associated minor igneous intrusives which have been altered by metamorphic, migmatitic and granitic processes.

From the evolution models of the southern Nigeria given by Rahaman, 1976, it appears that the major impetus for the formation of migmatites was widespread during the Eburnean orogeny of 2000±180 Ma ago. In the absence of absolute age determination of these rocks, only projections can be made. Grant (1969) gave the age of the Kaduna migmatites as 2220±30 Ma. In another study, Grant (1970) also obtained a whole-rock Rb-Sr isochron age of 2205±70 ma i.e Eburnean for the Ibadan granite gneiss. However, Rahaman et al, 1983 obtained an Eburnean age 1904+18 ma for the porphyroblastic (augen) gneiss of the Igbetti area.

2.2 Precambrian Basement Complex

The Precambrian Basement complex rocks are subdivided into four major petro-lithological units, namely:

i. The Migmatite-Gneiss Complex
ii. The Schist Belt (Metasedimentary and Metavolcanic rocks)
iii. The Older Granites (Pan African granitoids)
iv. Undeformed Acid and Basic Dykes

The Precambrian Basement Complex of Nigeria is exposed in five major areas, namely: Northeastern zone, Southwestern zone, Southeastern zone (extension of the Bamenda Massif into

Nigeria), Northeastern zone (the Hawal massif) and South-southeastern zone (the Oban Massif) (Obiora, 2005). Oyawoye (1965) subdivided the rocks of the Basement Complex into three major groups, namely:

i. The Older Meta-sediments consisting of calc silicate rocks, arkosic quartzite and high grade schists;
ii. The gneisses, migmatites and the Older granites; and
iii. The younger meta-sediments.

Rahaman (1976) subdivided the Basement Complex rocks into six major petrologic groups as follows:

i. Migmatite-Gneiss-Quartzite Complex
ii. Schist belt
iii. Charnockitic, gabbroic and dioritic rocks
iv. Rocks of the Older granite suite
v. Metamorphosed and unmetamorphosed calc-alkaline volcanics & hypabyssal rocks;
vi. Unmetamorphosed dolerite dykes, syenite dykes, etc.

2.2.1 Migmatite-Gneiss Complex

This is the commonest rock type in the Nigerian Basement complex. It comprises two main types of gneisses: the biotite gneiss and the banded gneiss. Very widespread, the biotite gneisses are normally fine-grained with strong foliation caused by the parallel arrangement of alternating dark

and light minerals. The banded gneisses, on the other hand, show alternating light-colored and dark bands and exhibit intricate folding of their bands. The migmatite gneiss complex is the oldest basement rock, and is believed to be of sedimentary origin but was later profoundly altered into metamorphic and granite conditions.

The older metasediments were also among the earliest rocks to form on the Nigerian Basement Complex. Many areas in northern, western and eastern Nigeria are covered by rocks of the Migmatite – Gneiss Complex including, but not limited to, Abuja, Keffi, Akwanga, Bauchi, Kaduna, Kano, Okenne, Egbe, Ajaokuta (in northern Nigeria); Ibadan, Ile-Ife, Akure, Ikerre, (in western Nigeria) and Obudu and the Oban Massif areas (in eastern Nigeria).

2.2.2 Schist Belt

The Schist Belts also referred to as metasedimentary and metavolcanic rocks comprise low grade, metasediment-dominated belts occupying N-S trending synformal troughs that are in-folded into the older Migmatite-Gneiss Complex. Prominent lithologies in the schist belts are aplites, semi-pelites, quartzites, marbles, banded iron formations, amphibolites, ultramafites and minor felsic to intermediate metavolcanics and greywackes (Rahaman, 2006). Some may include fragments of ocean floor material from small back-arc basins.

The schist belts are mostly developed in the western part of Nigeria (figure 7) where they have been extensively studied and classified into groups, though smaller occurrences are also found in the eastern part. The groups include: the Kusheriki Schist Group, the Karaukarau Schist Belt, the

Kazaure Schist Belt, the Maru Schist Belt, the Anka Schist Belt, the Zuru Schist Belt, the Iseyin-Oyan River Schist Belt, the Ilesha Schist Belt and the Igarra Schist Belt (Obaje, 2009).

2.2.3 Pan African Granitoid (Older Granite)

The Older Granites, a term introduced by Falconer (1911), is now preferably called Pan-African granitoids because of its merit on age and the fact that it covers several important petrologic groups formed at the same time (Dada, 2006). Pan African as a name was introduced by Falconer (1911) to distinguish this rock type based on morphology and texture from Jurasic, anorogenic younger granites" in north central Nigeria. The term "Pan African granitoid" covers group of rocks that include biotite and biotite-muscovite granites, syenites, charnokites, diorites, monzonites (Bauchite), serpentines, anorthosites, etc. (Rahaman, 2006). It is good to note that the Older Granites occur intricately in association with the Migmatite-Gneiss Complex and the Schist Belts into which they generally intruded. This means that the rocks occur in most places where rocks of the Migmatite-Gneiss Complex or of the Schist Belt occur (Obaje, 2009). The Older Granites, e.g the coarse-grained biotite-hornblende granites, have concordant foliation with the MGC or schists (Oyawoye 1965) though they vary in composition, texture and colour.

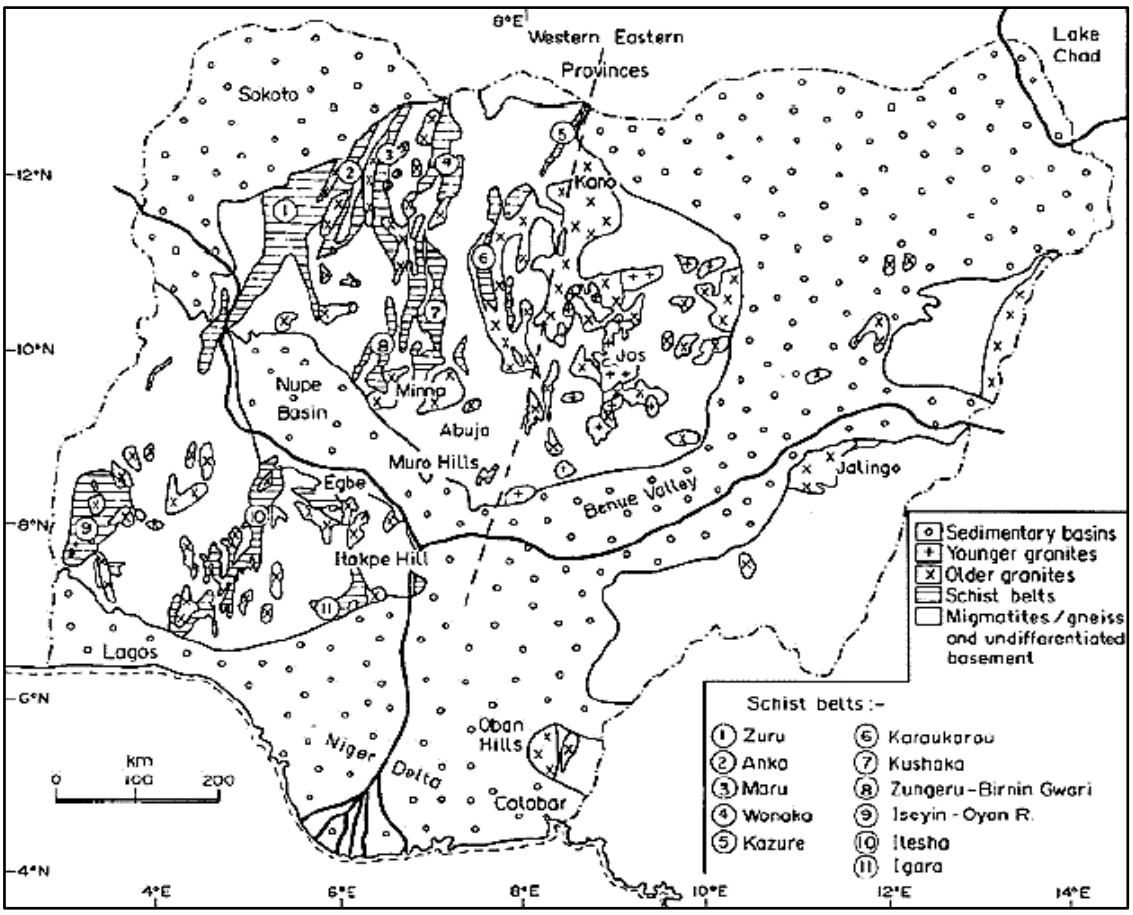


Figure 7: Geological map of Nigeria showing the schist belts (After Woakes et al., 1987)

2.2.4 Undeformed Acid and Basic Dykes

The undeformed acid and basic dykes constitute the crosscutting intrusives that are emplaced during late to post-tectonic Pan African time. This intruded into the three main rock units described above. They include felsic dykes that are associated with Pan-African granitoids on the terrain such as the muscovite, tourmaline and beryl-bearing pegmatites, micro-granites, aplites and syenite dykes (Dada, 2006); and Basic dykes (the youngest units) that are generally regarded as the less common basaltic, doleritic and lamprophyric dykes.

2.2.5 Jurassic Anorogenic Younger Granite

The Mesozoic Younger Granite ring complexes of Nigeria form part of a wider province of anorogenic magmatism. They occur in a zone 200km wide and 1,600km long, extending from northern Niger State to south central Nigeria. The most prominent are the younger granite (Jos plateau) in Northern Nigeria. The Jos Plateau covers an area 8,600 square kilometers in central Nigeria with elevation of 1,250m. The highest peak occurs in Shere Hills at 1,777m (above mean sea level). The younger granite are found in ring complexes (circular, semicircular and cresentic) controlled by ring fracture, dykes and faults.

The Younger Granites have been studied in great details mainly due to their recognition as the source of rich alluvial cassiterite deposits that had long been known to exist on and around the Jos Plateau as well as the fact that they provide comparative data for study of similar formations elsewhere in the world. Detailed field mapping of the ring complexes has demonstrated a

consistent succession of magmatic activity from volcanism to plutonism associated with the emplacement of mainly granite melts at high levels in the crust.

More than 50 ring complexes occur in Nigeria varying from <2 to >25 km in diameter (Kinnaird, 1981) with over 95% of the rocks composed of rhyolites, quartz-syenites or granites, while the basic rocks constitute the remaining 5%. Many of the rocks are strongly alkaline to peralkaline while others are aluminous to peraluminous in composition.

2.3 The Cretaceous-Tertiary Sedimentary Basins

The formation of the sedimentary basins in Nigeria is related to the geo-dynamic processes of the dispersal of the Gondwanaland which led to the separation of the African and south-American plates as well as the formation of the south Atlantic. The opening of the Atlantic in the Early Mesozoic era triggered the crustal fragmentation of west-central African craton into a rift system. In similar trends, isostatic adjustment following lithospheric movement on the bumps created by thermal mantle swell and its deflation after cooling are believed to be responsible for the crustal arches and adjacent intracrustal basins.

Another postulation is that of the reactivation of Pan African fault system in the underlying Precambrian basement. The Nigerian sedimentary terrain is underlain by eight major sedimentary basins whose successions range in ages from middle Mesozoic to Recent. Older sedimentary deposits were not preserved, probably because during the Paleozoic-early Mesozoic, what is now Nigeria was broad regional basement uplift, with no major basin subsidence for sediment

accumulation (Whiteman, 1982) and (Ofoegbu, 1985). Based on tectonic activities, the following types of basins area found in Nigeria:

i. Passive coastal margin basins;
ii. Intracratonic sag/faulted basins;
iii. Aulacogen; and
iv. Basin of tectonic inversion

The Nigerian sedimentary basins which are all rift-related, sediment-filled and ranges in ages between Cretaceous to Tertiary include:

i. Benin Basin/ Dahomey Embayment
ii. Bida/Mid Niger basin
iii. Sokoto/SE Iullemeden basin
iv. Borno/SW Chad Basin
v. Upper Benue Trough
    a. Gongola sub-Basin
    b. Yola Arm
vi. Middle Benue Trough
vii. Lower Benue Trough
    a. Mamfe Embayment
    b. Calabar Flank
    c. Abakaliki Anticlinorium

d. Anambra Basin

e. Afikpo Syncline

viii. Niger Delta

However, the sedimentary successions in these basins are broadly divisible into three:

i. Basal continental sandstones, siltstones, and mudstones;

ii. Middle marine shales and limestones interbedded with sandstones and siltstones; and

iii. Upper sandstone sequence that is continental or paralic (Whiteman, 1982) and (Ofoegbu, 1985).

2.4 Geology of the Basement Complex of Southwestern Nigeria

The area covered by the southwestern Nigeria basement complex is bounded by latitudes 7°N to 10°N and longitudes 3°E to 6°E lying within the equatorial rain forest region of Africa. The evolution of the Nigerian Basement complex during the Pan-African can best be discussed in the regional context of the Pan-African orogenic belt of West Africa. Geological and geophysical evidence from the western province of the belt and the cratonic margin has been used to erect geophysical evidence for the evolution of the belt (Grant, 1970; Burke and Dewey, 1972; Bertrand and Caby, 1978; Black *et. al*., 1979; Caby *et. al*., 1981). Essentially, the evolution of the belt is seen as a collision type orogeny with an eastward dipping subduction zone.

Initial crustal extension and continental rifting at the West African cratonic margin, about 1000 Ma, led to the formation of graben-like structures in the western Nigeria and the subsequent deposition of the rocks of the Schist belts. Closure of the ocean at the cratonic margin, about 600

Ma and crustal thickening in the Dahomeyan led to the deformation of the sediments, reactivation of the pre-existing rocks and the emplacement of the rocks of the Pan-African granites (McCurry, 1976). The granitoids have been emplaced within both the migmatite-gneiss complex and the Schist belts, and they occur in all parts of the Nigerian Basement Complex, though the extent of the Pan-African plutonism had not been fully understood (Rahaman 1976). Fitches *et. al.* (1985) have shown that the Older Granites are high level intrusions emplaced by stoping and diapiric processes in different parts of the country.

The migmatite-gneiss complex is considered to contain rocks of the Archaean age which have been deformed and modified several times prior to the Pan-African orogeny (Rahaman 1976). The Precambrian ages are mostly related to the Pan-African (900-450 Ma) thermotectonic event, with few imprints of the older events such as the Liberian, Eburnean and the Kibaran (Obiora, 2005). Evidence from the Ibadan area indicates that Archaean rocks included meta-sedimentary and meta-volcanic rocks which were deformed prior to the emplacement of the Eburnean granite-gneisses (Burke *et. al*., 1976). The main lithologies include the amphibolites, migmatite gneisses, granites and pegmatites. Other important rock units are the schists, made up of biotite schist, quartz schist, talc-tremolite schist and muscovite schist. The crystalline rocks intruded into these schistose rocks.

The basement complex rocks in south western Nigeria constitute over 75% of the surface area and evolved through 3 major geotectonic events:

i. Initiation of crust forming process during the Early Proterozoic (2000Ma) typified by the Ibadan (Southwestern Nigeria) grey gneisses considered by Woakes *et al*; (1987) as to have been derived directly from the mantle;

ii. Emplacement of granites in Early Proterozoic (2000Ma); and

iii. The Pan African events (450Ma-750Ma).

On the basis of wide geochemical analyses and interpretation, geotectonic studies, field mapping and plumbotectonics, Oyinloye (1998 and 2011) had suggested a modified sequence of ten evolutionary events of Burke et al; (1976) in the Southwestern basement complex of Nigeria, with the emplacement of dolerite dykes as the youngest as presented in Table 1.

Table 1: A modified sequence of events in the basement rocks in Ibadan-Ile-Ife-Ilesha area

SN	Sequence of Evolutionary Events in the South Western Nigeria basement complex
10.	Shearing, Chloritic and Zeolite mineralization of uncertain age.
9.	Emplacement of dolerite dykes and gold mineralization at about 550Ma (Oyinloye, 2006b)
8.	Formation of unsheared pegmatite, unfolded granitic veins of mid-Pan African age.
7.	Major remobilization and deformation in Early Pan-African
6.	Minor metamorphic deformation in Kibaran
5.	Emplacement of micro-diorite
4.	Emplacement of Ibadan-Ile-Ife-Ilesha Granite gneiss: F2 folding fabrics in Granite, Gneiss.
3.	Emplacement of micro-diorite dykes of uncertain age
2.	Emplacement of semi-concordant aplite sheets in the banded gneiss, collision of plates subduction of ocean slab into the mantle
1.	Deposition of ocean sediments covering the whole basement complex

2.4.1 Metamorphism in the basement rocks of southwestern Nigeria

Rahaman (1988) has used petrological evidence to suggest a medium pressure (Barrovian) and low-medium pressure types of metamorphism for the Precambrian basement rocks in south western Nigeria based on the occurrence of index minerals like chlorite, biotite and sillimanite in the rocks. He therefore concluded that metamorphism in all Nigerian Precambrian complex rocks especially that of Ife-Ilesha (Southwestern Nigeria) ranges from green schist to lower amphibolite metamorphic facies. However, Oyinloye (1992) on the basis of petrology, field and structural evidence reported that the prominent gneissic foliations observed on some of the gneisses suggest that metamorphism actually reached an upper amphibolite facies in the rocks of the basement complex in southwestern Nigeria.

Egbuniwe (1982) suggested 3 phases of metamorphism (M_1, M_2 and M_3) associated with 3 phases of deformations (D_1, D_2, D_3) within the crystalline rocks of the basement complex in northern Nigeria. According to this author M_1 represents a period of progressive metamorphism to lower amphibolite facies. M_2 is described as retrogressive and reached only green schist grade as did M_3. In the southwest, Boesse and Ocan (1988) recognized 3 phases of metamorphism but only 2 phases of deformation. M_1 is considered to be a syn-tectonic progressive phase of low to middle amphibolite facies with isoclinal folding, mineralogical banding and of staurolite, sillimanite and garnet.

2.4.2 Geochronology of the Basement Rocks of Southwestern Nigeria

It has been established that the Precambrian basement complex of Nigeria including Nigeria is polycyclic in nature, (Ajibade and Fitches 1988). Previous works on the basement complex of southwestern Nigeria show that the area had undergone 3 major orogenesis in:

i. Liberian (Archaean), 2500Ma-2750± 25Ma

ii. The *Eburnean* orogeny (Early Proterozoic), 2000Ma-2500Ma

iii The Pan African Orogeny, 450Ma-750Ma

Of all the above, the *Eburnean* and the Pan-African are major events which modified the Precambrian Geology of Nigeria including the Southwestern Nigerian basement complex. The Eburnean event is marked by the emplacement of the Ibadan granite gneiss in Southwestern Nigeria which has been dated to be 2500±200Ma (Rahaman 1988) and the pink granite gneiss at Ile-Ife Southwestern Nigeria dated 1875Ma based on U-Pb dating on Zircon. Thus Archaean to Pan African ages had been suggested for the basement rocks of the Southwestern Nigeria. Oyinloye (2006b), based on Pb-Pb model age suggested Archaean age (2750±25Ma) for the gneisses in Ilesha area, Southwestern Nigeria.

2.5 History of Gold Exploration in Nigeria

Several workers in various parts of the Nigerian Basement Complex including Turner (1983), Woakes and Bafor (1984), Akande *et al* (1988), Akande (1991), Garba and Akande (1992) and Garba (1996, 2000, and 2002) have identified gold within the Schist belts (figure 8) which are closely associated with N-S trending shear zones. The first report of gold occurrences in Nigeria was

described by Dunstan (1911) leading to small scale mining of the resource in 1913. However, official record of production of gold in Nigeria started in 1933 and peaked in 1943 when about 1.4 tons of gold were reportedly produced in the north western part of Nigeria (Russ 1957). A decline in production was recorded due to mines abandonment during the Second World War which led to a further decrease in production as a result of inadequate attention to exploration and development; a consequence of the discovery of crude oil in late 1950s and its domination of the nation's economy.

Gold has also been reported to occur in Nigeria as alluvial and elluvial placers as well as primary lodes in veins, veinlets or lenses associated with Late Proterozoic supracrustal (schist) belt and basement rocks. Although some gold occurrences have been mapped in the southeast, prominent gold mineralization in Nigeria are mostly restricted to the western half of the country (Garba 2001, 2002) as documented in *Iperindo*, Ilesha in the south west, *Okolom, Odogbe, Ejiba, Ndanaku, Bishewa* and *Alagbede* in the north central and *Birnin Gwari, Birnin Yauri, Anka, Maru* and *Mararaba* areas in the north west (Woakes and Bafor, 1982). The associated rocks include amphibolites, gneiss, phyllites, schist and quartzites (Wright et al, 1985).

Schwartz (1944), Cook and Chryssoulis (1990) and Ciobanu *et al*. (2012) have demonstrated the common occurrence of gold in many primary hydrothermal gold deposits as mineral inclusions (native gold or electrum and, less commonly, Au-(Ag) tellurides) or as invisible gold hosted by sulfide minerals such as pyrite and arsenopyrite. This, according to Seward (1973), Bancroft and Hyland (1990), Mikhlin and Romanchenko (2007), Williams-Jones *et al*. (2009), Liu *et al*. (2014),

Pokrovski *et al*. (2014) and Zhong *et al*. (2015a), is because gold is commonly transported as a bisulfide complex in hydrothermal fluids and subsequently precipitated in response to factors that reduce the contents of reduced sulfur in the solution, such as sulfidation or boiling, or through changes of pH or redox potential that reduce gold solubility.

The isotopic age of the basement complex rocks on which the schist belts, hosting most of the gold deposits, were unconformably deposited have been determined by many workers. For instance, Bruguier et al., (1994) obtained a U/Pb age on a zircon fraction extracted from an orthogneiss in Kaduna to be Early Archaean (>3.05Ga), while putting the age of emplacement and crystallization of the original granodiorite prior to its deformation at >3.65Ga. Ekwueme (1991) and Dada (1998) also obtained similar Archaean ages on Nigerian migmatites. Garba (2000) and Oyinloye (2006) have worked on the metallogenesis of gold within some parts of the basement complex.

2.5.1 Gold Exploration Techniques

The mode of occurrence of gold mineralization dictates the type of techniques to be adopted in exploring and exploiting the resource. However, the current research was carried out taking into consideration the structural setting, distribution of thermotectonic deformations and geology of the area. The work involved both geological mapping, geochemical analysis and age dating of rocks and grab samples of minerals Laser Ablation ICP-MS method. Exploration work undertaken includes:

i. Basic complimentary geological mapping;

ii. Systematic observation and study of the structural elements;

iii. Geochemical sampling of rocks and residual soils.

iv. Study and interpretation of the geological, geochemical and isotopic data obtained on rocks and mineral samples in the study area.

The dominance of alluvial and elluvial ores which are being won by artisanal miners in some rivers and streams within the Nigerian schist belt areas suggest a possible presence of sizable primary lode deposits awaiting discovery close to source. To locate these primary lodes, it becomes necessary to carry out a detailed litho-structural study of the areas under consideration. This, it is envisaged, will lead to the establishment of a litho-geochemical data base for anomalous areas of gold values with indications of the threshold and enhancements of other metal associations, anomalous elements and gangue minerals in the soil profiles with spatial associations with secondary gold mineralization.

2.5.2 Genetic Model

Breaking new grounds in gold exploration in virgin areas, such as the relatively unknown Alagbede gold goldfield, requires an understanding of the footprints of known gold deposits elsewhere and a combination of various exploratory methods in geology for the discovery of the orebodies. A section of this work is therefore focused on reviewing the characteristic features of the main types of gold deposits and their regional setting with a view to determining the best method to recognize the key components of their imprints so as to assist in determining and testing new approaches and techniques to locate new gold deposits at Alagbede area and elsewhere.

Each of the thirteen globally recognized gold deposit types has its own distinct features and characteristic environments of formation. Many of these gold deposit types have, however, been assigned into different major groups that are either formed by related processes or that are distinct products of large scale hydrothermal systems (Robert *et.al*, 2007), corresponding to the main classes of gold models, such as the orogenic, reduced intrusion-related, and oxidized intrusion-related, Carlin, Au-rich VMS, low-sulfidation, high- and intermediate sulfidation and alkalic epithermal deposits (Hagemann and Brown, 2000).

Most major deposits are known to fit into one of the three main models as outlined below, but some may possess unique characteristics which make them not easily classifiable into the schemes. It is therefore not unlikely to find a major discovery which could be of a different style of mineralization or may occur in an unusual geologic setting as favored by any of the classical models (Robert *et.al*, 2007).

Oxidized Intrusion-Related Model

These include the porphyry and high-sulfidation epithermal gold deposit types, as well as skarn and manto type deposits, formed in continental and oceanic convergent plate settings. These deposits are best regarded as components of large hydrothermal systems centered on high-level, generally oxidized, intermediate to felsic porphyry stock works.

Reduced Intrusion-Related Model

According to Lang et al. (2000), these model are better distinguished by Au-Bi-Te-As metal association occurring mainly in reduced siliciclastic sedimentary rock sequences and a close spatial and temporal association with moderately-reduced equigranular granitic intrusions (Thompson and Newberry, 2000) and are commonly orogenic deposits. These include the intrusion-hosted deposits of mesozonal to epizonal character, and more distal, sediment-hosted mesozonal equivalents.

Orogenic-Related Model

According to Robert et.al (2007), this model can be defined to include the syn-tectonic quartz-carbonate vein-type deposits and their equivalents that are formed at mid-crustal levels, including the turbidite-hosted and greenstone-hosted vein deposits, as well as the BIF-hosted veins and sulfidic replacement deposits. Orogenic deposits type consist of variably complex arrays of quartz-carbonate vein that display significant vertical continuity, commonly in excess of 1 km, without any significant vertical zoning. At the regional scale, a majority of deposits are spatially associated with regional shear zones and occur in greenschist-grade rocks, consistent with the overall brittle-ductile nature of their host structures.

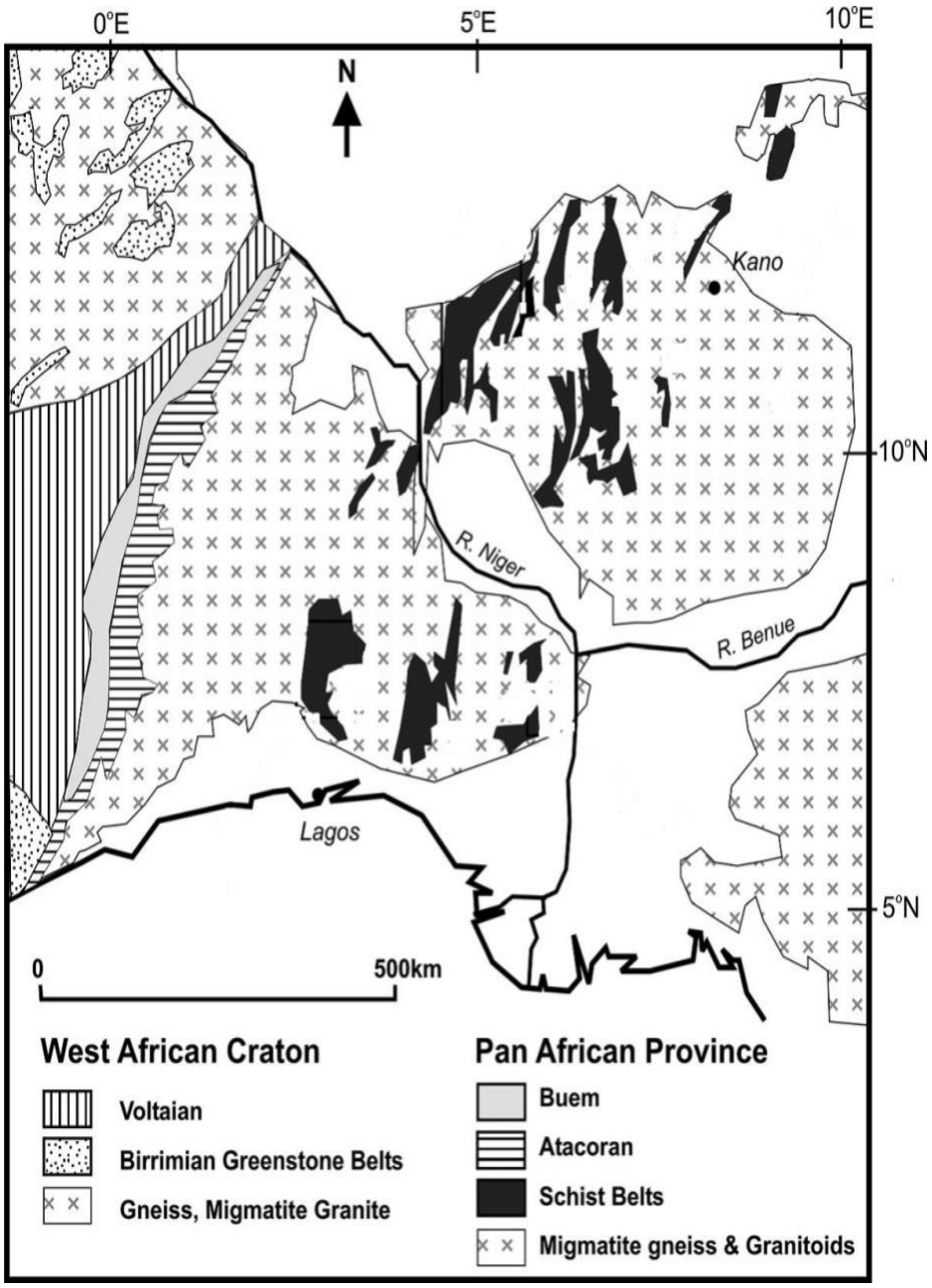


Figure 8: Simplified Geological map of Nigeria showing the schist belts on the eastern margin of the West African Craton (after Turner (1983).

CHAPTER 3

MATERIALS AND METHODS

3.1 Methodology

The methods used to accomplish the stated objectives of this research involved the acquisition of necessary geological and structural data based on the geological field mapping and laboratory analysis. These methods entail proper observation, identification and systematic description of the rocks, collection of structural data including types of folds and their various shapes, styles, amplitude, symmetry, axial trends, plunge and orientation as well as other structural features such as joint, shear, lineation and foliation. This was followed by rock characterization, map production and laboratory data analysis relating to elemental composition for rocks to determine petrogenesis and isotopic ratio for age dating of the rocks.

3.2 Fieldwork

Pre-field activities include consultation of relevant literatures, acquisition and study of topographic, satellite imagery and aeromagnetic maps and purchase of field equipment. Reconnaissance survey of the area was initially carried out for a period of one week during which the access roads to localities in the study area were first checked and mapped out with a view to preparing adequately for possible field challenges. The main geological mapping was carried out on a scale of 1:25,000 intensively over a period of six weeks using a combination of road and compass traversing methods to access rock outcrops. This aspect of the work involved a rapid litho-structural mapping and rock sampling around the study area. Global Positioning System (GPS) was

used for precise siting of rock outcrops while the compass clinometer was used to measure trend and dip of lithologies as well as other structural features observed on outcrops. Representative rock samples for petrographic studies were taken from outcrops with an eclogite hammer and chiseled into sample bags which were carefully labeled with permanent makers to avoid mixed-up. On the field, each rock outcrop was observed and described based on its lithological characteristics and association, mode of occurrence, cross-cutting relationships, macroscopic characteristics and structural features. Hand specimens were described based on macroscopic features including texture, colour, outcrop pattern and extent, and mineralogical composition. In all, a total of one hundred and four fresh rock samples were collected from various locations within the study area.

3.3 Laboratory Work

Laboratory activities including sample preparation, thin sectioning, petrography and ore microscopic studies were carried out at the geosciences laboratory of the Kwara State University, Malete, Nigeria and the geosciences laboratory of the Witwatersrand University, Johannesburg, South Africa. Geochemical analysis and interpretation was carried out at the mineral laboratories of the Bureau Veritas in Canada and the geosciences laboratories of the Witwatersrand University, Johannesburg, South Africa. Spectron Electron Microscopy (SEM) and Cathodoluminiscence (CL) imaging of 7 rock samples were done at the University of Johannesburg, South Africa. Radiometric age dating using the in situ LA-ICP-MS technique for U-Th-Pb on zircon recovered from 7 rock samples was carried out at the EarthLab of the Witwatersrand University, Johannesburg.

Interpretation of rock petrogenesis was achieved using Petrograph, isotopic data reduction by Iolite and age data interpretation by VizualAge and Isoplot 3.7.

3.4 Geochemical Laboratory Instrumentation

A total of 42 rock samples were prepared for geochemical analysis for rock characterization and petrogenetic studies. X-ray Fluorescence (XRF) was used to determine the major elements concentration while the Inductively Coupled Plasma Mass Spectrometer (ICP-MS) was used to determine the composition of trace elements, including the rare earth elements for petrogenetic studies. The procedure for laboratory geochemical analysis involved sample preparation by pulverization and digestion before applying the XRF and ICP-MS techniques. For a start, the fresh rock sample to be analyzed was broken with the aid of a jaw crusher into gravel-sized pieces and then pulverized into powder using the disk grinder preparatory to the production of fusion disks for XRF and analysis.

3.4.1 Preparation of Fusion Disks for Major Element Analysis by XRF

i. Clean platinum (Pt) (95% Pt and 5% Au) crucibles and silica porcelain (LOI) dishes were placed in the furnace (figure 9) at 1020^{o}C for half an hour to remove any organic residues and impurities.

ii. The Pt crucibles and LOI dishes were removed from the furnace and allowed to cool in a desiccator (containing silica crystals to absorb the heats) for 25 minutes and 1 hour respectively.

iii. Once clean and cool, approximately 1g of each sample was placed into each LOI dish, recording both the LOI dish ID number and the weight of the LOI dish on the weight chart excel sheet on the laptop before and after sample addition.

iv. The LOI dishes (with the samples in them) were placed back in the furnace and ignited at 1020^{o}C for 40 minutes after which the dishes were removed from the furnace and allowed to cool in a desiccator for 1 hour.

v. Approximately 1.75g of flux (Spectroflux 105) composed of 47% lithium tetraborate, 37% lithium carbonate and 16% lanthanum oxide, was weighed into each Pt crucible, recording both the Pt crucibles ID numbers and the weight of the Pt crucibles on the weight chart excel sheet on the laptop before and after flux addition.

vi. The Pt crucibles (with flux in them) were then placed back in the furnace and ignited at 1020^{o}C for 40 minutes after which they were removed and allowed to cool in a desiccator for 25 minutes.

vii. Once both the LOI dishes and the Pt crucibles have cooled down, the after ignition weights of the LOI dishes were measured and recorded in the excel sheet to determine the samples LOIs. Similarly, the after ignition weights of the Pt crucibles were measured and recorded to obtain the actual flux weights.

viii. The Pt crucible ID and LOI dishes ID numbers were matched with the samples, and approximately 0.34g of the pre-ignited samples were measured from the LOI dishes into

each corresponding Pt crucibles. The weight of the Pt crucibles were recorded after the addition.

ix. The remaining ignited samples from the LOI dishes were transferred into corresponding pre-labelled vials and store for future use while the LOI dishes were cleaned.

x. The Pt crucibles (with flux + sample) were placed in the furnace and ignited at 1020^{o}C for 50 minutes after which the crucibles were removed from the furnace and allowed to cool in a desiccator for 25 minutes.

xi. The Pt crucibles (with the fused mixture) were weighed, recorded and returned to the furnace at 1020^{o}C.

xii. The fused mixtures were individually poured and pressed into the fusion beads with *the 'dye press'* in the furnace room on the hot plate which had been switched on at least 1 hour prior to pouring.

xiii. The beads were allowed to set for 90 minutes on the hot plate set at 60^{o}C before switching off the hot plate.

xiv. The crucible ID numbers were matched with the fused beads which were allowed to anneal overnight and appropriately labeled the following day.

xv. The LOI values, sample weights, flux weights and the count rates obtained from the XRF machine (figure 10) where the fused beads were irradiated with the X-ray beam, were used to calculate the major elements concentrations of the samples in percentages.

3.4.2 Sample Dissolution for Trace Element Analysis by ICP-MC

The ICPMS is a more sensitive machine and the procedure for sample digestion is a bit more complicated and carried out substantially in the fume hood (figure 11a) to prevent health hazards which may be associated with the digestion processes.

i. 50mg of the pulverized rock sample is weighed into the weighing boat and transferred into the Teflon vessel. The Kevlar sleeves were used to keep the Teflon vessels in shape so as not to lose its shape under intense heat.

ii. 6ml of 2:1 HF:HNO_3 was added to the sample in the Teflon vessel and the cap was tightened.

iii. The Teflon vessel was placed in the microwave digester (figure 11b) at 190^{o}C for 40-60 minutes and then allowed 30 minutes to cool down before removal.

iv. The Teflon was taken to the fume hood, where the sample was then transferred into a labeled 15 ml Savillex beaker. The cap and the vessel were carefully rinsed with 10% nitric acid to ensure that no sample was lost.

v. The sample was dried down on the hot plate at 70 ^{o}C in the fume hood, after which 2ml nitric acid was added, capped and kept on the hot plate at 60 ^{o}C for 24 hour. Then dried down to 70^{o}C.

vi. When dried, the sample was further added a 2ml nitric acid and again dried down on the hot plate at 70 ^{o}C.

i. The sample was then removed from the hot plate and added 300ml nitric acid, capped, kept overnight and the digested sample was then ready to be fed into the ICPMS machine (figure 12) for analysis.

3.5 Heavy Mineral Separation for U-Pb on Zircon Dating

The mineral separation preparation was carried out at the mineral separation laboratory where the rock samples were processed for zircon separation. The knowledge about the relative abundances of minerals in the rocks as obtained from petrographic studies was used as a guide to the quantity of the rock sample to be processed for zircon separation. For this work, about 1 to 1.2kg of rock samples were crushed for mineral separation which involve the following procedures:

3.5.1 Rock Crushing

1. The fresh rock sample is broken into gravel-sized pieces (1 – 2” pieces) using a jaw crusher.
2. A disk grinder was then used to break the gravel-sized rock samples down to sand-sized particles.
3. The samples were sieved using the 50 and 200 micron meshes to obtain the fine fractions which were washed in distilled water thoroughly and the supernatant that is dusty were decanted.
4. The fraction is then placed in an oven to dry for gravity separation on the Wilfley Table.

3.5.2 Density Separation using a Wilfley Table

The Wilfley table is a gravity separator with a tilted separation surface on which a series of grooves have been cut at an angle to the tilt.

1. The fine rock fraction was gradually fed on to the high side of the surface and a controlled source of water was allowed to flow over it to move the grains while the tabled surface is vibrated.
2. The heavier grains flow through the first two grooves of the upper tilt and collected in a designated glass beaker on the upper slope while the lighter grains were washed down the grooves of the lower tilt and were also collected into another glass beaker on the lower slope surface.
3. The Wilfley table was used to significantly separate the light fractions from the heavies and the heavies were then further subjected to heavy liquid separation.



Figure 9: (a) Furnace used for Platinun crucibles (b) Lenton Scientific Furnace used for LOI crucibles.



Figure 10: XRF Machine (PANalytical) at the EarthLab of the University of Witwatersrand, SA.



Figure 11: (a) ESCO Lab Fume hood showing Savillex beakers on the hot plates, Teflon vessels and caps (b) Microwave Acceleration Reaction System (MARS-6 CEM) used for sample digestion at the EarthLab of the University of Witwatersrand, South Africa.



Figure 12: RESOlution and Perkin Elmer ICPMS machines at the EarthLab of the University of Witwatersrand, South Africa.

3.5.3 Density Separation using Heavy Liquids

Different minerals are known to possess different densities which could be used to separate a mixture of minerals with different densities when passed through a liquid with an intermediate density. While the grains with densities less than that of the liquid will float, the grains with densities greater than that of the liquid will sink. Most common rock-forming (silicate) minerals generally have densities ranging between 2.5 and 3.5 g/cc, making bromoform (density = 2.84 g/cc) and diiodomethane (density = 3.31 g/cc) very suitable liquids for density separation. The densities of bromoform and diiodomethane can be adjusted by adding acetone (density of about 0.7 g/cc) so as to bring their densities slightly close to those of the minerals to be separated. The following procedures were observed to separate the heavy minerals from where transparent zircons crystals needed for U-Pb dating were extracted:

1. The heavy fraction from the Wilfley gravity separation was placed in the separatory funnel and the bromoform was added in a fume hood to prevent the possible health hazards from the halogenated organic heavy liquids.
2. The funnel was left for some time to allow the fraction to separate; while the light minerals floated, the heavies sank to the bottom of the funnel.
3. The separatory funnel was then opened and the heavy minerals transferred onto a piece of weighing paper in a funnel where the heavy liquid was allowed to drain away in the fume hood.

4. The heavy mineral separate was then washed with acetone, put in the ultrasonic machine for 5 minutes to remove the toxic odour of the heavy liquid and then left for some time in the oven to dry.
5. The dried separate was spread on a clean while paper while a magnet was moved across it (without touching) to pick up all strongly magnetic minerals before the remaining non-magnetic separate was then pass through the Frantz Isodynamic Separator.

3.5.4 Mineral Separation using Magnetic Susceptibility

The Frantz Isodynamic Separator generates electromagnetic field which filters minerals based on their specific magnetic susceptibility. Frantz is typically set up with a slope of 5^{o} to 10^{o} and a tilt of 10^{o} to 15^{o} away from the operator. The electric current was then varied from 0.3A to 1.2A to separate the different minerals as they move down the chute. The slope angle and the feeding rate could be adjusted to speed up (or slow down and improve) the separation process. The feeding funnel was screwed into the chute while the two metal beakers were placed at the end of the chute.

1. The dried heavy fraction from the heavy liquid separation (after the strongly magnetic fraction has been removed with a magnet) was poured into the feeding funnel.
2. The Frantz separator was plugged into the power supply, the magnetic field and the oscillator turned on and the current control knob was slowly turned clockwise to the required current starting from 0.3A to 1.2A and sometimes up to 1.5A if necessary.

3. The result of the electromagnetic separation was observe as the mineral fraction separates through the chute into the two beakers.
4. At the end of each separation process, the two fractions were examined optically for purity using a binocular and whenever the separation was unsatisfactory, the amperage and tilt angle was adjusted to improve the quality of the separation.
5. The process was repeated many times by progressively increasing the amperage until the best separation possible was achieved.
6. Successive magnetic fraction which was collected in the beaker on the outside was stored in a labeled bottle bearing the sample name, tilt angle and amperage for that separation.
7. Table 2 (after Rosenblum, 1958 and Flinter, 1959) showing the standard magnetic susceptibilities of minerals in the Frantz Isodynamic Magnetic Separator was used as a guide to the appropriate settings for the separation of different minerals.
8. On completion of the separation, the Frantz system was shut down the sieves and the Frantz were cleaned with compressed air and a brush.
9. The final heavy mineral separate was then observed optically under the reflective binocular microscope for purity while the transparent zircon crystals were then hand-picked, mounted, cut and polished preparatory to U-Th-Pb on zircon dating.

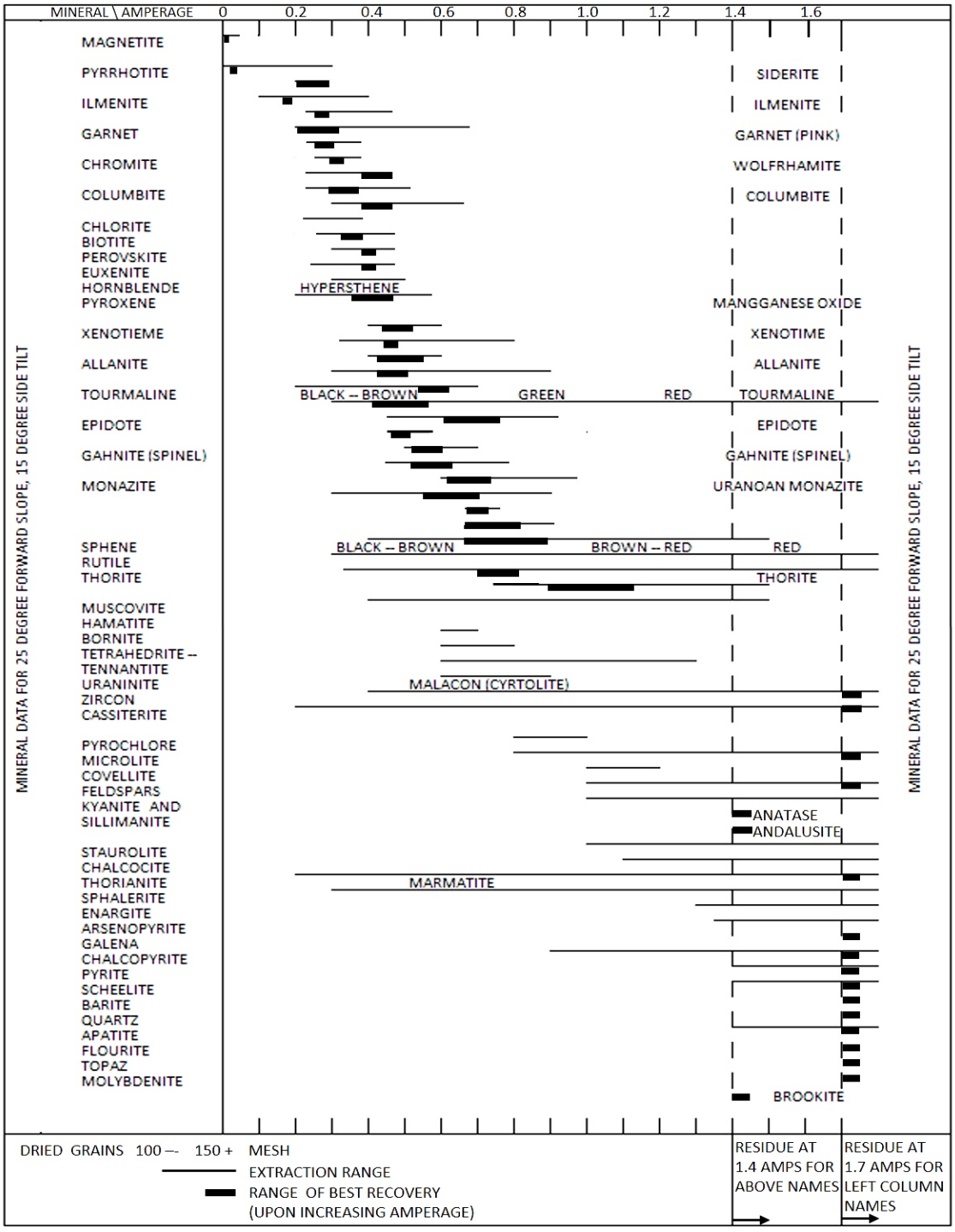
3.6 Laser Ablation Technique

The ICP-MS machine was connected to an UP-193 solid-state laser with an automatic positioning system. The laser spot size, energy density and repetition rate were set to 36 µm, 8.5 J/cm^2 and 10

Hz respectively. The laser sampling was comprised of pre-ablation (5 seconds), sample-chamber flushing (20 seconds) and sampling ablation (40 seconds). The ablated material was carried into the ICP-MS through a high-purity helium (He) gas stream with a flux of 0.8 L/min. The entire laser path was fluxed with nitrogen molecule (N_2) (15 L/min) and argon (Ar) (1.15 L/min) to increase energy stability. The Concordia ages and diagrams were obtained using Isoplot 3.75 (Ludwig, 2003). Common lead was corrected following the method of Andersen (2002).

Data corrections were achieved by comparing raw data of analyzed samples to raw data of a matrix-matched calibration standard GJ-1 or alternatively 91500 (Wiedenbeck et al., 1995). To check if instrumentation and data reduction worked, an external control standard (Plesovice) for baseline and calibration was included in the analysis and returns an age that agrees within errors to a published reference value (eg. Plesovice with an age of 337 Ma) so as to monitor the deviation in the age measurements/ calculations, using the VisualAge add-on within iolite splines.

Table 2: Magnetic susceptibilities of common minerals. Data from Rosenblum (1958) and Flinter (1959) for the Frantz Isodynamic Magnetic Separator. Thick lines indicate the frequent range; the thin lines indicate the fuller range that may occasionally occur.



CHAPTER 4

LITHOLOGY, STRUCTURE AND GEOCHEMISTRY OF ROCKS IN ALAGBEDE AREA

4.1 Local Geology

Alagbede area is underlain by rocks of the southwestern sector of the Nigerian basement complex which include the migmatite-gneiss complex comprising the biotite-gneiss and migmatitic gneiss; the metasediments including massive and foliated quartzite, quartz-mica schist, meta-ultramafite represented by the talc-tremolite-actinolite schist as well as various granitic suites ranging from porphyroblastic granite, porphyritic granite, porphyritic diorite, medium- to coarse-grained alkali granite, medium-grained granodiorite, alkali syenite, pegmatite/aplite and vein quartz. These lithological units are presented in figure 13 (a and b) and listed as follows, some of which show metamorphic imprints that are indicative of various degree of deformation.

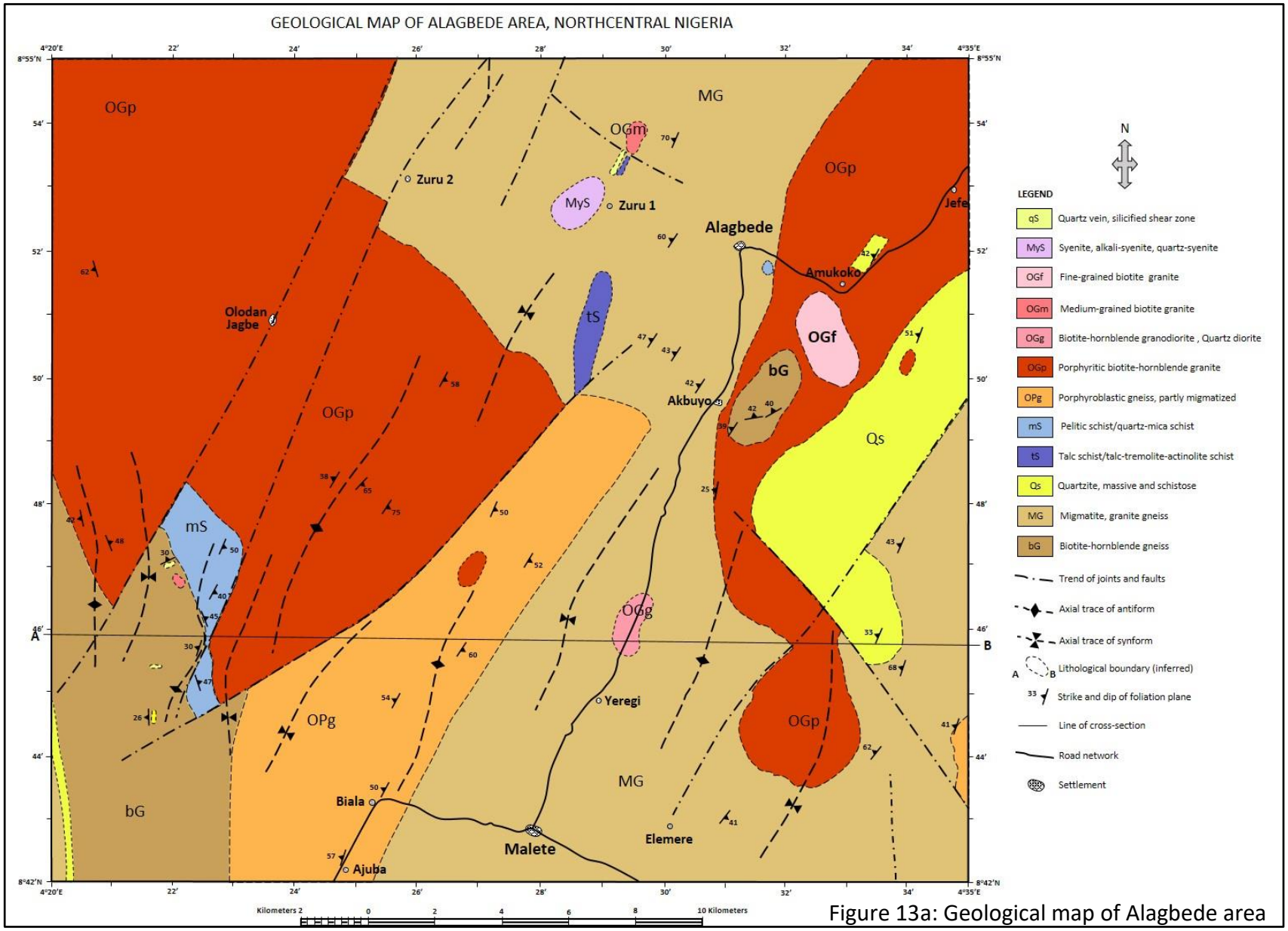


Figure 13a: Geological map of Alagbede area

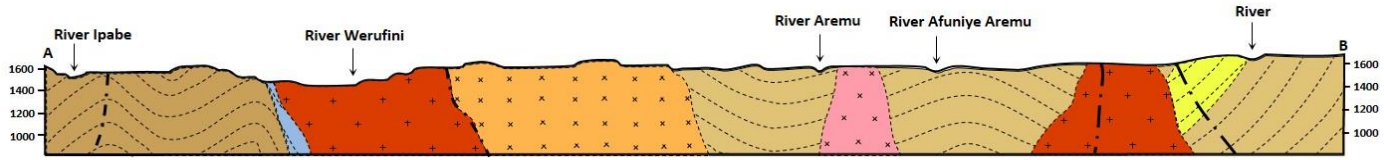


Figure 13b: Geological cross-section of Alagbede area.

4.1.1 Biotite Gneiss

Occurrence and Field Characteristics

The rock occurs as a biotite quartzo-feldspathic gneiss of tonalitic to granodioritic composition. It outcrops frequently as deformed concordant lenses and rafts within the migmatitic gneiss terrain and sometimes as mafic xenoliths within the widespread granitic rocks of the Alagbede area. Hand specimen observation indicates that the rock is composed of alternating felsic and mafic bands with a characteristic fine foliation on millimetric scale (figure 14). The felsic bands are composed of quartz, plagioclase feldspar and subordinate muscovite while the mafic bands comprised essentially of biotite and hornblende. In some instances, the various gneissic units outcrop as discrete mappable bodies such as the fine-grained flaggy biotite gneiss outcropping between Gbara and Ejidongari villages (figure 15) and the biotite-hornblende outcrops in the eastern and southwestern parts of the study area respectively.

Petrography

In thin section, the biotite gneisses show variable grains of minerals sizes which are closely packed and strongly foliated (figure 16). The rock is composed of quartz + andesine $\pm$ labradorite $\pm$ bytownite + biotite + orthoclase + hornblende $\pm$ muscovite $\pm$ ore mineral. Quartz is colourless under PPL and easily distinguished by its low birefringence uniaxial positive, and absence of cleavage and alteration. Quartz shows wavy extinction with triple junction. Plagioclase is anhedral in shape and ranges from andesine, labradorite and bytownite with low relief and colourless under

a plane polarized light. Its crystals are strongly pleochroic and are characterized by polysynthetic (repeated) twinning; where the crystal is divided up, into narrow lamellae with alternate orientation. The anorthite content of the plagioclase varies from 30-80%. Biotite is seen as large plates, brown to dark green in colour and contains inclusions of opaque minerals.

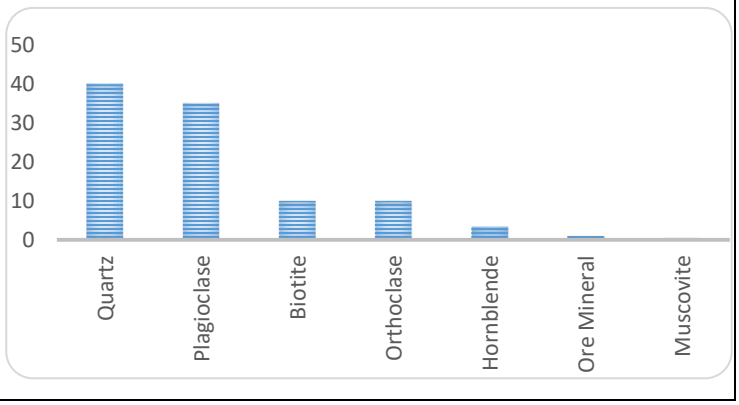
The biotite crystals are elongated and define the strong foliation pattern observed. It shows pleochroism from dark brown to black and a perfect cleavage in one direction. Biotite occurs as lath-shaped euhedral to subhedral crystals and are aligned in a preferred direction. Orthoclase shows cloudy anhedral crystals. Hornblende is anhedral in shape. The modal composition and mineralogical description of the rock's thin section studies are presented in table 3 below.



Figure 14: Hand specimen sample of the biotite gneiss showing millimetric foliation.



Figure 15: A bouldery outcrop of a flaggy biotite gneiss along Gbara and Ejidongari road.

Table 3: Modal concentration of minerals in Biotite Gneiss		
Mineral	Modal Composition (%)	Bar chart
Quartz	40	
Plagioclase	35	
Biotite	10	
Orthoclase	10	
Hornblende	3.5	
Ore Mineral	1	
Muscovite	0.5	

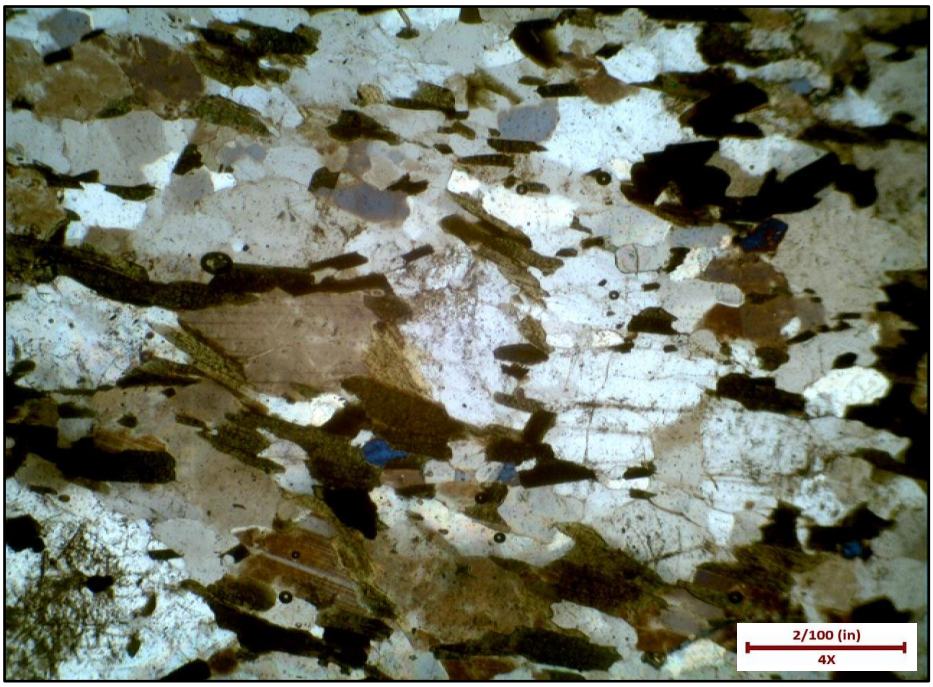


Figure 16a: Photomicrograph of biotite gneiss in thin section under plain polarized light.

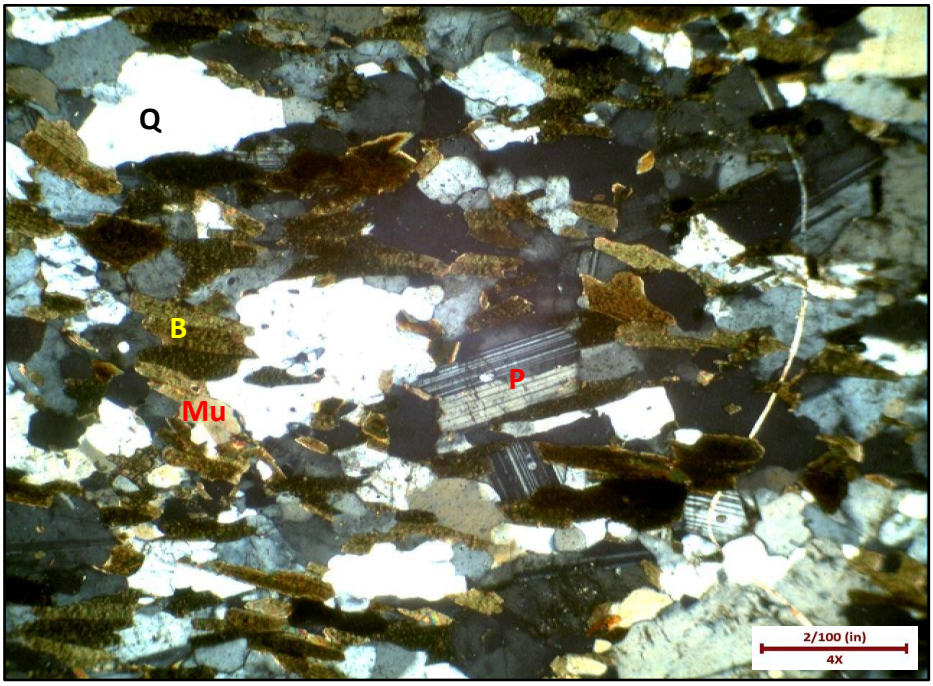


Figure 16b: Photomicrograph of biotite gneiss in thin section under crossed polarized light. (B=biotite, Mu=muscovite, P=plagioclase, Q=quartz)

4.1.2 Migmatitic Gneiss

Occurrence and Field Characteristics

The rock underlain about 45% of the study area and in fact constitutes the country rock hosting other rock types in the area. The migmatitic gneiss outcrops was observed to have been exposed in a variety of ways; mostly as broad low lying exposures and sometimes as low ridges and inselbergs. The migmatitic gneiss also occurs along the break of slope of some prominent laterite capped hills. The palaesome in the migmatitic gneiss are made up of biotite gneiss, granite gneiss as well as augen gneiss which are mostly fine- to medium-grained in hand specimen, the occurrences of whose on a single outcrop together with the intruding leucosomes comprising of granitic rocks, pegmatite, aplite and vein quartz, led to the formation of a number of migmatitic structures which were mapped as ophthalmic, schollen and stromatitic migmatites (figures 17, 18 and 19). The gneissic portion of the rock sometimes contains abundant nodules of almandine garnet which are restricted within the mafic bands.

Petrography

Observations on hand specimen samples of the migmatitic gneiss shows leucocractic bands which are persistently thicker and are quartzo-feldsparthic in composition, alternating with mafic bands which are thinner and are composed predominantly of biotite and hornblende. Under the thin section (Figure 20), the rock is composed of quartz + labradorite $\pm$ andesine + orthoclase $\pm$ microcline + biotite + hornblende $\pm$ myrmeckite $\pm$ muscovite $\pm$ sphene. Quartz is subhedral with triple junction. Plagioclase ranges from andesine to labradorite with anorthite content from 45-

70%. It occurs as large anhedral to subehedral crystals with polysynthetic twining and disintegrates to sericite at the edges.

Crystals of orthoclase are seen as dirty cloudy tabular minerals. Microcline occurs in short tabular euhedral crystals. Some largely altered phenocrysts of feldspar are embayed by biotite crystals. Biotite is seen as euhedral to subhedral tabular crystals, are aligned in the same direction, pleochroic from dark brown to dark green, undergoing alteration to muscovite and bears micro cross-cutting joints. Small biotite crystals are poikilitic in quartz. Muscovite replaces biotite and sometimes occurs as fracture filling laths along intra-granular micro joints. Isolated crystals of sphene as seen as showing high relief. Table 4 shows the modal concentration of minerals in the migmatitic gneiss.



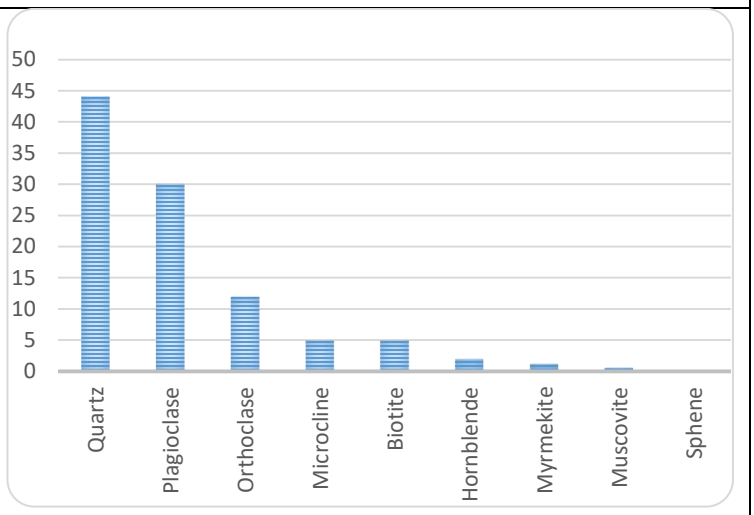
Figure 17: A section of an outcrop of migmatitic gneiss showing ophthalmic structure.



Figure 18: A section of an outcrop of migmatitic gneiss showing schollen structure.



Figure 19: A section of an outcrop of migmatitic gneiss showing stromatic structure.

Table 4: Modal concentration of minerals in migmatitic gneiss		
Mineral	Modal Composition (%)	Bar chart
Quartz	44	
Plagioclase	30	
Orthoclase	12	
Microcline	5	
Biotite	5	
Hornblende	2	
Myrmeckite	1.2	
Muscovite	0.6	
Sphene	0.2	

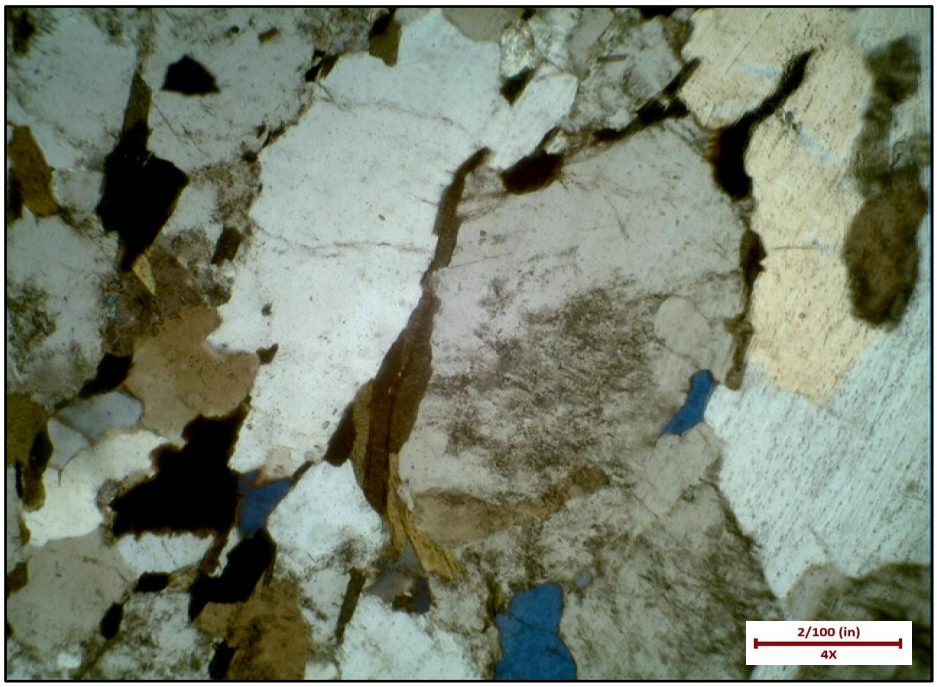


Figure 20a: Photomicrograph of the migmatitic gneiss in thin section under plain polarized light.

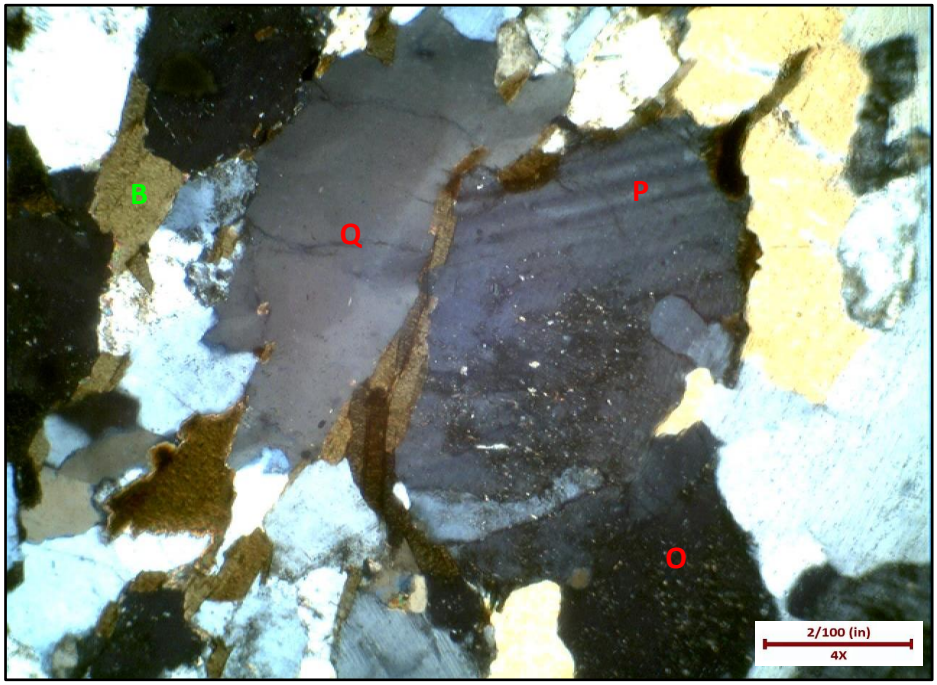


Figure 20b: Photomicrograph of the migmatitic gneiss in thin section under crossed polarized light. (B=biotite, O=orthoclase, P=plagioclase, Q=quartz)

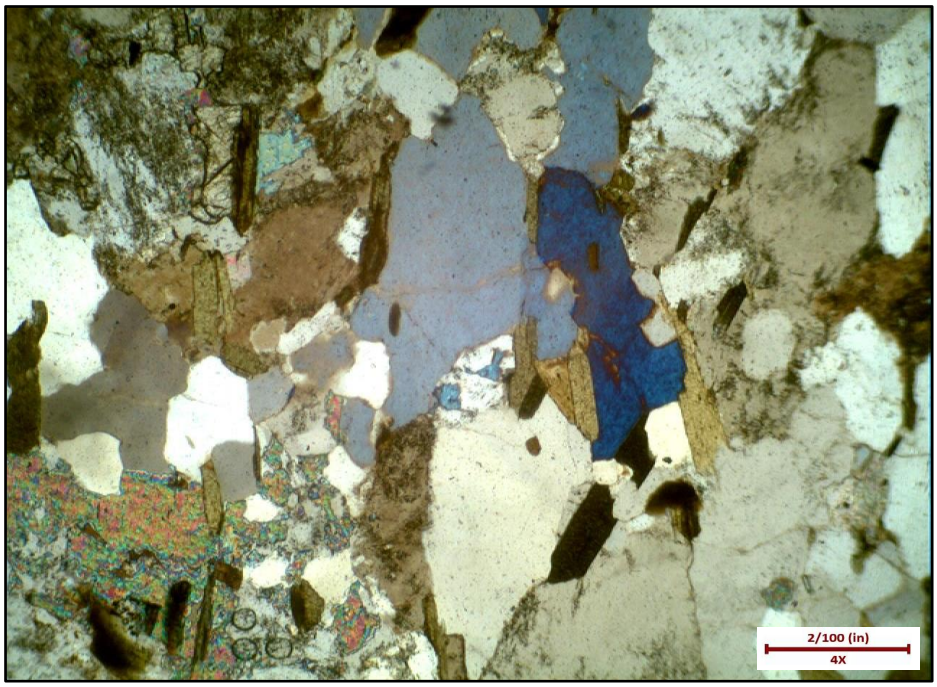


Figure 20c: Photomicrograph of the migmatitic gneiss in thin section under plain polarized light.

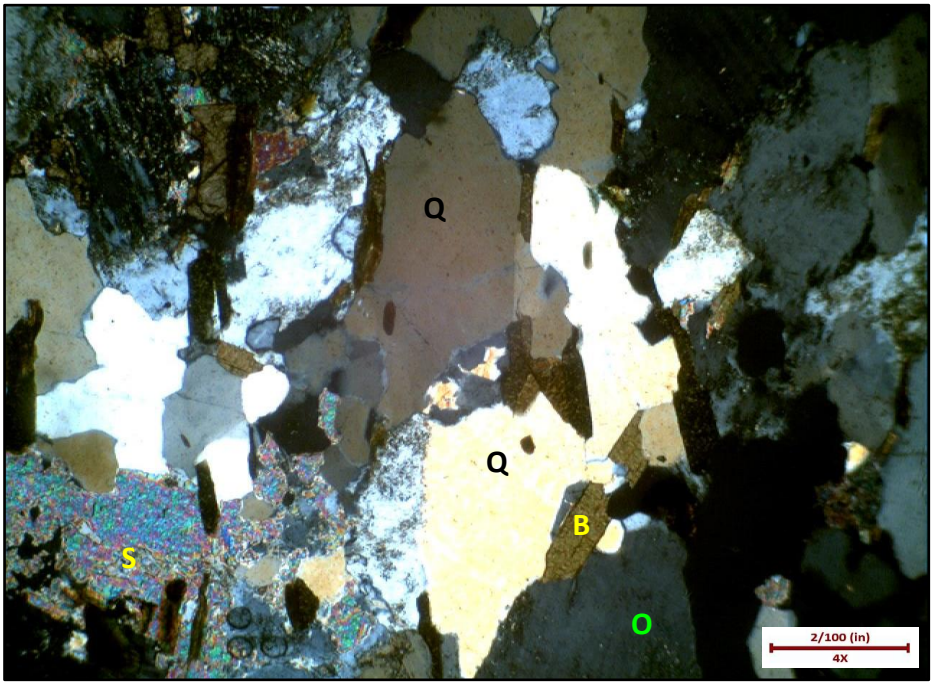


Figure 20d: Photomicrograph of the migmatitic gneiss in thin section under crossed polarized light. (B=biotite, O=orthoclase, Opx=orthopyroxene, Q=quartz, S=sericite)

4.1.3 Quartzite

Occurrence and Field Characteristics

Quartzite bodies in the study area mostly occurs in angular blocks of rubbles, cobbles and boulders generally trending almost N-S (figure 21). The quartzite occupies less than 5% of the total study area occurring discontinuously along strike. Two textural varieties of quartzite were mapped in the study area; the milky coloured massive and the muscovite-bearing foliated types. Field observations revealed that the rock dips easterly. The N-S trend of the quartzite and its foliation is generally concordant to the trend of schistocity in the surrounding quartz-mica schist.

Hand specimen samples shows that the quartzite is generally coarse-grained, milky white (Figure 22) to greyish brown in colour with a greasy luster and is essentially composed of quartz with some minor muscovite whose abundance and platy arrangement in some outcrops defines the banding in the rock with some degree of foliation (Figure 23). The micaceous foliation planes as well as the presence of the numerous longitudinal and transverse joints in the rock serve as pathways through which weathering is initiated and accentuated, breaking down the in situ rock into small angular blocks which accounts for why foliated quartzite is rarely found in situ in the study area.

Petrography

Observations on hand specimen shows that the quartzite is essentially composed of over 95 – 100 % quartz with little or no accessory muscovite. In thin section, quartz occurs mostly in a mosaic of large rectangular sheets of subhedral crystals of various sizes with smoothly interlocking edges,

showing strain shadows and undulose extinction (figure 24). Micro-joints in some tabular quartz are healed with recrystallized quartz. Muscovite is slightly pleochroic and occurs as aligned interstitial flakes. The modal composition of minerals in the foliated quartzite as observed under the thin section is presented in Table 5.



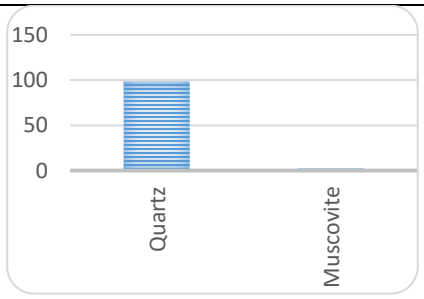
Figure 21: An outcrop of quartzite showing angular blocks and quartzite rubbles.



Figure 22: A hand specimen sample of a milky white colored, coarse-grained massive quartzite.



Figure 23: A hand specimen sample of a mica-rich, coarse-grained foliated quartzite.

Table 5: Modal concentration of minerals in Quartzite		
Mineral	Modal Composition (%)	Bar chart
Quartz	98	
Muscovite	2	

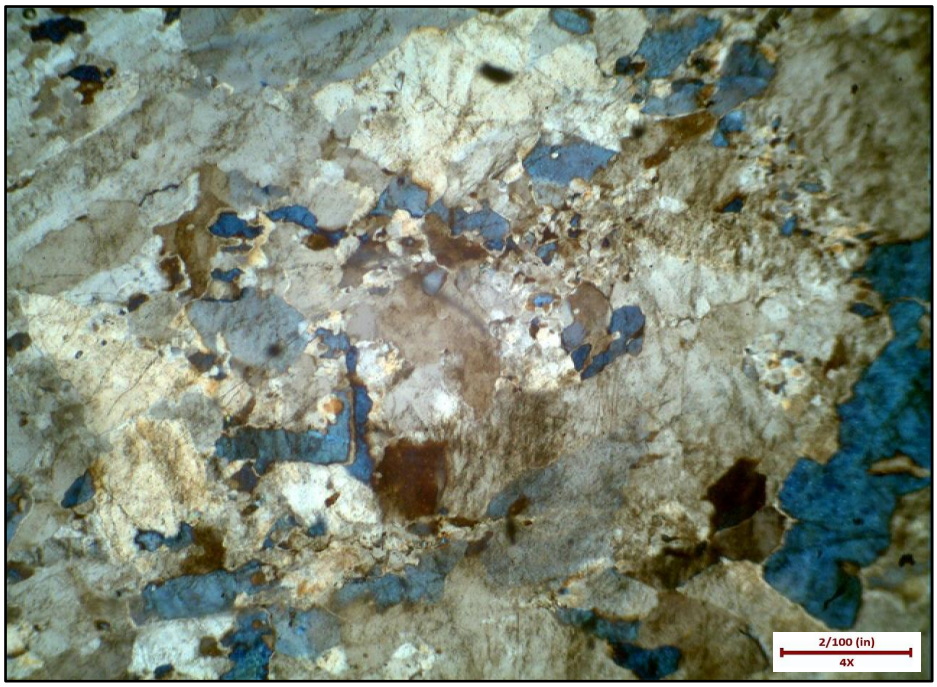


Figure 24a: Photomicrograph of the massive quartzite in thin section under plain polar.

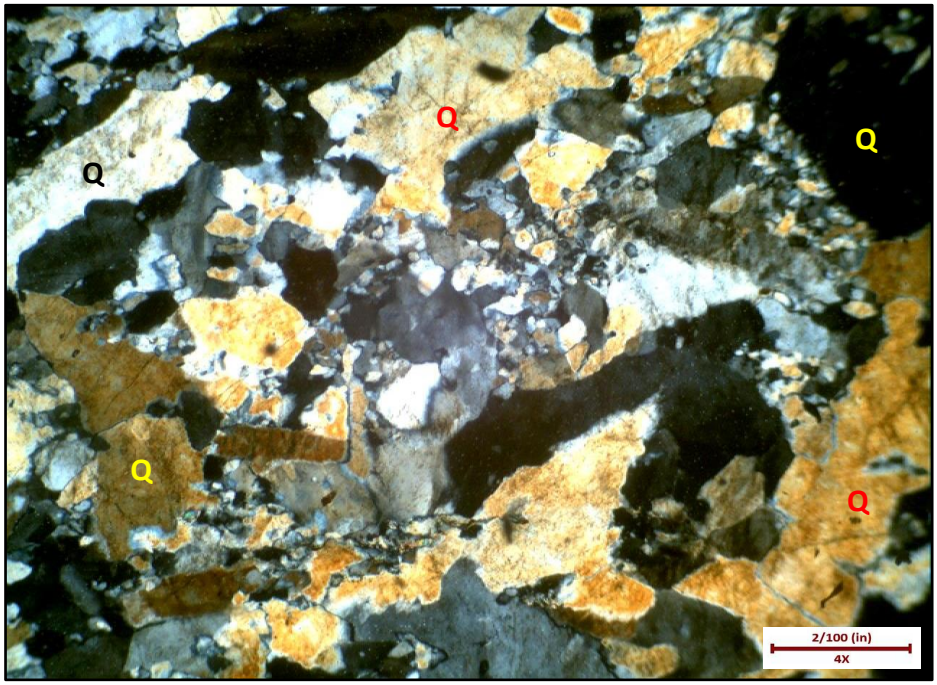


Figure 24b: Photomicrograph of massive quartzite in thin section under crossed polar. (Q=quartz)

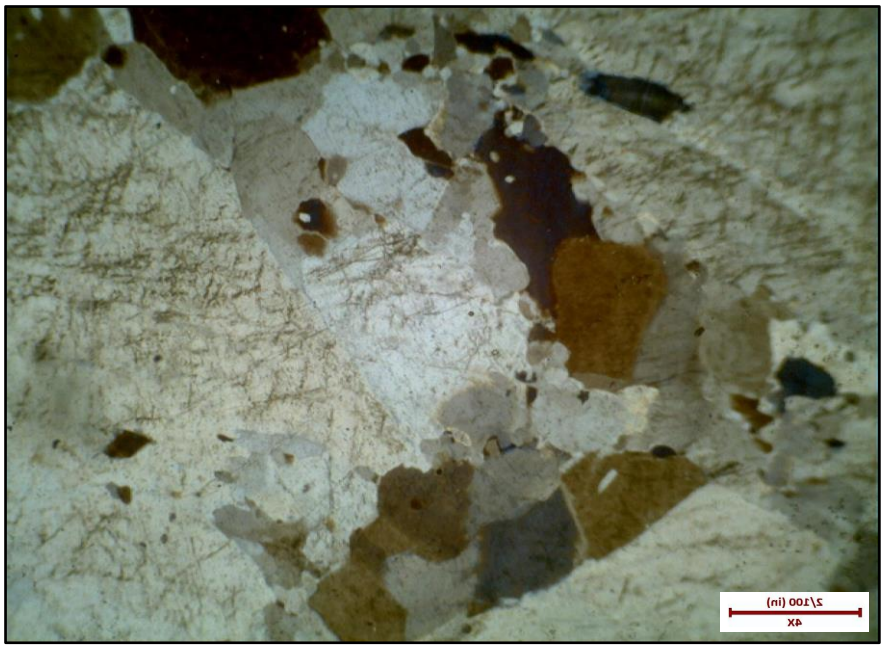


Figure 24c: Photomicrograph of the foliated quartzite in thin section under PPL. Note the micro cross joints in large quartz crystals and the recrystallized quartz.

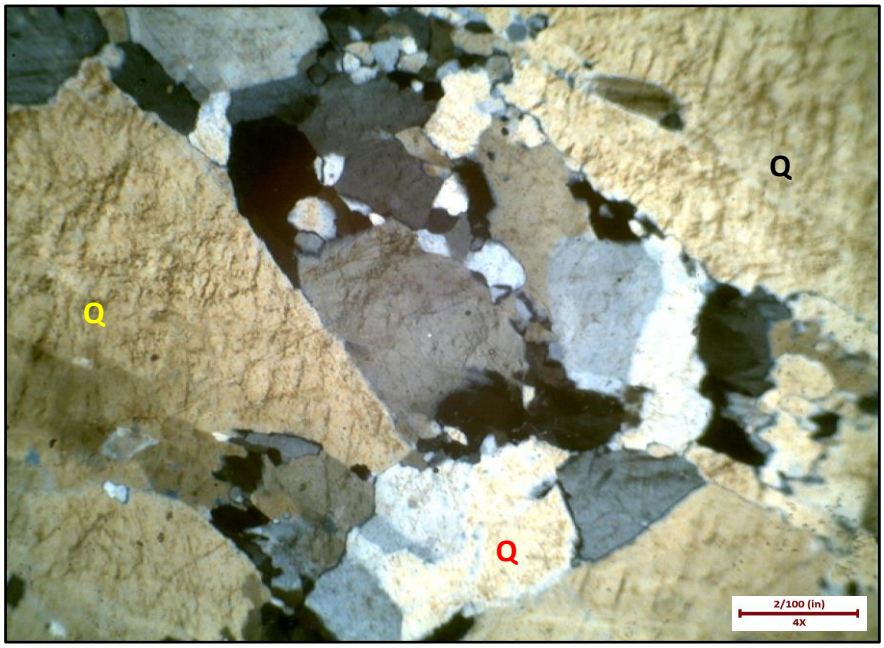


Figure 24d: Photomicrograph of the foliated quartzite in thin section under crossed polarized light. Note the micro cross joints in large quartz crystals and the recrystallized quartz crystals.

4.1.4 Quartz-Mica Schist

Occurrence and Field Characteristics

The schist mapped in the study area is a dark greyish coloured, thinly foliated rock with well-developed millimetric schistose foliations constituted by alternating psammitic and pelitic bands which makes the rock to show tendency to split along preferred plane (figure 25). The former is consistently thicker than the latter. The quartz-mica schist outcrops as discrete concordant body inter-banding with psammitic bands in some parts of the major quartzite bodies in the study area. Good exposures of this rock unit are rare and observed mainly along some major rivers and streams in the area. The rock generally exhibits distinct schistocity with sheen due to the abundance of micaceous minerals in the rock. The quartz mica schist appear to have the highest susceptibility to weathering amongst the rocks mapped in the area and it is therefore commonly found as lowlands and its bare rock exposures are rare. A narrow band of quartz-mica-schist located within a NE-SW trending shear zone was observed to contain lenses and pods of greyish-green peridotitic rock with a soapy feel along a major tributary of river Weru in the northern part of the main quartz vein in the area. Field observation on hand specimen (figure 26) sample shows the leucocratic bands to be composed of quartz, feldspars and muscovite while the melanocratic bands are comprised of biotite, hornblende and ore minerals.

Petrography

In thin section (figure 27), the quartz-mica schist is composed of fine flaky muscovite and biotite distributed within a matrix of abundant quartz and varying amounts of feldspars. The rock

consists of quartz + biotite + orthoclase ± andesine + muscovite ± chlorite ± myrmeckite ± epidote ± zircon ± titanite ± ore minerals. Muscovite and biotite account for about 20% of the modal composition of minerals in the mica schist.

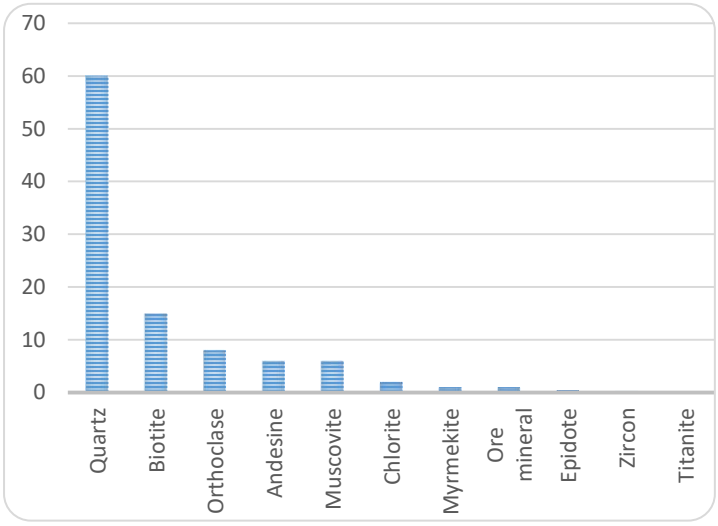
The mica usually develops flaky columnar crystals, which are clustered along definite foliation directions defining the schistocity. Biotite crystals shows pleochroism varying from brown to green. Small crystals of biotite are poikilitic in plagioclase feldspar. Muscovite is seen as alteration product of biotite. Open micro fold was observed in biotite. Quartz occurs in small subhedral crystals. Plagioclase has anorthite content of 30-50% (andesine) and occur in large anhedral crystals. Orthoclase is seen as anhedral cloudy crystals which is partly eating up the andesine. Ore mineral is opaque with euhedral cubic-shaped crystals. Table 6 shows the modal composition the quartz-mica schist in thin section.



Figure 25: A low-lying outcrop of the quartz-mica schist showing finely foliated schistocity.



Figure 26: Hand specimen samples of the quartz-mica schist.

Table 6 shows the modal composition of the Quartz-mica schist		
Mineral	Modal Composition (%)	Bar chart
Quartz	60	
Biotite	15	
Orthoclase	8	
Andesine	6	
Muscovite	6	
Chlorite	2	
Myrmeckite	1	
Ore mineral	1	
Epidote	0.5	
Zircon	0.3	
Titanite	0.2	

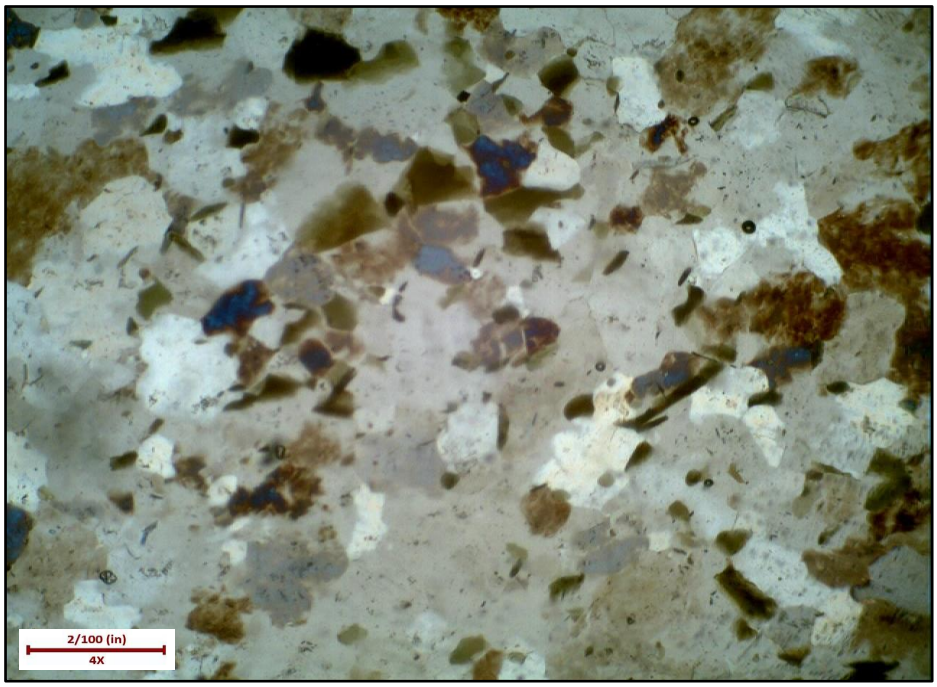


Figure 27a: Photomicrograph of the quartz-mica schist in thin section under plain polarized light.

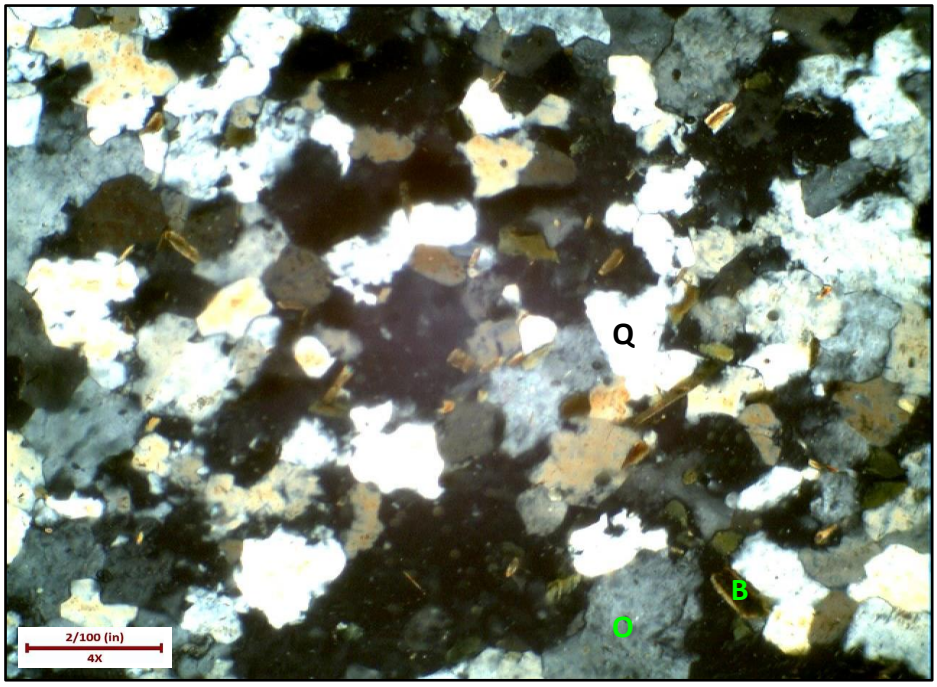


Figure 27b: Photomicrograph of the quartz-mica schist in thin section under crossed polarized light. (B=biotite, O=orthoclase, Q=quartz)

4.1.5 Talc-tremolite-actinolite Schist

Occurrence and Field Characteristics

The greyish green coloured rock outcrops either as in-situ boulders (figure 28) or as low ridges around the main auriferous quartz vein in the study area. The coarse-grained granular rock which is largely un-metamorphosed, feels soapy to touch. The schist is believed to have been formed from the hydrothermal alteration of a peridotitic precursor which resulted from the considerably varied alteration and replacement products of its constituent minerals particularly biotite and amphiboles. On a tributary to river Weru around the main gold-bearing quartz vein in the study area, a band of the talcose rock trending 176^{o} with an easterly dip of about 60^{o} and measuring 10-15m wide was exposed on both sides of the bank of the stream within the quartz-mica schist host. Hand specimen sample (figure 29) shows that the rock is composed of talc + tremolite $\pm$ actinolite $\pm$ ore mineral.

Petrography

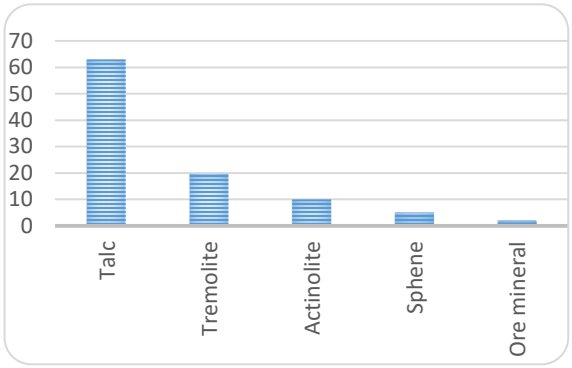
In the thin section (figure 30), the talcose rock occurs as a greyish fibrous mass of talc with anhedral crystals which forms the groundmass to the phenocrysts of pinkish brown actinolite and greyish green tremolite crystals observed. Ore minerals occur as isolated anhedral mafic crystals sparsely disseminated within the rock. The mineral composition of the the talcose rock include talc + tremolite $\pm$ actinolite $\pm$ ore minerals. Table 7 below shows the modal composition of minerals in the talc-tremolite-actinolite schist in thin section.



Figure 28: An outcrop of the talc-tremolite schist showing insitu boulders.



Figure 29: A hand specimen sample of the talc-tremolite-actinolite schist.

Table 7 shows the modal composition of the Talc-tremolite-actinolite schist		
Mineral	Modal Composition (%)	Bar chart
Talc	63	
Tremolite	20	
Actinolite	10	
Sphene	5	
Ore mineral	2	

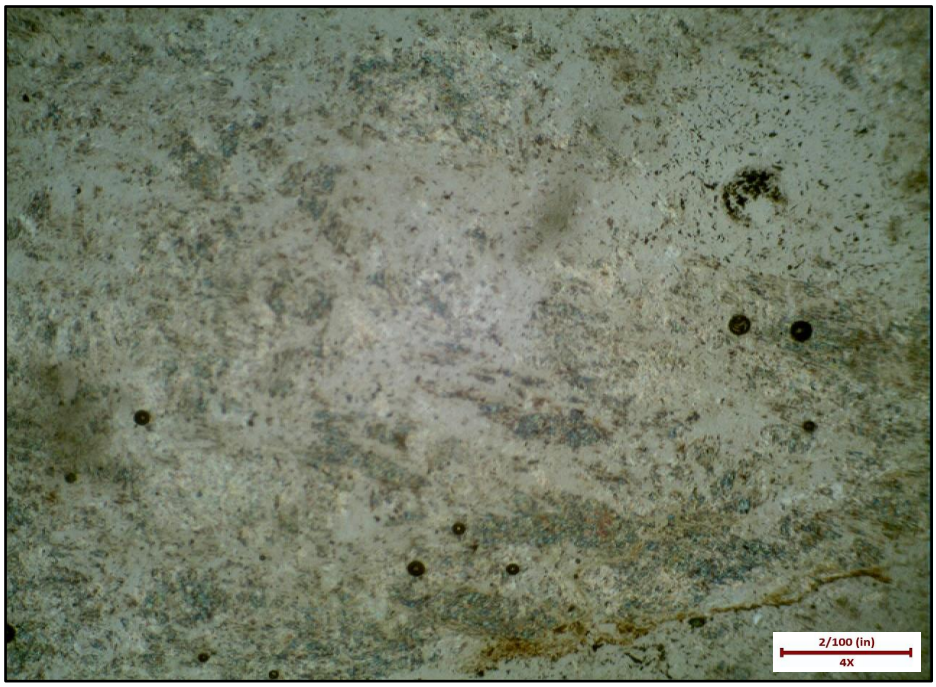


Figure 30a: Photomicrograph of the talc-tremolite-actinolite schist in thin section under PPL.

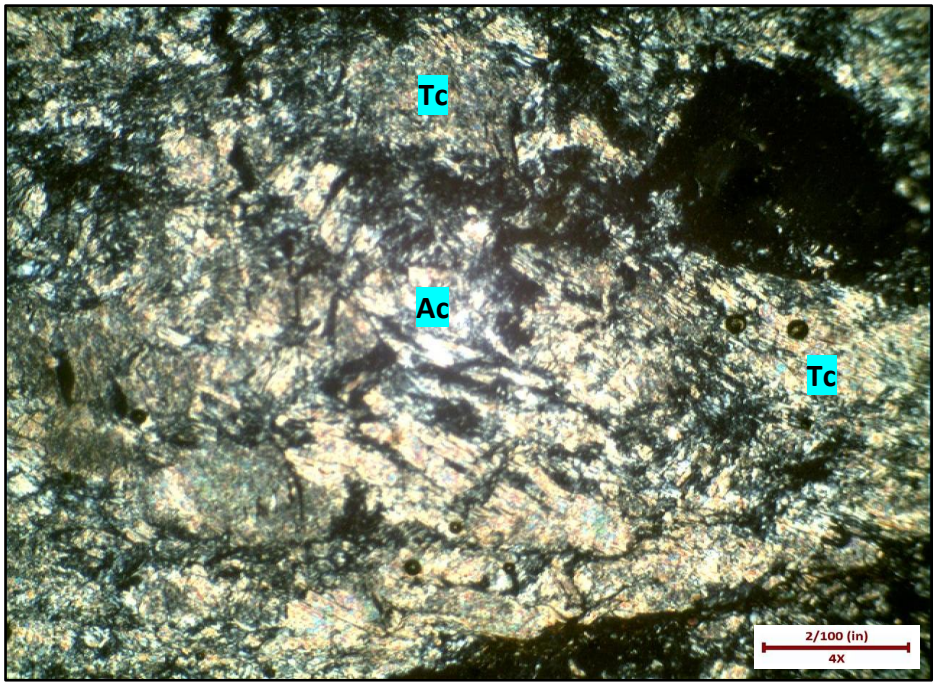


Figure 30b: Photomicrograph of the talc-tremolite-actinolite schist in thin section under XPL. (Ac=actinolite, Tc=talc)

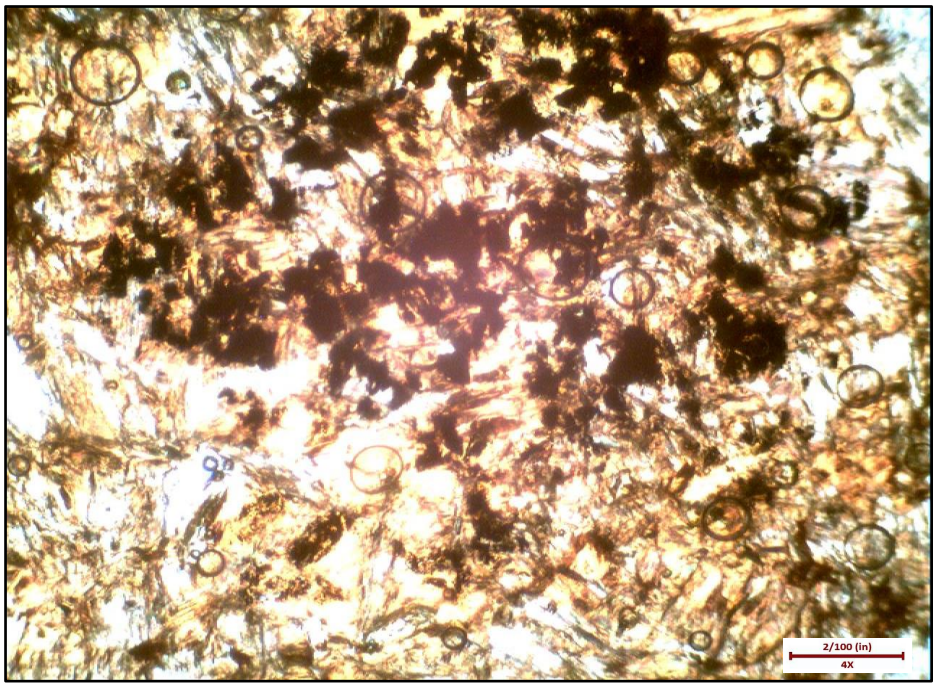


Figure 30c: Photomicrograph of the talc-tremolite-actinolite schist in thin section under PPL.

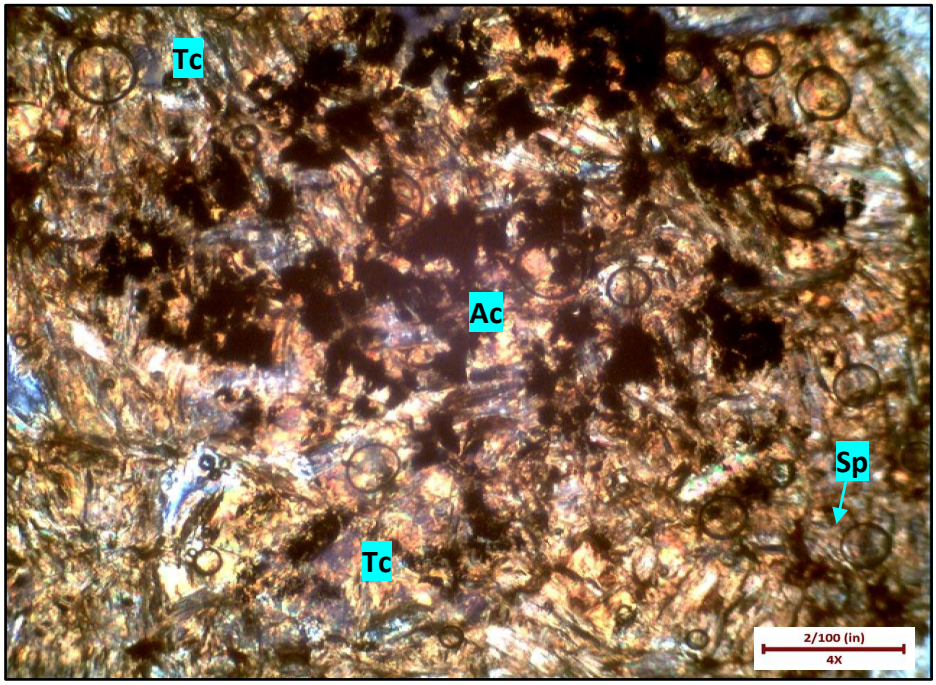


Figure 30d: Photomicrograph of the talc-tremolite-actinolite schist in thin section under XPL. (Ac=actinolite, Sp=sphene, Tc=talc, Tr=tremolite)

4.1.6 Gabbro

Occurrence and Field Characteristics

Gabbro was mapped in the study area as small discrete bodies, occurring as dyke of a dark-greenish coloured rock which are sometimes found as small lenses in few areas of the granitic terrain mostly within the porphyritic granite host rock. Hand specimen sample (figure 31) shows that the rock is fine- to medium-grained, melanocratic in colour and exhibits a general greenish tinge due to the abundance of olivine and pyroxene in its mineral constituents.

Petrography

Thin section studies (figure 32) shows that the gabbro is composed of calcic plagioclase bytownite + labradorite + clinopyroxene + olivine + quartz. Plagioclase is euhedral shaped and shows 60%-70% anorthite content ranging from labrodorite to bytownite with polysnthetic twining and sometimes contain dirty inclusions. Pyroxene shows fine lamellar structure in some crystals. Olivine occurs as phenocrysts showing characteristic fracture cleavage. Quartz is observed as small euhedral intergranular crystals. Biotite is seen as euhedral lath shaped crystals and appears to be mostly aligned along preferred orientation with pleichroism ranging from yellowish brown to dark brown. Subhedral pyroxene crystals show characteristic fracture cleavages with pleichroism varying from grey yellow to deep brown colour. Table 8 shows the modal composition of minerals in the gabbro under the thin section.

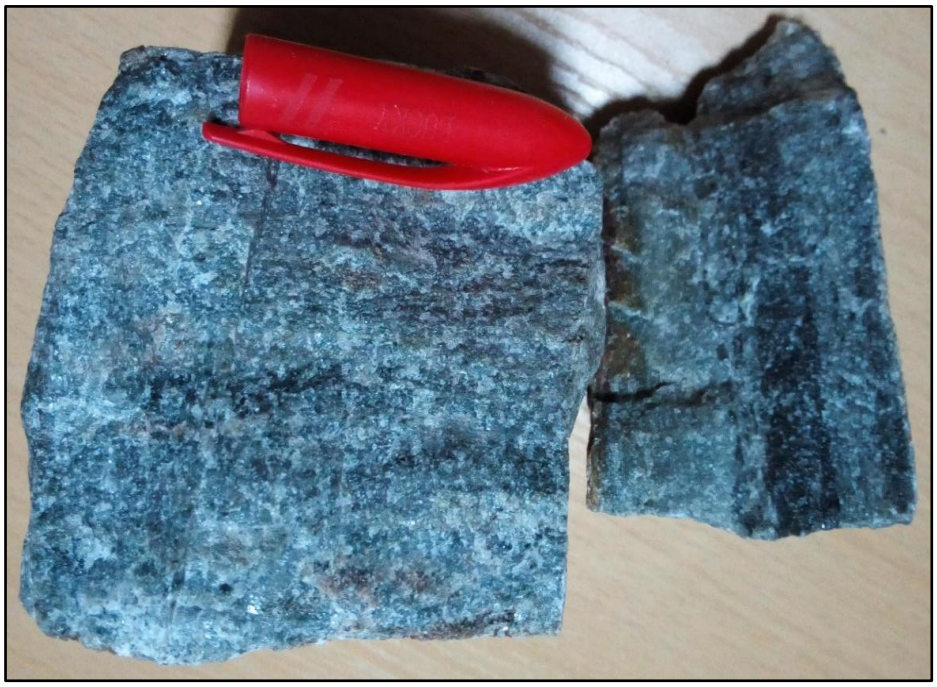
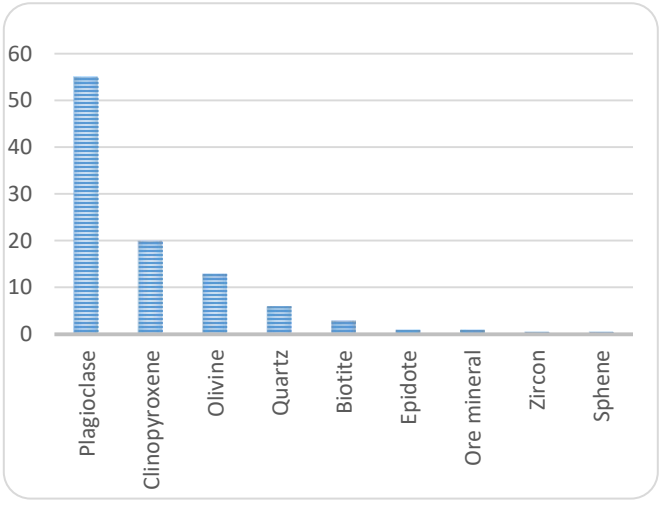


Figure 31: Hand specimen samples of the gabbro showing the characteristic greenish tinge.

Table 8 shows the modal composition of the Gabbro		
Mineral	Modal Composition (%)	Bar chat
Plagioclase	55	
Clinopyroxene	20	
Olivine	13	
Quartz	6	
Biotite	3	
Epidote	1	
Ore mineral	1	
Zircon	0.5	
Sphene	0.5	



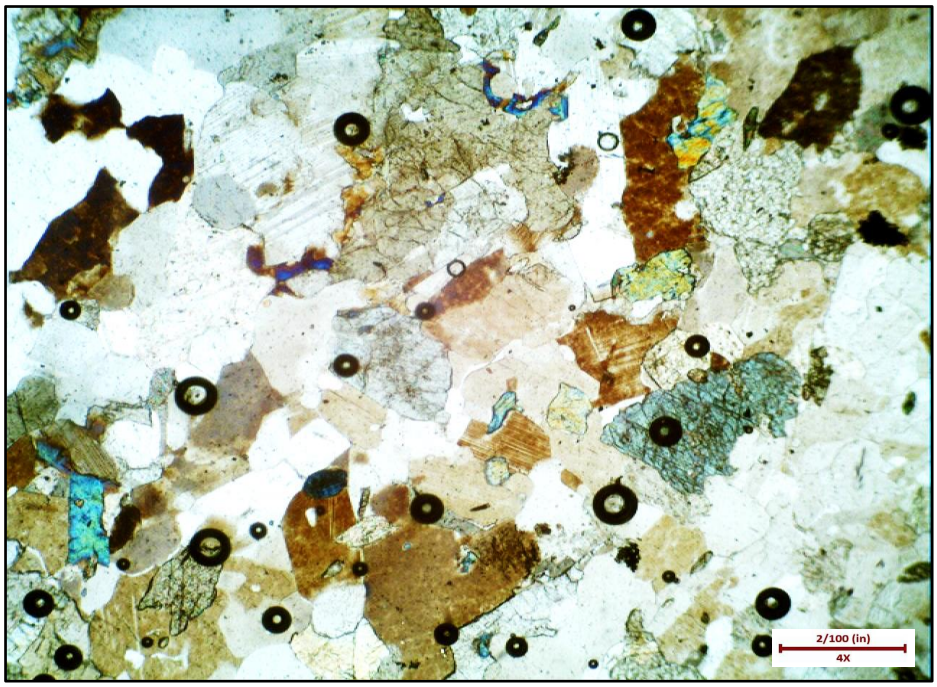


Figure 32a: Photomicrograph of the gabbro in thin section under plain polarized light.

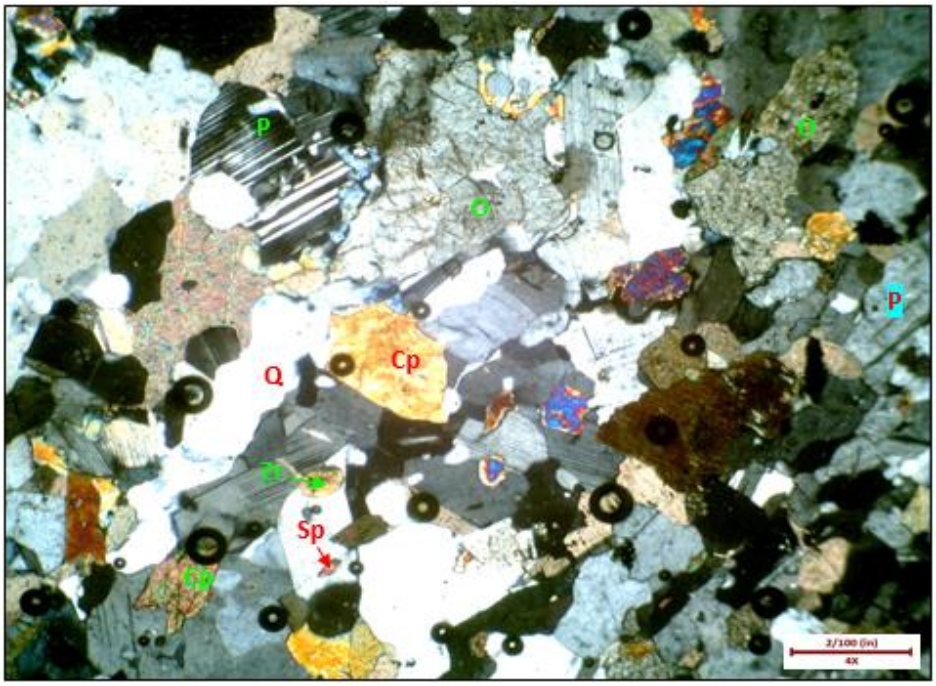


Figure 32b: Photomicrograph of the gabbro in thin section under crossed polarized light.
(Cp=clinopyroxene, O=olivine, P=plagioclase, Q=quartz, Sp=sphene, Zr=zircon)

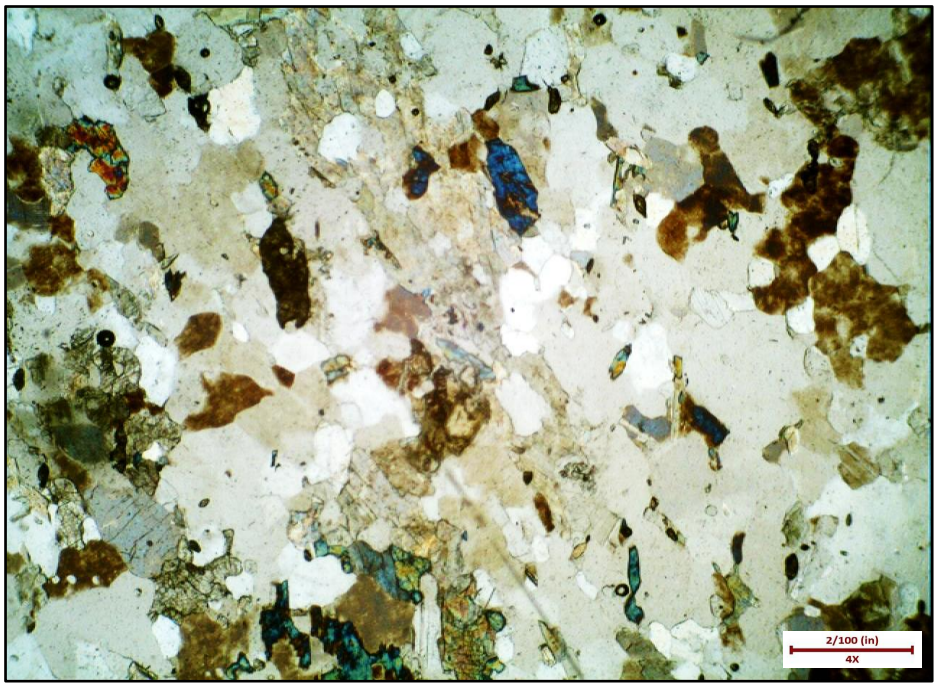


Figure 32c: Photomicrograph of the gabbro in thin section under plain polarized light.

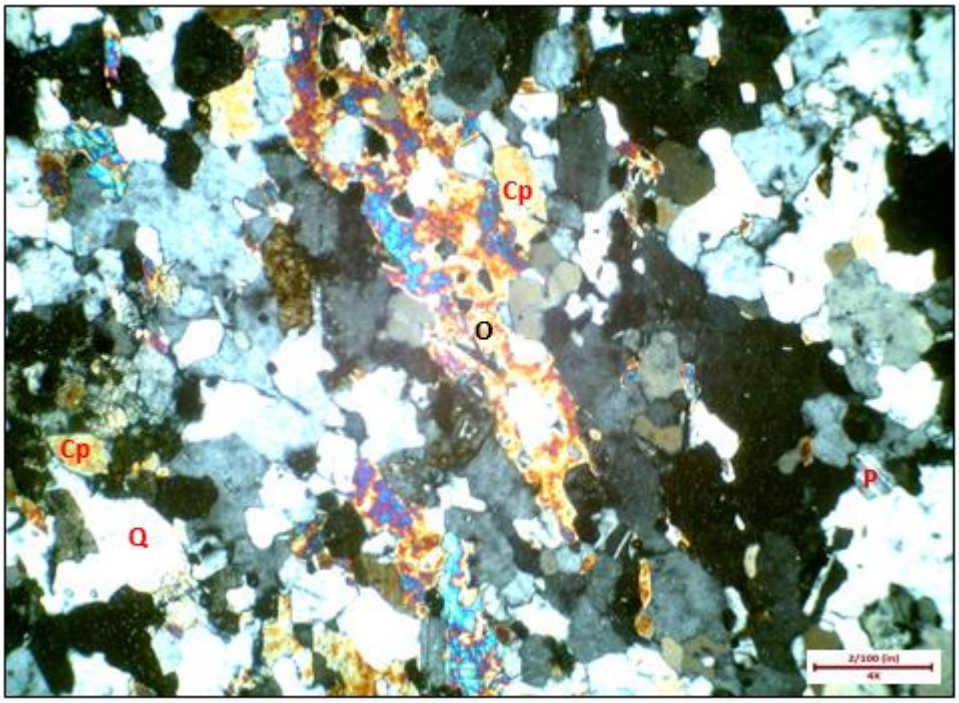


Figure 32d: Photomicrograph of the gabbro in thin section under crossed polarized light. (Cp=clinopyroxene, O=olivine, P=plagioclase, Q=quartz)

4.1.7 Porphyritic Granite

Occurrence and Field Characteristics

The occurrence of porphyritic granite is widespread in the central part of the study area. It occurs as extensive well-exposed low-lying outcrops and minor intrusion within the gneissic host rock. The porphyritic granite in the study area develops only few joints and consequently, its outcrops are not usually littered with the rock boulders, cobbles and pebbles due to slow weathering rate affecting the rock. The long axis of the rock outcrops trend generally N-S. Generally, the rock is phenocryst supported which accounts for why the matrix is subordinate to the phenocrysts. Porphyritic granite underlay about 25% of the study area and the feldspar megacrysts in the rock generally exhibit a dull chalky luster under weathering condition.

Hand specimen sample (figure 33) shows that the rock is coarse grained to porphyritic textured and it is characterized by tabular phenocrysts of subhedral crystals of pink feldspar embedded within a matrix of fine- to medium-grained plagioclase feldspar, quartz, biotite, hornblende and muscovite. The predominance of the pink feldspar gives the rock a characteristic pinkish colour. The parallel arrangement of the long axes of the large feldspar phenocrysts and biotite imparted a vertical to sub-vertical N-S trending foliation on the outcrop, particularly around its sharp contact with the neighboring gneissic rock (figures 34).

Petrography

Thin section studies (figure 35) show that the coarse porphyritic granite consists of phenocrysts of microcline and orthoclase within a groundmass of quartz + oligoclase + orthoclase + biotite +

hornblende ± sericite ± garnet ± ore mineral. Microcline is seen as subhedral to euhedral porphyroblasts showing cross-hatch twining; Anhedral crystals of quartz show triple junction. Oligoclase occurs as small anhedral crystals forming inter-locking mosaic with quartz in the groundmass.

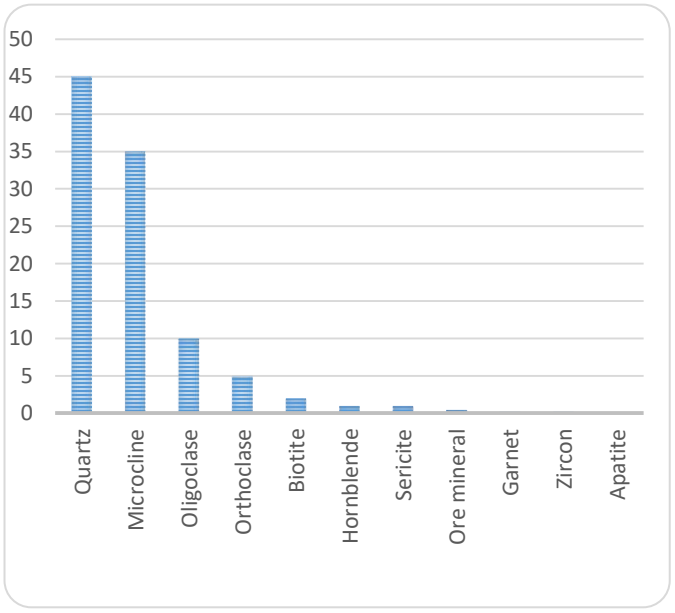
The irregular grains of oligoclase are locally invaded by microcline marginally leading to the development of myrmekite. Pericline twinning occurs together with albite twinning to produce a crosshatched appearance somewhat similar to that of microcline. Medium-sized zircon occurs as isolated nodular crystals; Sericite is seen as alteration products around the edges of microcline in some places. Ore mineral occur as both disseminated and clustered blebs of anhedral crystals. Table 9 shows the modal composition of minerals in porphyritic granite.



Figure 33: A hand specimen sample of the porphyritic granite showing feldspar megacrysts within the groundmass.



Figure 34: An outcrop of the coarse porphyritic granite showing sharp contact with biotite-hornblende gneiss.

Table 9: Modal composition of the Porphyritic Granite		
Mineral	Modal Composition (%)	Bar chart
Quartz	45	
Microcline	35	
Oligoclase	10	
Orthoclase	5	
Biotite	2	
Hornblende	1	
Sericite	1	
Ore mineral	0.5	
Garnet	0.2	
Zircon	0.2	
Apatite	0.1	

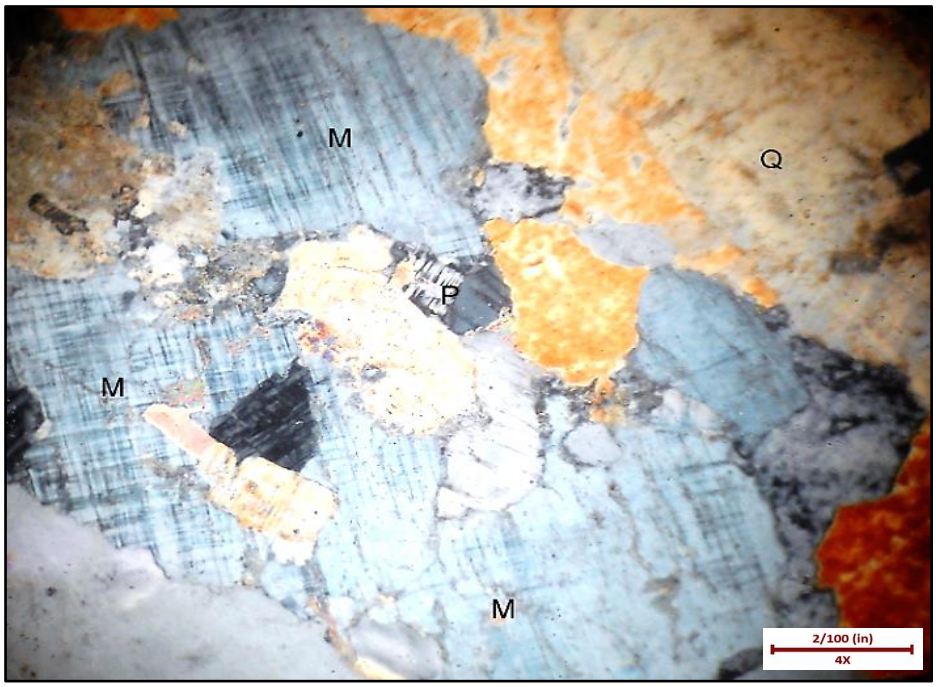


Figure 35a: Photomicrograph of the porphyritic granite in thin section under plain polar. (M=microcline, P=plagioclase, Or=orthoclase, Q=quartz)

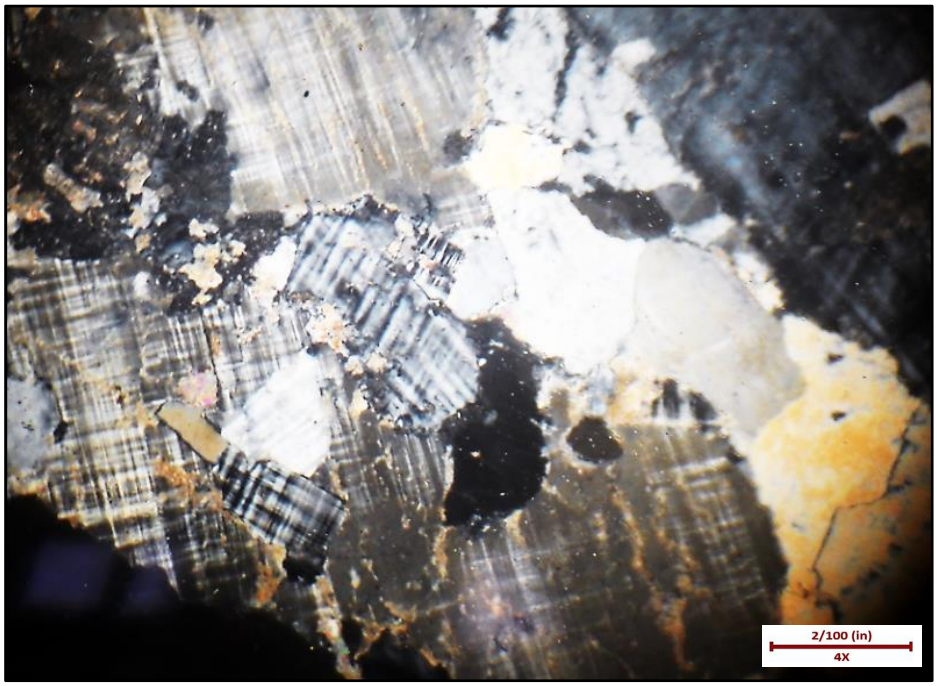


Figure 35b: Photomicrograph of the porphyritic granite in thin section under crossed polar.

4.1.8 Porphyroblastic Granite

Occurrence and Field Characteristics

The Porphyroblastic Granite outcrops mostly as low bare rock ridges in the southeast part of the study area and exhibits an inferred contact with the biotite gneiss to the east. Elsewhere, the porphyroblastic granite outcrops as small intrusive exposures within its gneissic host rock. Hand specimen sample (figure 36) shows that the rock is composed of phenocrysts which have been slightly tectonized into porphyroblasts of feldspars within a groundmass of largely undeformed quartz, feldspar, biotite and hornblende. The porphyroblasts are formed mainly by microcline and minor plagioclase, where they range in sizes from 1.2cm - 4.3cm in length. The porphyroblasts are stretched and are generally aligned in the direction N38^{o}E.

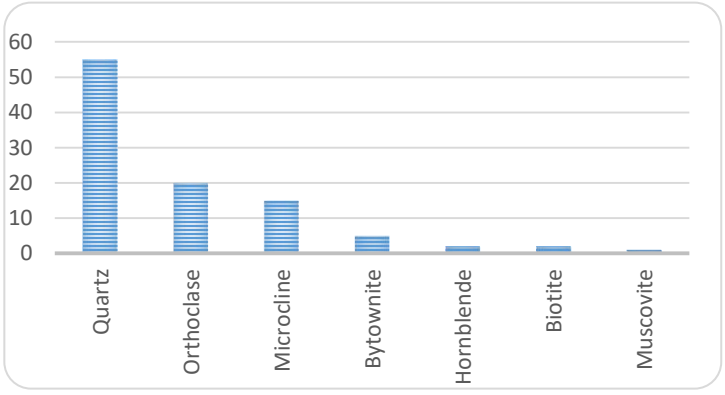
Petrography

Thin section study (figure 37) shows that the porphyroblastic granite is made up of biotite, plagioclase feldspar, microcline and quartz in order of increasing abundance. Microcline is the most abundant after quartz and make up to about 25% of the total mineral composition of the rock. Microcline is colourless under PPL and shows no pleochroism and a very low birefringence. It shows both albite and pericline twinning, forming a remarkable cross-hatched grid called “tartan plaids”, which distinguishes it from other feldspars. Quartz which is colourless under PPL, with no pleochroism, low refractive index and birefringence, makes up about 55% of the rock.

Quartz which is anhedral to subhedral in shape and contain triple junction sometimes appears smoky, stretched and exhibits a wavy extinction; Microcline occurs in subhedral shaped crystals with grid twinning; Plagioclase constitutes about 5% of the rock modal composition and it is composed of bytownite with 80% anorthite content. Orthoclase occurs in large phenocrysts embedded within the groundmass of smaller crystals and sometimes appear to be eating up the bytownite at the edges; Biotite occurs as small lath-shaped crystals and are aligned along a preferred direction. Hornblende is seen as euhedral crystals with cleavage in two direction at 120^{o}. Muscovite occurs in lath shape and shows alignment. Table 10 shows the modal composition of the porphyroblastic granite.



Figure 36: A hand specimen sample of the porphyroblastic granite showing sheared feldspar megacrysts.

Table 10: Modal composition of the Porphyroblastic Granite		
Mineral	Modal Composition (%)	Observations
Quartz	55	
Orthoclase	20	
Microcline	15	
Bytownite	5	
Hornblende	2	
Biotite	2	
Muscovite	1	

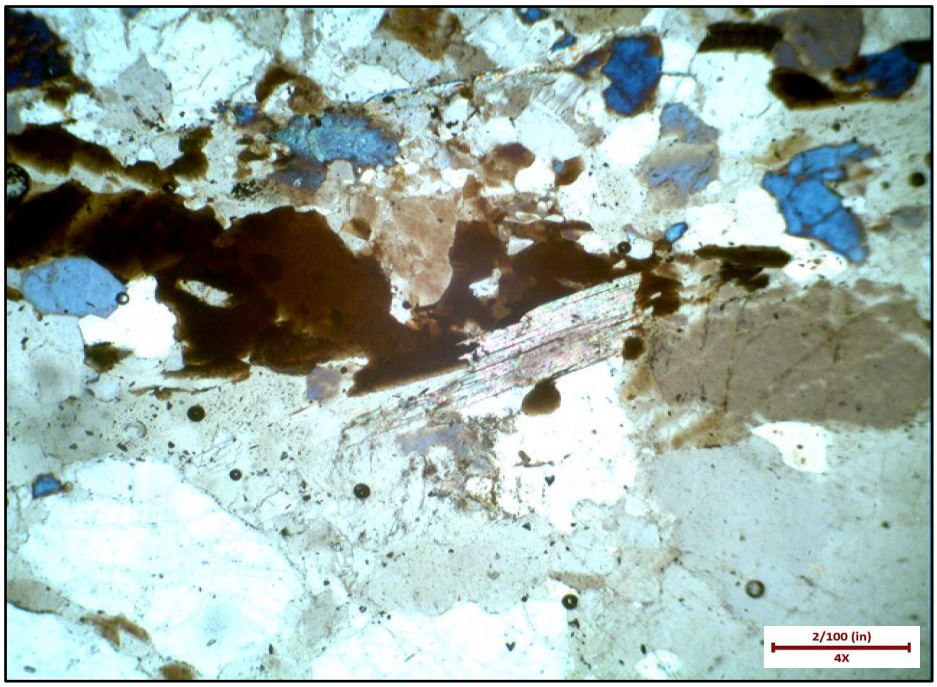


Figure 37a: Photomicrograph of the porphyroblastic granite in thin section under PPL.

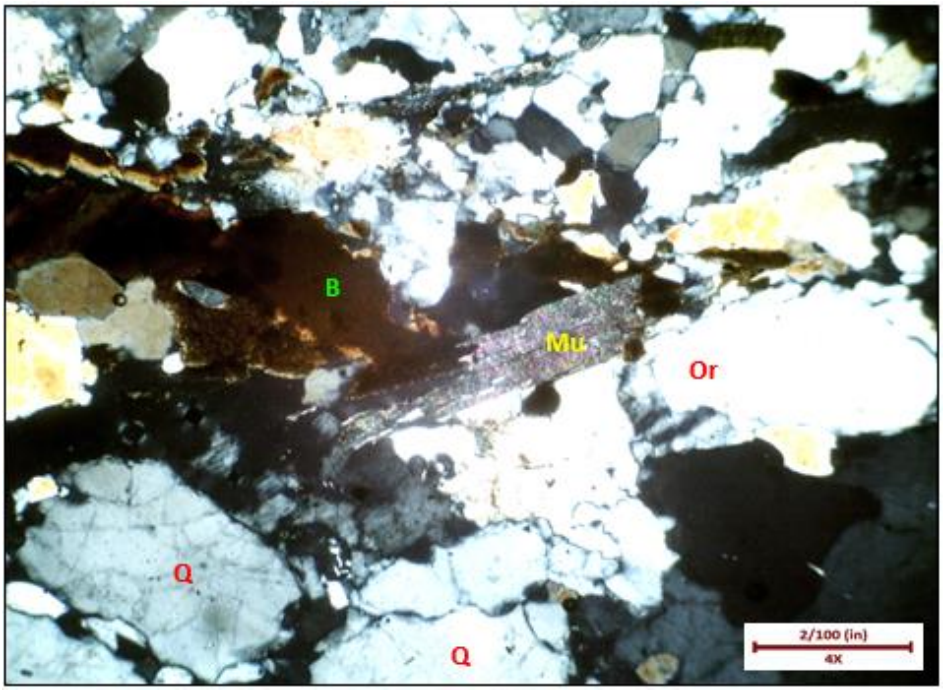


Figure 37b: Photomicrograph of the porphyroblastic granite in thin section under XPL. (B=biotite, Mu=muscovite, Or=orthoclase, Q=quartz)

4.1.9 Porphyritic Quartz Diorite

Occurrence and Field Characteristics

The rock outcrops mainly as low lying exposures with limited areal extent and shows the arrangement of calcic feldspar megacrysts set within a matrix composed of quartz, plagioclase, hornblende and biotite. The rock is coarse to porphyritic textured and the parallel arrangement of the longer axis of the feldspar megacrysts along N24^{o}E gave the rock a general sense of foliation. Most of the megacrysts are tabular and show clear evidence of twin (figure 38). Generally, the rock is melanocratic in colour due to the abundance of mafic minerals.

Petrography

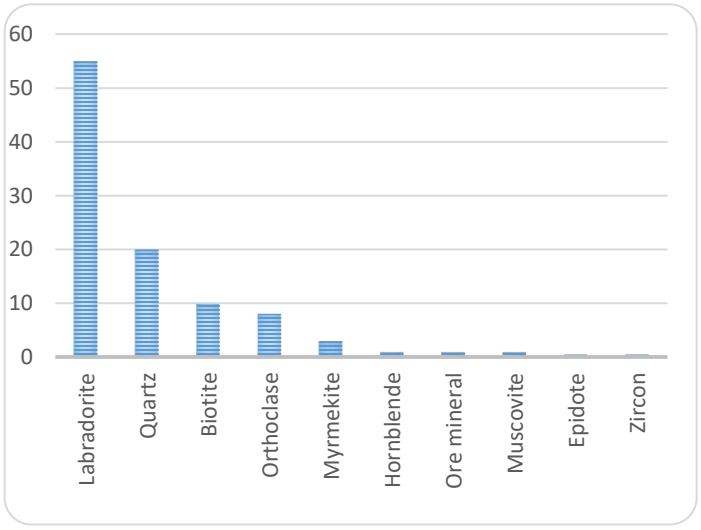
The study of the rock under thin section (figure 39) shows that the rock is composed predominantly of labradorite + quartz + biotite + orthoclase + myrmeckite + hornblende + muscovite + epidote + zircon + ore mineral. Quartz crystals appeared stretch concordantly along the direction of preferred orientation of the biotite. Plagioclase is labradorite with anorthite content ranging from 50 to 70% and occurs mostly as large phenocrysts with polysynthetic twinning. Orthoclase occurs as anhedral alteration product of the labradorite. Myrmeckite is seen as anhedral crystals occurring close to tabular feldspars. Biotite ranges in shape from euhedral lath to tabular crystals and appears to be mostly aligned along preferred orientation with pleochroism ranging from yellowish brown to dark brown. Small biotite crystals are poikilitic in quartz and feldspar. Hornblende is pleochroic from green to dark green and exhibits twinning in 2 directions at angle

120^{o}. Muscovites eats up biotite in some places. Table 11 shows the modal composition of the porphyritic diorite.



Figure 38: Hand specimen sample of the porphyritic diorite showing twined feldspar crystals

Table 11: Modal composition of the porphyritic diorite		
Mineral	Modal Composition (%)	Bar chart
Labradorite	55	
Quartz	20	
Biotite	10	
Orthoclase	8	
Myrmeckite	3	
Hornblende	1	
Ore mineral	1	
Muscovite	1	
Epidote	0.5	
Zircon	0.5	



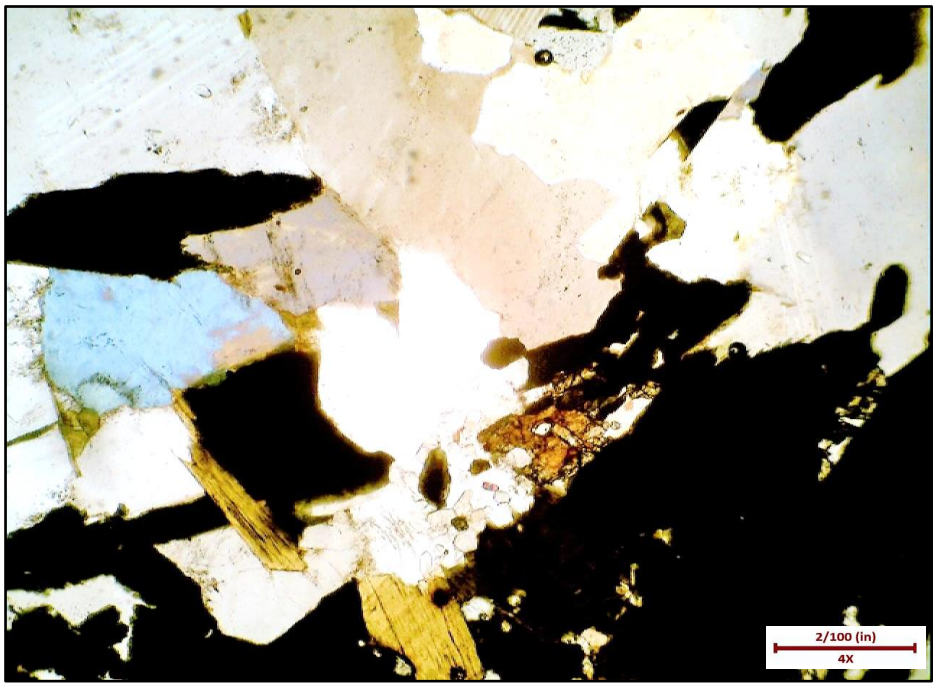


Figure 39a: Photomicrograph of the porphyritic diorite in thin section under PPL.

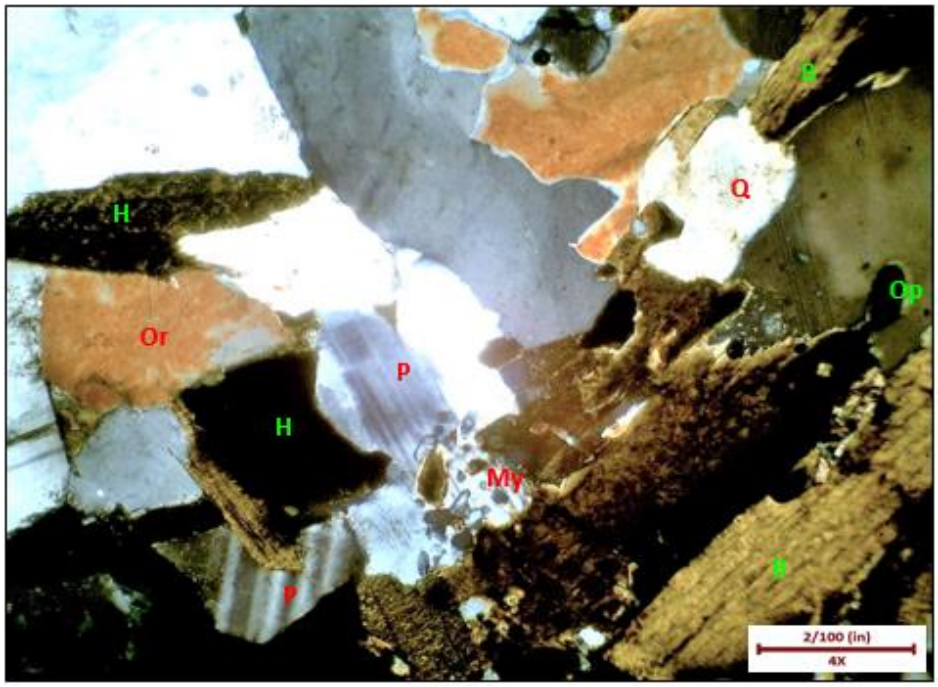


Figure 39b: Photomicrograph of the porphyritic diorite in thin section under XPL. (B=biotite, H=hornblende, P=plagioclase, My=myrmeckite, Op=opaque, Or=orthoclase, Q=quartz)

4.1.10 Coarse-grained Granite

Occurrence and Field Characteristics

Coarse grained granite outcrops as low-lying ridges and dome shape hill of bare rock exposures as well as large in-situ boulders. In some outcrops the rock is mapped as minor intrusive body cutting through gneisses and porphyritic granite host rocks and sometimes bear the xenolith of the bedrock through which it intrudes (figure 40). In hand specimen (figure 41), the rock is texturally coarse-grained, granoblastic, massive and consists of interlocking crystals of quartz and feldspar dotted with mafic minerals of biotite and hornblende. The preponderance of the alkali feldspar makes the rock leucocratic with a greyish pink colour.

Petrography

Thin section studies (figure 42) shows that the rock is composed of quartz + orthoclase + oligoclase + microcline + biotite ± muscovite + hornblende ± myrmeckite ± ore mineral ± sphene ± zircon ± titanite. Quartz is seen as anhedral to subhedral crystal with wavy extinction and shows triple junctions with micro joints occurring in some large crystals. Orthoclase eats up the Oligoclase. Orthoclase occurs as anhedral cloudy crystals which is partly eating up plagioclase. Plagioclase shows large anhedral crystals of oligoclase with anorthite content of 30%. Microcline occurs in large tabular euhedral phenocrysts embedded within a medium-grained ground mass.

Biotite is pleochroic from yellowish brown to dark greenish brown and occurs as euhedral to subhedral shaped crystals in isolated clusters or disoriented laths and is sometimes poikilitic in

tabular microcline phenocrysts and quartz with alteration halos around its edges. Open micro fold was also observed in biotite. Myrmeckite is subhedral in shape. Hornblende occur in small tabular crystals which alters to biotite at the edges and shows cleavage in two directions at 120^{o}. Sphene occurs as isolated large euhedral rhombic crystals. Ore mineral is opaque in color and octahedral in shape while some other opaque minerals show euhedral cubic shaped crystals. Muscovite in subordinate quantity was observed eating up biotite at the edges. Table 12 shows the modal composition of the coarse-grained granite.



Figure 40: A bare rock exposure of the coarse-grained granite.

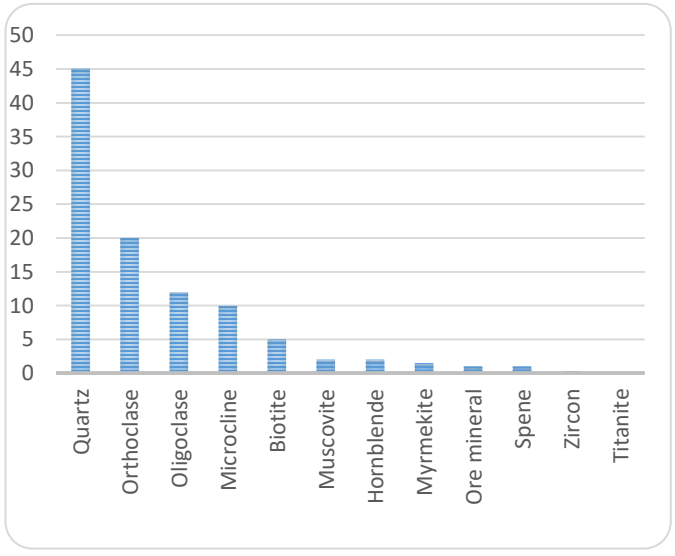


Figure 41a: Hand specimen sample of the coarse-grained granite showing abundance K-feldspar.



Figure 41b: Hand specimen sample of the coarse-grained granite showing abundance K-feldspar.

Table 12: Modal composition of the coarse-grained granite		
Mineral	Modal Composition (%)	Bar chart
Quartz	45	
Orthoclase	20	
Oligoclase	12	
Microcline	10	
Biotite	5	
Muscovite	2	
Hornblende	2	
Myrmeckite	1.5	
Ore mineral	1	
Sphene	1	
Zircon	0.3	
Titanite	0.2	



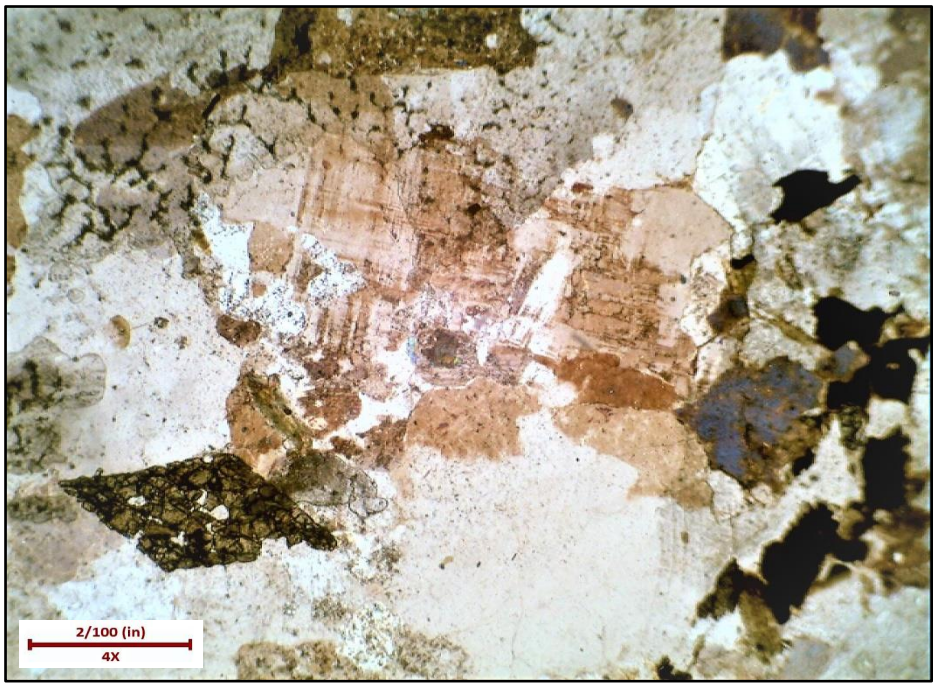


Figure 42a: Photomicrograph of the coarse-grained granite under PPL.

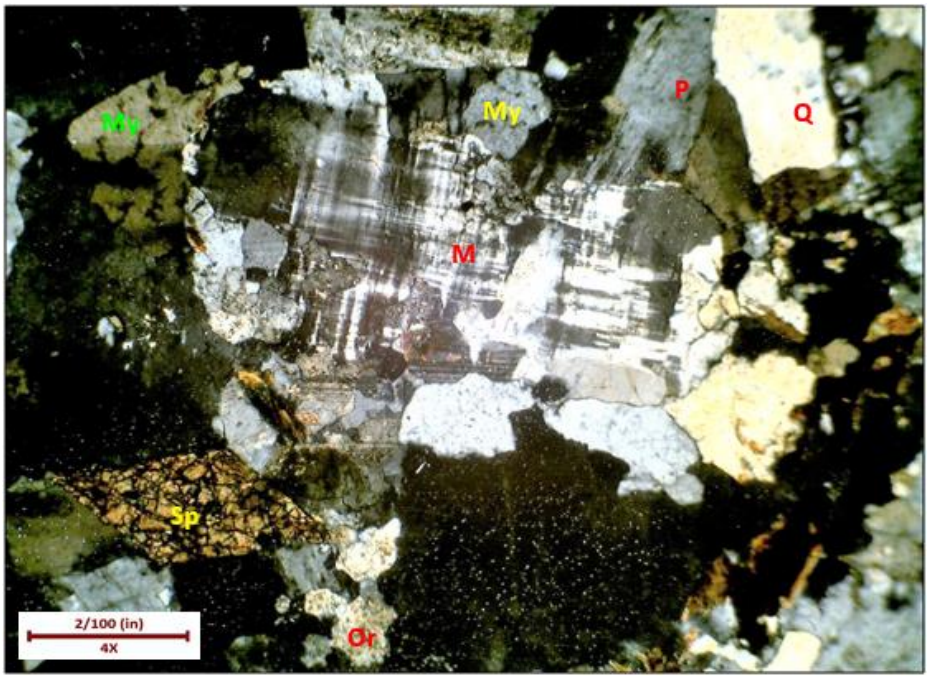


Figure 42b: Photomicrograph of the coarse-grained granite in thin section under XPL. (M=microcline, My=myrmeckite, Or=orthoclase, P=plagioclase, Q=quartz, Sp=sphene)

4.1.11 Granodiorite

Occurrence and Field Characteristics

Granodiorite occurs as minor intrusive bodies particularly restricted within the migmatitic gneiss terrain of the study area. They are found as small discordant intrusions cutting the general trend of fabrics in the host rock. A low lying outcrop of the rock was mapped showing intrusions of quartzo-feldspatic veins (figure 43). Hand specimen sample (figure 44) shows that the rock is medium to coarse-grained and mesocratic to melanocratic in texture which is predominantly dark coloured with small white tinge of light coloured minerals composed of quartz and feldspar. The granodiorite is frequently associated with xenoliths of gneissic rock whose long axes are variously disoriented. Boudinaged veins of quartz are found as small concordant lenses within the rock.

Petrography

Thin section study (figure 45) reveals that the granodiorite is composed of quartz + labradorite + andesine + orthoclase + microcline + biotite $\pm$ hornblende $\pm$ sericite $\pm$ muscovite $\pm$ myrmeckite $\pm$ orthopyroxene $\pm$ zircon $\pm$ sphene $\pm$ apatite $\pm$ ore mineral. The rock is rich in plagioclase feldspar composed of labradorite and andesine with polysynthetic twining. Orthoclase eats up the plagioclase feldspar especially at the edges. Microcline is seen as subhedral crystals with cross hatch twining. Sericite is seen as alteration product in microcline feldspar. Biotite is predominant and occurs in clusters of euhedral crystals with no preferred planar orientation and sometimes shows alteration halos at the edges.

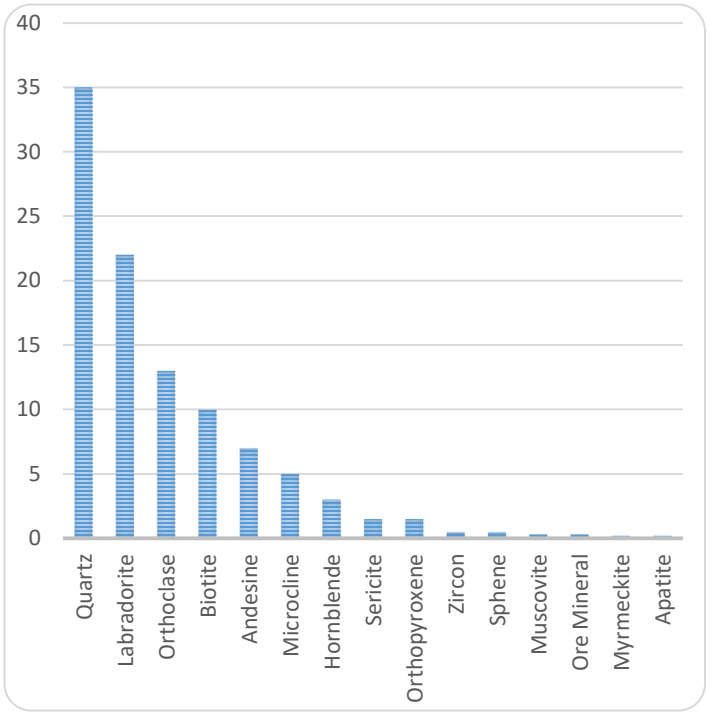
Muscovite is poikilitic in biotite as alteration product. Orthopyroxene occurs in large subhedral platy crystals and shows characteristic fracture cleavage in two directions. Quartz crystals are anhedral with triple junction and sometimes occurs in granular intergrowth with cloudy orthoclase crystals to form myrmeckite. Ore mineral occurs as small nodular crystals while zircon, apatite and sphene occur as accessory minerals. Apatite occurs as needle-shaped crystals and shows high relief. The average modal composition of minerals in the granodiorite as observed under the thin section is presented in Table 13.



Figure 43: An outcrop of a coarse-grained granodiorite showing aplitic vein intrusions



Figure 44: Hand specimen sample of the granodiorite.

Table 13: Modal composition of the medium-grained granodiorite		
Mineral	Modal Composition (%)	Bar chart
Quartz	35	
Labradorite	22	
Orthoclase	13	
Biotite	10	
Andesine	7	
Microcline	5	
Hornblende	3	
Sericite	1.5	
Orthopyroxene	1.5	
Zircon	0.5	
Sphene	0.5	
Muscovite	0.3	
Ore Mineral	0.3	
Myrmeckite	0.2	
Apatite	0.2	

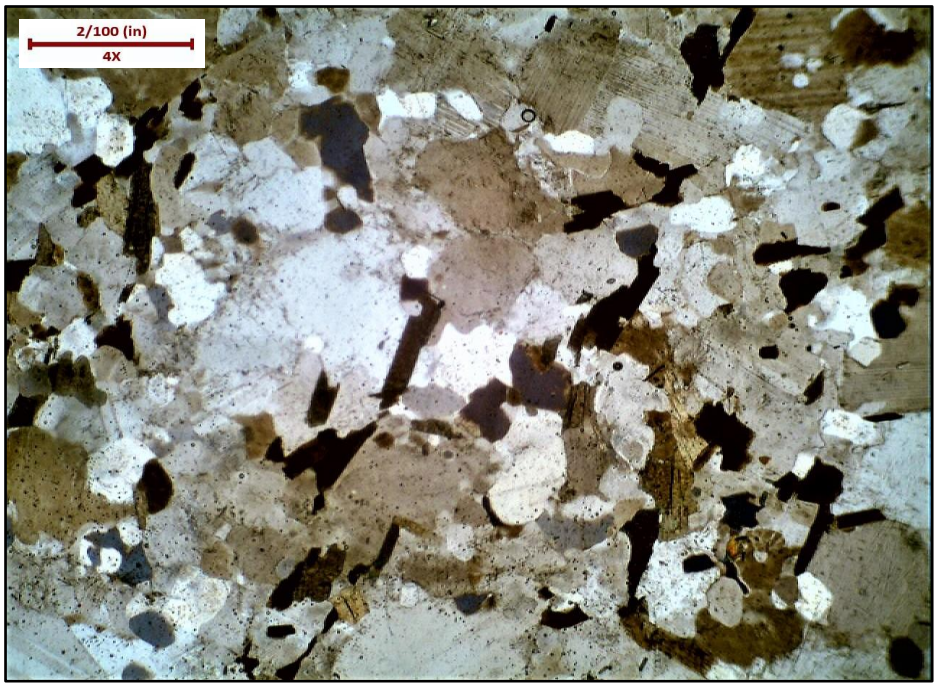


Figure 45a: Photomicrograph of the granodiorite in thin section under PPL.

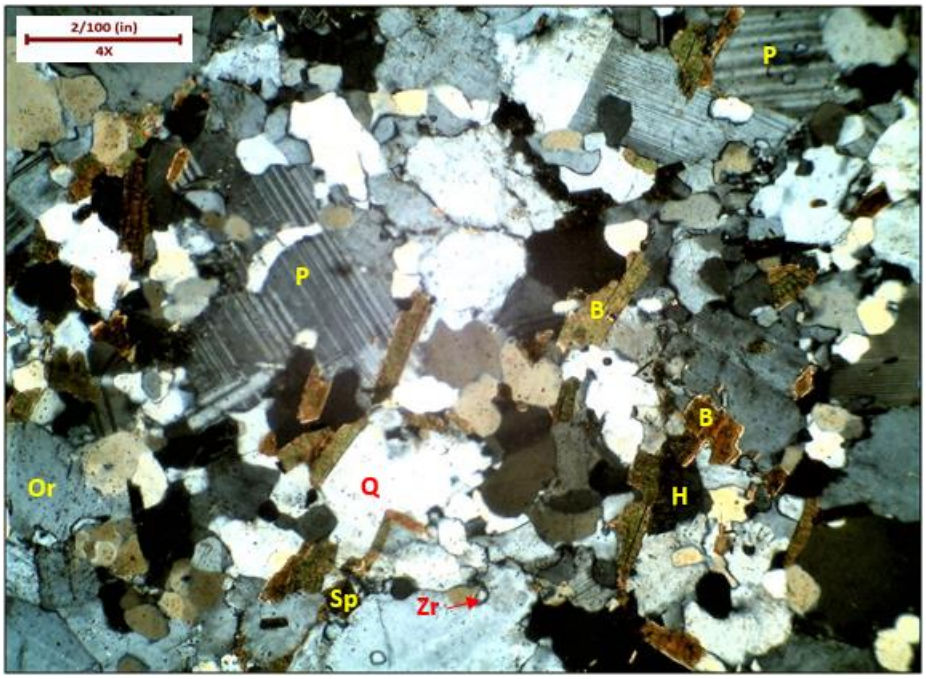


Figure 45b: Photomicrograph of the granodiorite in thin section under XPL. (B=biotite, H=hornblende, Or=orthoclase, P=plagioclase, Q=quartz, Sp=sphene, Zr=zircon)

4.1.12 Medium-grained biotite-hornblende Granite

Occurrence and Field Characteristics

The medium-grained biotite-hornblende granite is massive, granulitic textured and leucocratic to mesocratic in colour due the abundance of biotite, hornblende and feldspar. The rock outcrops as N-S trending low lying exposure (figure 46) and exhibits sharp contrast and contacts with the porphyritic granite and migmatitic gneiss within which it frequently occurs as intrusive bodies. Xenoliths of older gneissic rock suspected to be biotite gneiss, which have been partly granitized is common on some outcrops of this rock. Observations on field relationship show that the emplacement of the medium-grained biotite-hornblende granite postdates that of the coarse-grained granite. The NNE-SSW orientation of the outcrops of this rock conforms to the general trend of foliation in the surrounding host rocks. In hand specimen (figure 47), the rock appears to be equigranular textured and underlain only about 8% of the mapped area, occurring mostly in the northeastern sector of the area.

Petrography

Under the thin section (figure 48), the medium-grained granite is composed of equigranular crystals of subhedral quartz, microcline and orthoclase set within a groundmass of fine- to medium-grained quartz, plagioclase, biotite and hornblende. In some slides, few muscovite crystals occur at the grain boundaries of the plagioclase and biotite. Quartz is subhedral with triple junction. Plagioclase is andesine with 50% anorthite content. Microcline is subhedral to anhedral and partly breaks down to orthoclase.

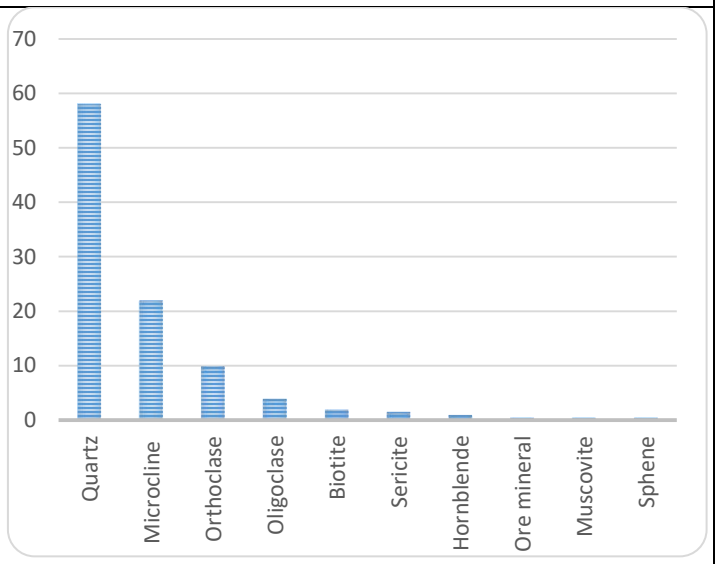
Biotite occurs as isolated long slender lath-shaped euhedral crystals and are mostly aligned along a preferred direction with pleochroic colour varying from brown to green. Muscovite eats up biotite in some places. Hornblende occurs in small patches of greenish to bluish to yellowish-coloured subhedral crystals and it is strongly pleochroic from green to dark green while it exhibits twinning in 2 directions at angle 120^{o}. Euhedral crystals of opaque ore minerals sometimes border the hornblende. Table 14 shows the average modal composition of minerals in the medium-grained biotite granite.



Figure 46: A low ridge outcrop of the medium-grained granite.



Figure 47: Hand specimen sample of the medium-grained granite

Table 14: Modal composition of the medium-grained Granite		
Mineral	Modal Composition (%)	Bar chart
Quartz	58	
Microcline	22	
Orthoclase	10	
Oligoclase	4	
Biotite	2	
Sericite	1.5	
Hornblende	1	
Ore mineral	0.5	
Muscovite	0.5	
Sphene	0.5	

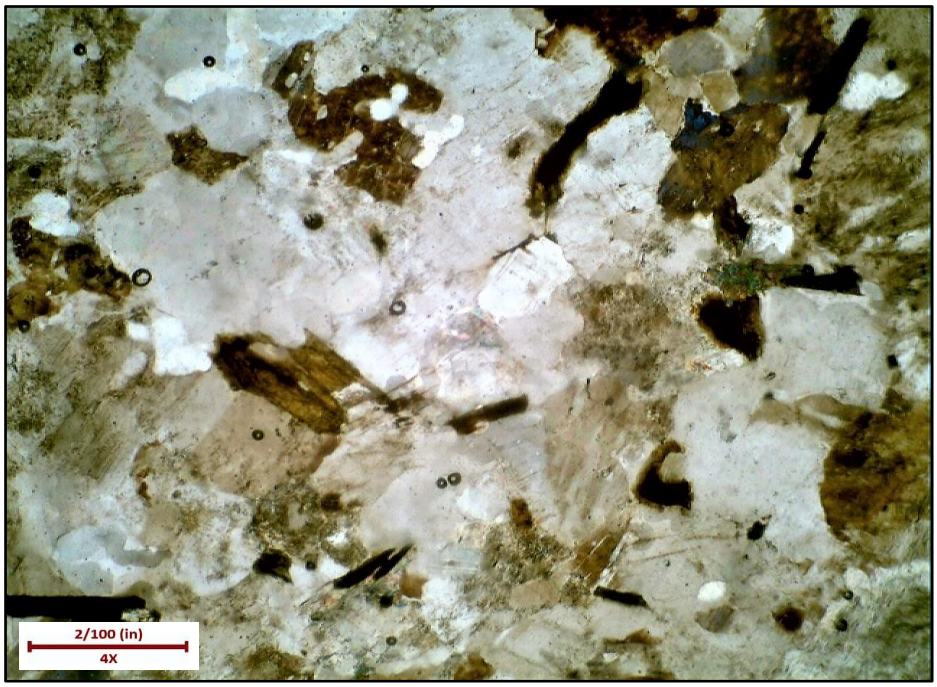


Figure 48a: Photomicrograph of the medium-grained granite in thin section under PPL.

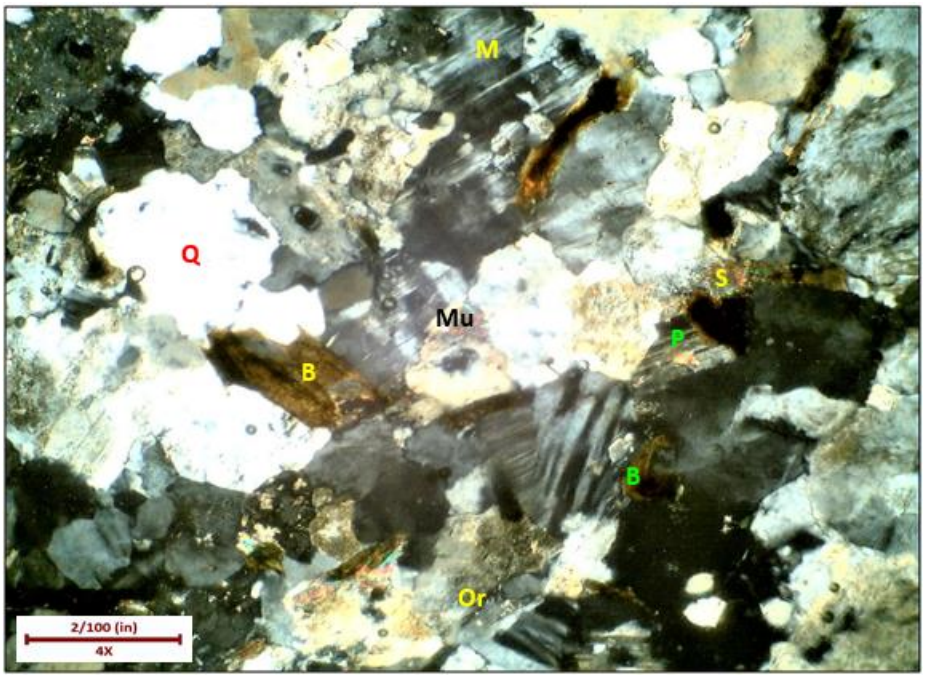


Figure 48b: Photomicrograph of the medium-grained granite in thin section under XPL.
(B=biotite, M=microcline, Mu=muscovite, Or=orthoclase, P=plagioclase, Q=quartz, S=sericite)

4.1.13 Alkali Syenite

Occurrence and Field Characteristics

The syenite found within the study area occurs as lenticular, irregular intrusive bodies and dykes in different parts of the migmatitic gneiss, medium-grained granite and porphyritic granite where the rock occurs as small bosses within the host rocks. In some localities, the syenite is mapped as low-lying bare rock outcrops (figure 49). The leucocratic alkali syenite is a feldspar-rich, fine- to medium-grained massive rock showing weak preferred mineral alignment and a flinty fraction.

The rock is equigranular and greyish to creamy white in colour. Hand specimen sample (figure 50) of the syenite mapped in the study area is characterized by small needle-like mafic streaks composed essentially of biotite clots. Parallel arrangements of these mafic streaks give the rock some weak sense of mineral alignment. The presence of biotite clusters produces some tiny flakes of biotite when a weathered surface of the rock is scratched with fingernail due to the abundance of the mineral. Field relationship, such as its occurrence as discordant intrusions, shows that the syenite post-dates its gneissic and granitic hosts.

Petrography

The interlocking relationship between quartz and feldspar gives the rock a granoblastic texture in thin section. The syenite is composed of a fine mosaic of quartz, orthoclase, microcline, andesine, minor muscovite, biotite and accessory minerals. Thin section study (figure 51) shows that the rock is composed of quartz + orthoclase + andesine + microcline + biotite + hornblende + muscovite +

ore mineral ± bytownite ± sericite ± zircon ± allanite ± sphene ± myrmeckite. Quartz is subhedral with triple junction. Plagioclase is andesine with 50% anorthite content.

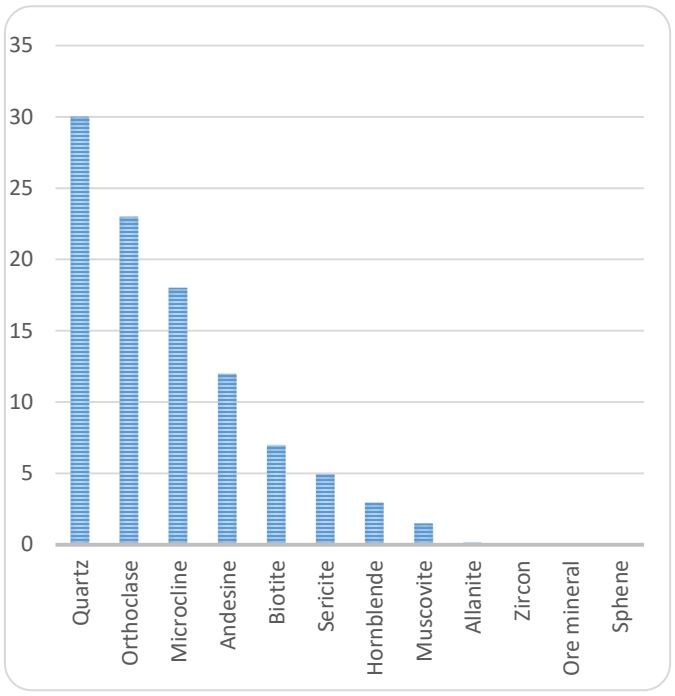
Microcline is subhedral to anhedral and partly breaks down to orthoclase. Biotite occurs as isolated long slender lath-shaped euhedral crystals and are mostly aligned along a preferred direction with pleochroic colour varying from brown to green. Hornblende is pleochroic from green to dark green and exhibits twinning in 2 directions at angle 120^{o}. Ore mineral occurs as cubic euhedral crystals. Muscovite eats up biotite in some places. Table 15 shows the modal composition of the Alkali Syenite.



Figure 49: A low ridge outcrop of the Alkali Syenite.



Figure 50: Hand specimen sample of the Alkali Syenite.

Table 15: Modal composition of the Alkaline Syenite		
Mineral	Modal Composition (%)	Bar Chart
Quartz	30	
Orthoclase	23	
Microcline	18	
Andesine	12	
Biotite	7	
Sericite	5	
Hornblende	3	
Muscovite	1.5	
Allanite	0.2	
Zircon	0.1	
Ore mineral	0.1	
Sphene	0.1	

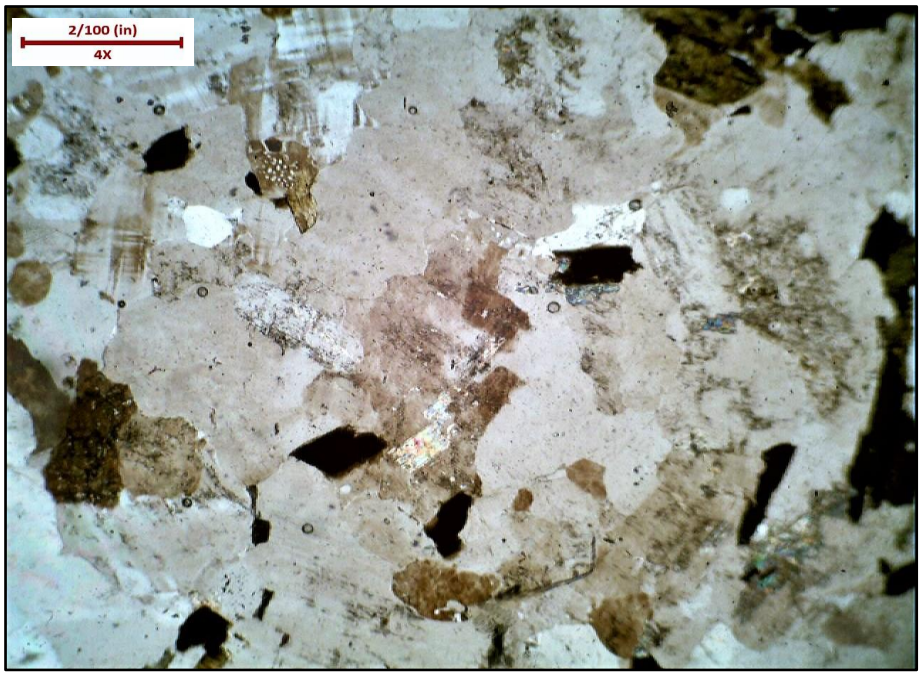


Figure 51a: Photomicrograph of the alkali syenite in thin section under PPL.

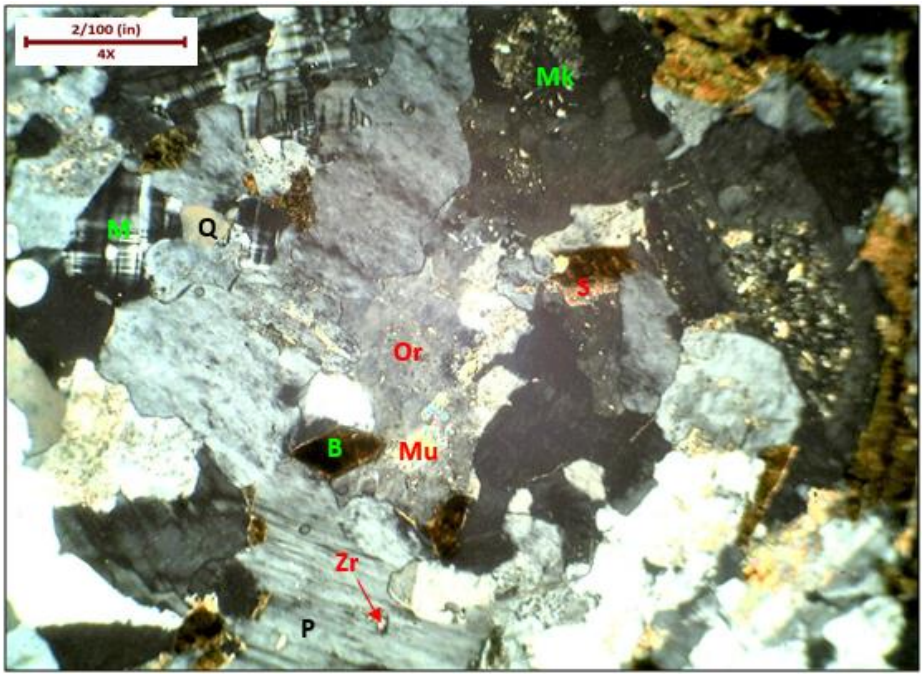


Figure 51b: Photomicrograph of alkali syenite in thin section under XPL. (B=biotite, M=microcline, Mk=myrmeckite, Mu=muscovite, Or=orthoclase, P=plagioclase, Q=quartz, S=sericite, Zr=zircon)

4.1.14 Pegmatite and Aplite

Occurrence and Field Characteristics

Pegmatite and aplite are widely distributed within the study area, intruding virtually all the major rock units in various forms and shapes ranging from veins and dykes (figure 52). Two generations of pegmatites have been recognized in the study area based on structure and extent of deformation. Early pegmatites and aplites intrude biotite and migmatitic gneisses as well as the metasediments in the area while the late stage (post granite) pegmatites and aplites intrude all the rock types in the study area and are relatively undeformed.

The pegmatites and aplites occur mostly as minor discordant veins which when locally numerous may coalesce to form large pegmatite bodies. The pegmatites are mainly the muscovite bearing type which frequently host important mineralization within the Nigerian Basement Complex and range in size from veinlets of a few millimeters wide to dykes of few meters wide. Hand specimen samples comprised of coarse-grained quartz, pink feldspars and books of muscovite.

Petrography

Thin section observation (figure 53) shows that the pegmatite is composed of quartz + orthoclase + oligoclase + andesine + microcline + muscovite $\pm$ biotite $\pm$ ore mineral $\pm$ sphene $\pm$ zircon $\pm$ apatite. Quartz shows wavy extinction with triple junction. Orthoclase is seen as cloudy anhedral crystals. Plagioclase ranges from Oligoclase to Andesine and is anhedral to subhedral shaped with anorthite content ranging from 10-30% and 30-50% respectively and are being altered to orthoclase.

Microcline shows grid twinning. Biotite occurs as lath-shaped euhedral to subhedral and isolated tabular crystals which are randomly oriented. Muscovite occurs as minor flakes formed from alteration of feldspar. Ore mineral is opaque with euhedral cubic-shaped crystals. Table 16 shows the modal composition of the pegmatite and aplite under the thin section.



Figure 52a: An outcrop of medium grained granodiorite showing pegmatitic intrusion.

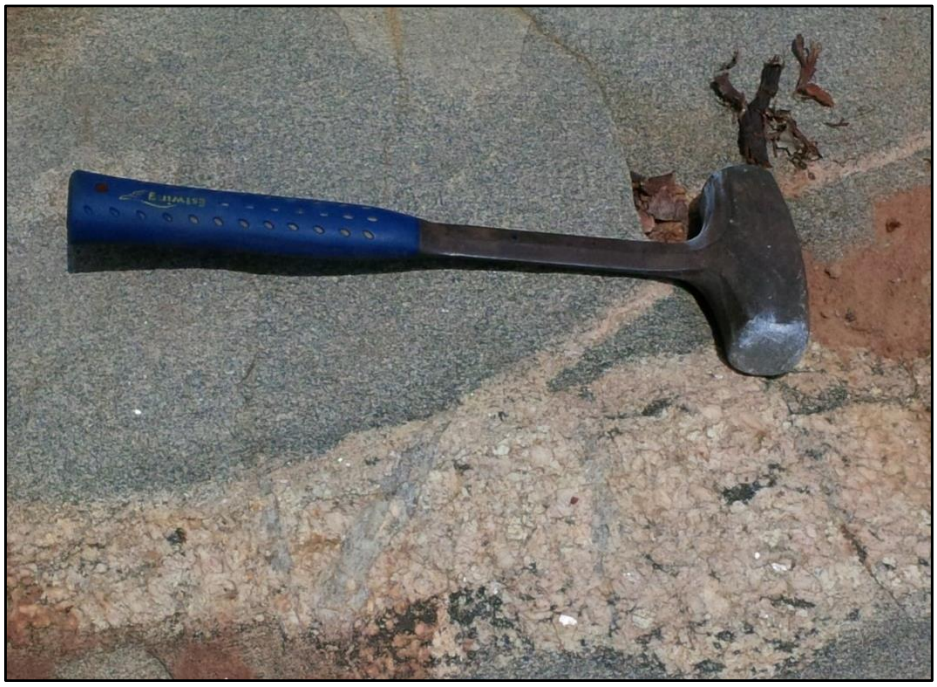
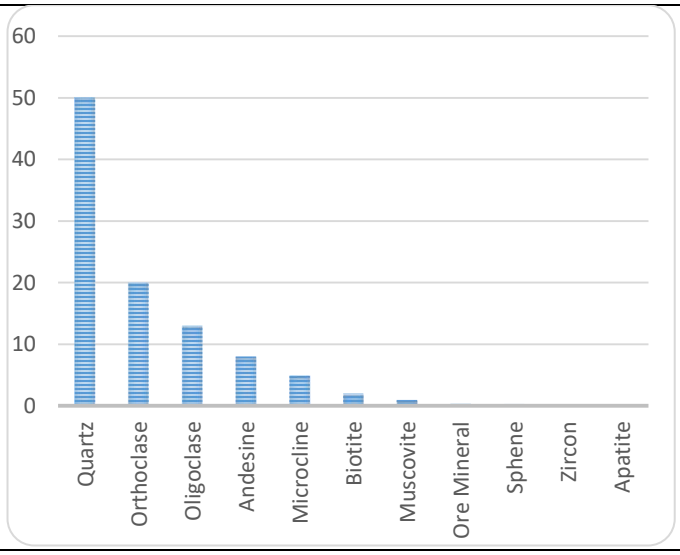


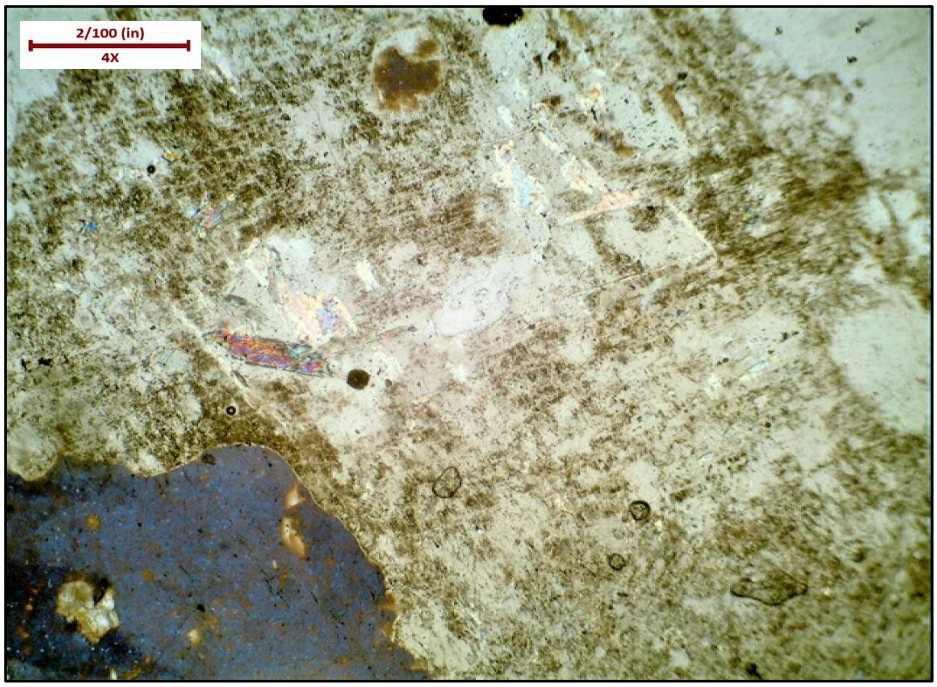
Figure 52b: An outcrop of medium grained granodiorite showing k-feldspar-rich pegmatite intrusion.



Figure 52c: Hand specimen of the aplite showing abundance of k-feldspar.

Table 16: Modal composition of the Pegmatite/Aplite		
Mineral	Modal Composition (%)	Observations
Quartz	50	
Orthoclase	20	
Oligoclase	13	
Andesine	8	
Microcline	5	
Biotite	2	
Muscovite	1	
Ore Mineral	0.4	
Sphene	0.3	
Zircon	0.2	
Apatite	0.1	





53a: Photomicrograph of the pegmatites in thin section under PPL.

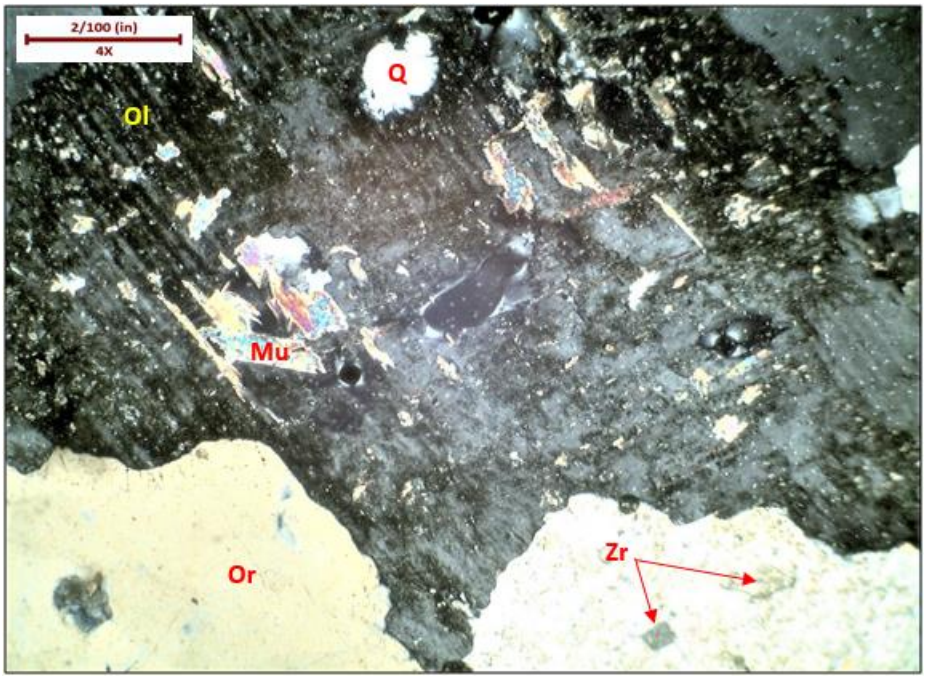


Figure 53b: Photomicrograph of the pegmatites in thin section under XPL. (Mu=muscovite, Ol=Oligoclase, Or=orthoclase, Q=quartz, Zr=zircon)

4.1.15 Vein Quartz

Occurrence and Field Characteristics

Vein quartz occurs as small irregular bands, lenses and veins of concordant or discordant quartz infusions cutting all rock types in the study area. Generally, they range in thicknesses from about 1cm to over 1m and trend mostly NE-SW. Most of the quartz veins in the schists and gneisses occur concordantly along the schistose foliation planes exhibiting similar trend and dip azimuth as the host rock (figure 54). Discordant quartz veins occur usually along healed joints and fractures in various directions.

The concordant quartz veins, from field relationships, appear to have been involved in tectonism affecting their host rocks while most of the discordant veins are relatively undeformed. Some of the concordant quartz veins have been boudinaged into short lenses. Large volumes of quartz veins of about 400m long and 12 to 35m wide was mapped around the central part of the study area, trending 030^{o} discontinuously in the NE-SW direction and affected in the northern end by a strike-slip fault which displaced the main quartz vein sinistrally by 30m (figure 55).

Other minor discrete irregular bands, lenses and veins of concordant or discordant quartz veins were mapped cutting rocks of granites, gneisses as well as the pegmatites of the study area. Hand specimen observation revealed that the quartz veins are made up of almost entirely quartz (figure 56) with or without subordinate muscovite and ore minerals. Where the quartz veins are

tectonized along fault and share zones, visible growth of recrystallized quartz, muscovite and euhedral sulphide crystals developed within crevices are observed (figure 57).

Petrography

Thin section study (figure 58) reveals that the rock is almost entirely composed of crystals of quartz with muscovite and ore mineral as accessory minerals. Quartz appeared stretched and observed as anhedral to subhedral crystals, showing triple junctions. Muscovite occurs as isolated intergranular lath-shaped crystals while ore mineral exhibits subhedral to euhedral crystals with cubic shapes. The mafic minerals tend to be aggregated probably due to recrystallization, which must have been either syn-tectonic or post-tectonic. Table 17 shows the modal composition of the vein quartz.



Figure 54: A section of an outcrop of the biotite gneiss showing a band of concordant quartz vein.

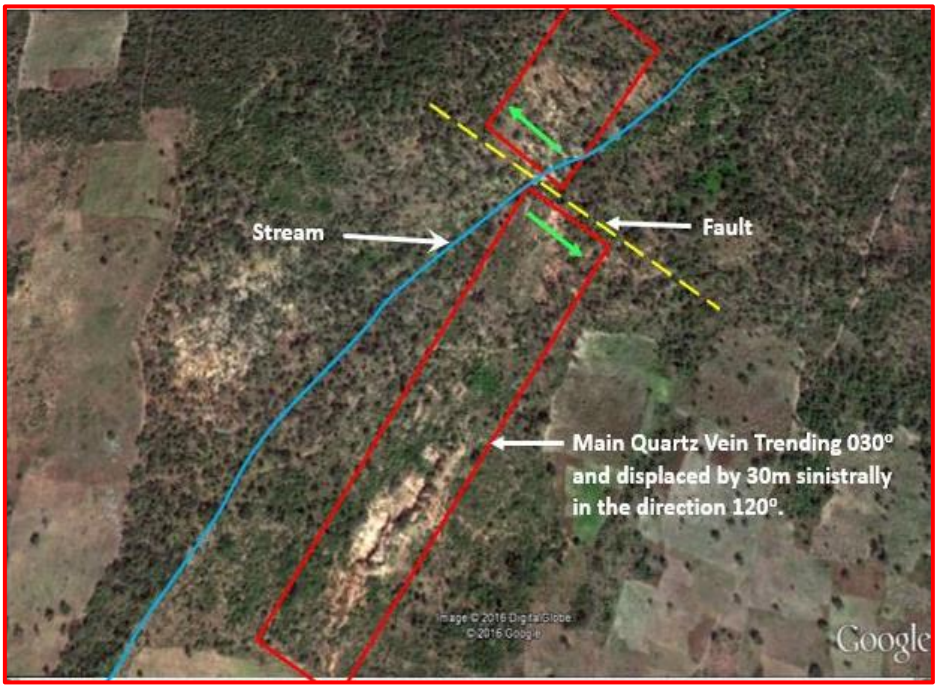


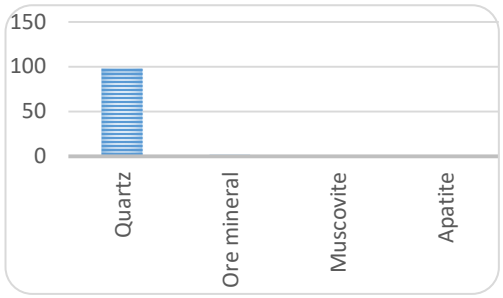
Figure 55: Satellite Image of Alagbede area showing the NE-SW trending mineralized quartz vein.



Figure 56: Hand specimen of the vein quartz.



Figure 57: Hand specimen of the tectonized vein quartz with sulphide mineralization.

Table 17: Modal composition of the **v**ein quartz		
Mineral	Modal Composition (%)	Bar chart
Quartz	98	
Ore mineral	1.7	
Muscovite	0.2	
Apatite	0.1	

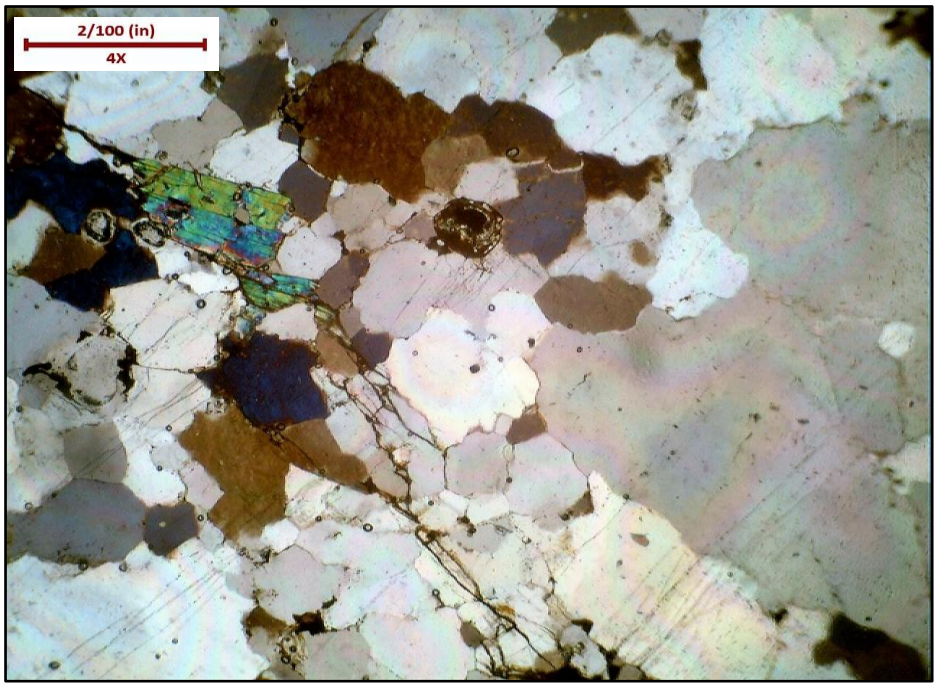


Figure 58a: Photomicrograph of vein quartz in thin section under PPL.

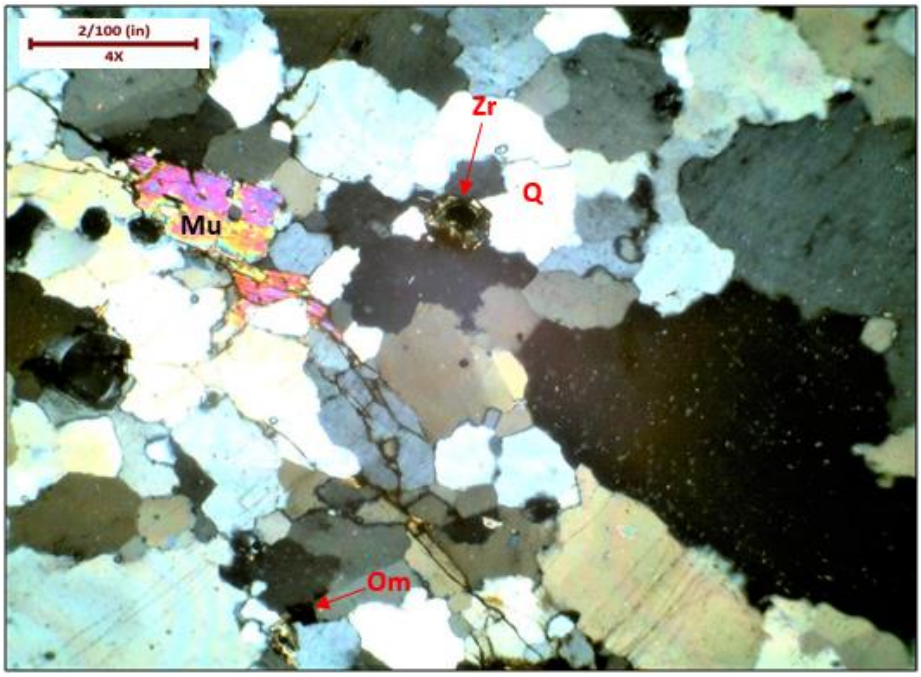


Figure 58b: Photomicrograph of vein quartz in thin section under XPL. (Mu=muscovite, Om=ore mineral, Q=quartz, Zr=zircon)

4.2 Structural Geology

Field observations on the architecture of rocks, stress-strain relationships, form, arrangement, and internal structure of rocks in the study area were made to study the deformation that has affected the area. The heat and pressure that form metamorphic rocks was responsible for the deformation of these rocks, giving rise to a variety of textures and structures collectively referred to as metamorphic fabrics. Structures found on the outcrops include the primary and the secondary structures which were observed, analyzed and, their orientations documented. Secondary structures encountered in the course of this field mapping can be divided into two namely:

i. Ductile structures which include lineation, foliations, folds, pinch and swell;
ii. Brittle structures such as fractures (joint and fault).

4.2.1 Ductile Structure

Field and structural evidence have shown that the Nigerian Basement Complex has suffered several episodes of deformation leading to multiple reactivations of the crustal rocks which bear tectonic fabrics of ductile deformation. These include lineation, foliation, folds, shears, pinch and swell, etc. These ductile fabrics form the most prominent structures in the study area whose extent, scope and magnitude varies from one outcrop to another particularly within the migmatite-gneiss terrain.

Lineation

Lineation was observed in the biotite gneiss and the migmatitic gneiss terrains due to intersection between the foliation planes and the fold axial planes, which gives rise to intersection lineation

and sometimes lead to the formation of mullion structure. Streaks of biotite and aligned feldspar and quartz crystals constitute some of the few mineral lineation observed in some gneissic outcrops in the study area. Most of the mineral lineation observed on foliation surfaces particularly on gneissic outcrops varies in plunges from 20^{o} to 40^{o} with plunge azimuth ranging between 050^{o} (NE) and 310^{o} (NW).

Foliation

Foliation is the most distinctive evidence of tectonic deformation as observed on gneissic outcrops in the study area. The foliation planes may have been formed by several ways such as segregation of planar minerals into alternating mafic and felsic bands, forming the gneissose or schistose foliation planes, axial-planar cleavage foliation, as well as anatectic or alternating psammitic and pelitic bands in relict lithologic bedding of sedimentary origin. The orientation of the foliation planes were observed and measured as strike and dip of the planar surfaces on deformed rocks which include the biotite gneiss, migmatitic gneiss, porphyroblastic gneiss, quartzite, schists and porphyroblastic granites mapped in various locations in the study area.

Most foliation planes in the study area trend NE-SW with fewer NW-SE trends. The dip amount range in magnitude from 25-75^{o} while the dip direction revealed a predominantly westerly dipping attitude of the foliations with fewer easterly dipping foliation planes. The intermittent E-W dips of the foliation gave rise to series of inferred alternating antiformal and synformal folds with N-S fold axes particularly in the southern half of the study area (see figure 13). This is also evident on the plot of the pole to point of foliation planes of foliated rocks of the study area (figure 59).

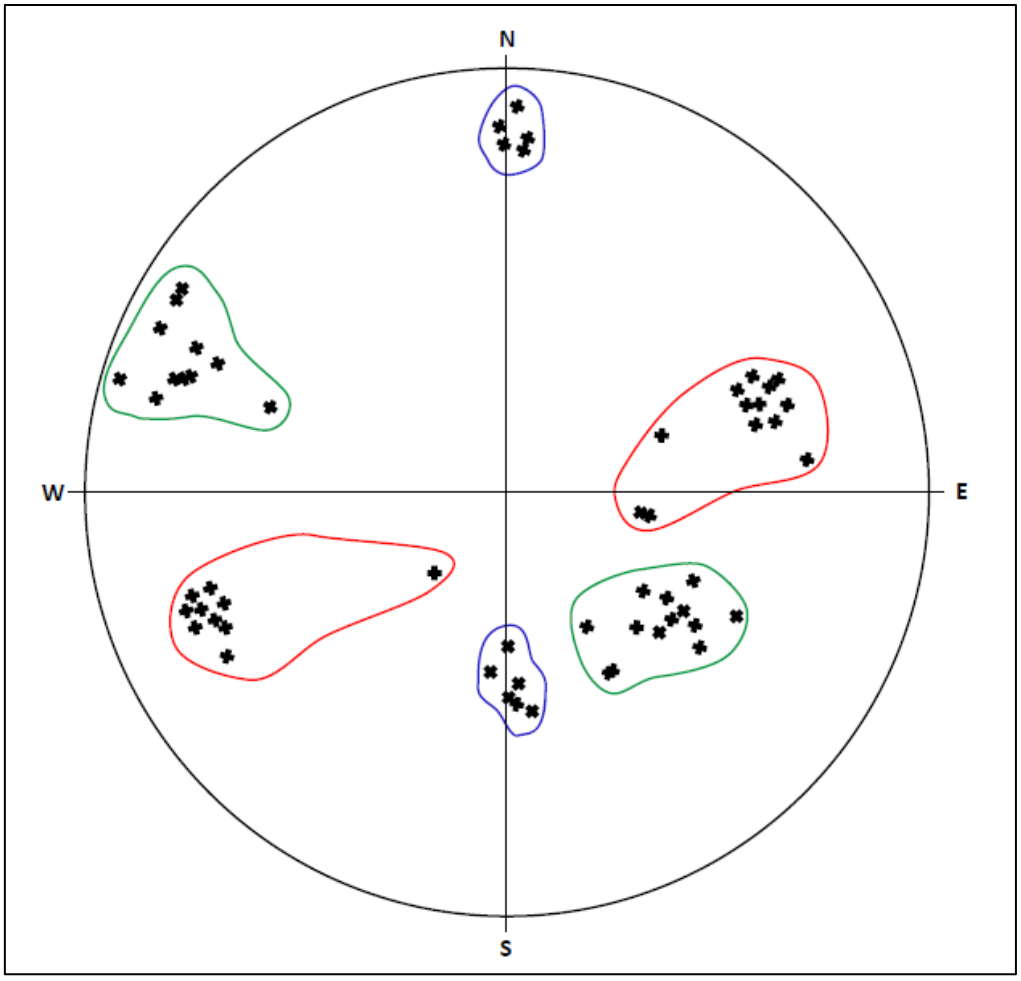


Figure 59: Plot of the pole to point on foliation planes in the gneisses of the study area showing three (3) regional antiformal fold closures.

Folds

The most striking and commonest deformation features mapped on the basement terrain of the study area are folds which are readily observable on gneissic outcrops. Tectonism in the area is represented by polyphase deformation episodes, resulting in the formation of numerous folds including the observed minor folds on outcrop scale and the inferred folds on regional scale. The observed minor asymmetric tight isoclinal folds (figure 60) on the gneisses represent the earliest folding episode and their axes are parallel to the pervasive axial planar gneissosity that defines the structural grains of the gneissic terrain in the study area.

The average plunge of the fold axes of these tight isoclinal folds is 15^{o} to 22^{o} in the directions 010^{o} to 045^{o} and some of the folds are locally recumbent with fold axial planes dipping between 36^{o} and 60^{o} either easterly or westerly. Closely related to the tight isoclinal folds are the ptygmatic folds, which are mostly found in the migmatitic gneisses (figure 61). Another folding episode is expressed as flow structures defining open folds in the gneisses some of whose axial plane are locally recumbent with an average plunge of about 55^{o}-70^{o} in the direction 110^{o}-140^{o}. On some intensely deformed outcrops, interference between two open folds were observed, resulting in the formation of basin and dome structure (figure 62).

A major episode of folding is inferred from the set of distinctive bands of gneissosity associated with the gneisses which form excellent structural markers that define regional antiformal and synformal folds whose axes trend almost parallel and N-S particularly in the southern half of the

study area. This episode of folding is perhaps accompanied by the semi-brittle deformation that forms the various parallel shears observed on many gneissic outcrops and may in fact be responsible for tectonizing a section of the porphyritic granite into porphyroblastic granite and gneiss in the area.

Shears

Shears occur in transitional areas between intense ductile to semi brittle deformation just before the inception of brittle faulting in the basement. These are narrow (usually few millimeters wide), vertical to sub-vertical structures along which some amount of dragging occur, thereby resulting in drag folds that deform foliation planes (figure 63) as evident in areas of intense deformation in the schist, biotite gneiss and migmatitic gneiss. Some of the shears are brittle and their planes are sometimes healed with mylonite or quartzo-feldspathic materials. Most of these shears trend in the NNE-SSW direction with steep to near-vertical dips, crosscutting most pre-existing structures in the study area. The intensity of the deformation depends on the rock types affected and varies within and across the shear zone. A typical example of a shear related structure of ductile nature is the pinch and swell (boudinage) structure.



Figure 60: An outcrop of a migmatitic gneiss showing tight isoclinal fold.



Figure 61: A section of a migmatitic gneiss outcrop showing ptygmatic fold.



Figure 62: An outcrop of a migmatitic gneiss showing deformed basin structure.



Figure 63: An outcrop of porphyroblastic granite showing a ductile shear with drag folds.

4.2.2 Brittle Deformation

Brittle deformation results from tectonic movements in the earth's crust in which the rock experiences fracturing or crack along definite planes, usually occurring at shallow depths when compared with ductile deformation such as folding which takes place at deep depths. Faults and joints are the two fracture types mapped in rocks of the area. While some of the fractures are healed either with quartz of quartzo-feldspatic materials and are either concordant or discordant to the tectonic fabrics of the host rocks, others are not healed and are either open or closed.

Fault

Faults are observed as fractures in rocks where relative movements between two blocks have taken place which may include the strike slip fault (displacement along strike) and the dip slip fault (displacement along dip). Both dextral and sinistral faults were mapped in the study area trending averagely between 100^{o} to 130^{o} with varying degree of displacements and intensity. A major inferred fault as observed on aeromagnetic map of the study area trends in the direction 120^{o} and shows a sinistral displacement of the northern part of the main gold-bearing quartz vein by 30m (see figure 55).

Joints

Joints are fractures or cracks in a rock along which no visible displacement has occurred. These are products of brittle deformation of rocks when acted upon by tectonic forces, along the areas of weakness in the rocks. Orientation data on jointing holds valuable information about the

orientation of stress fields at the time of failure. The joints are either concordant or discordant and may be unhealed or healed with quartzo-feldspatic materials (figure 64). All the rock types in the study area exhibit various joint sets and their measurements are spatially represented on rosette diagrams to evaluate the dominant joint directions and ultimately to determine the tectonic deformation dynamics and shear-strain trajectory within the rocks of the study area.

The rosette plots of joint trends in the granites (figure 65) and gneisses (figure 66) of the study area show two (2) dominant strain; the E-W trending fracture resulting from a N-S compressive shear stress and the subsidiary strain whose trend varies from NW-SE to NNW-SSE directions with a tangential NNE-SSW compressive force. The rosette plot of joint directions in the schist (figure 67) shows a NNE-SSW strain, indicating a WNW-ESE deformational shear stress. The rosette plots of healed joints also show most vein quartz trending mainly WNW-ESE and NE-SW (figure 68) while the aplo-pegmatitic veins trends in the NW-SE and NNW-SSE directions (figure 69).



Figure 64: An outcrop of granodiorite showing healed concordant and discordant joints.

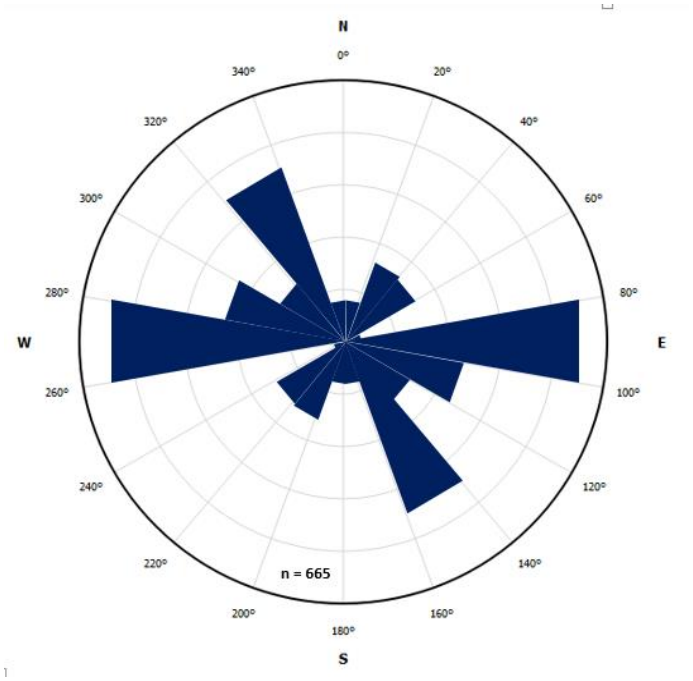


Figure 65: Rosette diagram showing the trend of joints in granite of the study area.

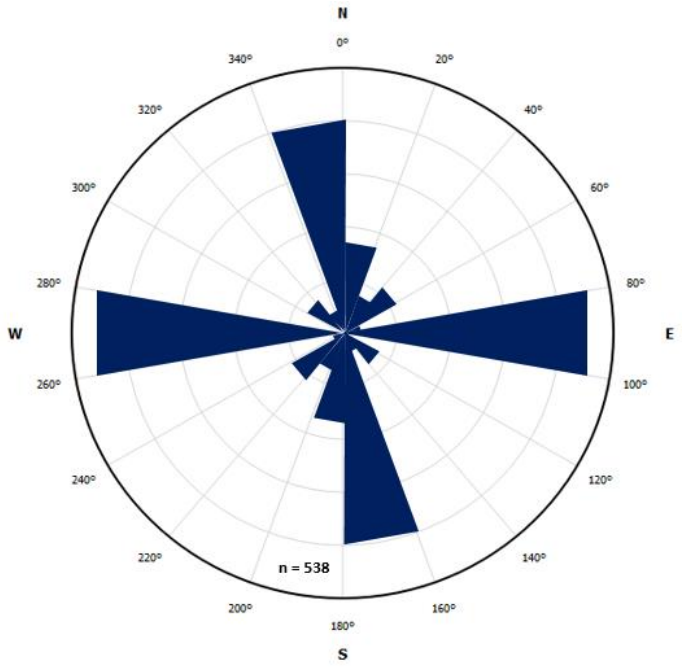


Figure 66: Rosette diagram of the trend of joints in the gneisses of the study area.

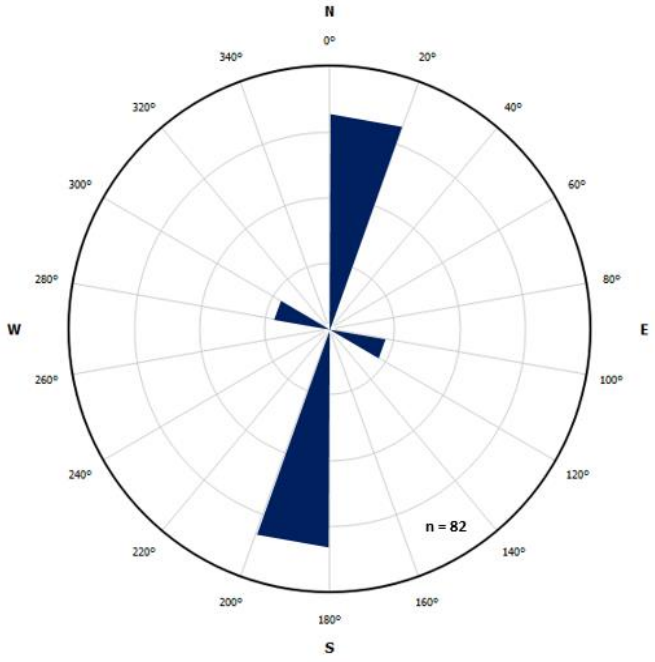


Figure 67: Rosette diagram of the trend of joints in the schists of the study area.

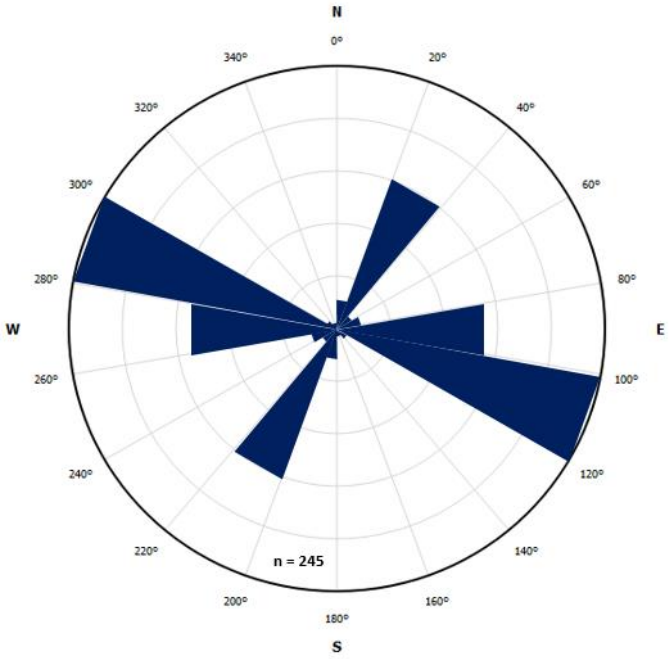


Figure 68: Rosette diagram of the trend of joints healed with vein quartz.

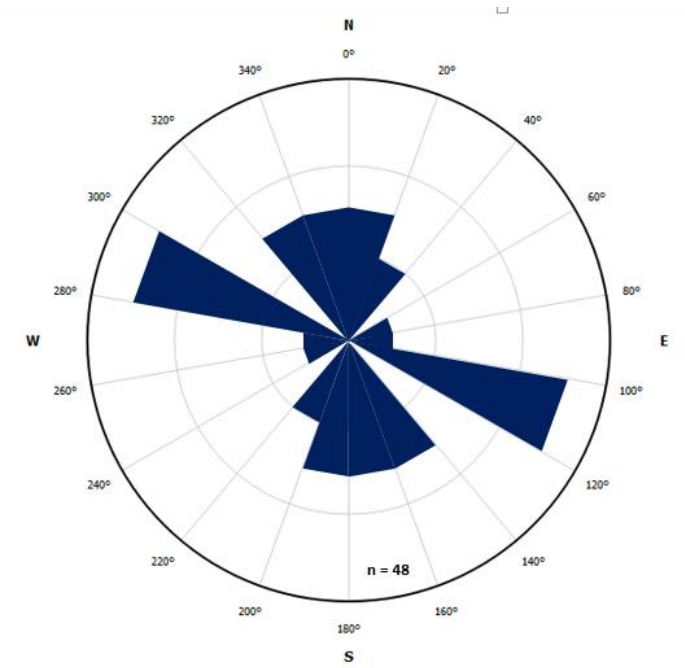


Figure 69: Rosette diagram of the trend of joints healed with pegmatites and aplites.

4.2.3 Structural Evolution

The Nigerian basement is polycyclic in nature and is characterized by different histories of metamorphism, orogenies and structural modifications (Odeyemi, 1981; Rahaman *et al*., 1983; Caby, 1989) which is reflected in its complex petrological and structural composition with successive events overprinting, reworking and modifying the earlier events. Field and structural evidence revealed that the basement rocks underlying the study area have suffered multiple episodes of deformations. The gneissic rocks in the area show structural elements with varying degree of deformation ranging from simple stromatic to contorted (intensely deformed) foliation planes. The study of the present-day rock geometry with respect to the three-dimensional distribution of the various lithological units provided information about the history of deformation (strain) in the rocks, and ultimately, the stress field that resulted in the observed strain and geometries.

Field and petrological evidence suggest at least three episodes of deformation in the study area. The structural deformation (D_1) in the area probably constitute the first tectonic episode which changed the physico-chemical structure of the sedimentary precursor leading to primary metamorphic fabrics that are observed as lithological and mineralogical banding (S_oS_1) preserved in some biotite gneisses located in tectonic shadows. The second tectonic deformation episode (D_2) was responsible for folding the S_oS_1 surfaces into tight isoclinal folds (F_1) which produced the S_2 surfaces that are axial planar to F_1 as observed in figure 60.

The third episode of tectonic deformations (D_3) refolded the S_2 surfaces resulting in the formation of the crenulation cleavages which formed the incipient (S_3) surfaces that are superimposed on S_2 surfaces in tectonic shadows on some outcrops. This produced the second filial generation of major folds (F_2), which are upright, open or close and may sometimes be recumbent and plunging. The tectonic features produced by D_3 include pinch and swell structure, similar, asymmetric and chevron folds. D_3 is also perhaps responsible for the formation of the inferred regional folds in the study area and may have resulted in the formation of several regional fractures, minor joints, shears, faults as well as basin and dome structure which may have been produced by the interference between two D_3 fold patterns (figure 62).

4.3 Metamorphic Geology

Petrographic and field evidences revealed that the study area have suffered from at least three (3) episodes of regional metamorphism (M_1, M_2 and M_3) which are associated with the main episodes of deformations (D_1, D_2 and D_3). The first episode of deformation/metamorphism (M_1) recognized in the area resulted in the development of foliation surfaces marked by the millimetric mineralogical banding recognized on some biotite-hornblende gneiss outcrops. This fabric was affected by the second episode of deformation/ metamorphism (M_2) resulting in the formation of axial planar folds in the area. This metamorphism probably did not exceed the biotite grade of the upper green schist facies.

The third episode of deformation/metamorphism (M_3) probably produced the crenulation cleavage fabrics observed in some parts of the migmatitic biotite-hornblende gneiss. The most

obvious signs of recrystallization seen under the microscope are the widespread development of polygonal grains of quartz with triple junction in some of the rock thin sections studied. This is probably the effect of reheating during contact metamorphism. The biotite flakes are short and tabular in the gneisses and they possibly grew during the same episode of metamorphism.

4.3.1 Metamorphic Mineral Assemblages and Grades

Temperature and pressure conditions at depth within the earth crust cause mineralogical and structural changes in solid rock. These changes produce metamorphism, which involves partial or complete recrystallization of the original rock in solid state, producing a set of minerals in mutual association that constitute a metamorphic mineral assemblage (Winkler, 1979). These metamorphic mineral assemblages help to classify rocks into various metamorphic grades. The metamorphic mineral assemblages as contained in the various rocks studied in the area are as follow:

Biotite Gneiss

The biotite gneiss contains the following metamorphic mineral assemblage similar to those contained in the migmatitic gneiss but for the absence of garnet: quartz + andesine $\pm$ labradorite $\pm$ bytownite + biotite + orthoclase + hornblende $\pm$ muscovite $\pm$ pyroxene. This metamorphic assemblage represents the medium grade, middle amphibolite facies metamorphism.

Migmatitic Gneiss

The following metamorphic mineral assemblage was observed to co-exist in the migmatitic gneiss: quartz + labradorite ± andesine + orthoclase ± microcline + biotite ± sericite + hornblende ± myrmeckite ± muscovite. This metamorphic assemblage represents the medium grade, middle amphibolite facies metamorphism.

Quartz Mica Schist

The quartz-biotite-muscovite schist consists of quartz + biotite + muscovite ± orthoclase ± andesine ± chlorite ± myrmeckite ± epidote ± zircon. This metamorphic assemblage represents the low to medium grade, low green schist facies metamorphism.

Amphibolite

The following metamorphic mineral assemblage represents the amphibolite facies as observed in the study area: hornblende + garnet + quartz + plagioclase + biotite + actinolite. This mineral assemblage represents the medium grade, epidote-amphibolite facies metamorphism.

Talc-Tremolite-Actinolite Schist

The talc-tremolite-actinolite schist consist of the following mineral assemblages: talc + tremolite ± actinolite, which corresponds to the medium grade, middle amphibolite facies metamorphism.

4.4 Economic Geology

The study of the various minerals of economic values and uses to which the different rock types in the study area could be put to is one of the major objectives of this work. The study area is underlain by the Precambrian basement rocks, intruded in places by decomposing pegmatitic veins which offer good prospects for gemstones, feldspar and quartz mineralization.

4.4.1 Mineral Resources

The most prominent mineral exploration and exploitation activities observed in the course of this study, was those of the artisanal miners wining gold from the main quartz veins in the area. This gold mineralization offers a huge prospect for the economic emancipation of the host community. Some of the minerals of potential economic values include feldspars, quartz, gemstones and construction aggregates.

4.4.2 Construction Materials

Laterite, sand and gravels which are nonmetallic economic resources and are found in abundance in the study area can be exploited for building and other engineering construction work purposes. Some of the crystalline rocks of the study area, including the porphyritic granites and gneisses which outcrop as ridges and inselbergs in some places are suitable to be quarried for construction purposes and for dimension stone. The incompressibility and ability to retain strength under stress without yielding to deformation under load make these rocks excellent engineering construction materials. The characteristic fabrics and colours of the porphyritic granite (pinkish) make the rocks

very suitable as dimension stones. The rich laterite soils at some locations are suitable for red brick making and as additive in cement making industry.

4.4.3 Hydrogeology

Rivers and streams which drained the area form a major source of surface water for both domestic and animals use. The rivers and streams are heavily flooded during the peak of the raining season, and reduce in volume during dry seasons thereby exposing huge deposits of sands and gravels along their channels and banks. Another important hydrological system in the study area is the underground water, obtained by the sinking of boreholes and hand-dug wells which serve as the main sources of water supply for domestic and laundry purposes (figure 70).

4.4.4 Geotourism Potentials

There are good scenic sites of touristic value such as the beautiful landscapes, mountains, hills and dams in the study area which can be developed as tourist centers to generate revenue for the locals and the State.



Figure 70: A hand-dug well and a manual borehole in Alagbede village.

4.5 Geochemistry

A total of one hundred and four fresh rock samples were collected from the studied area out which 42 were selected for whole-rock major, trace and rare earth element (REE) analyses. The whole-rock geochemistry of 20 samples were analyzed at the Bureau Veritas Analytical Laboratories Ltd., in Canada while the remaining 22 were analyzed at the EarthLab of the School of Geosciences, University of Witwatersrand in South Africa. The major elements concentrations were measured by XRF after the pulverized rock samples were converted to fusion disks while the trace elements concentrations (appendices 1a and 1b) were analyzed by ICP-MS on digested samples.

4.5.1 Interpretation of Geochemical Data

The binary plot of Streckeisen LeMaitre (1979) for general classification of volcanic rocks shows the volcanic rocks of Alagbede plotting within the alkali granite, syeno-granite and monzogranite field (figure 71). The AFM diagrams for chemical classification of common volcanic rocks of Kuno (1968) and Irvine and Baragar (1971) (figures 72 and 73) revealed that the granites are calc-alkaline in composition.

The K_2O vs SiO_2 plots of Peccerillo and Taylor (1976) (figure 74) and of Middlemost (1975) (figure 75) for general classification of volcanic rocks indicate that the alkali granite and syenite of Alagbede are predominantly high K calc-alkaline to shoshonitic and alkalic in composition respectively. The TAS discriminatory plots of LeBas et al. (1986) (figure 76) and Cox-Bell-Pank (1979) (figure 77) for volcanic rocks revealed that the alkali granite and syenite of Alagbede area tend towards a rhyolite in composition while the TAS discriminatory plots of Cox-Bell-Pank (1979)

(figure 78) for plutonic rocks shows the porphyritic granite, porphyroblastic granite, porphyritic diorite and granodiorite of Alagbede area plotting within the granitic field.

The binary plots of logs of (Nb) vs (Y) (figure 79), (Ta) vs (Yb) (figure 80) and (Rb) vs (Yb+Ta) (figure 81) of the trace element discrimination diagrams for tectonic interpretation show the granitic rocks of Alagbede area plotting within the syn-collisional granite (Syn-COLG) and volcanic arc granite (VAG) fields of Pearce *et al*, 1984. However, all the Alagbede granites plots on the volcanic arc granites (VAG) field on the log (Rb) vs Log (Y+Nb) discrimination diagrams for tectonic interpretation (figure 82). This is interpreted as a volcanic arc source for the granitic rocks of Alagbede area with significant contribution from the partial melting of the continental crust materials.

The basic rocks of Alagbede area including talc schist, gabbro, amphibolite and porphyritic diorite mostly plotted close to the island-arc tholeiitic field on the Ti vs Zr binary discriminatory diagram of Pearce Cann (1973) (figure 83) while on Th/Yb versus Ta/Yb of Pearce 1982 (figure 84), these rocks plotted between volcanic arc and within plate basalts. On the Ti-Zr-Y ternary diagram (figure 85) of Pearce Cann (1973), Gab 40B & Amph 46B plotted within and TSch 79, 80A1 and OGd 43B plotted close to the Calc-Alkali basalt field while samples OGd 42A, Gab 52, TSch 80B & 80F plotted around the Island Arc Tholeiitic field.

On the Ti-Zr-Sr ternary diagram (figure 86) of Pearce Cann 1973, Gab 40B & TSch 80A1 plotted within and Amph 46B plotted around the Calc-Alkali field while samples TSch 80B & 80F plotted on the Island Arc Tholeiitic field. On the Nb-Zr-Y ternary diagram (figure 87) of Meschede, 1986 for

the basaltic rocks of Alagbede area, TSch 79, Gab 40B, OGd 43B, Amph 46B plotted within Within Plate Alkali basalts, TSch 80B & 80F plotted close to within plate alkali basalt field, while TSch 8A1 plotted within E-type MORB.

On the Hf-Th-Ta ternary diagram (figure 88) of Wood, 1980 for the basaltic rocks of Alagbede area, TSch 79 & 80A1, Gab 40B plotted within Alkali within plate basalts while OGd 43B, Amph 46B, TSch 80F plotted close to Alkali within plate basalts. Although, talc schist and amphibolite are metamorphic and therefore are not of same age with the gabbro and diorite, these geochemical plots show that the gabbro, amphibolite and porphyritic diorite were derived from within plate alkali basalt of island arc tholeiitic origin while the composition of the talc schist ranges from calc-alkaline to within plate basaltic precursor.

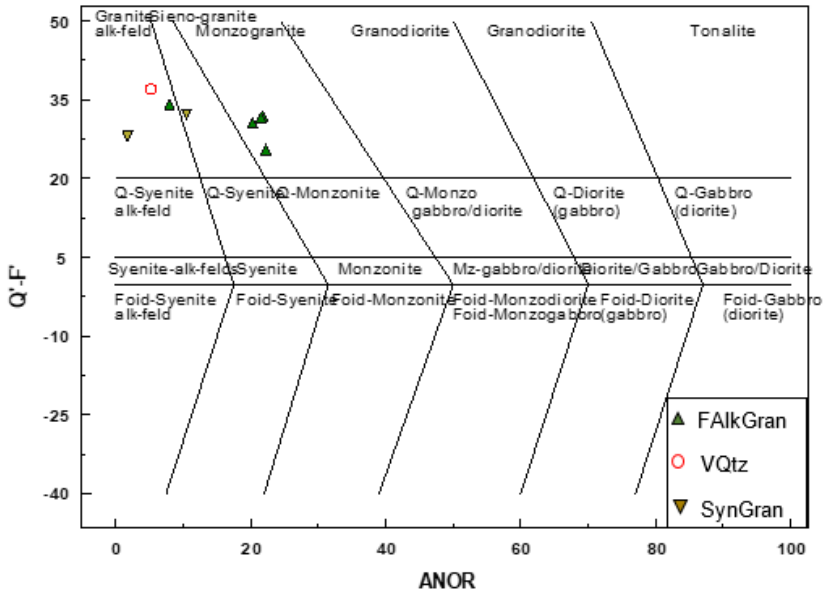


Figure 71: Binary plot for general classification of volcanic rocks of Alagbede (after Streckeisen LeMaitre 1979).

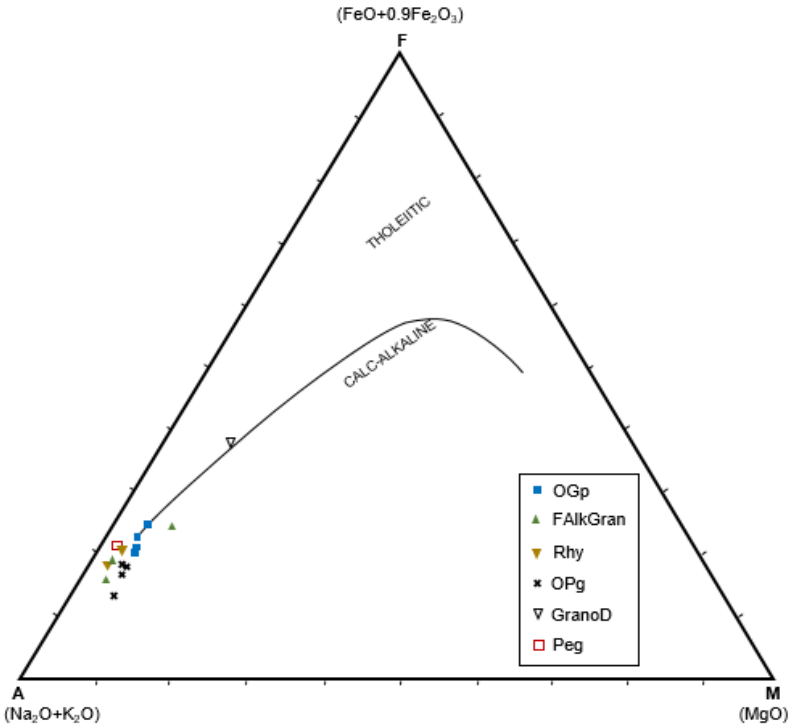


Figure 72: AFM diagram for chemical classification of common volcanic rocks of Alagbede area (after Kuno, 1968)

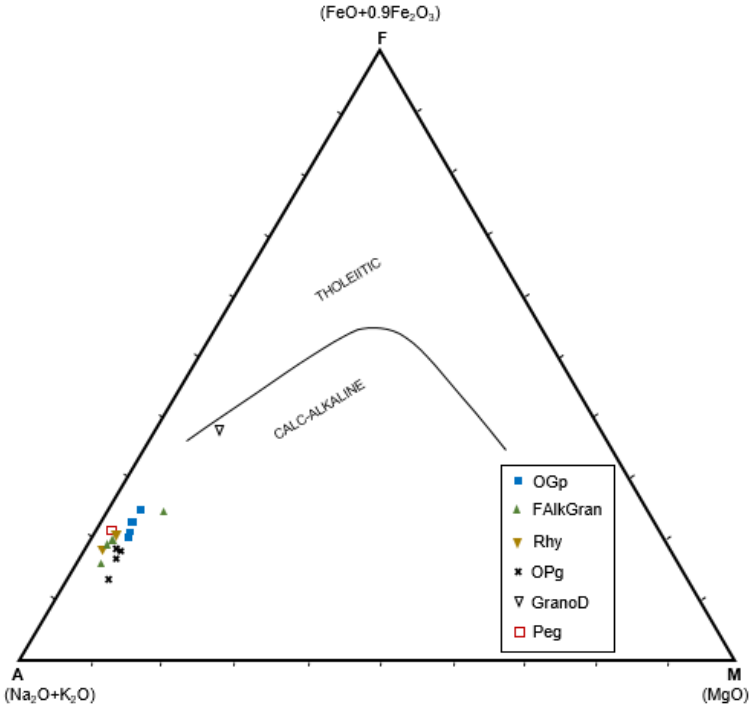


Figure 73: AFM diagram for chemical classification of common volcanic rocks of Alagbede area (after Irvine and Baragar, 1971)

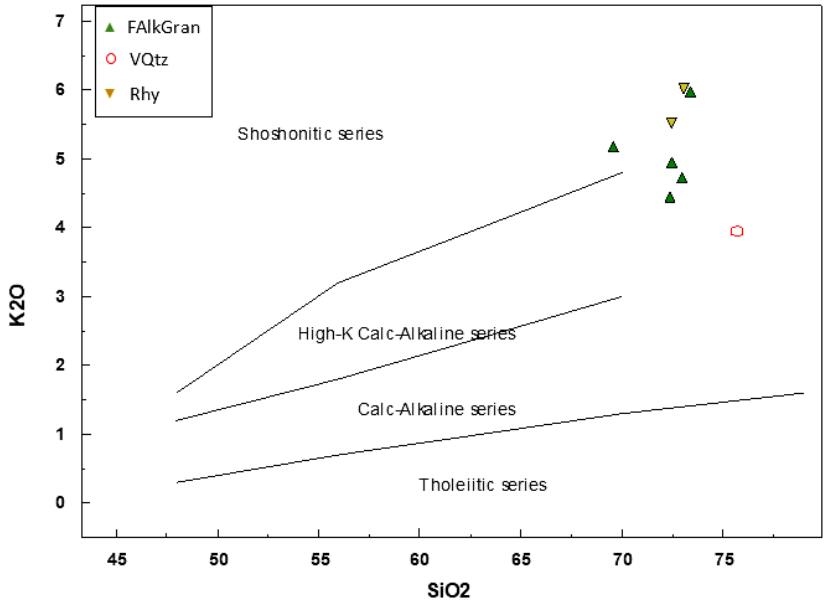


Figure 74: K_2O vs SiO_2 for general classification of volcanic rocks at Alagbede (after Peccerillo and Taylor 1976).

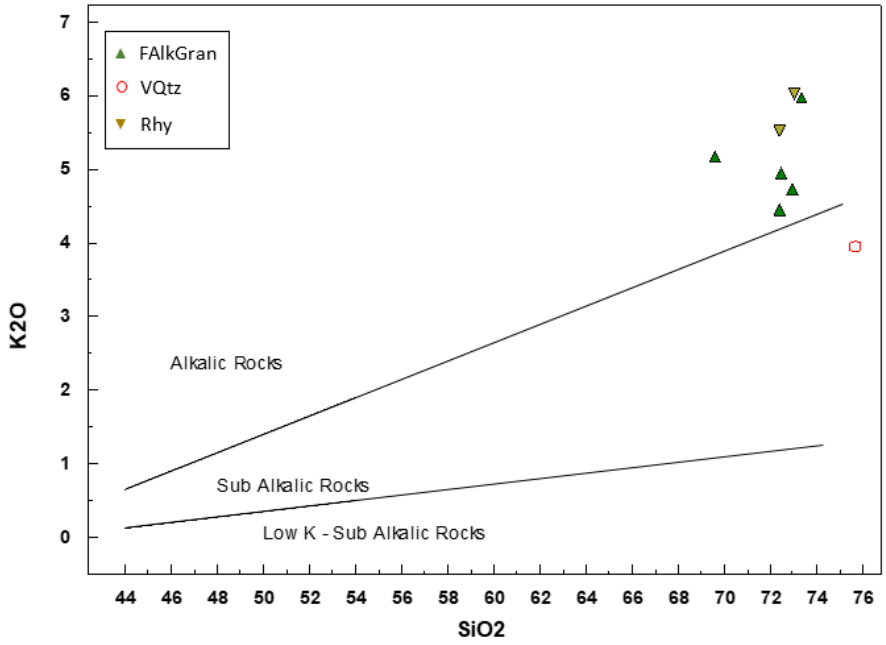


Fig. 75: K_2O vs SiO_2 for general classification of volcanic rocks at Alagbede (after Middlemost 1975).

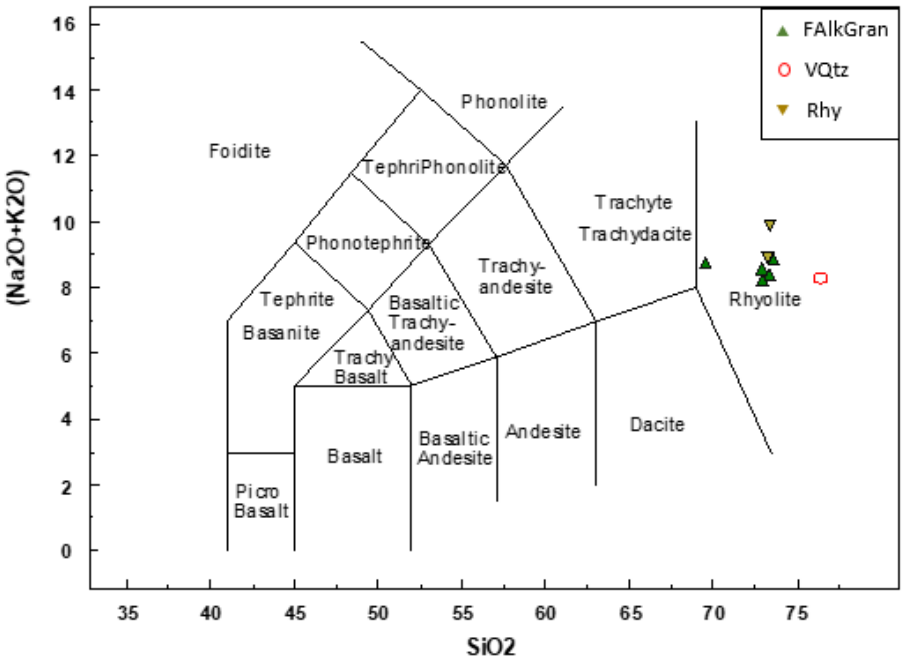


Fig. 76: TAS discriminatory plot for volcanic rocks of Alagbede area (after LeBas et al., 1986).

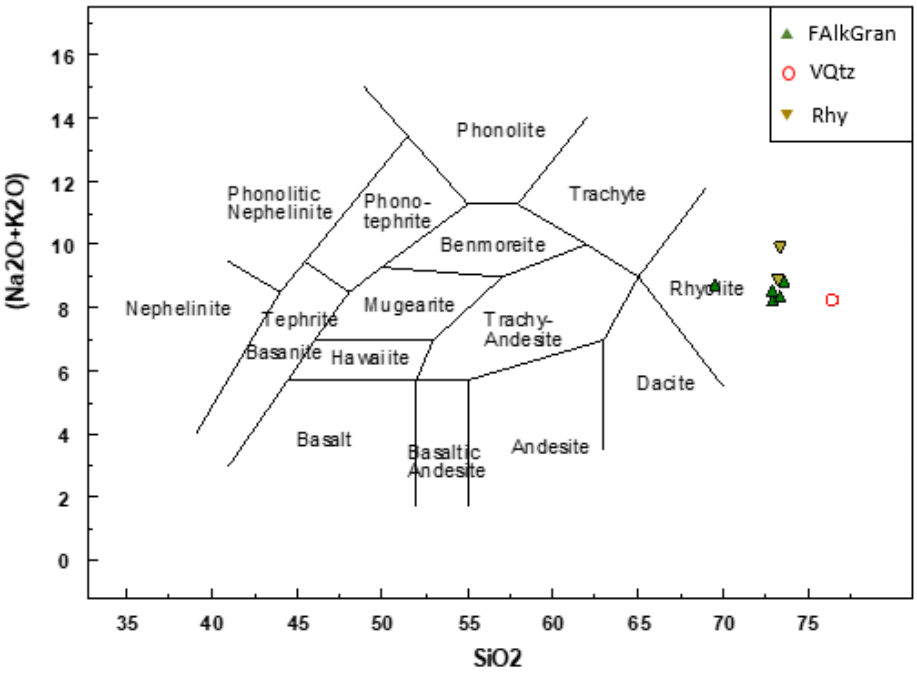


Fig. 77: TAS discriminatory plot for volcanic rocks of Alagbede area (after Cox-Bell-Pank, 1979).

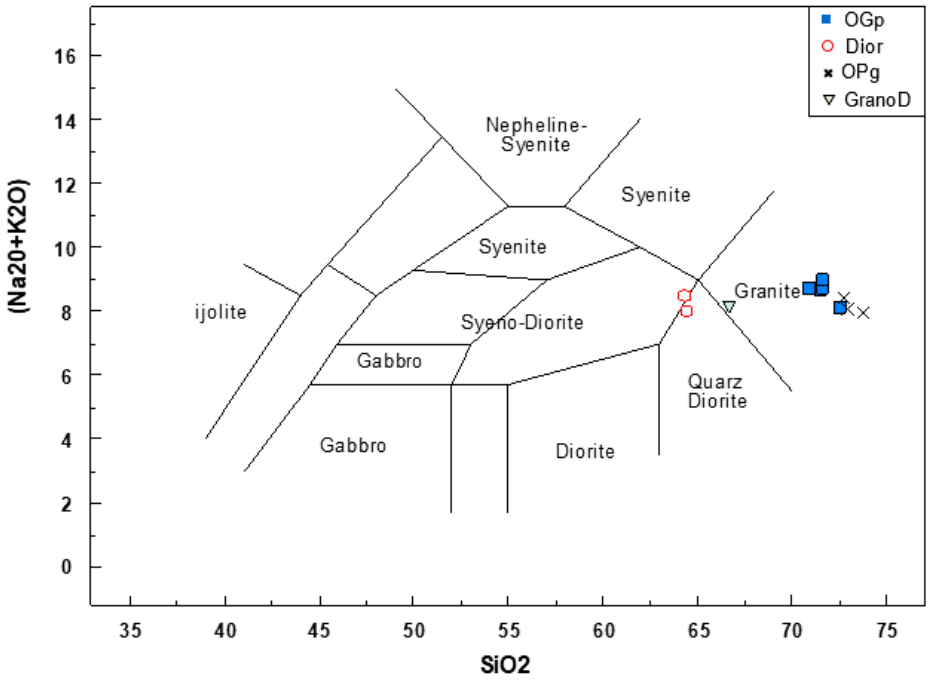


Fig. 78: TAS discriminatory plot for plutonic rocks of Alagbede area (after Cox-Bell-Pank, 1979).

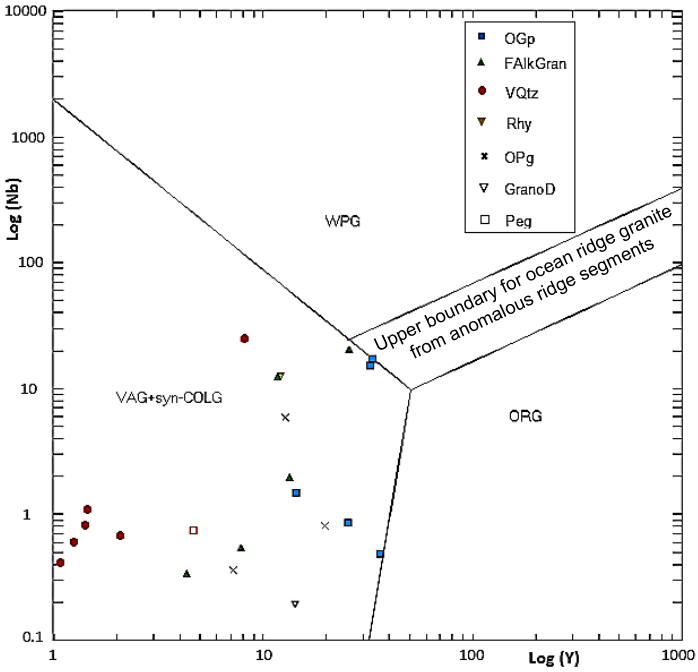


Figure 79: Log (Nb) vs Log (Y) binary plot for granites of Alagbede area (after Pearce et. al, 1984).

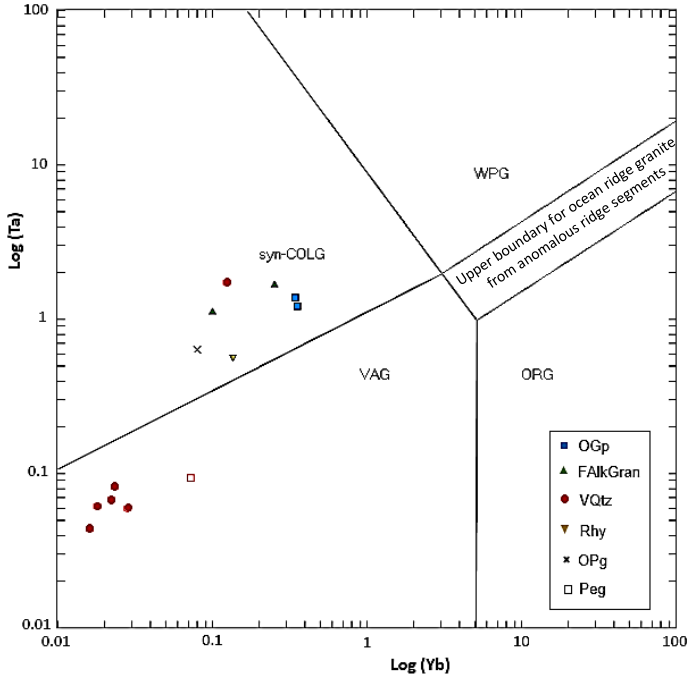


Figure 80: Log (Ta) vs Log (Yb) binary plot for granites of Alagbede area (after Pearce et. Al, 1984).

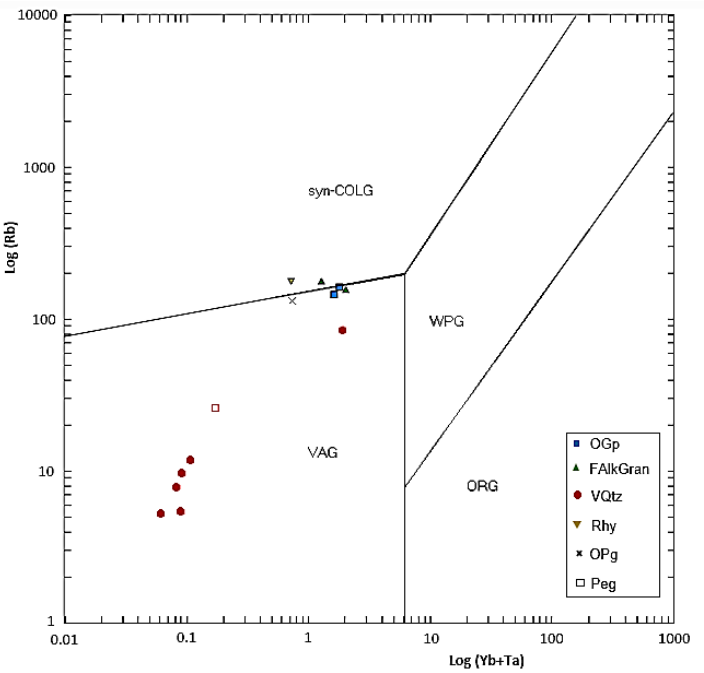


Figure 81: Log (Rb) vs Log (Yb+Ta) binary plot for granites of Alagbede area (after Pearce et. al, 1984).

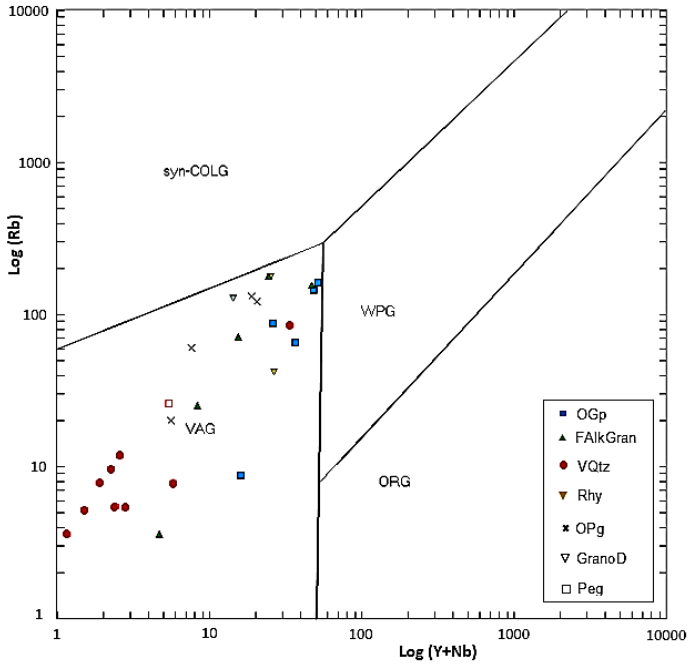


Figure 82: Log (Rb) vs Log (Y+Nb) binary plot for granites of Alagbede area (after Pearce et. al, 1984).

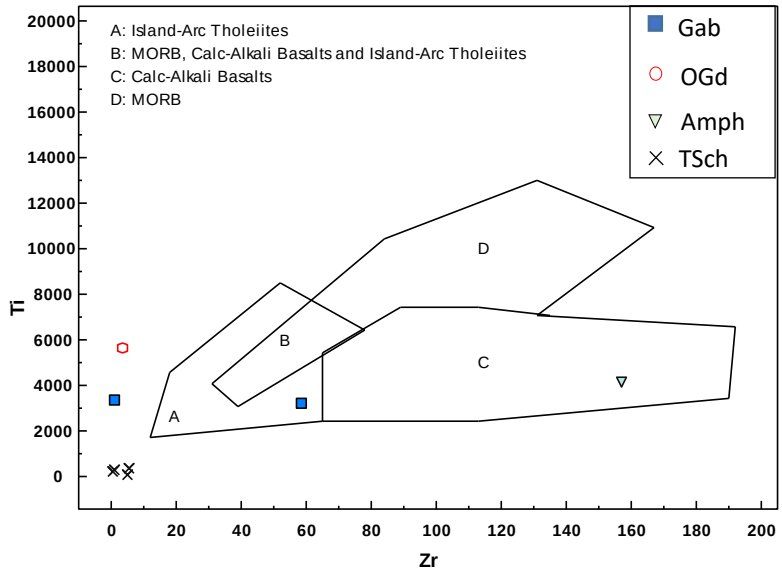


Figure 83: Ti vs Zr discriminatory diagram for basaltic rocks of Alagbede area (after Pearce Cann 1973)

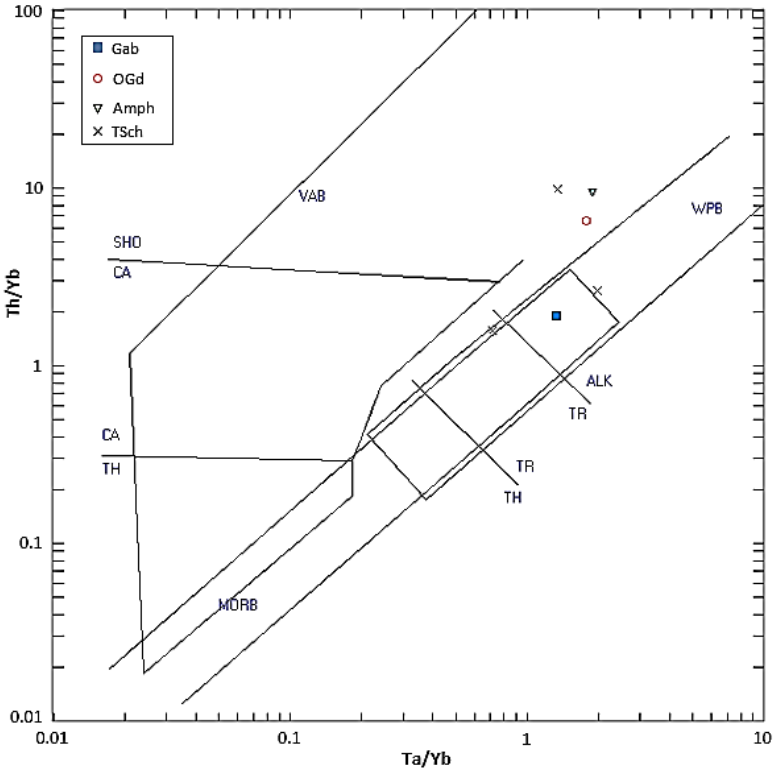


Fig. 84: Discriminatory plots of Th/Yb v Ta/\Yb for the basaltic rocks of Alagbede area (after Pearce 1982).

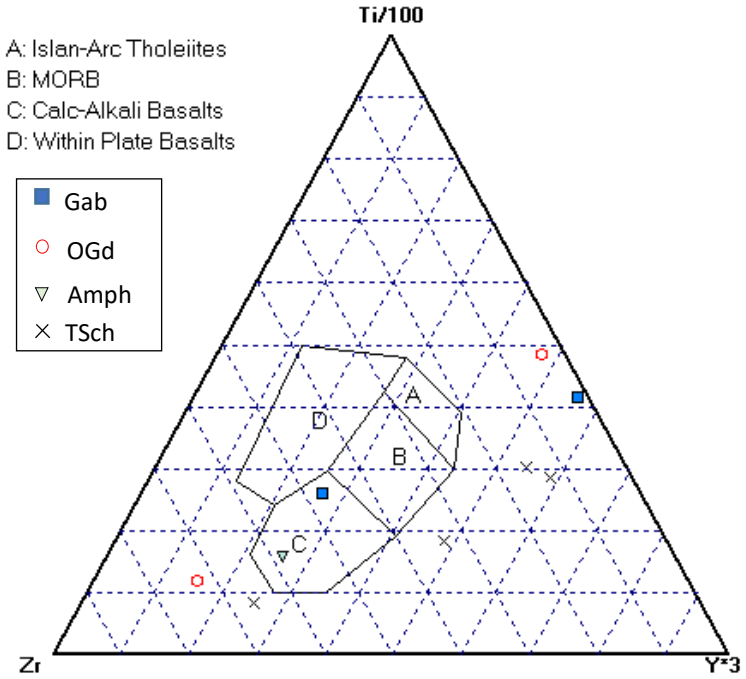


Fig. 85: Ti-Zr-Y ternary diagram for the basaltic rocks of Alagbede area (after Pearce Cann, 1973).

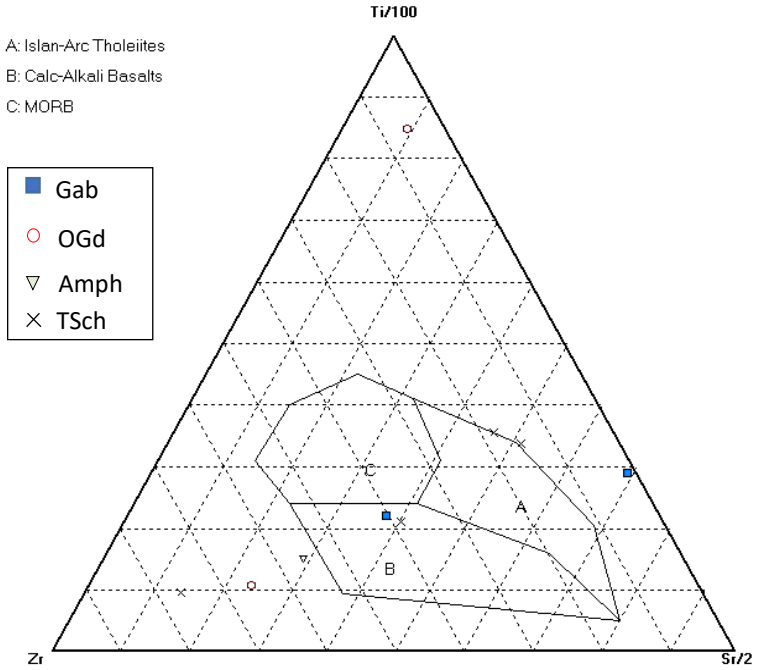


Fig. 86: Ti-Zr-Sr diagram for the basaltic rocks of Alagbede area (after Pearce Cann, 1973).

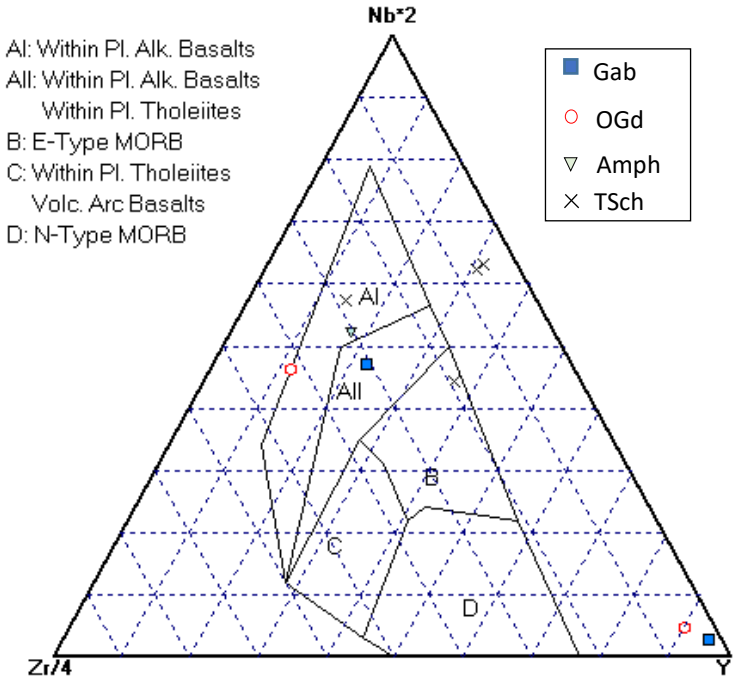


Fig. 87: Nb-Zr-Y diagram for the basaltic rocks of Alagbede area (after Meschede, 1986).

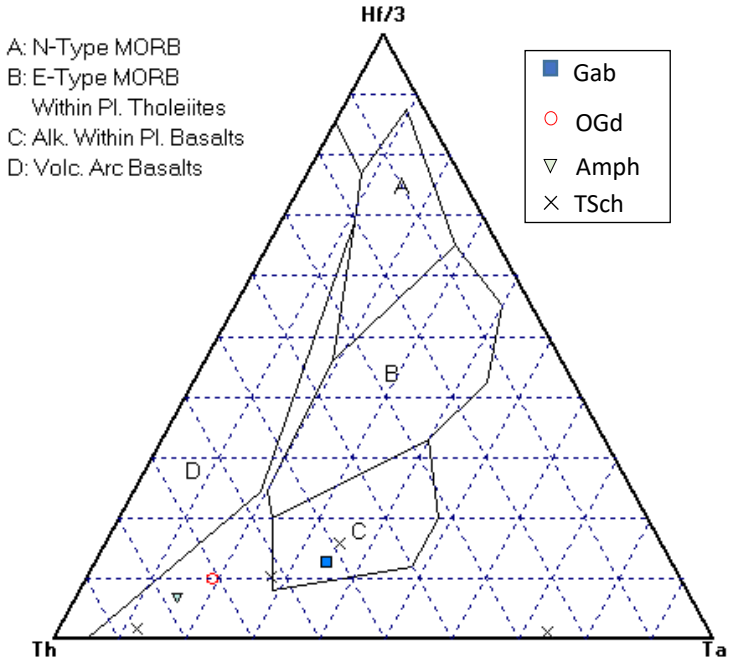


Fig. 88: Th-Hf/3-Ta diagram for the basaltic rocks of Alagbede area (after Wood, 1980).

4.6 Petrogenesis

4.6.1 Major Element Fractionation Pattern

The fractionation pattern on the Harker's diagrams (figure 89) for the igneous rocks of Alagbede area show marked chemical variability that are not compatible with any simple fractionation scheme based on the chemistry of the feldspar phenocryst present in the melt as discussed by Rollinson (1993). Progressive fractional crystallization in a crystal-liquid equilibria shows a trend on the major element variation (Harker's) diagram which is controlled by the chemistry of the solid phase (feldspar phenocrysts) being removed from the crust-derived melt. A process of simultaneous assimilation of the country rock and fractional crystallization (AFC) model as put forth by Bowen (1928) who argued that the latent heat of crystallization during fractional crystallization can provide sufficient thermal energy to consume the wall-rock, is hereby proposed as the fractionation model to explain the major element chemistry of rocks in Alagbede area.

4.6.2 REE Fractionation Pattern

The degree of fractionation of a REE pattern can be expressed by the concentration of a light REE (La or Ce) rationed to the concentration of a heavy REE (Yb or Y) (Rollinson, 1993). The ratio of the chondrite-normalized La/Yb was plotted against each of the normalized concentrations of Ce and Yb on a bivariate graph which indicate the degree of the light REE fractionation with changing REE content (figure 90a & b). Similar diagram was constructed to measure the degree of heavy REE fractionation by plotting the ratio of the chondrite-normalized Gd/Yb against normalized concentration of Yb (figure 90c).

At low oxygen activities, partition coefficients for Europium (Eu) between plagioclase and basaltic melts are high (generally > 1.0) and anomalous relative to the other REE, whereas at high oxygen activities, partition coefficients for Eu are low and Eu behaves in a similar way to the other REE as demonstrated by Drake and Weill (1975) and discussed by Rollinson (1993).

Europium (Eu), in its divalent state, is compatible in plagioclase and potassium feldspar and this, according to Rollinson (1993), accounts for why Eu anomalies are mostly controlled by feldspars particularly in felsic magmas. Thus the removal of feldspar from a felsic melt by crystal fractionation or the partial melting of a rock in which feldspar is retained in the source will give rise to a negative Eu anomaly in the melt. Other mineral phases in a felsic melt such as orthopyroxene, clinopyroxene, sphene, hornblende and garnet may also contribute to a Eu anomaly in the opposite sense to that of the feldspars.

The slight concave-upward pattern, presence of strong negative Eu anomalies with progressive enrichment in LREE in most of the rocks mapped in Alagbede area (figures 91-94) is consistent with the fractionation pattern controlled by fractional crystallization of the feldspar phenocrysts from the felsic melt. The composition of the igneous rocks of Alagbede falls within the continental arc array suggesting their formation from magma similar to that found in modern-day continental arcs.

The REE fractionation pattern of the Alagbede quartz-sulfide-gold ore is also found to be consistent with the work of Graf (1977) and Hanson (1980) which suggest that aqueous fluids in equilibrium with greenstone belt volcanics would have light REE-enriched, heavy REE-depleted patterns with

a negative Eu anomaly and with abundances of all REE lower than that of the parent rocks. This suggest that the Alagbede gold-bearing vein quartz was, perhaps, precipitated from hydrothermal solution of continental arc origin.

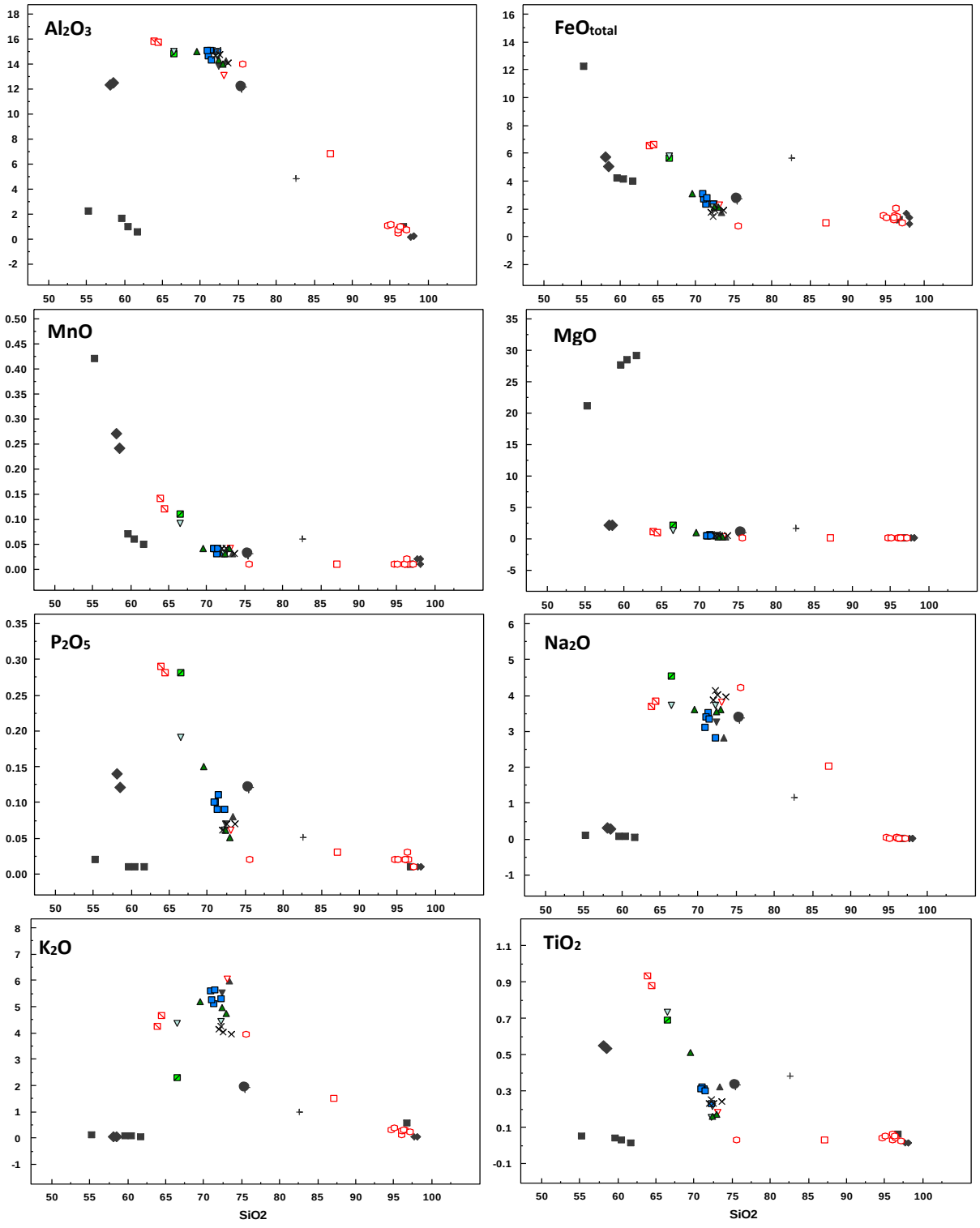


Figure 89a: The Harker's (major element bivariate) diagrams for igneous rocks of Alagbede area.

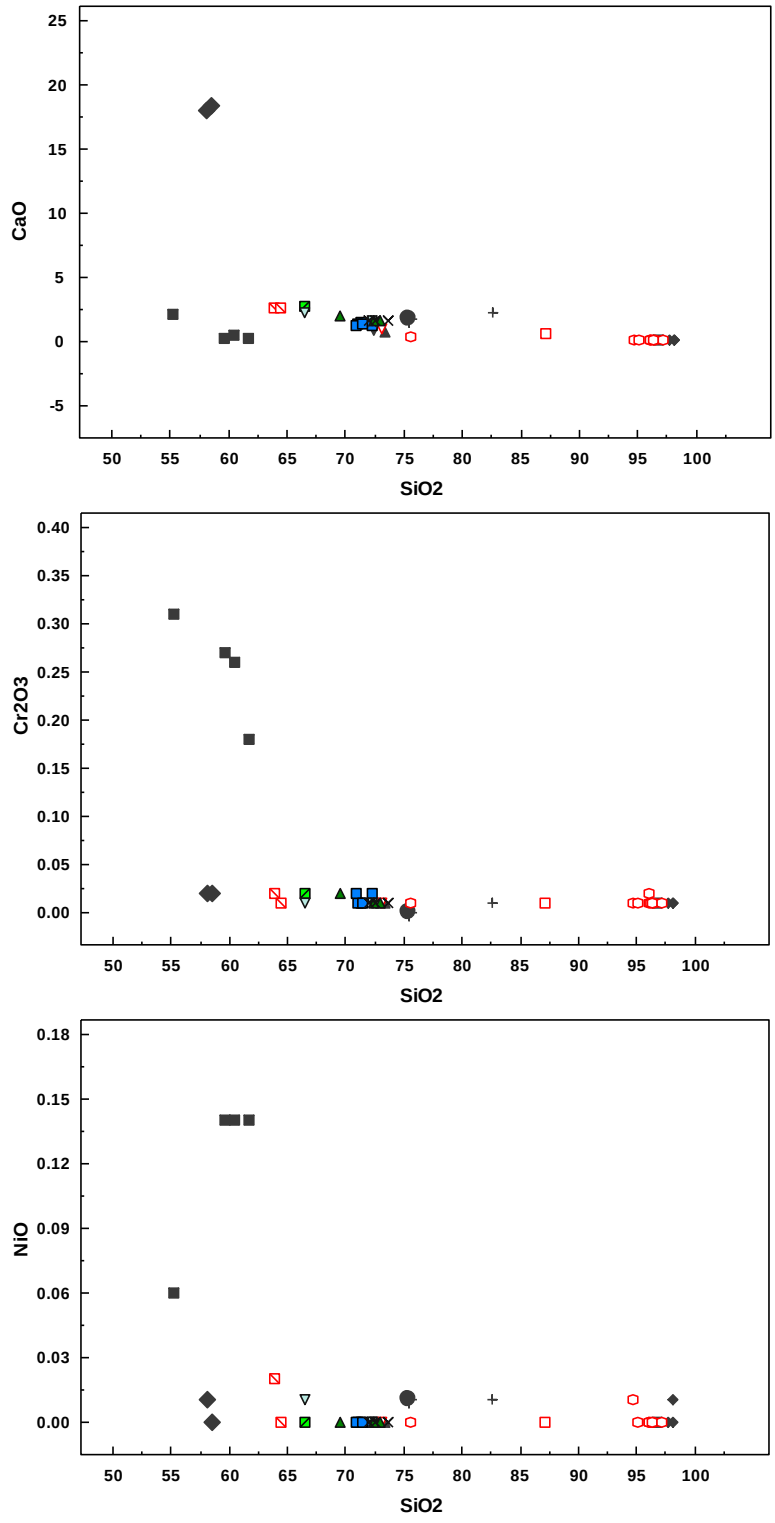


Figure 89b: The Harker's (major element) diagrams for igneous rocks of Alagbede area.

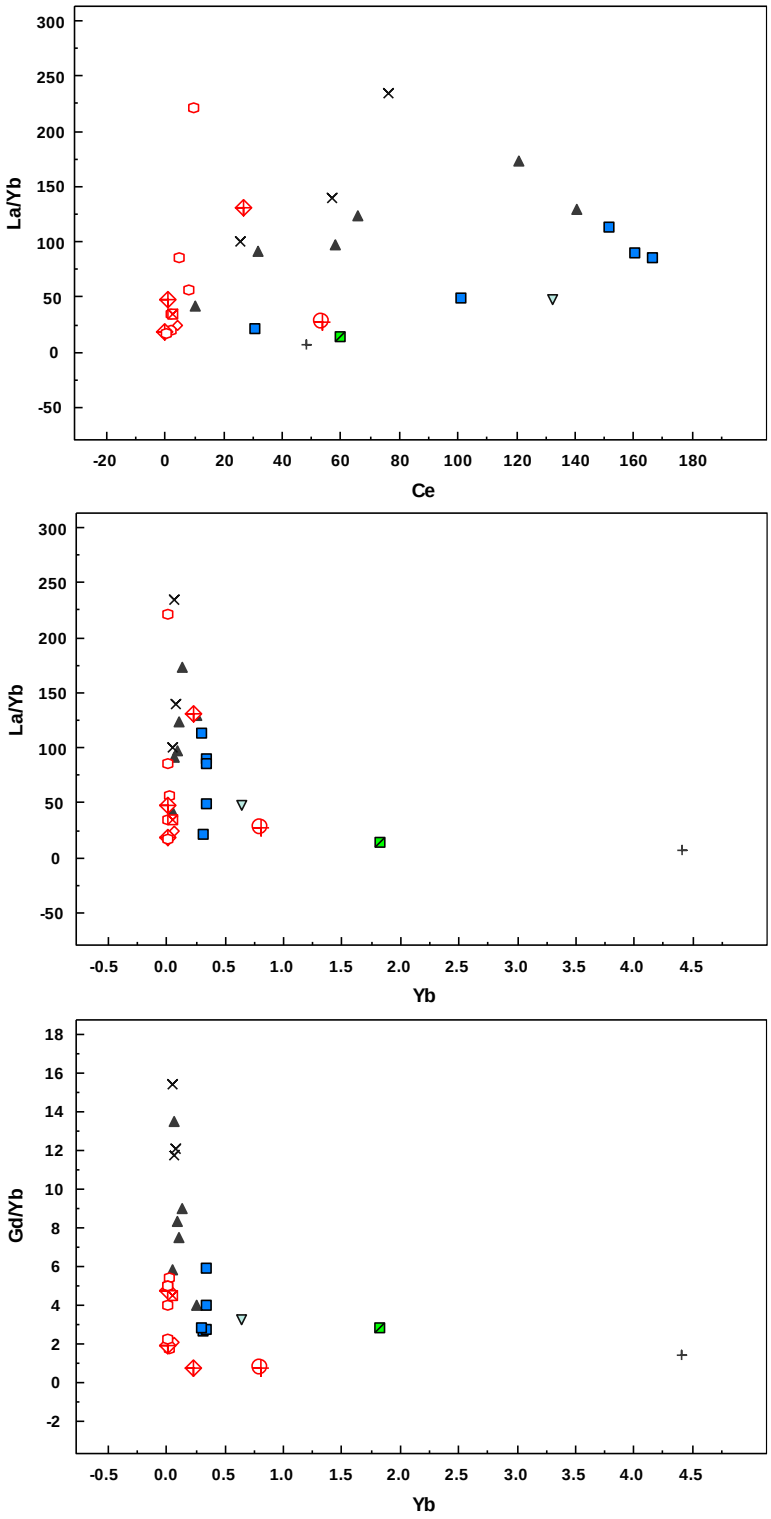


Figure 90: The bivariate graph showing the degree of fractionations of (a & b) LREE (c) HREE.

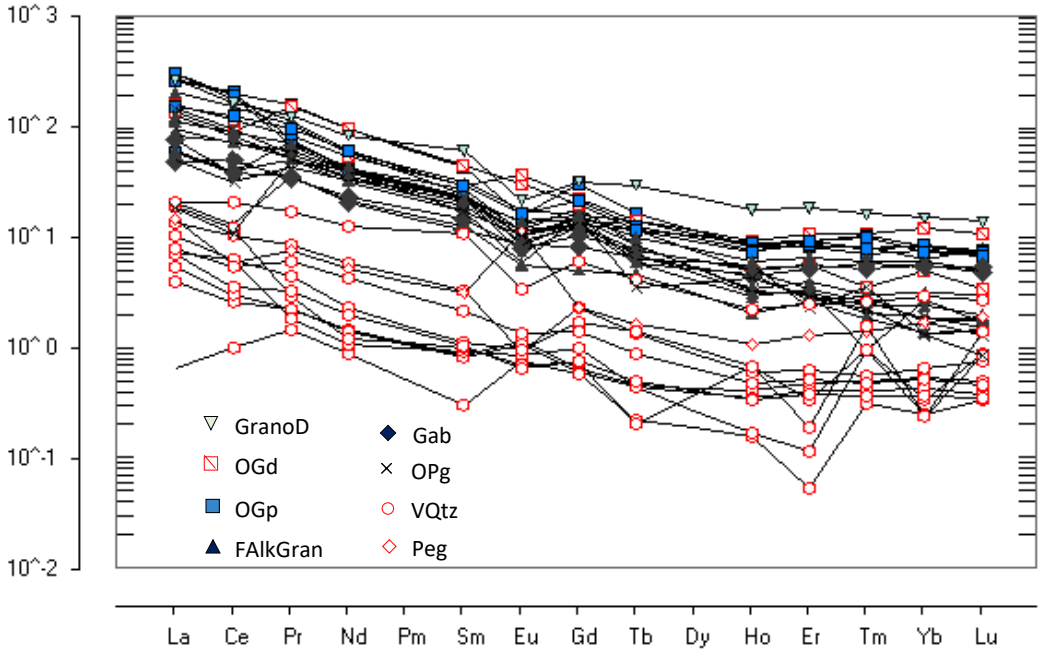


Fig. 91: Chondrite-normalized REE spider diagram for igneous rocks of Alagbede area (after Haskin et al, 1968).

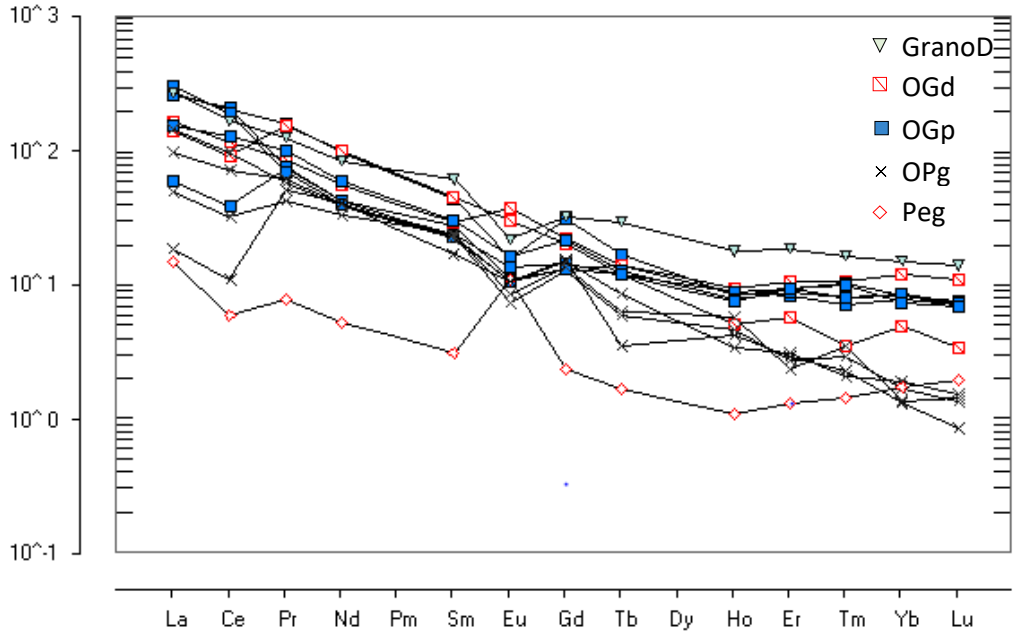


Fig. 92: Chondrite-normalized REE spider diagram for plutonic rocks of Alagbede area (after Haskin et al, 1968).

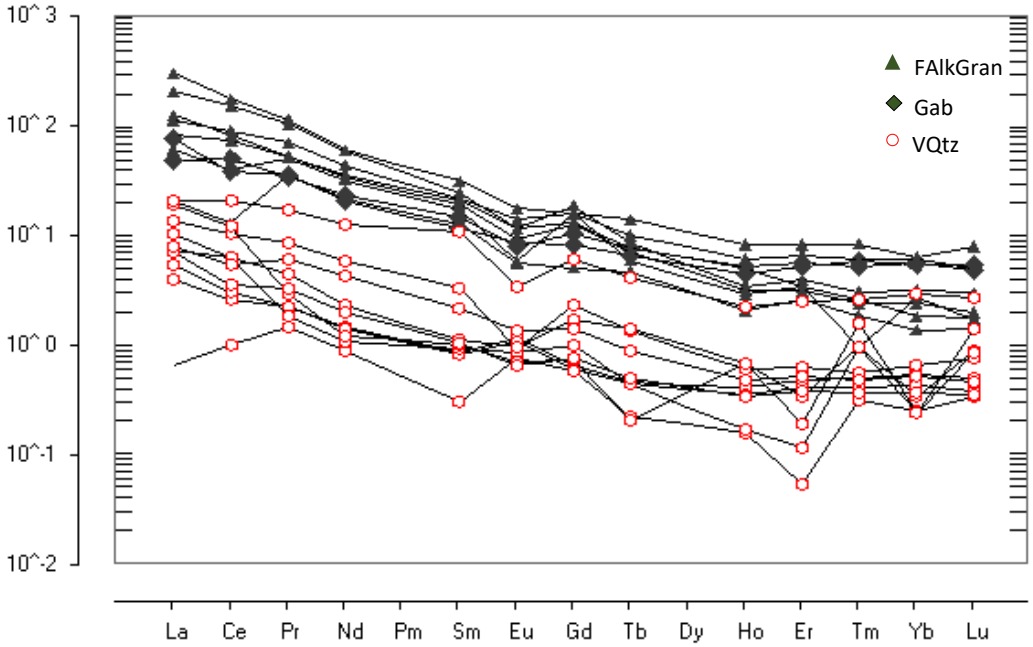


Fig. 93: Chondrite-normalized REE spider diagram for volcanic rocks of Alagbede area (after Haskin et al, 1968).

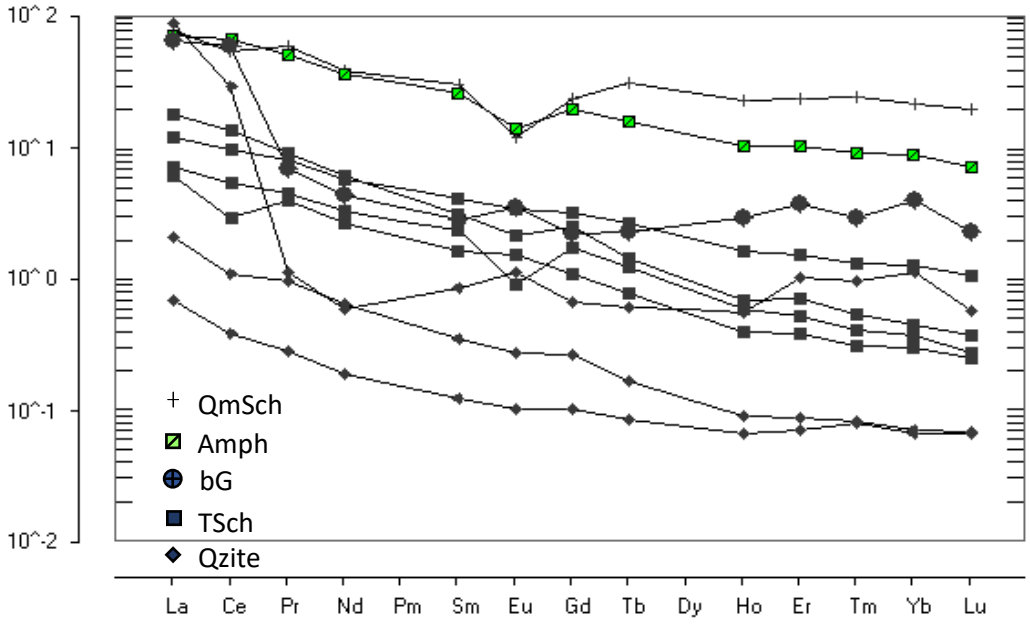


Fig. 94: Chondrite-normalized REE spider diagram for metasedimentary rocks of Alagbede area (after Haskin et al, 1968).

4.6.3 Trace Element Geochemistry

Figures 95-98 are the plots of the trace element concentrations of upper and lower continental crust (log scale) against atomic numbers normalized to the composition of the primordial mantle and plotted from left to right in order of increasing compatibility in a small melt of the mantle for igneous, plutonic, volcanic and metasedimentary rocks of Alagbede area respectively indicating that elements with even atomic numbers are more stable and therefore have higher abundances than those with odd atomic numbers, and producing a zig-zag pattern on a composition-abundance diagram. This, according to (Rollinson 1993), allows any fractionation of the REE group relative to chondritic meteorite to be identified.

The concentrations of the more mobile large ion lithophile element (LILE), also known as low field strength (Cs, Rb, K, Ba, Sr, Eu) are usually controlled by the behavior of the liquid phase while the high field strength (HFS) (Y, Hf, Zr, Ti, Nb, Ta) element concentrations are dependent on the chemistry of the source and the crystal/melt processes which have taken place during the evolution of the rock (Rollinson, 1993). Negative Nb anomalies are also characteristic of the continental crust and may be an indicator of crustal involvement in magma process.

4.6.4 Source Characteristics

The structure of the Alagbede gold-bearing vein quartz and its mode of occurrence suggest that the mineralization was structurally-controlled and from the observed similarities in orientation and shear movement directions within the quartz vein and in the surrounding gneisses, the vein mineralization may perhaps be linked to the collision tectonics that affected the western part of

Nigeria in the Pan African around 500 Ma. Field and petrographic evidence suggest that the hydrothermal ore fluids responsible for ore mineralization is perhaps derived from metamorphic dewatering and minor contribution from magmatic sources due to extreme metamorphism leading to anatexis. Mineralogical and geochemical evidence shows that the Alagbede vein deposit is similar to other Pan African vein-type gold deposits.

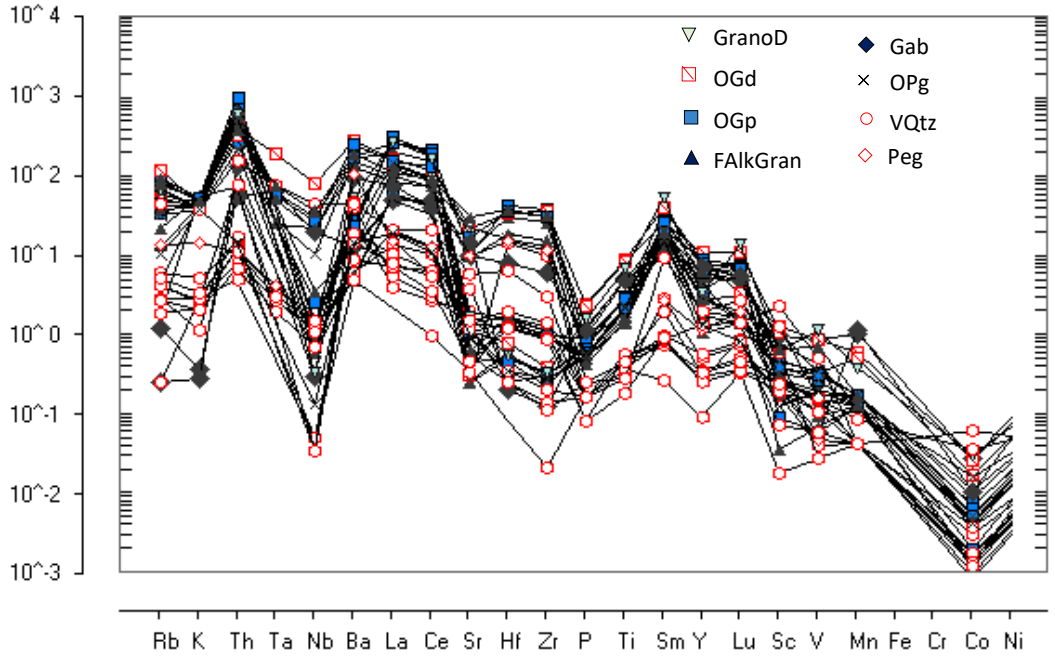


Fig. 95: Chondrite-normalized spider diagram for igneous rocks of Alagbede area (after Wood et al., 1979b).

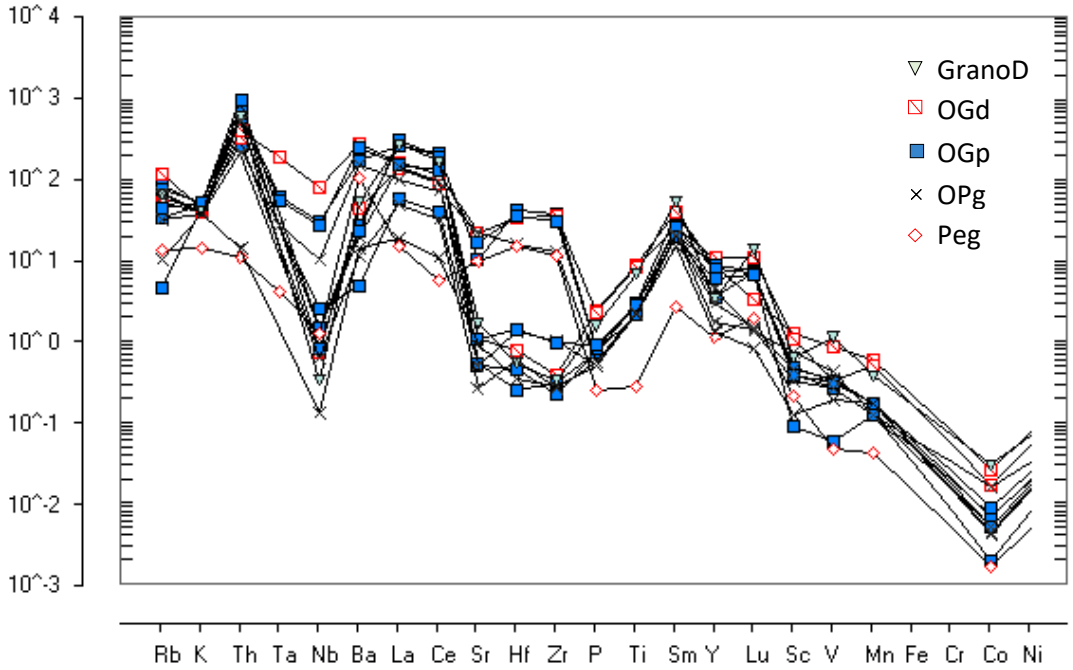


Fig. 96: Chondrite-normalized spider diagram for plutonic rocks of Alagbede area (after Wood et al., 1979b).

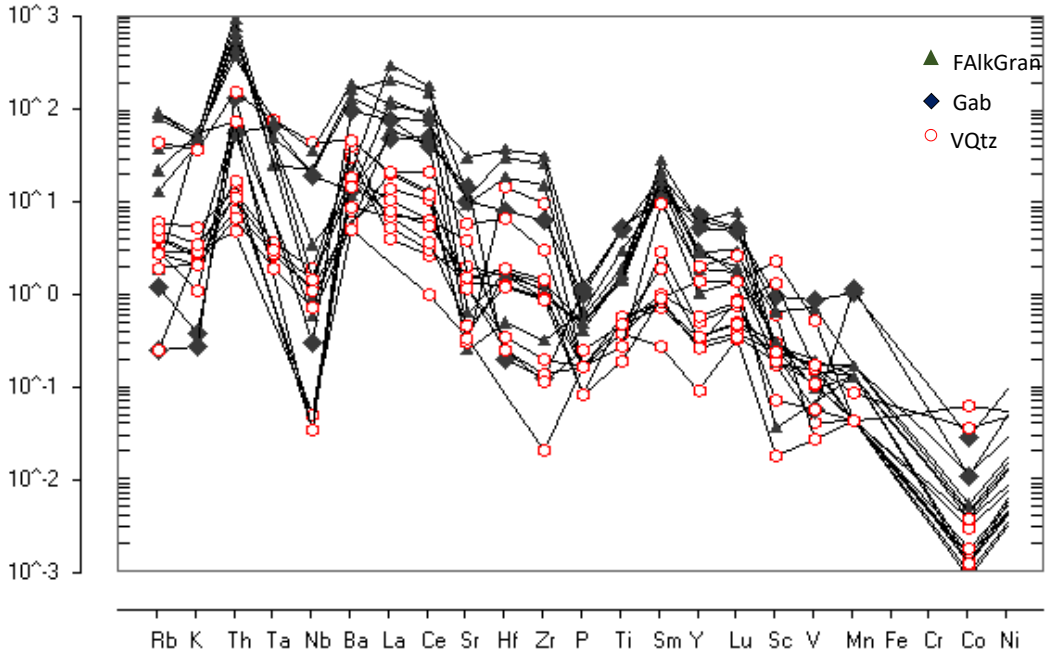


Fig. 97: Chondrite-normalized spider diagram for volcanic rocks of Alagbede area (after Wood et al., 1979b).

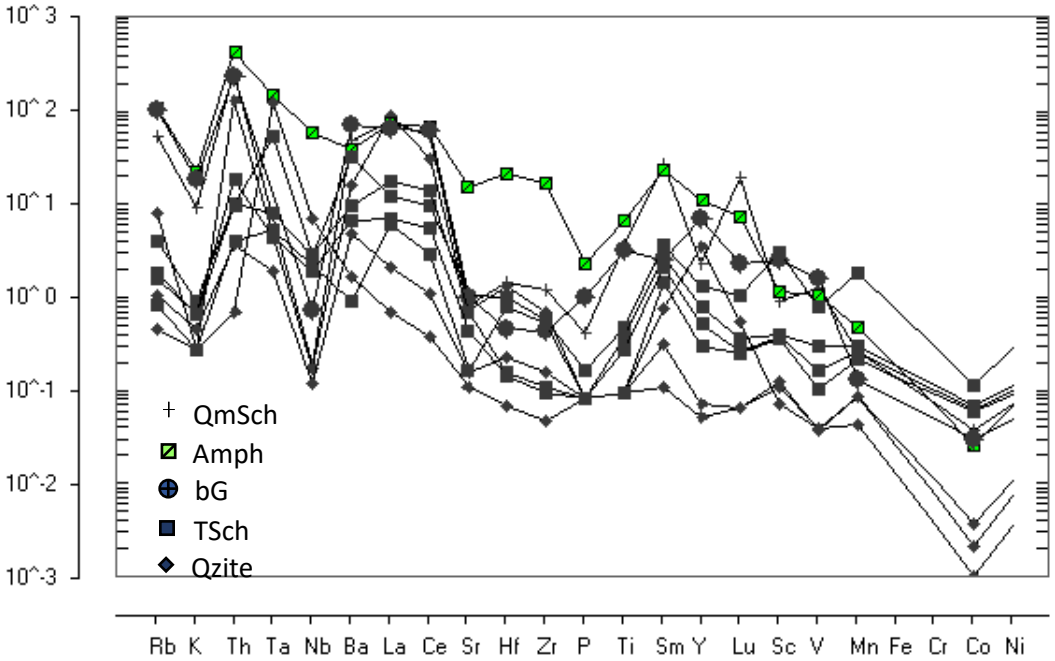


Fig. 98: Chondrite-normalized spider diagram for metamorphic rocks of Alagbede area (after Wood et al., 1979b).

CHAPTER 5

AGE OF GOLD MINERALIZATION IN ALAGBEDE AREA

5.1 Gold Exploration in Alagbede Area

In the course of geochemical survey to explore for gold around Alagbede area, soil and rock samples were collected around the mineralized vein quartz using appropriate sample collection techniques. A total of 32 soil samples were collected randomly from the three main layers identified as the topsoil 'A' horizon, middle 'B' horizon and saprolitic 'C' horizon at depths mostly ranging from 0.4 to 1m, with the aid of a hand auger, depending on the thickness of the overburden on the underlying basement rocks. Visual observation of samples from all the three horizons in the trench shows visible specks of gold which were observed particularly within the saprolitic horizon. The soil samples were homogenized by mixing and panning produced an average of 0.4g of gold in 50kg of regolith soil samples particularly collected from the altered (weathered) zone of the quartzite, syeno-granite and talc schist. For rock sampling, grab samples were collected from fresh surfaces of exposed rock outcrops in abandoned trenches and pits (figure 99) dug previously by artisanal miners to explore for gold in the gold-bearing quartz vein measuring about 12 to 35m wide and 400m long around Alagbede village (see figure 55). The fresh grab samples were crushed into gravel-sized fractions and pulverized into about 200 micron size to obtain fine fractions which were analyzed for elemental composition to determine gold concentrations in each rock sample.

5.2 Estimation of Ore Grade

A total of 42 rock samples were analyzed, out of which 17 rock samples presented in table 18 indicated appreciable enrichment in gold based on a general background concentration of below 3 ppb of gold for whole rock and stream sediment samples in the study area. Table 18 below shows that gold prospectivity in Alagbede area, from cursory panning of residual soil samples and from fire assay results of rock samples is promising with average gold enrichment values which varies from rock to rock. The result of geochemical analysis of rock samples from the area indicates that lithologies such as quartzite, granites, gabbro and talc schist are enriched in primary gold ranging from an average of 0.24 oz/ton in residual soils, 0.62 oz/ton in gabbro which occur as minor lenses within the gneisses, 0.82 oz/ton in porphyritic granite, 8.12 oz/ton in talc schist, 45.9 oz/ton in syeno-granite, 2.27 oz/ton in low grade vein quartz and 58.64 oz/ton in high grade vein quartz. The low and high grade gold ores in vein quartz have an average combined grade of 23.12 oz/ton.



Figure 99: One of the artisanal exploratory pit for mining of gold in Alagbede.

Table 18: Gold concentration and ore grade in mineralized rocks of Alagbede area.

Sample ID	Fe2O3 %	Cu ppm	Pb Ppm	Zn Ppm	Au (ppb)	Au Crustal Enrichment	Au Ore Grade		Av. Ore Grade For Au (Oz/ton)	
							(g/kg)	Oz/ton		
OGp 36	2.32	10.02	12.59	12.1	3.7	1.23	0.0037	0.111	0.822	
OGp 40	2.67	8.154	34.224	53.162	51.1	17.03	0.0511	1.533		
Gab 40B	5.00	8.214	1.892	135.87	17	5.67	0.017	0.510	0.6165	
Gab 52	5.72	31.59	20.82	19.2	24.1	8.03	0.0241	0.723		
VQtz 77	1.46	13.01	7.801	3.275	961	320.33	0.961	28.83		23.12
VQtz 78	1.41	394.6	3190.2	4589.3	3723	1241	3.723	111.69	58.64	
VQtz 80	1.33	23.85	693.22	16	1179.6	393.2	1.1796	35.388		
VQtz 80A	1.52	16.17	3.75	68.7	8.3	2.77	0.0083	0.249		
VQtz 80C	0.75	7.482	25.198	6.983	82	27.33	0.082	2.46		
VQtz 80D	2.05	6.63	2	39.9	62.7	20.9	0.0627	1.881	2.27	
VQtz 80E	0.94	24.38	481.6	11.551	122	40.67	0.122	3.66		
VQtz 81	1.37	40.55	1736.2	25.524	27	9	0.027	0.81		
TSch 79	3.94	4.028	1.115	70.931	662	220.67	0.662	19.86	8.123	
TSch 80A1	12.23	25.65	1.986	190.03	113	37.67	0.113	3.39		
TSch 80B	4.20	42.34	0.788	245.82	217	72.33	0.217	6.51		
TSch 80F	4.14	5.079	1.951	135.07	91	30.33	0.091	2.73		
FAlkGran 85	3.09	59.78	31.437	41.018	4.6	1.53	0.046	45.9	45.9	
Soil samples					-	-	0.008	0.24	0.24	

5.3 Ore Microscopy

Electron probe microanalysis (EPMA) and mineral separation work shows that Alagbede gold occurs rarely as small free gold in syeno-granite (figure 100) and mainly as microfracture-fillings (figure 101) or as inclusions in pyrrhotite, arsenopyrite and pyrite (figures 102, 103, 104) in the deposit and, less commonly, as inclusions or intergrowths in chalcopyrite, suggesting that it is coeval with the precipitation of the sulphide phases. This is consistent with the work of Morey *et al*. (2008) and Large *et al*. (2009) whose studies have shown that gold is primarily hosted in chalcopyrite, arsenopyrite, pyrrhotite and pyrite in most hydrothermal gold deposits, and that its concentration in sulphide varies to a great extent, and can vary from 0.07 to 1.96 ppm within a single sulphide grain. The work of Cygan and Candela (1995) and Jugo (1997) have also shown that gold behaves as an incompatible element and tends to concentrate in residual melts in which sulfur dissociates, while demonstrating that the concentration of gold hosted in sulphide minerals is in the following decreasing order: bornite > chalcopyrite > pyrrhotite > pyrite.

The work of Siddaiah and Rajamani (1989) has demonstrated some general correlation between gold and arsenopyrite; but that however, all arsenopyrite-rich zones are not necessarily gold rich. Native gold and electrum are hosted by sulfides as nanometer- to micron-sized inclusions (10nm – 10µm) and as micro-fracture infills in vein quartz (Siddaiah and Rajamani, 1989). The current work conforms to all these previous studies which have demonstrated that gold, in hydrothermal ores, is commonly hosted by sulphide minerals due to its affinity for reduced sulfur.

Arsenopyrite is observed as blebs of reddish to yellowish brown subhedral grains with deformed pentagonal shape and exhibits irregular pinching and internal triple-junction micro fractures developed as a result of deformation (figure 102). Chalcopyrite is the dominant phase and forms euhedral to subhedral patchy grains, which in most cases are fracturerd, in association with pyrrhotite, occurring around grain boundaries and fills fractures in arsenopyrite. Chalcopyrite occurs as isolated euhedral grains and are sometimes found as tiny blebs disseminated within the silicate matrix. In places chalcopyrite exhibits granoblastic texture. Gold has been observed as inclusions within the chalcopyrite.

Pyrite occurs as coarse-grained, euhedral crystals and also as small rounded grains in association with arsenopyrite, chalcopyrite and pyrrhotite. Sometimes, the small pyrite grains are found to cluster in aggregates. Some of the euhedral pyrite crystals are surrounded by fractured chalcopyrite and pyrrhotite grains. This constitute a kind of zoning in the sulphides with pyrite in the core, rimmed by chalcopyrite and then pyrrhotite at the fringes (figure 103). Pyrite exhibits typical metamorphic recrystallization textures such as triple junctions with other sulphides. Cataclastic deformational textures such as cracks in pyrite filled with chalcopyrite also occur. The existence of bubble voids in some grains of pyrite and arsenopyrite (figure 104) is suggestive of the prominent role of fluid in the formation and deposition of the sulphide and auriferous quartz veins in the study area. Discrete anhedral grains of galena were observed in disseminations and clusters within the vein quartz.

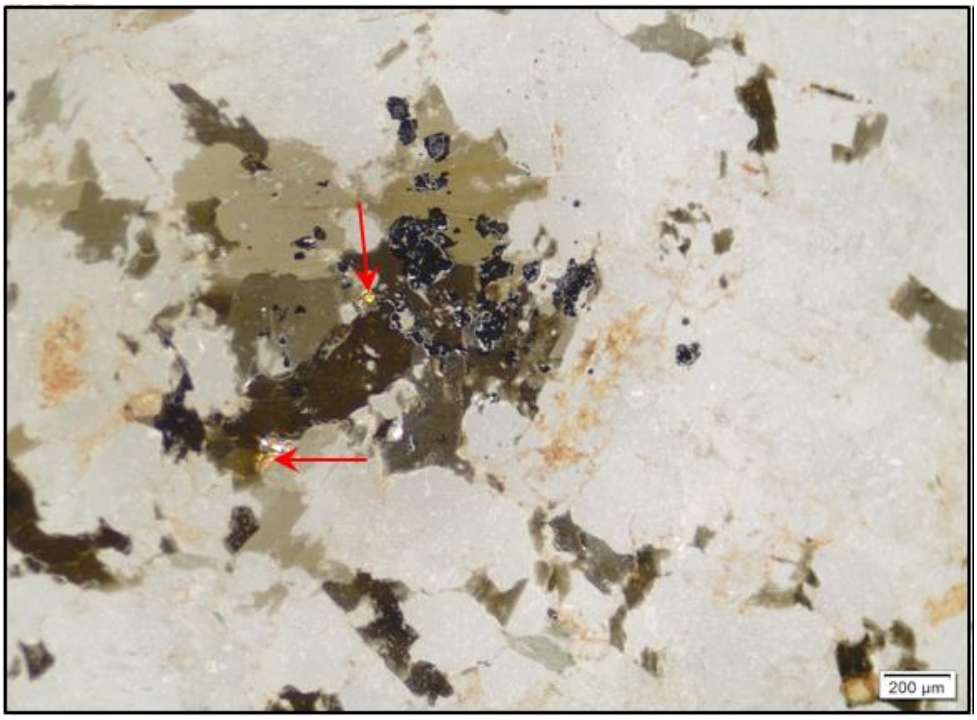


Figure 100: Occurrence of small free gold in syeno-granite.

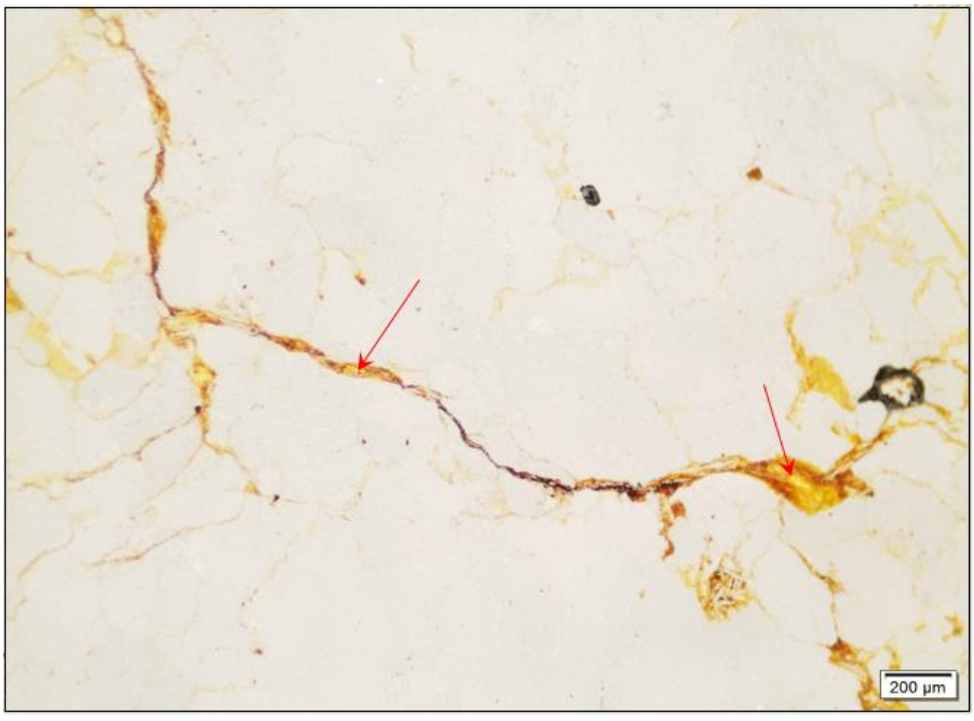


Figure 101: Microfracture-filling gold inclusions within the vein quartz.

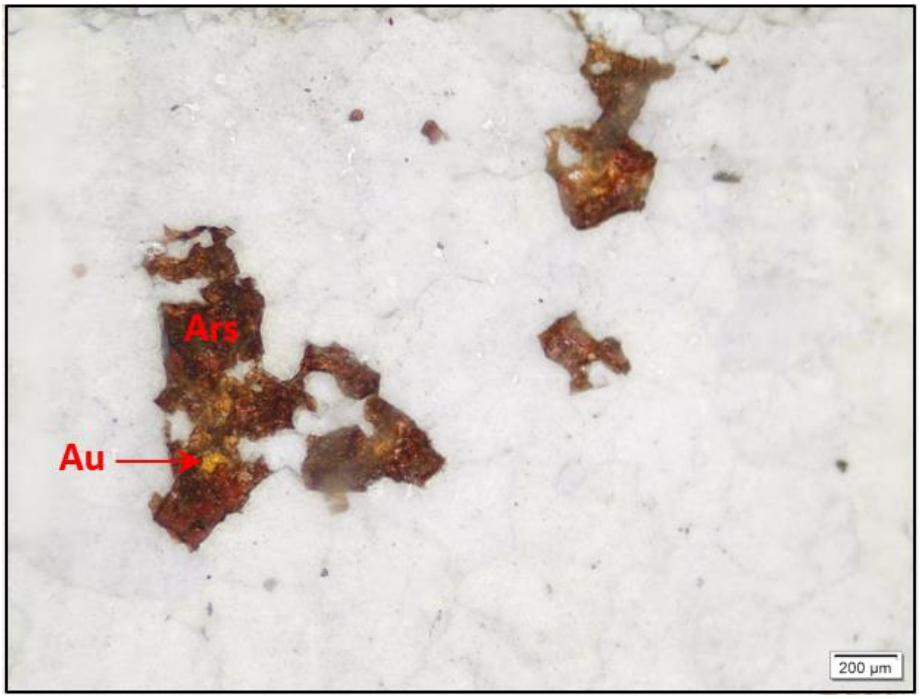


Figure 102: Blebs of arsenopyrite with gold inclusions within the vein quartz.

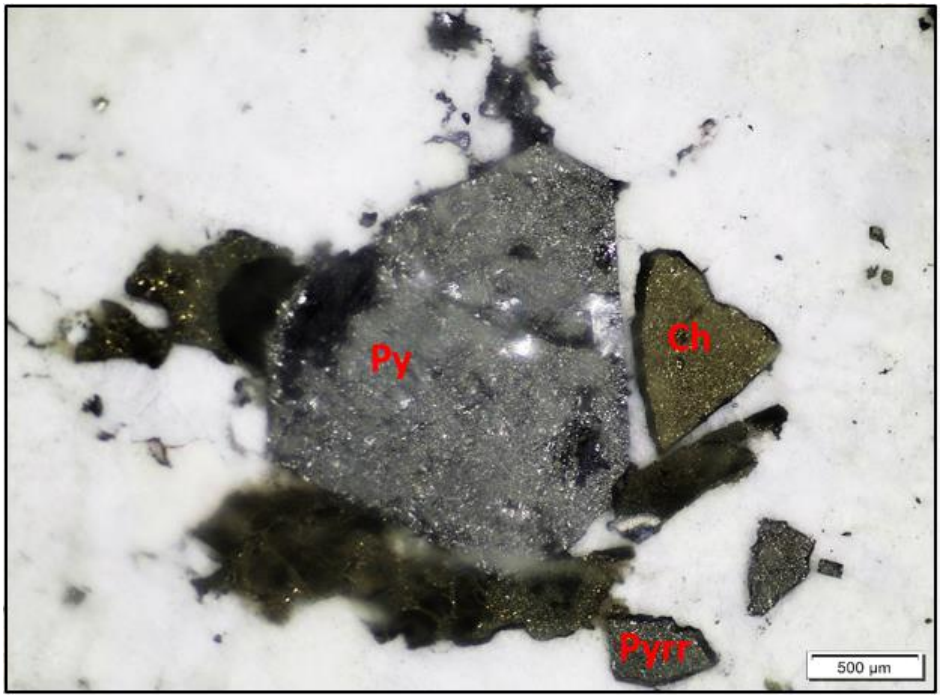


Figure 103: Zoning of sulphide: pyrite – chalcopyrite – pyrrhotite assemblage with gold inclusions within the vein quartz.

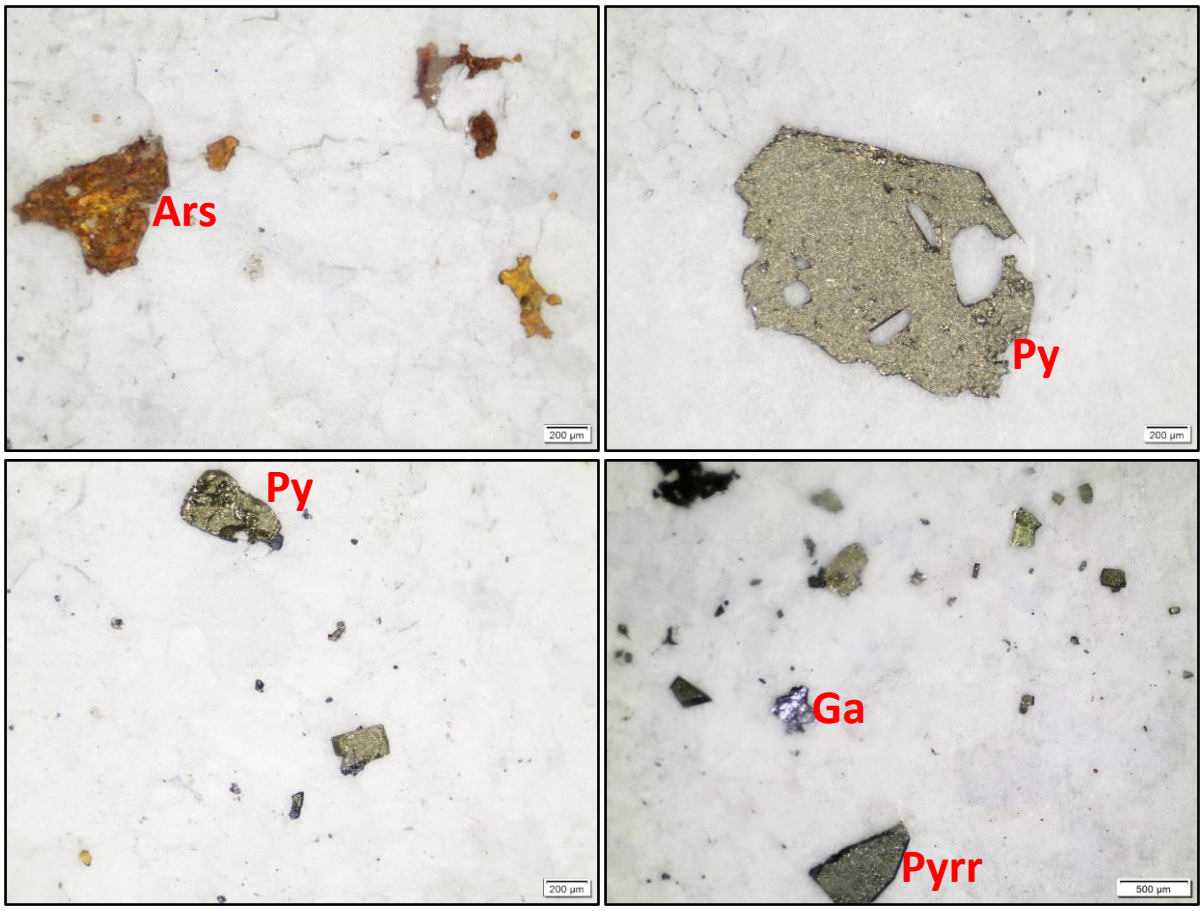


Figure 104: inclusions of sulphide mineralization within the vein quartz (Ars = arsenopyrite, Ga = Galena, Py = pyrite, Pyrr = pyrrhotite).

5.4 Mineralization Pattern

Several previous studies carried out on primary gold deposits within the Nigerian Schist belts have related the mineralization, in most cases, to structural lineaments linked to period of felsic magmatism in the belt and have therefore inferred the timing of the gold mineralization to be the time of such magmatic activities. There is, however, no record of any attempt made to date the gold deposit in order to establish the absolute age for the gold mineralization event.

Alagbede gold deposit is spatially related to vein quartz, fine grained syeno-granite and talc schist, and the determination of its actual time of the gold mineralization would, therefore, allow a robust assessment of the economic potential of host felsic intrusions, which, no doubt, would assist gold exploration in the area and in the Nigerian Schist belts in general. The primary deposits are being exploited by artisanal miners mainly in the southern segment of the main quartz vein which forms a NNE-SSW-striking belt, extending locally for 500m with a width ranging from 20 to 50m.

5.5 Geochronological Dating of Alagbede Gold Deposit

U-Th-Pb zircon dating was carried out using the LA-ICP-MS machine at the Earth-Lab of the School of Geosciences, University of the Witwatersrand in South Africa. Zircon grains for U-Th-Pb dating were extracted from 7 rock samples by heavy-liquid and magnetic separation, and further hand-picked under a binocular microscope before mounting, cutting, polishing and carbon-coating of zircon grains preparatory to microprobe and laser ablation studies.

5.5.1 Mounting, Cutting and Polishing of Zircon Grains

The selected grains of zircon for each of the rock samples were size-graded and arranged in an ordered manner on double sided adhesive tape fixed on to a piece of glass slide. Each group of zircon grains picked from the same sample was photographed and assigned the sample identification number for easy correlation when required after mounting. Measurements of sizes and shapes of the grains were made before they were placed in a special mould and encased in a block of epoxy resin. The picking and mounting of the zircon grains were carried out painstakingly to avoid mix up and minimize the risk of loss of small grains. Standard polishing techniques was maintained to expose the details of the internal variation, particularly the presence of zoning and inclusion in the grains.

The size-grading of the zircon grains before mounting was done to ensure that each grain was cut and exposed by half its original width as much as possible before they were finely polished and carbon-coated (figure 105) for electron probe micro analyses (EPMA) work. The studied felsic volcanic and plutonic rocks from Alagbede area contain well preserved, euhedral to subhedral colourless to pinkish-coloured prismatic zircons. The abundance of zircon and sizes of grains vary between samples. The quartz porphyritic volcanic rock contains abundant zircons with many relatively large grains while the alkali granite shows smaller but euhedral zircon grains.

5.5.2 Electron Microprobe Studies

The microprobe instrument uses a very fine beam of electrons to generate X-rays which make possible, in situ chemical analyses of spots in the grain around 1µm diameter as well as any other

mineral inclusions. The electron microprobe was used to study and characterize the internal variation within zircon grains. The finely polished and carbon-coated zircon and rock thin sections were examined in details using the scanning electron microscope to identify common variation in phases of mineral growth that had taken place and particularly which minerals had formed during the same mineralization events as the gold. Prior to LA-ICPMS analysis, cathodoluminiscence (CL) images of all crystals were obtained in order to avoid apatite and potassium feldspar inclusions as well as cracks and fissures during analysis.

5.5.3 Scanning Electron Microscope (SEM) – Cathodoluminiscence (CL)

Scanning electron microscope–Cathodoluminiscence (SEM-CL) has found its application in hydrothermal ore systems as a robust research technique used in the past two decades (Götte *et al*., 2011; Rusk, 2012. The geochemical and structural variations within in a crystal determine the intensity of SEM-CL emissions which makes this technique suitable for structural, textural and compositional examination for any given sample. In a potentially ore-bearing vein, the CL image could be used to identify multiple quartz generations with distinct textural variations which could enable a preliminary interpretation of quartz growth histories related to ore deposition.

CL patterns can therefore be applied, in conjunction with trace element compositional variation and isotopic compositional analyses, to determine the nature and origin of a specific mineralization events (Götze *et al*., 2001; Leeman *et al*., 2012; Rusk, 2012). The acquisition of high quality CL images at the initial research phase of ore-bearing vein quartz is therefore imperative for a proper follow-up analyses (Frelinger *et al*., 2015). The work of Frelinger *et al*., 2015 suggest

that quartz derived from plutonic, volcanic, metamorphic, and hydrothermal systems produce unique CL signatures that can be used to recognize various generations of quartz associated with a specific geologic environment.

Quartz of plutonic source typically produces bright rims around dark CL cores and may also display dark CL micro fractures, recrystallization or dissolution textures (Müller *et al.*, 2003). Oscillating CL intensities usually represent volcanic quartz phenocrysts which typically exhibit well preserved growth zones. Volcanic quartz usually become more rounded and embayed as a result of periods of crystal growth, readsorption and subsequent growth again (Corfu *et al*., 2003; Bernet and Bassett, 2005).

For this studies, cathodoluminiscence (CL) images were taken with VEGA3 TESCAN (figure 106) equipped with an X-Max energy-dispersive spectrometer (EDS) at the University of Johannesburg and used to examine the internal structures of individual zircon grains in order to ensure a good spots selection for laser analytical work as well as to evaluate minerals for heterogeneous growth (complex history, overgrowths, dissolution and crack infilling). Thus, SEM-CL imaging was used as a tool to delineate sequential episodes of quartz precipitation and define the paragenetic sequences of hydrothermal vein sets as suggested by Bernet and Bassett, 2005.



Figure 105: Carbon-coating machine (Quorum Q300T ES) at the University of Johannesburg



Figure 106: Cathodoluminiscence machine (VEGA3 TESCAN) fitted with EDS (Oxford X-Max) for in situ elemental mapping.

5.5.4 Textural classification of zircons

Medium-grained alkali Granite

Xenocrystic Inherited zircons: About 35% of zircons recovered from the medium-grained alkali granite show inherited core which exhibit growth zoning (oscillatory zoned core) with local intermediate resorption in magmatic zircons typical of analectic granites. The xenocrystic cores (figures 107c, d, e) are locally overprinted by zones of recrystallization (re-homogenization). The original euhedral zircon is cut by rapidly recrystallized or newly grown domains of more homogeneous composition.

Magmatic Zircon: These constitute about 50% of the zircons and are mostly seen as small euhedral zircons with oscillatory growth zoning that are masked by re-homogenization at the rims (figure 107a,b,e) while some are completely recrystallized and partly fragmental. Some of the locally resorbed magmatic zircons show hydrothermal alteration at the rims and dissolution structure (figure 107e).

Metamorphic Zircons: These accounts for 13% of the zircons and are mostly homogeneous, unzoned and fragmental. Some of the metamorphic zircons exhibit ghost xenocrystic core and hydrothermal alteration at the rims.

Eclogitic zircon: were observed to be replacing and rimming pre-metamorphic phase (figure 107c).

Porphyroblastic Granite

Xenocrystic Inherited Zircons: About 29% of the zircons are fragmental, homogeneous, partly recrystallized and contain xenocrystic core.

Magmatic zircon: Up to 49% of the zircons in the porphyroblastic granite are magmatic and show either simple or polymodal oscillatory zoning pattern (figure 108). Few of the zircons show convolute zoning attributed to post-crystallization purification of crystal structure with progressive migration of trace element rich bands. The polymodal oscillatory zoned zircons exhibit xenocrystic core with zones of homogenization (recrystallized).

Metamorphic Zircons: About 24% of the zircons recovered from the porphyroblastic granite are metamorphic, some of which appear homogeneous, recrystallized or acicular and patchy zoning with weak or no zoning.

Syenite

Xenocrystic Zircons: Some of the magmatic zircons, up to 45% show oscillatory grown zoning with evidence of recrystallization at the rims of some of the zircons and xenocrystic inherited cores.

Magmatic Zircons: About 55% of the zircons in the alkali granite (syeno-granite) are magmatic and show small euhedral grains that are partly homogeneous, fragmental, sometimes recrystallized with imprints of relict oscillatory zoning and hydrothermal alteration at the rims (figure 109).

Granodiorite

Xenocrystic Inherited Zircon: Inherited zircons account for about 22% of the zircons recovered from granodioritic rock, some of which are homogeneous with xenocrystic inherited cores (figure 110).

Magmatic Zircon: About 43% of the zircons are magmatic, broad and patchy zoning, partly resorbed, locally recrystallized, partly fractured with hydrothermal alteration at the rims.

Metamorphic Zircons: 35% of the zircons are metamorphic and are most homogeneous with hydrothermal alteration at the rims.

Pegmatite

Magmatic Zircons: The magmatic zircons constitute about 66% of the zircons recovered from pegmatite, some of which show oscillatory zoning (figure 111a, b), cross bedded zoning, broad patchy zoning, fragmental and sometimes contain xenocrystic cores (figure 111c, d).

Metamorphic Zircons: About 34% of the zircons are partly fractured, recrystallized and are therefore homogeneous with evidence of hydrothermal alteration at the rims.

Vein Quartz

Xenocrystic Inherited Core: Nearly about 5% of the zircon separated from the gold-bearing vein quartz show xenocrystic inherited cores overgrown by oscillatory zoned magmatic zircons.

Magmatic Zircons: 35% of the zircons are magmatic with oscillatory growth zoning (figure 112) and local intermediate resorption in magmatic zircons. Some of the magmatic zircons are locally overprinted by zones of recrystallization (re-homogenization). The original euhedral zircons are cut by recrystallized or newly grown domains of more homogeneous composition. Some of the zircons exhibit radially fractured outer zone, broad and patchy zoning, fragmental and broad oscillatory zoning.

Metamorphic Zircons: metamorphic zircons account for about 60% of the zircons recovered from vein quartz. Some of the zircons are homogeneous, no zoning, fractured, local recrystallization

within or at the rims of the grains. The existence of metamorphic zircon grains in vein quartz is suggestive of inherited cores indicating that the late stage melt that formed the vein quartz possibly incorporated and assimilated an older quartzitic rock in the course of its emplacement.

Syeno-Granite

Metamorphic zircons: About 23% of the zircons obtained from Syeno-granite are metamorphic which are homogeneous and exhibit no zoning.

Magmatic Zircon: 77% - oscillatory zoning, xenocrystic core, growth zoning with local intermediate resorption in magmatic zircons from anatectic granite, locally overprinted by zones of recrystallization (rehomogenization). The original euhedral zircon is cut by recrystallized or newly grown domains of rehomogenized composition (figure 113).

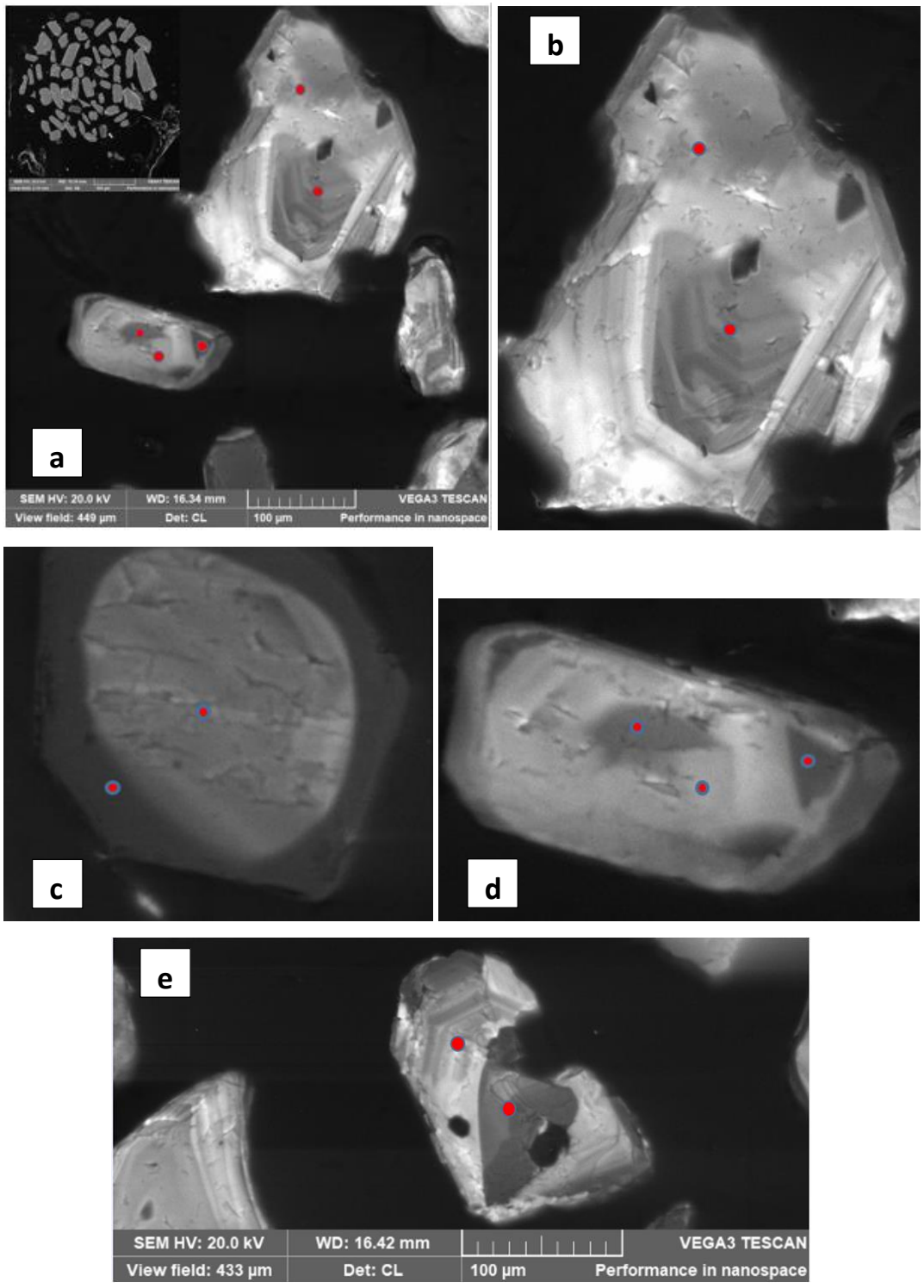


Figure 107: Cathodoluminiscence images of zircons in medium-grained alkali granite

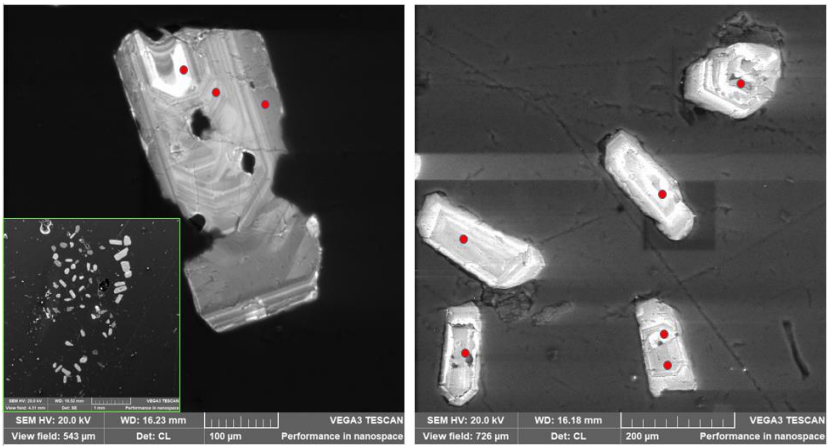


Figure 108: Cathodoluminiscence images of zircons in porphyroblastic granite

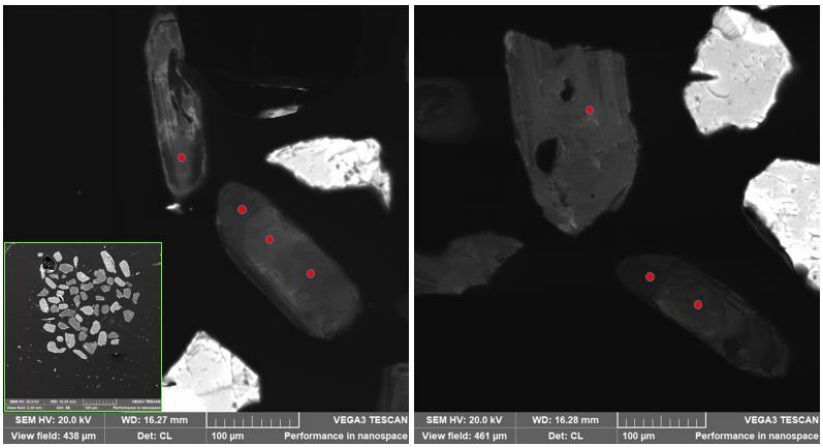


Figure 109: Cathodoluminiscence images of zircons in Syenite

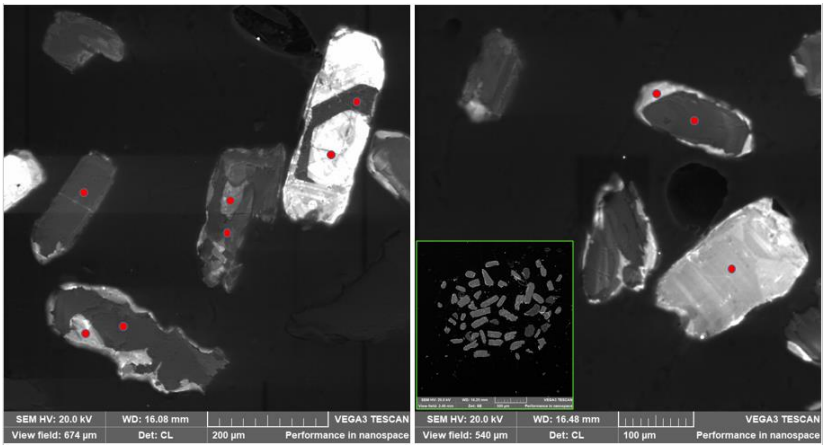


Figure 110: Cathodoluminiscence images of zircons in Granodiorite

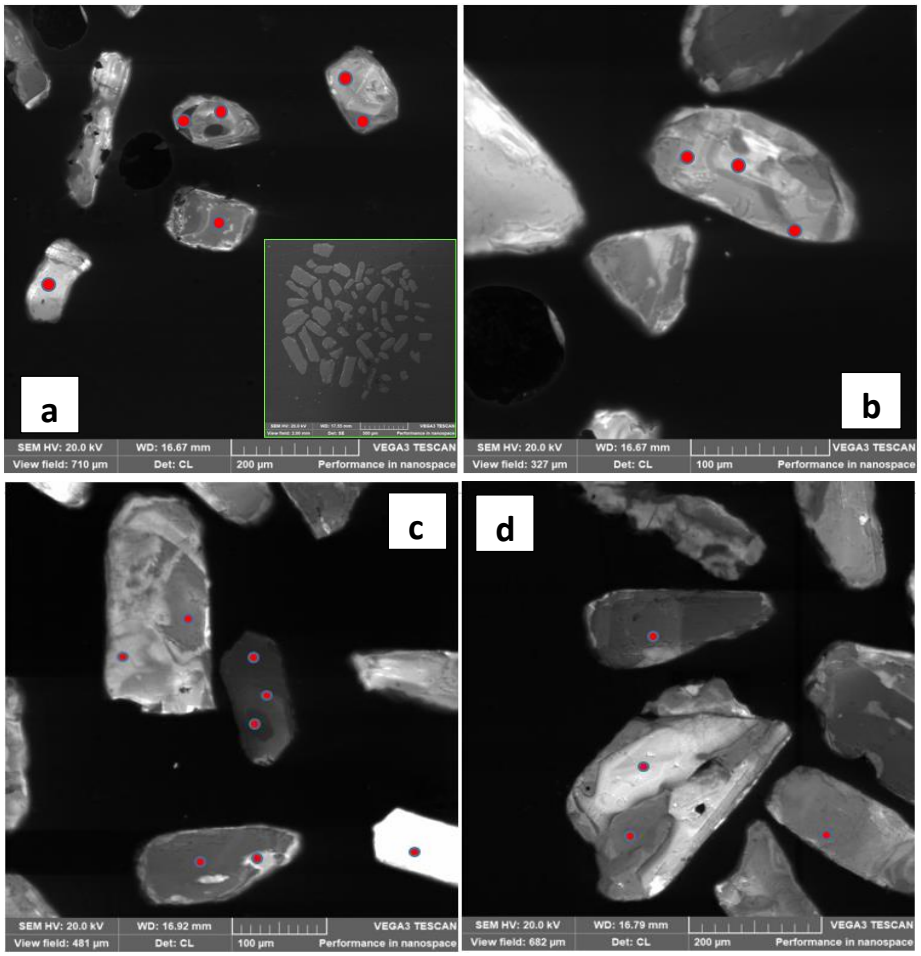


Figure 111: Cathodoluminiscence images of zircons in Pegmatite

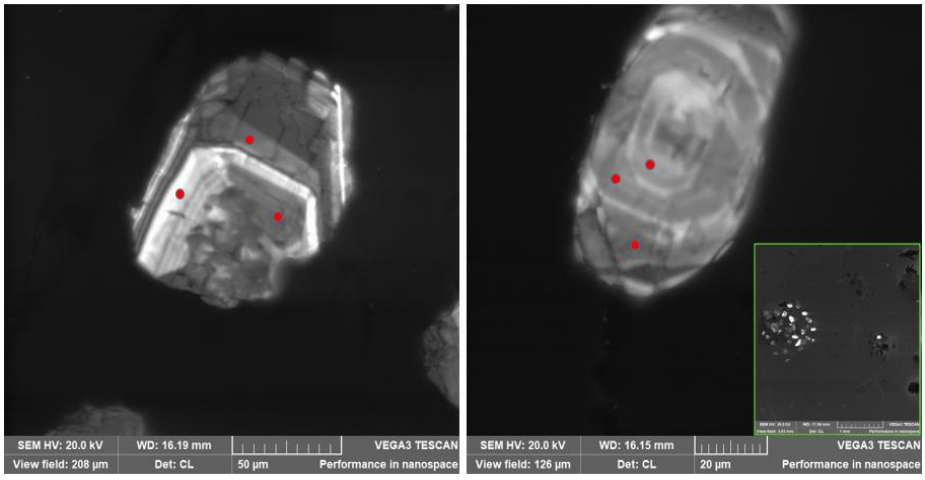


Figure 112: Cathodoluminiscence images of zircons in Vein Quartz

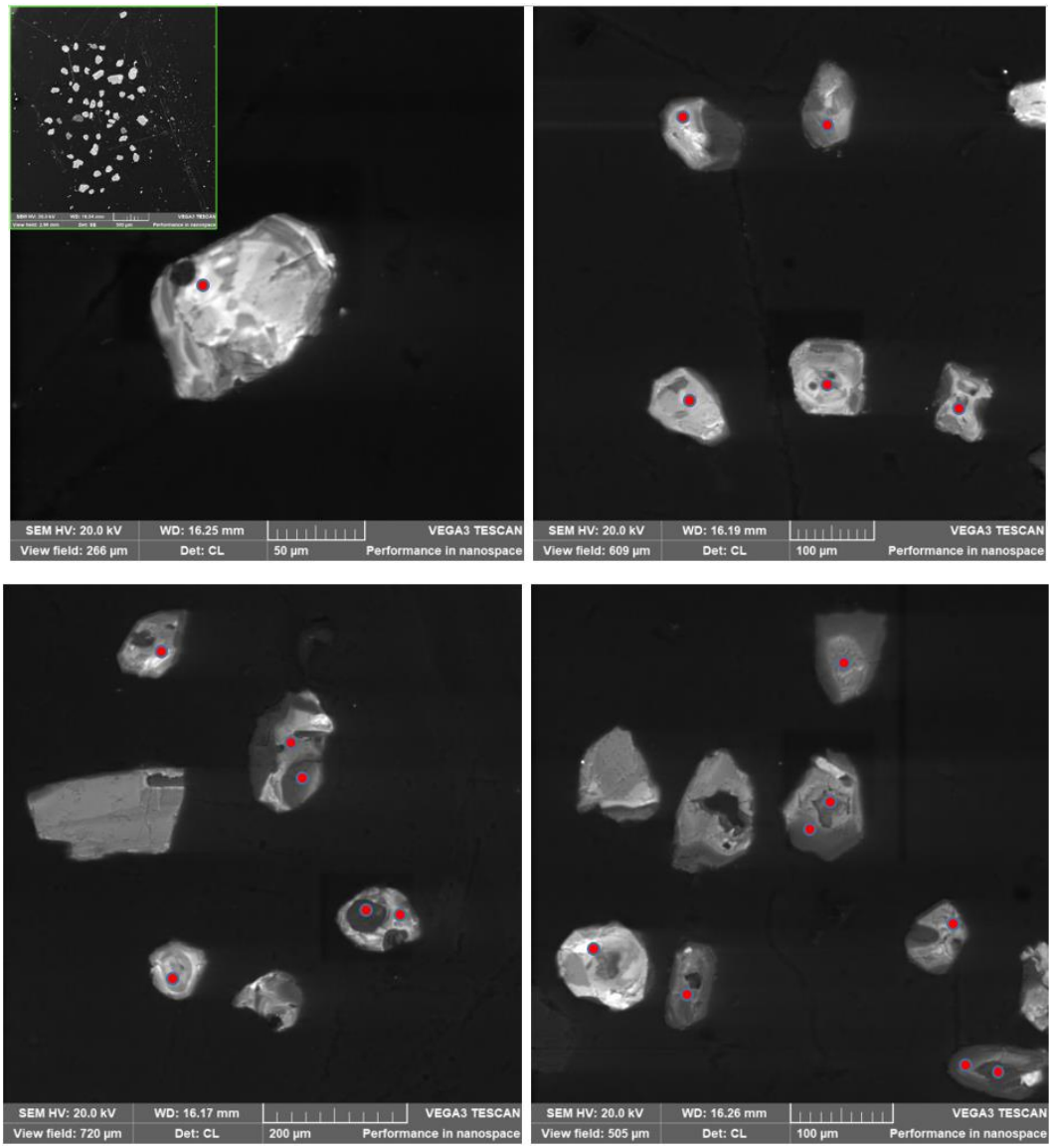


Figure 113: Cathodoluminiscence images of zircons in Syeno-granite

5.5.5 Laser Ablation ICP-MS Data Treatment

An age number (for a particular zircon domain) is never really a perfect or true age but it represents the best estimate when the most appropriate combination of calibration and reduction/correction parameters is used. The age of a rock (metamorphic or magmatic) was estimated by pooling individual ages together, and the less spread there is in individual ages (belong to one event/population) the smaller the error is on the mean age. Detrital ages give a fingerprint of the provenance. After LA-ICPMS analysis the data have to be reduced/processed using iolite. The primary data exported from the ICPMS instrument are raw data in counts per second (cps) which were analyzed after appropriate correction.

Corrections include baseline subtraction, instrumental drift, laser induced downhole fractionation correction, and conversion from count per second (cps) into concentrations. During data reduction using VizualAge, each analysis was cross-checked to ensure that no mixed ages exist and that only least discordant data are included. For detrital zircons, cores are typically magmatic while rims are typically metamorphic. Cores in zircons within an igneous rock can be inherited or magmatic while rims are magmatic. In metamorphic rocks, three or more age populations can be present and typically correlate with core-rim relationships. As a general rule, cores are either inherited or magmatic while rims are either magmatic or metamorphic. Every zircon domain (core, rim) yields four ages: $^{206}Pb/^{238}U$, $^{207}Pb/^{235}U$, $^{208}Pb/^{232}Th$ and $^{207}Pb/^{206}Pb$. Calculating mean ages and plotting of U-Th-Pb data is done using Isoplot 3.75.

Identification of metamorphic and magmatic ages can be done using Th/U ratios. Low Th/U (<0.1) is metamorphic, and high ratios (>0.1) are magmatic. But this is only a general rule and had to be confirmed by cathodoluminiscence (CL) imaging. Exceptions to this rule are documented in literature (Corfu et al, 2003). After data reduction each analysis was checked against the laser spot to ensure that the laser holes in the zircon grains, based on CL images, agree with targets defined during digitizing in order to avoid "mixed" ages. After visual inspection of a Wetherill (concordia) diagrams, efforts were made to identify populations among discordant dates. Where only one population exists, a lower and upper intercept ages (intercept between a regressed discordia and concordia) were calculated.

If more populations exist then multiple intercept ages were plotted in which the upper intercept are typically considered to be magmatic ages while the lower intercept are taken to be metamorphic or a resetting event during which Pb loss occurred. In addition for each age a common Pb corrected and uncorrected ages were obtained which gave a total of 8 individual ages. These individual ages were combined to calculate a mean age which gave either a concordia, discordia, lower and upper intercept or a mean error weighted age. Concordant ages are those where $^{206}Pb/^{238}U$ and $^{207}Pb/^{235}U$, ages agree perfectly. The more these two ages disagree for the same analysis the more discordant they are. For concordant ages, both weighted mean and concordia ages were calculated which should ordinarily be similar but usually are not perfectly identical.

In general for ages older than 1Ga $^{207}Pb/^{206}Pb$ ages are preferred and if the ages belong to the same event/population then an error weighted mean age was calculated. Populations were identified using density probably plots and histograms for the ages exhibiting near concordant $^{206}Pb/^{238}U$ ages. The $^{207}Pb/^{206}Pb$ ages were also taken to be valid if discordance exist but the lower intercept indicates recent Pb loss (projecting through origin). For ages younger than 1Ga, $^{206}Pb/^{238}U$ and $^{207}Pb/^{235}U$ ages were considered, using a histogram/density plots to identify populations for concordant ages while removing those ages that deviate most from an average age. This was done by gradually reducing the MSDW and error on the mean ages as individual ages on the left and right side of an age density curve are removed.

5.5.6 U-Th-Pb Zircon Dating

The progress made by several previous studies in U-Th-Pb dating techniques for zircon and other accessory minerals (Krogh 1973; Krogh 1982, Compston *et al*. 1984) has provided a precise and reliable chronometer for crustal rocks. To determine the time span of the gold metallogeny in Alagbede area, Au-sulfide-bearing rock samples were prepared for U-Th-Pb dating from the main quartz vein and disseminated ore-bearing felsic rocks which were analyzed by LA-ICPMS.

Although LA-ICP-MS methods for U–Pb age dating of zircon has disadvantages, mainly arising from the fractionation of U and Pb during ablation, transportation, and subsequent ionisation, as well as the difficulty to accurately correct for common Pb using ^{204}Pb (i.e., due to ^{204}Hg interference from the He and Ar sample gas used in the ICP-MS) (Frei and Gerdes, 2009), the reliability of LA-ICP-MS for U-Th-Pb age dating of igneous, metamorphic, and detrital zircon grains has been

conclusively demonstrated (e.g., Horn *et al.*, 2000; Košler *et al*., 2002; Jackson *et al*., 2004; Janoušek *et al*., 2006; Gerdes and Zeh, 2006; Zeh *et al*., 2007).

From U-Pb geochronological studies, chemical alteration of the damaged crystal lattice leading to diffusion, leaching and recrystallization (Mezger and Krogstad 1997) are known to be responsible for mobility (partial loss) of Pb in zircon and the preferential loss of radiogenic Pb relative to U. Although diffusion of Pb in crystalline zircon is known to be very slow (Bogomolov 1991, Cherniak et al. 1991, Lee *et al*. 1997), metamict zircon, with severely damaged lattice in which the diffusion may be faster, was avoided in the U-Th-Pb and Lu-Hf studies.

5.6 Interpretation of Results

The total U, Th and Pb concentrations in zircon grains extracted from 7 different rock samples from Alagbede area were measured, analyzed and interpreted at the EarthLab of the University of the Witwatersrand (South Africa) as presented below.

5.6.1 Alkali Granite

From appendix 2, single zircon (34_6_1) $^{207}Pb/^{206}Pb$ model ages of 3750±270 and 3320±180 Ma were obtained, after applying the Anderson's common Pb correction, which were interpreted as ages of Archean inherited xenocrystic cores. The weighted average of the corrected $^{207}Pb/^{206}Pb$ ages (figures 114, 115, 116) after identifying the various age clusters on the probability density plot (figure 117) are 1746±110, 1221±160 and 590±45 Ma. The weighted average age of 1746±110 Ma is interpreted as the imprints of the *Eburnean* thermotectonic magmatism which are common

within the Nigerian basement complex. Similar Eburnean ages have been obtained by Rahaman (1988) on the Pink granite gneiss at Ile-Ife and by U-Pb dating on zircon while 1221±160 is consistent with the relict *Kibaran* thermotectonic age earlier obtained by Rahaman et al., (1983) on Igbetti gneiss. The weighted average age of 590±45 is consistent with 603±180 Ma lower intercept age obtained on the $^{206}Pb/^{238}U$ versus $^{207}Pb/^{235}U$ plot (figure 118), which is interpreted as the age of a new magmatic emplacement during the Pan-African thermotectonic event.

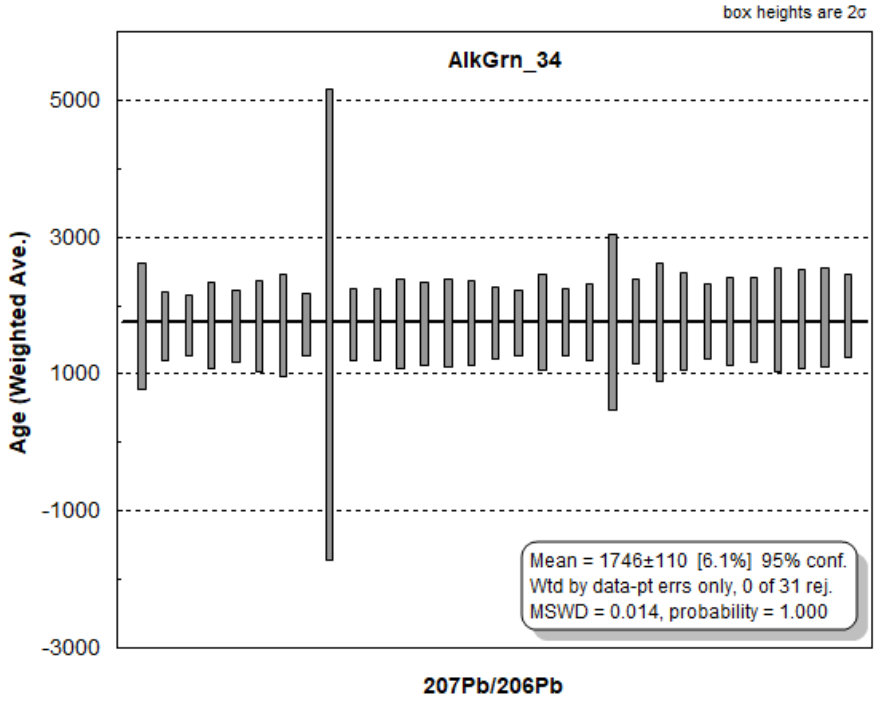


Figure 114: Weighted average age plot of 31 zircon grains from alkali granite.

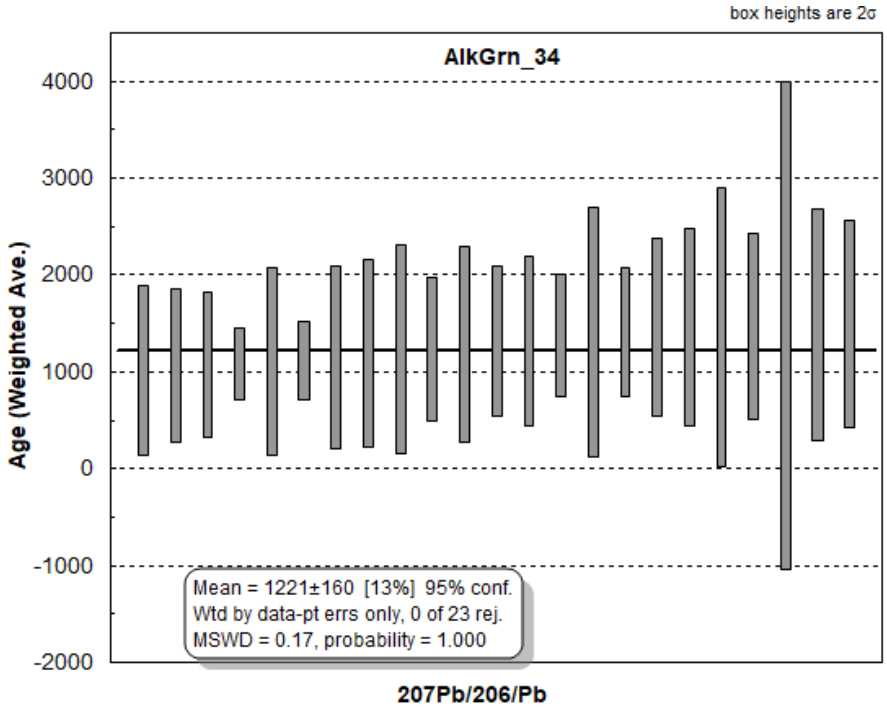


Figure 115: Weighted average age plot of 23 zircon grains from alkali granite.

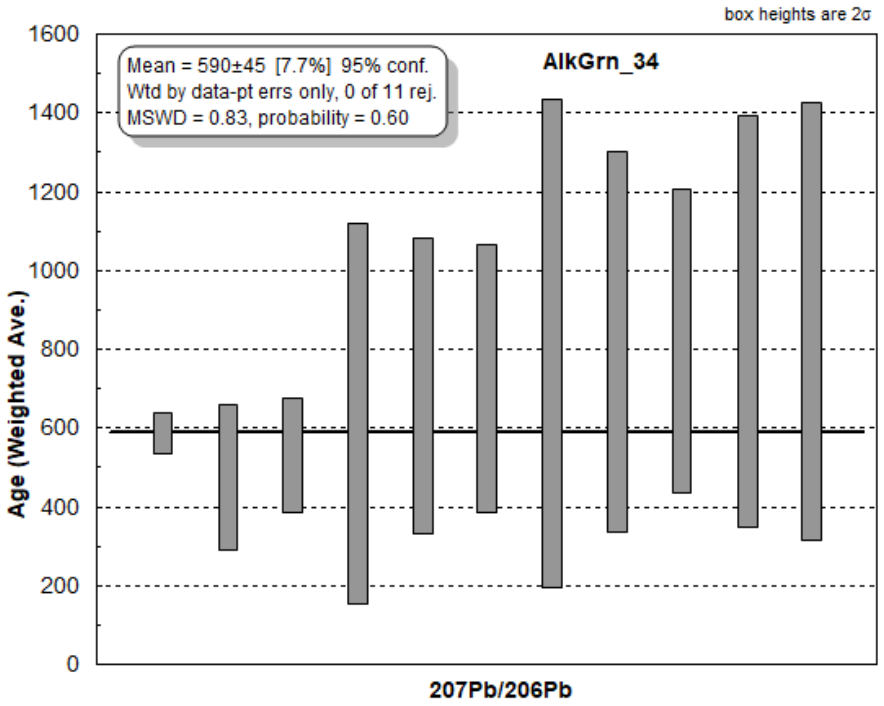


Figure 116: Weighted average age plot of 11 zircon grains in alkali granite.

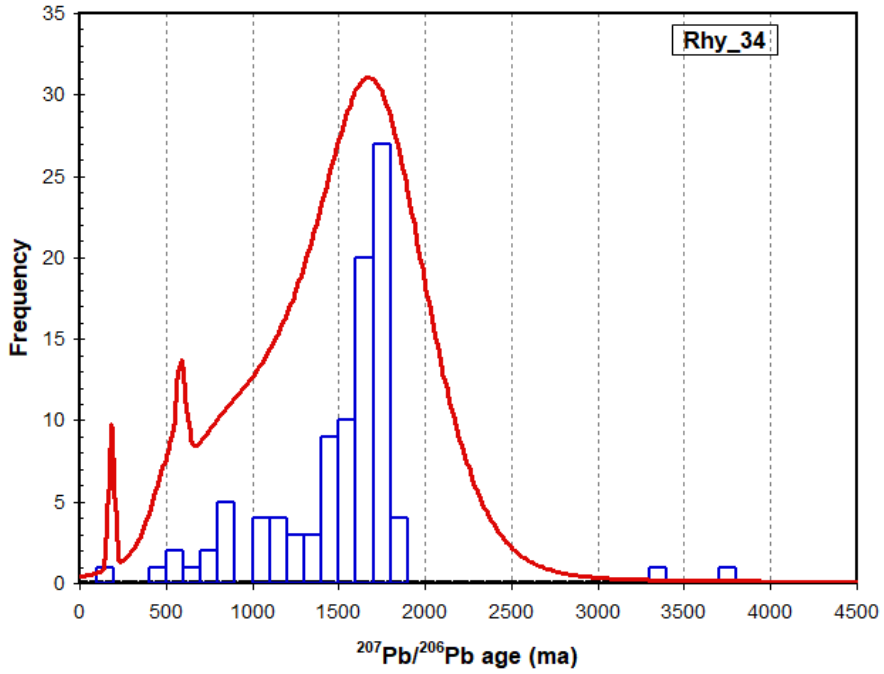


Figure 117: Probability frequency histogram for zircon ages in alkali granite.

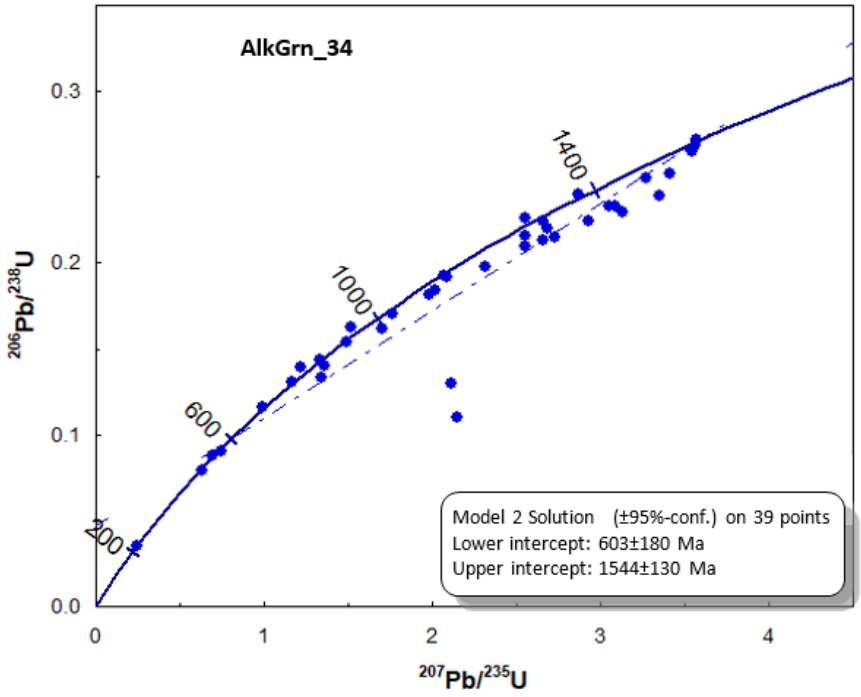


Figure 118: The $^{206}Pb/^{238}U$ versus $^{207}Pb/^{235}U$ Concordia diagram for zircons in alkali granite.

5.6.2 Porphyritic Granite

Appendix 3 shows single zircons (44_21_1 and 44_2_1) $^{207}Pb/^{206}Pb$ model ages, after applying the Anderson's common Pb correction, of 3780±260 and 3130±170 Ma respectively which are interpreted as ages of the Archean inherited xenocrystic cores. The mid-Proterozoic ages of 1771±200 Ma on the weighted average plot (figure 119) and the upper intercept age of 1800±73 Ma on the $^{206}Pb/^{238}U$ versus $^{207}Pb/^{235}U$ plot (figure 120) represent the age of magmatism that accompanied the Eburnean thermotectonic event whose clocks were reset by tectonism and metamorphism as recorded on the weighted average age plot (figure 121) and observed as one of the groupings on the age density probability histogram (figure 122). The weighted mean age of 527±41 (figure 123) and the lower intercept age of 484±82 on the $^{206}Pb/^{238}U$ versus $^{207}Pb/^{235}U$ plot (figure 120), which is slightly reduced as a result of Pb loss suffered by the zircons, are interpreted as the ages of a new magmatic overgrowth on inherited zircons by partial melting during the Pan-African thermotectonic event.

5.6.3 Syenite

The result of the U-Th-Pb dating on zircon (appendix 4) gave a single zircon (55_20_1) $^{207}Pb/^{206}Pb$ model age, after applying the Anderson's common Pb correction, of 3520±98 Ma which is interpreted as the magmatic age of a xenocrystic zircon core. The $^{207}Pb/^{206}Pb$ weighted mean age plots (figures 124, 125, 126) gave 1740±250 Ma (Eburnean), 1381±290 Ma (Kibaran) and 542±75 Ma (Pan-African) respectively. The probability density plot (figure 127) of the $^{207}Pb/^{206}Pb$ zircon ages shows clusters around 500 Ma, 1300 Ma and 1800 Ma. However, the $^{206}Pb/^{238}U$ versus

$^{207}Pb/^{235}U$ plot (figure 128) gave an upper intercept age of 1722±59 Ma which is interpreted as the age of metamorphism of the inherited xenocrystic core on which a new magmatic overgrowth took place at 507±100 Ma (lower intercept age) by partial melting during the Pan-African thermotectonic event.

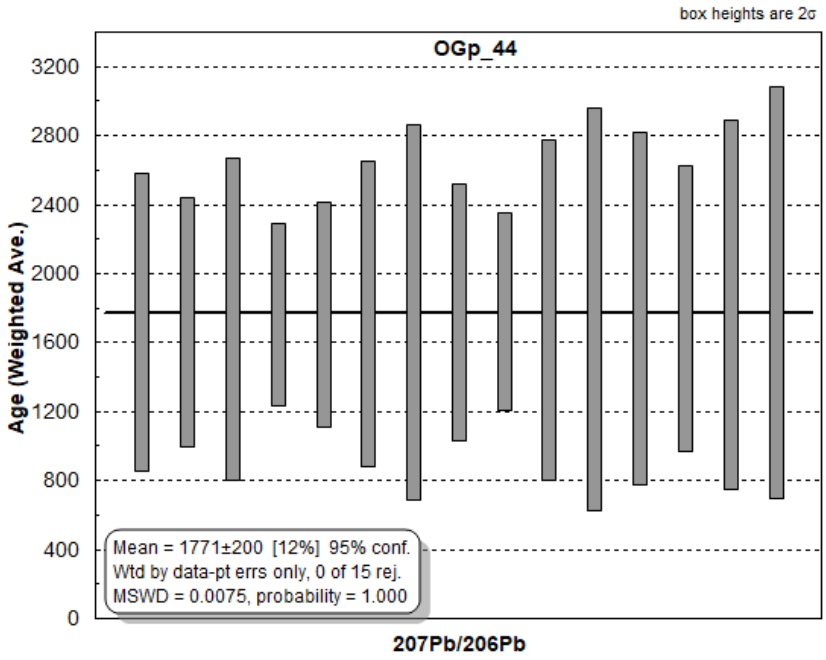


Figure 119: Weighted mean average age plot of 15 zircon grains in porphyritic granite.

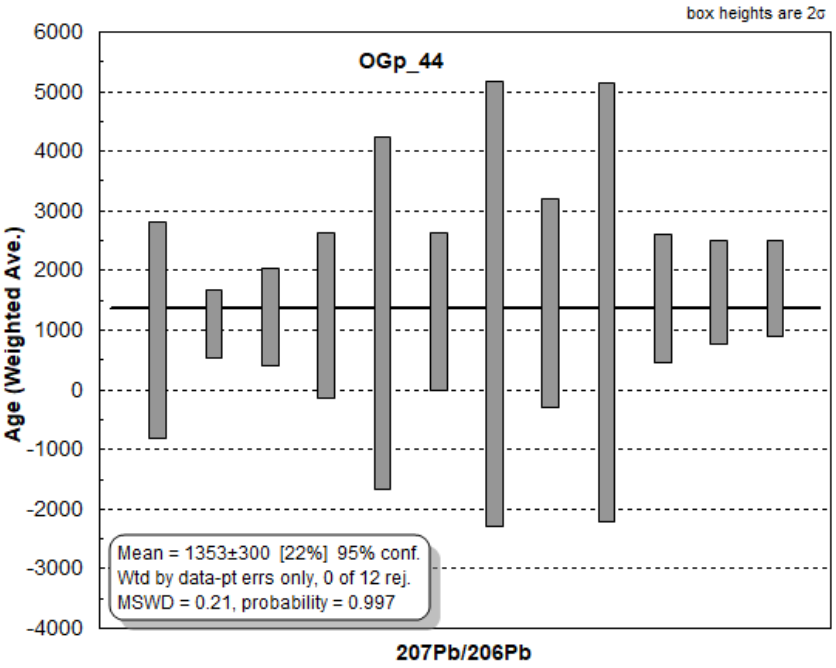


Figure 120: Weighted mean average age plot of 12 zircon grains in porphyritic granite.

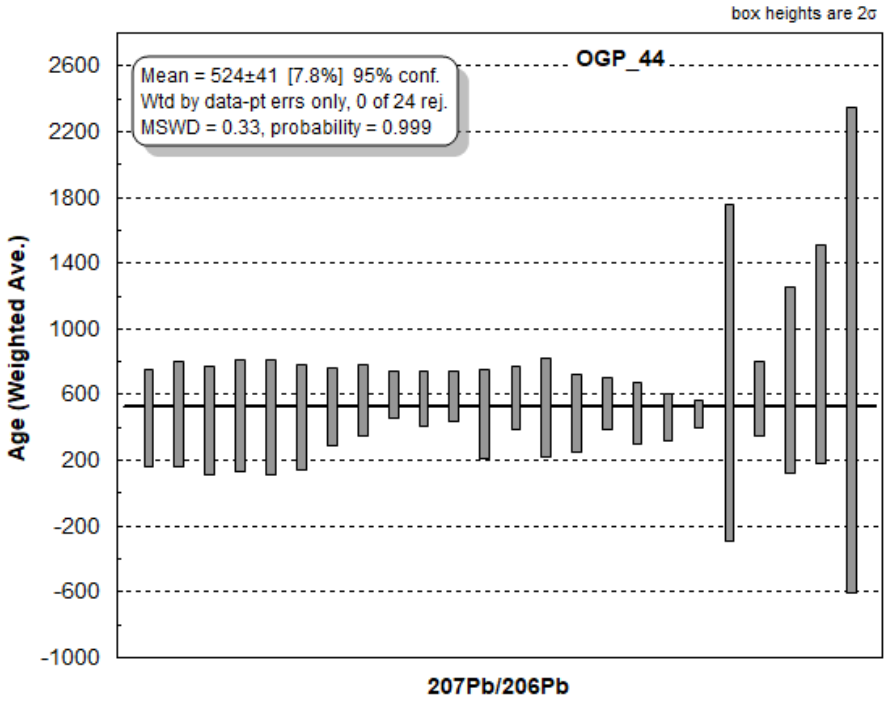


Figure 121: Weighted mean average age plot of 24 zircon grains in porphyritic granite.

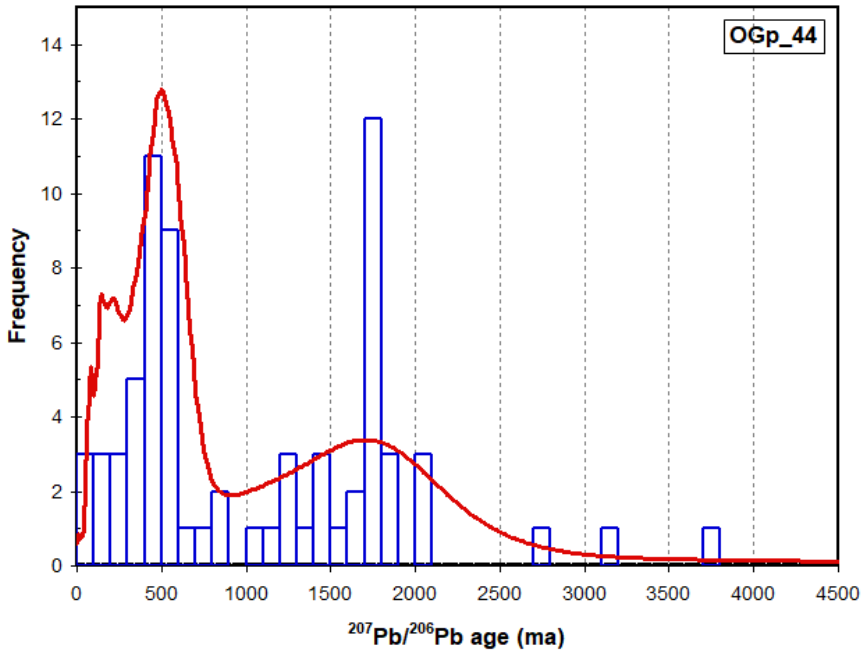


Figure 122: Probability frequency histogram for zircon ages in porphyritic granite.

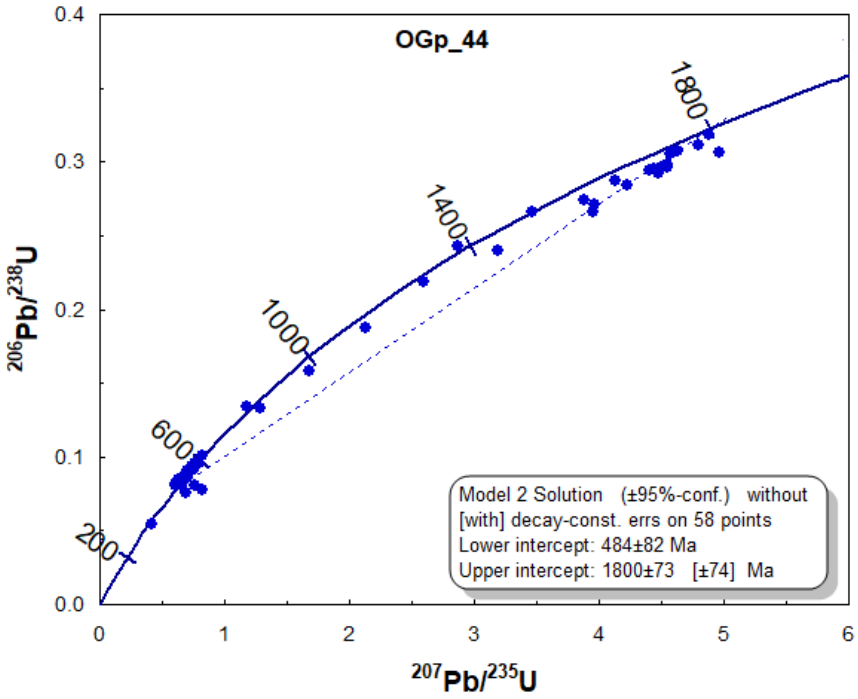


Figure 123: The $^{206}Pb/^{238}U$ versus $^{207}Pb/^{235}U$ Concordia diagram for zircons in porphyritic granite.

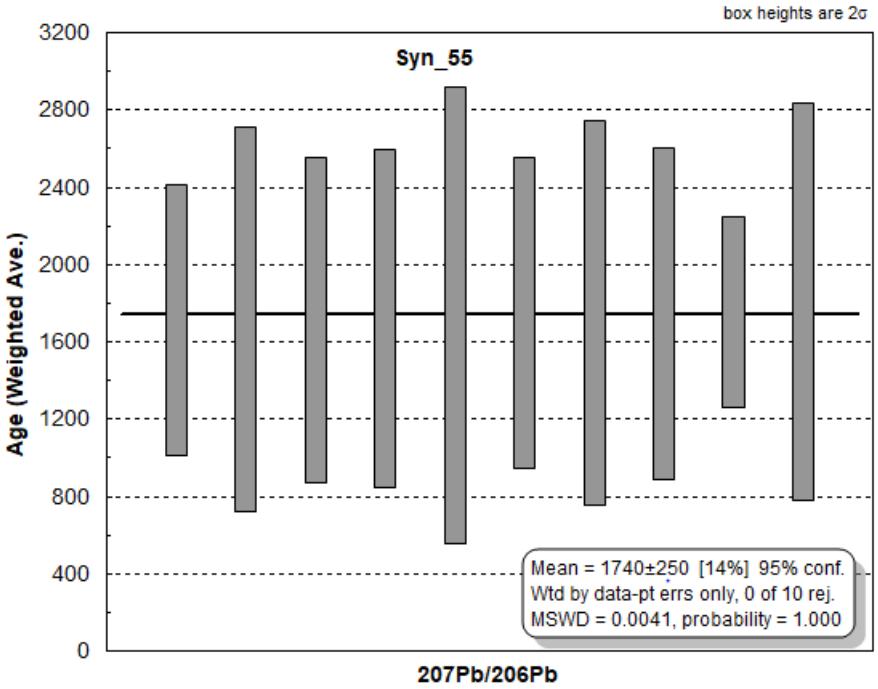


Figure 124: Weighted mean average age plot of 10 zircon grains in syeno-granite.

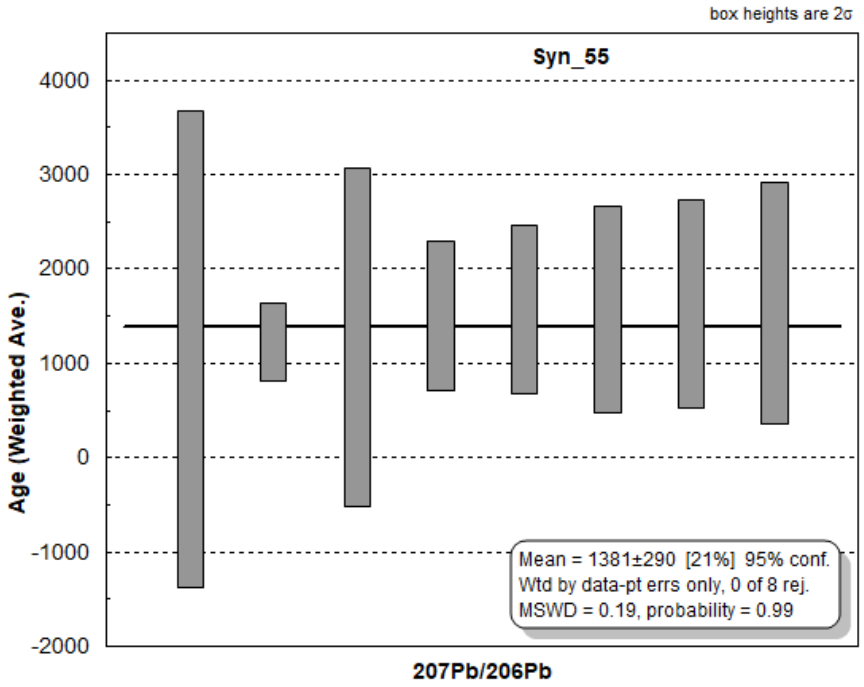


Figure 125: Weighted mean average age plot of 8 zircon grains in syeno-granite.

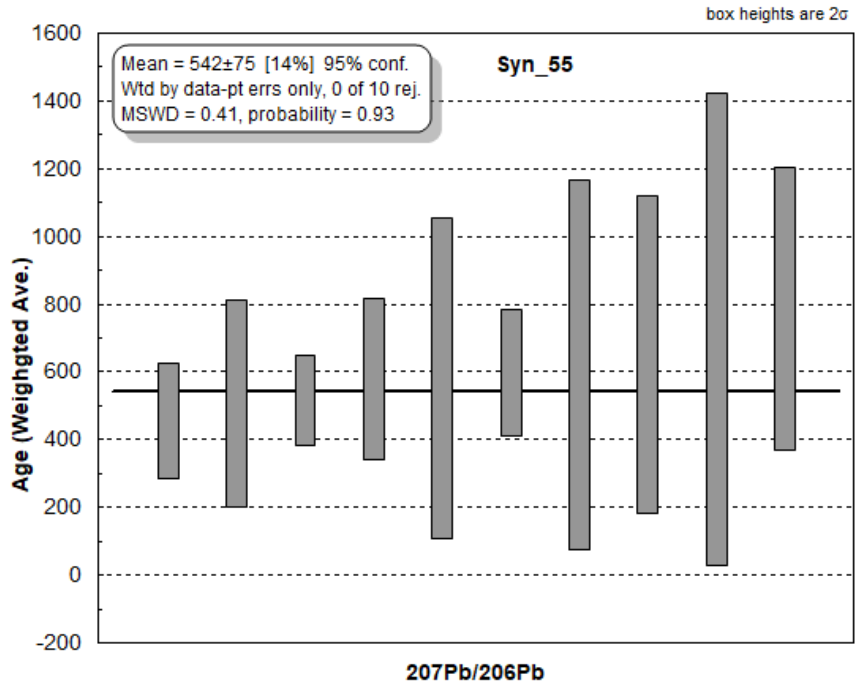


Figure 126: Weighted mean average age plot of 10 zircon grains in syeno-granite.

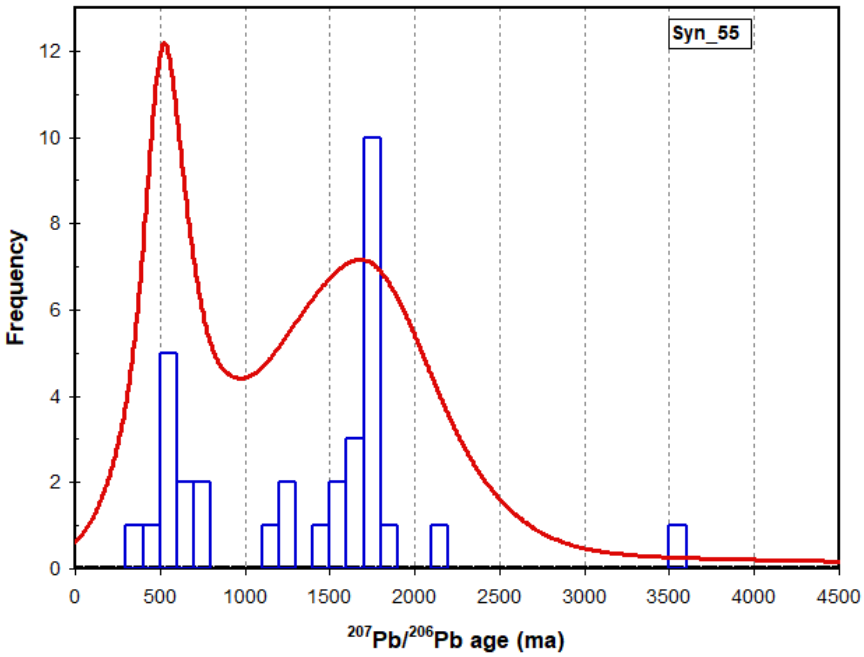


Figure 127: Probability frequency histogram for zircon ages in syeno-granite.

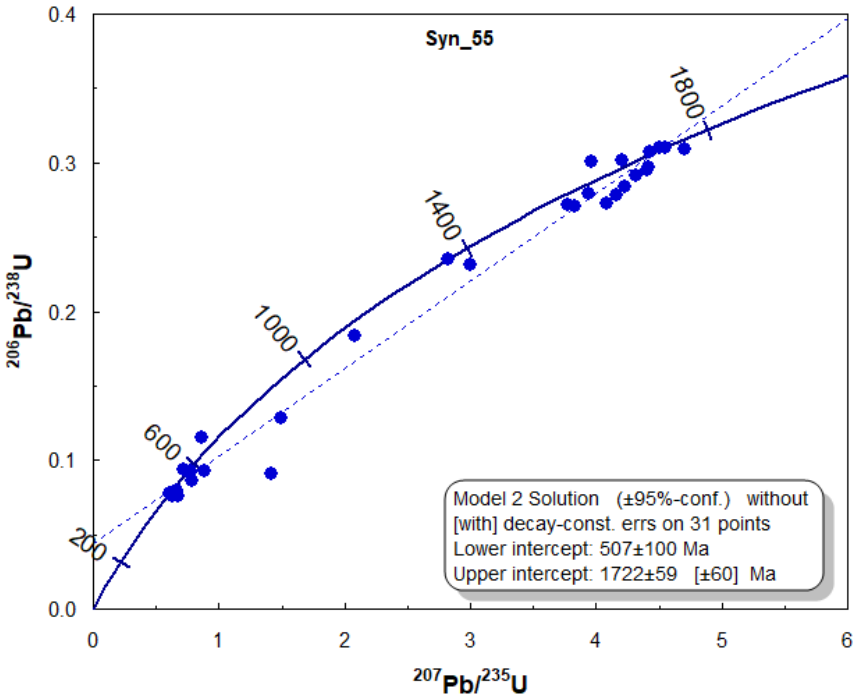


Figure 128: The $^{206}Pb/^{238}U$ versus $^{207}Pb/^{235}U$ Concordia diagram for zircons in syenite.

5.6.4 Granodiorite

Appendix 5 presents the result of the U-Th-Pb dating on zircon recovered from granodiorite which gave a single zircon (57_40_1) $^{207}Pb/^{206}Pb$ Eburnean age of 2010±170 Ma, after applying the Anderson's common Pb correction which is interpreted as the age of thermotectonic magmatism that produced the granodioritic melt which formed the rock. The $^{207}Pb/^{206}Pb$ weighted mean age plot (figures 129, 130) gave 1800±300 Ma (mid-Proterozoic age) and 543±16 Ma (Pan African age) respectively, based on the groupings on the age frequency probability histogram (figure 131). These ages are consistent with the mid-Proterozoic $^{206}Pb/^{238}U$ versus $^{207}Pb/^{235}U$ plot (figure 132) with upper intercept age of 1869±87 Ma which is interpreted as the magmatic age at the time of formation of the granodiorite which was reset by the Pan-African thermotectonic event as recorded on the lower intercept age of 570±47 Ma.

5.6.5 Pegmatite

The U-Th-Pb data presented in appendix 6 gave a single zircon (62_11_1) $^{207}Pb/^{206}Pb$ model age, after applying the Anderson's common Pb correction, of 2250±250 Ma which is interpreted as the age of a xenocrystic zircon formed in the Archean time. The $^{207}Pb/^{206}Pb$ weighted mean average plots for zircon ages (figures 133, 134, 135) gave 1760±71 Ma (Eburnean), 1198±160 Ma and 566±59 Ma (Pan-African). The probability density plot (figure 136) of the $^{207}Pb/^{206}Pb$ zircon ages shows clusters around 550 Ma, 950 Ma and 1800 Ma. The $^{206}Pb/^{238}U$ versus $^{207}Pb/^{235}U$ plot (figure 137) yielded an upper intercept age of 946±150 Ma in the Neoproterozoic which was later reset to 502±100 Ma, corresponding to the age of pegmatite magmatism during the waning stage of the

Pan-African dynamo-thermal event as represented in the development of new oscillatory growth on inherited zircons.

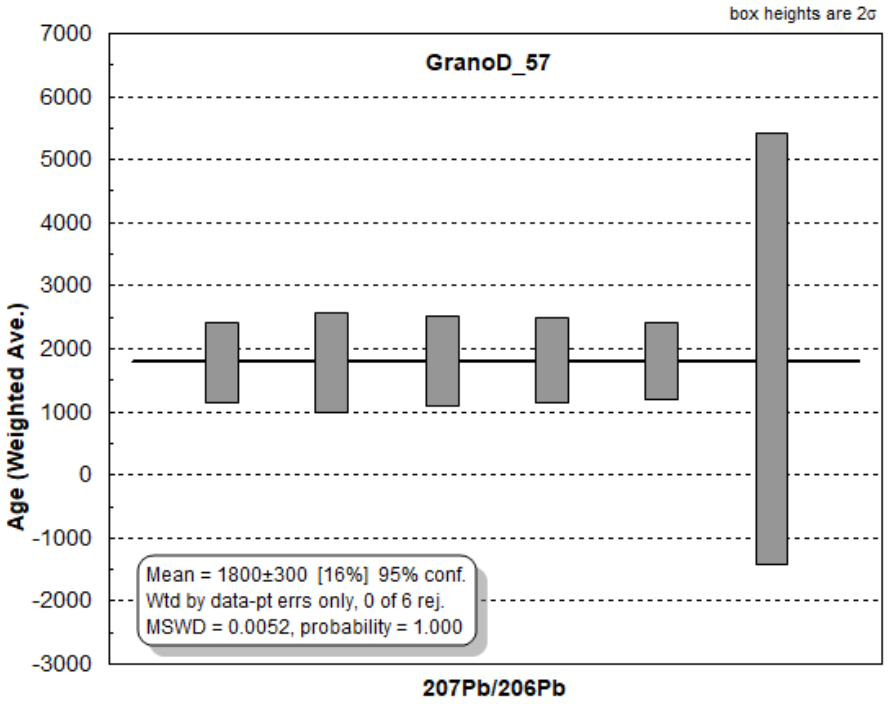


Figure 129: Weighted mean average age plot of 6 zircon grains in granodiorite.

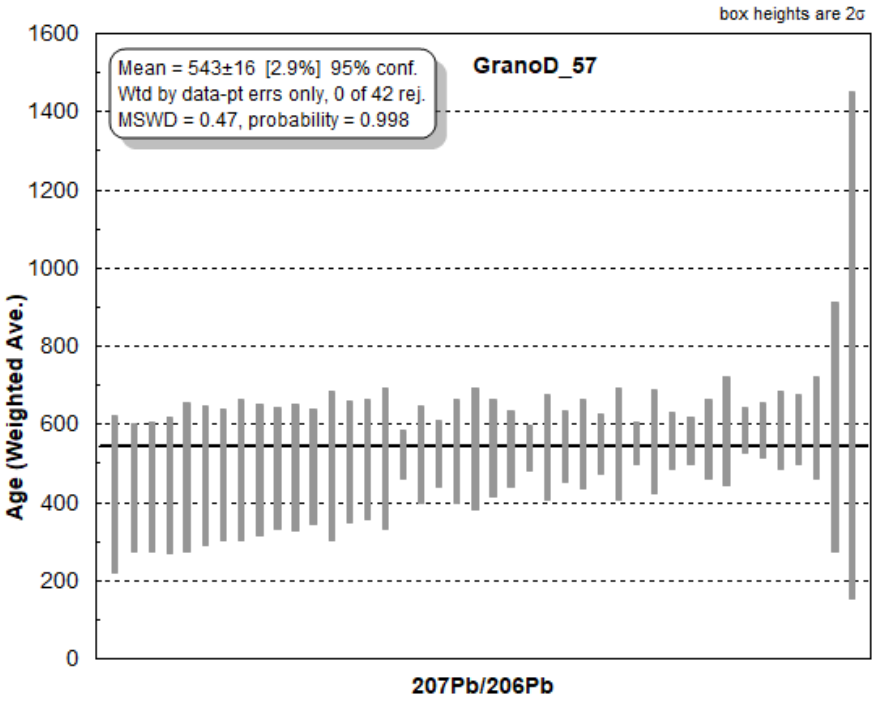


Figure 130: Weighted mean average age plot of 42 zircon grains in granodiorite.

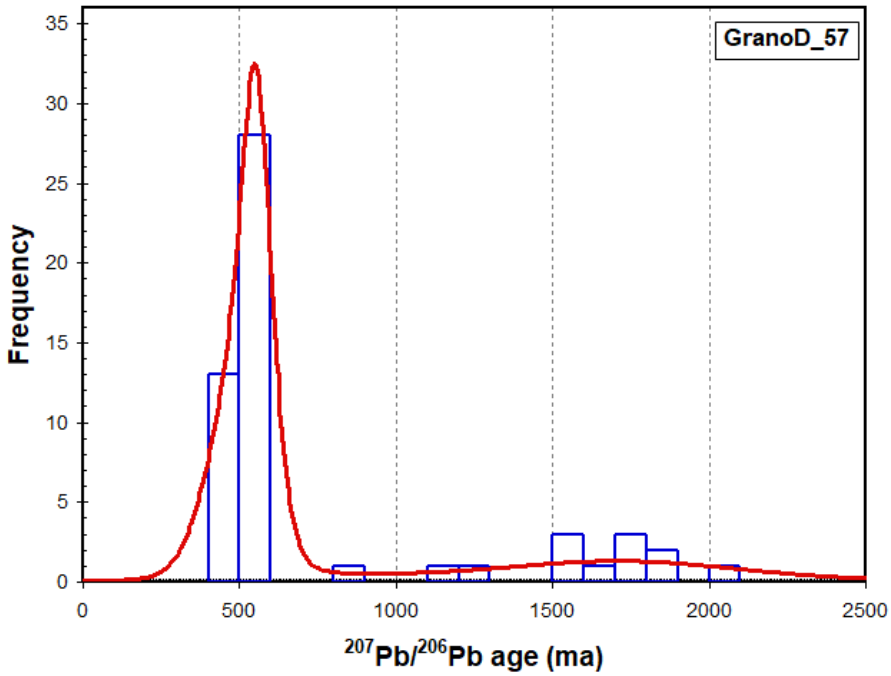


Figure 131: Probability frequency histogram for zircon ages in granodiorite.

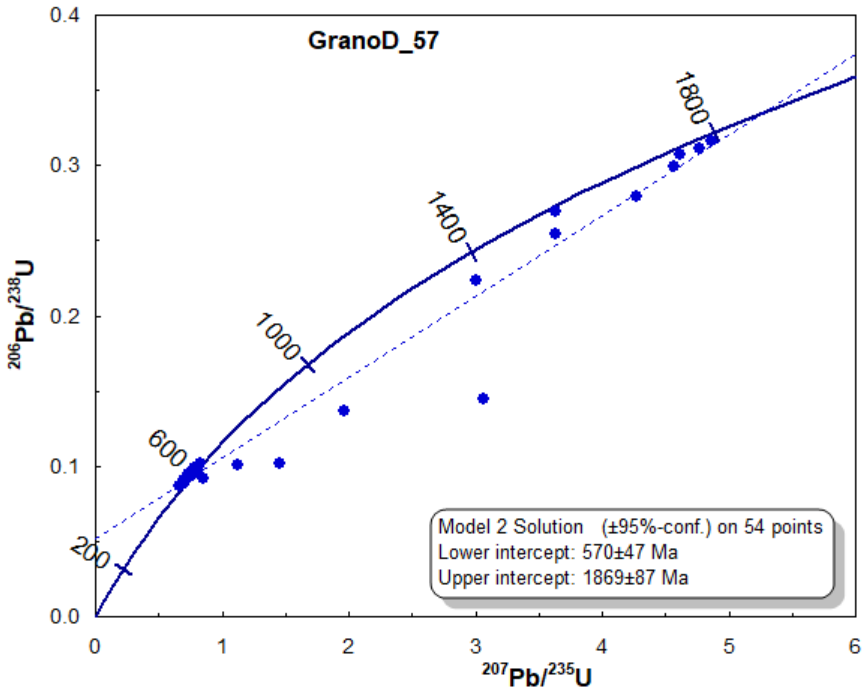


Figure 132: The $^{206}Pb/^{238}U$ versus $^{207}Pb/^{235}U$ Concordia diagram for zircons in granodiorite.

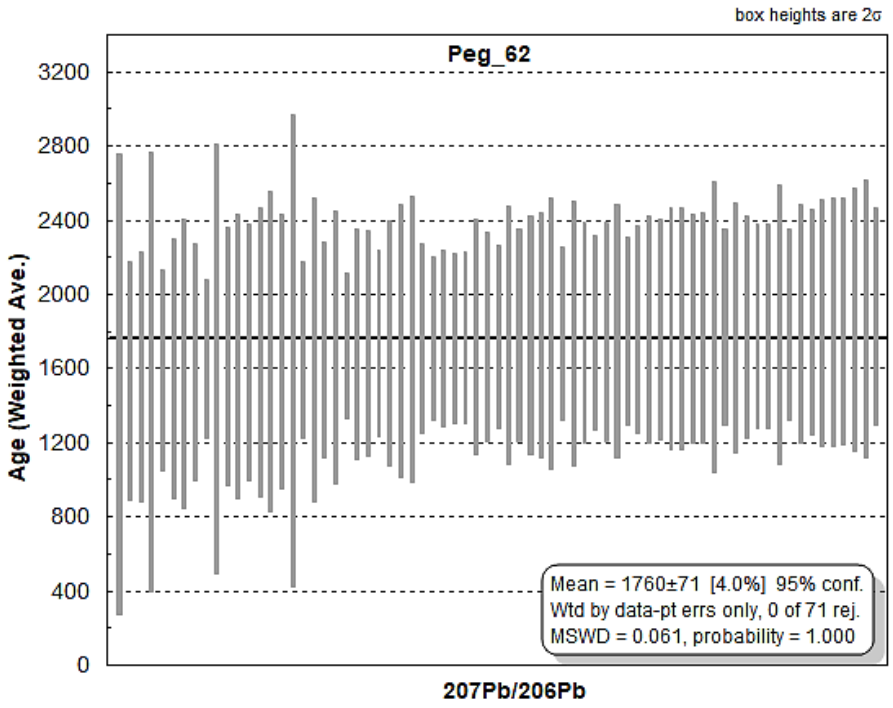


Figure 133: Weighted mean average age plot of 71 zircon grains in pegmatite.

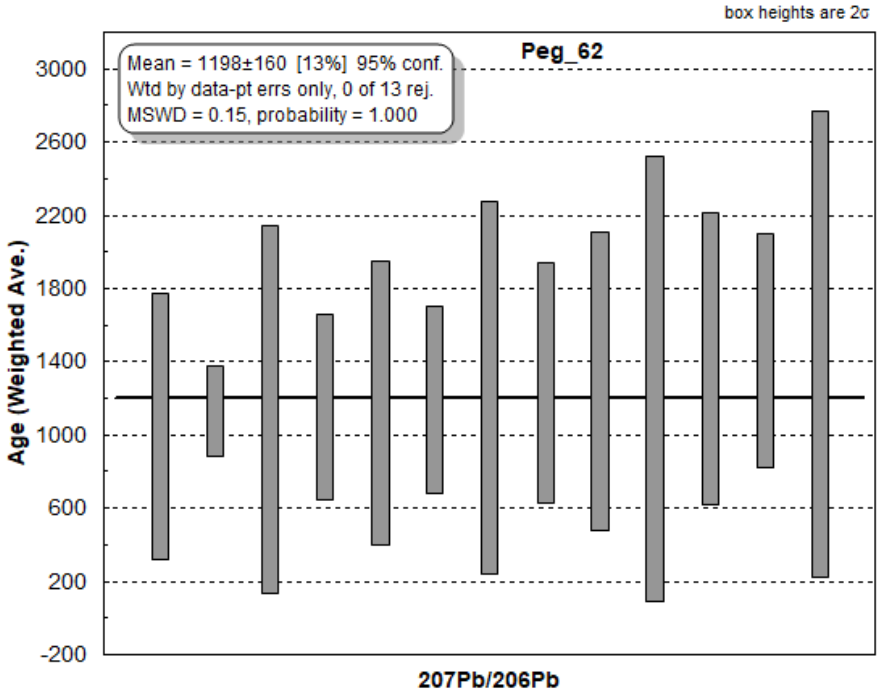


Figure 134: Weighted mean average age plot of 13 zircon grains in pegmatite.

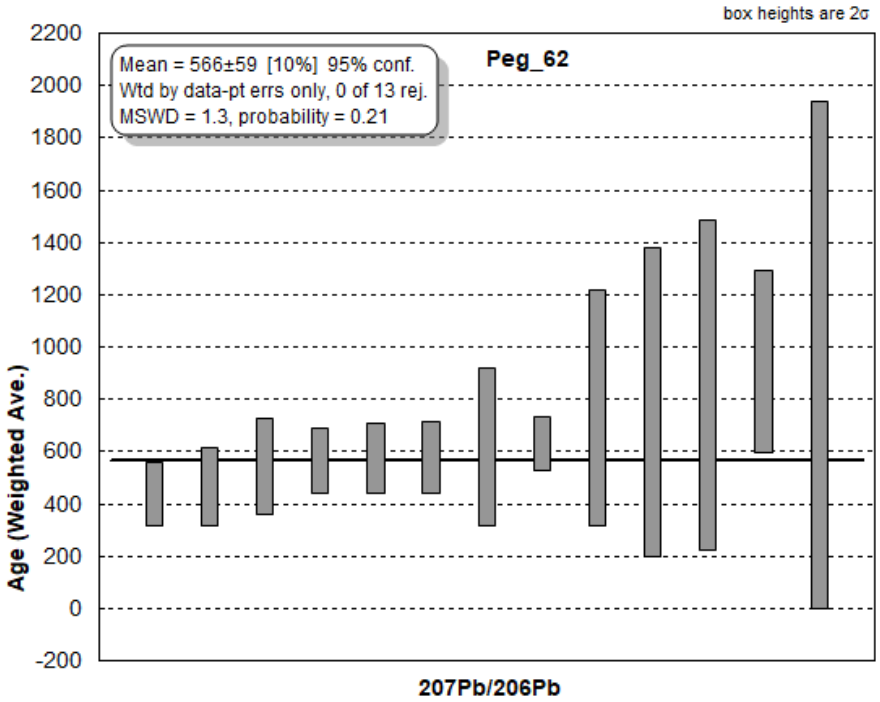


Figure 135: Weighted mean average age plot of 13 zircon grains in pegmatite.

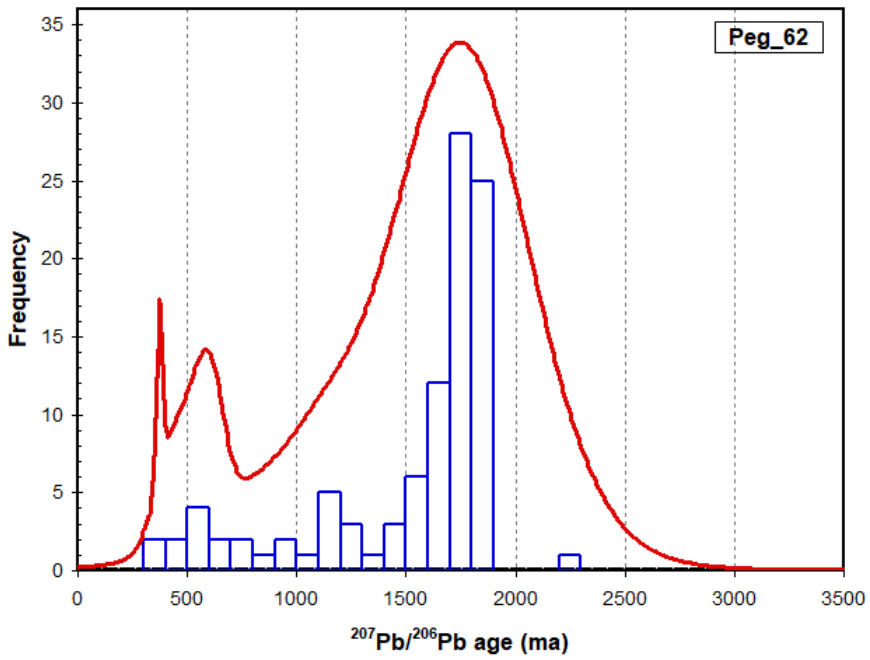


Figure 136: Probability frequency histogram for zircon ages in pegmatite.

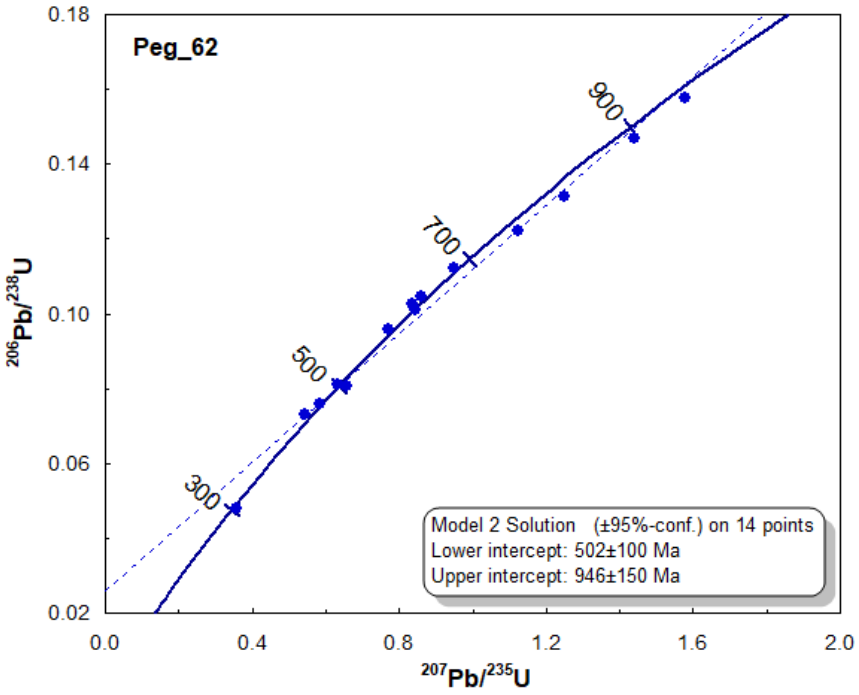


Figure 136: The $^{206}Pb/^{238}U$ versus $^{207}Pb/^{235}U$ Concordia diagram for zircons in pegmatite.

5.6.6 Vein Quartz

Appendix 7 contains the U-Th-Pb data for the gold-bearing vein quartz which when plotted on weighted mean age diagram (figure 138) gave a Pan African age of 583±19 Ma. The frequency probability plot (figure 139) shows an age clusters around 550 Ma. The plot of $^{206}Pb/^{238}U$ versus $^{207}Pb/^{235}U$ (figure 140) after applying the Anderson's common Pb correction yielded an upper intercept age of 1330±35 Ma. This is interpreted as the inherited age of metamorphism that affected the surrounding rocks and a lower intercept age of 590±27 Ma which is interpreted as the time of partial melting and emplacement of the gold-rich quartzitic melt which was remobilized and deposited along major structural trends during the Pan African thermotectonic events.

5.6.7 Alkali Granite (Syeno-granite)

The U-Th-Pb data in appendix 8 was used for the plot of the weighted average age (figure 141) which gave a Pan-African age of 596±28 Ma. The age frequency probability histogram also shows a cluster around 480 Ma (figure 142). Similarly, the plot of $^{206}Pb/^{204}Pb$ versus $^{238}U/^{204}Pb$ (figure 143), after applying the Anderson's common Pb correction, yielded an isochron age of 584±49 Ma which is consistent with the $^{206}Pb/^{238}U$ versus $^{207}Pb/^{235}U$ concordia diagram (figure 144) with a lower intercept age of 575±17 Ma and an upper intercept age of 2416±360 Ma. The upper intercept age is interpreted as the age of an inherited xenocrystic core of a zircon. The lower intercept Pan African age is interpreted as the age of magmatic emplacement of the Alkali Granite during the Pan-African time. Structural and radiometric age data therefore show that the

emplacement of the syeno-granite must have contributed to the gold-sulfide rich hydrothermal fluid which remobilized the gold and deposit it within regional lineament in Alagbede area.

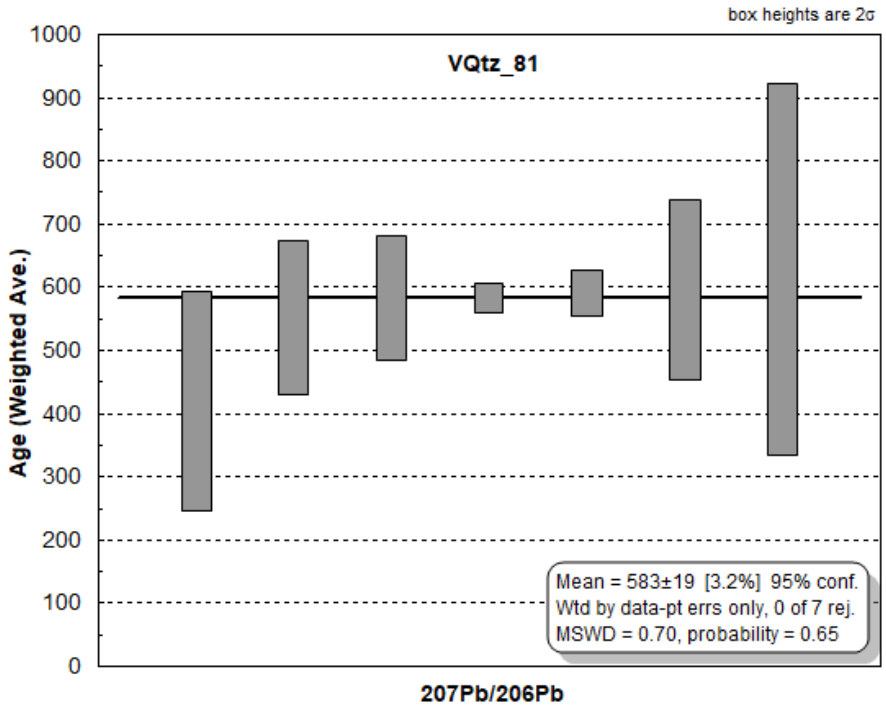


Figure 138: Weighted mean average age plot of 7 zircon grains in vein quartz.

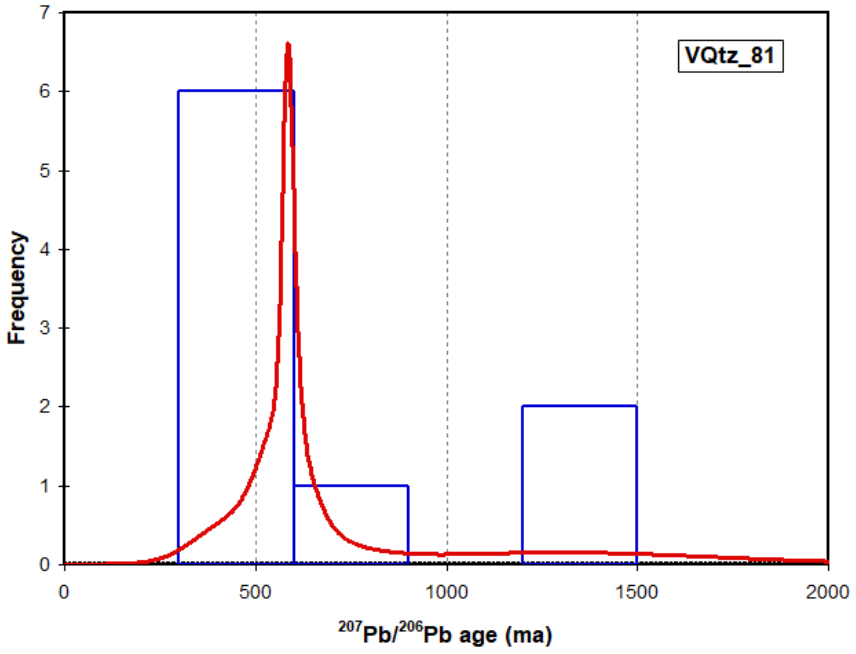


Figure 139: Probability frequency histogram for zircon ages in vein quartz.

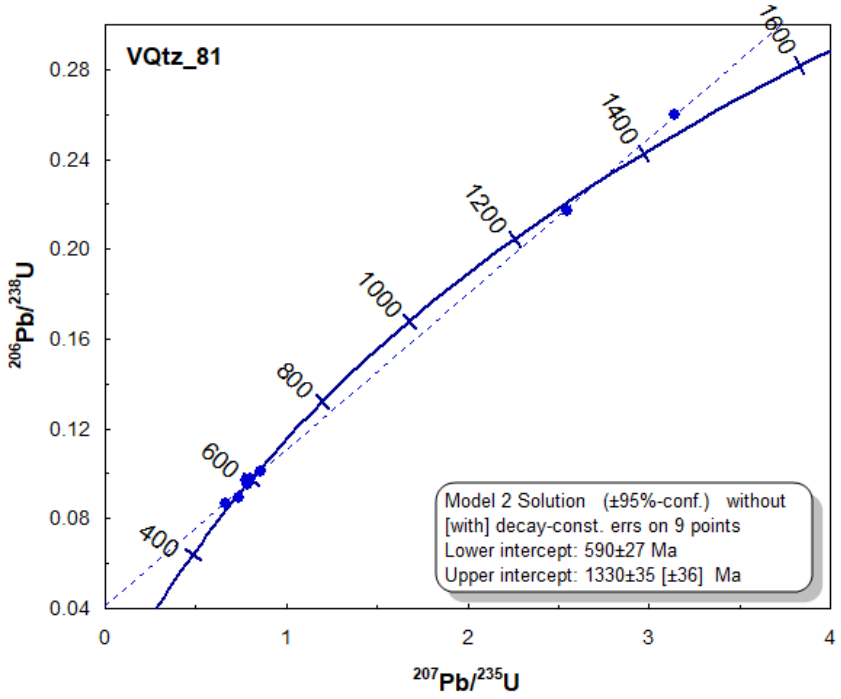


Figure 140: The $^{206}Pb/^{238}U$ versus $^{207}Pb/^{235}U$ Concordia diagram for zircons in vein quartz.

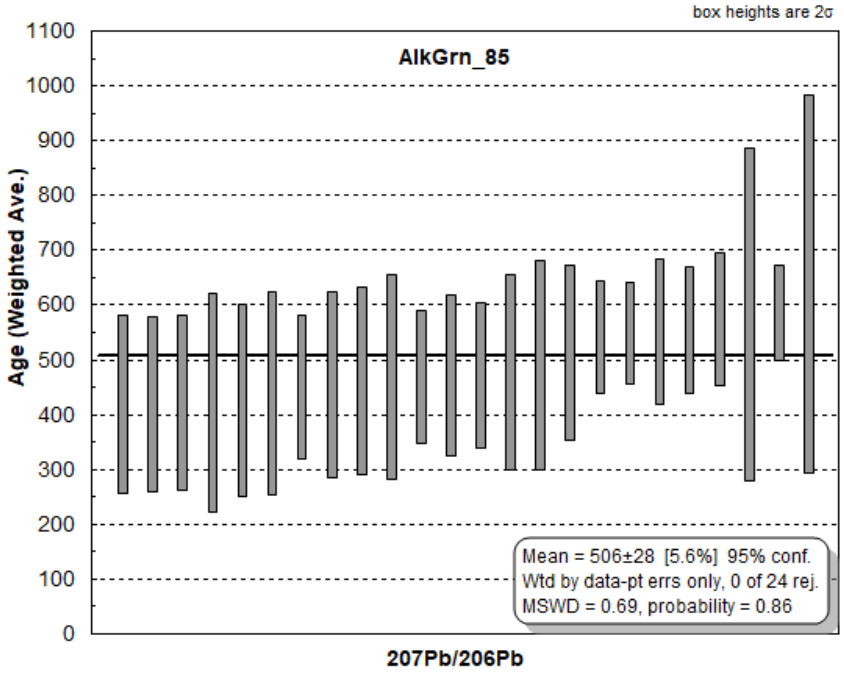


Figure 141: Weighted mean average age plot of 24 zircon grains in syeno-granite.

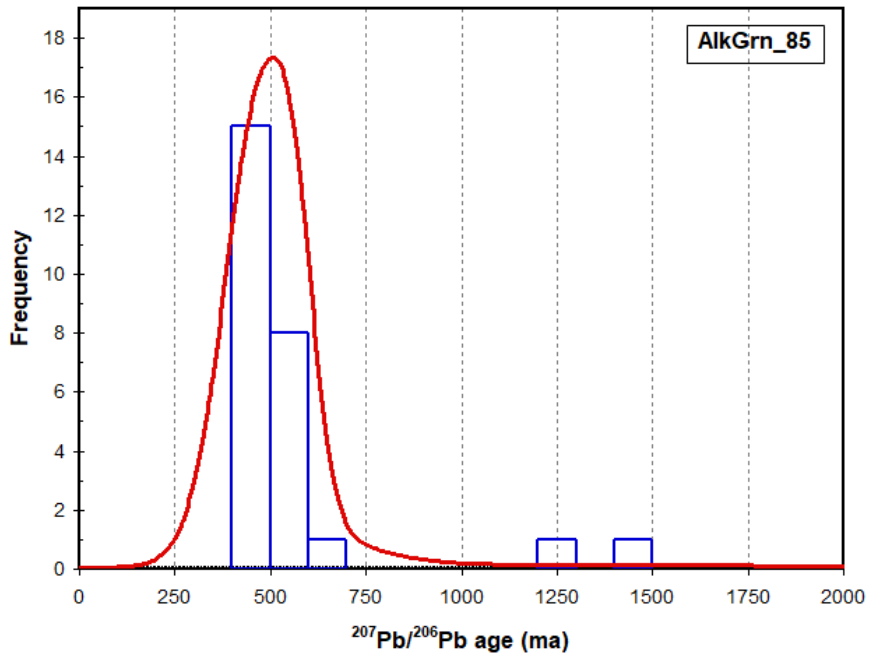


Figure 142: Probability frequency histogram for zircon ages in syeno-granite.

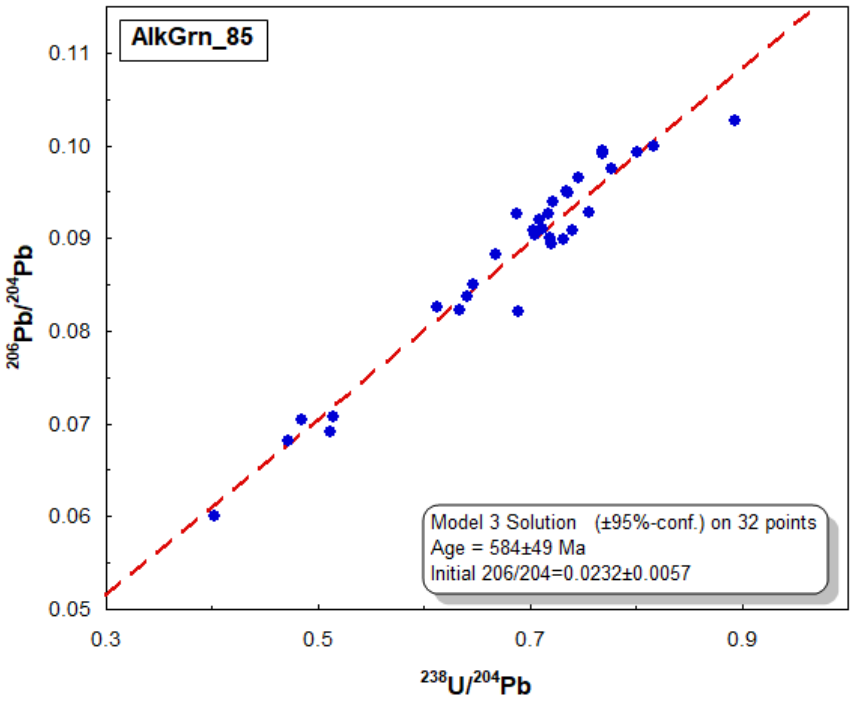


Figure 143: The $^{206}Pb/^{204}Pb$ versus $^{238}U/^{204}Pb$ isochron plot for syeno-granite

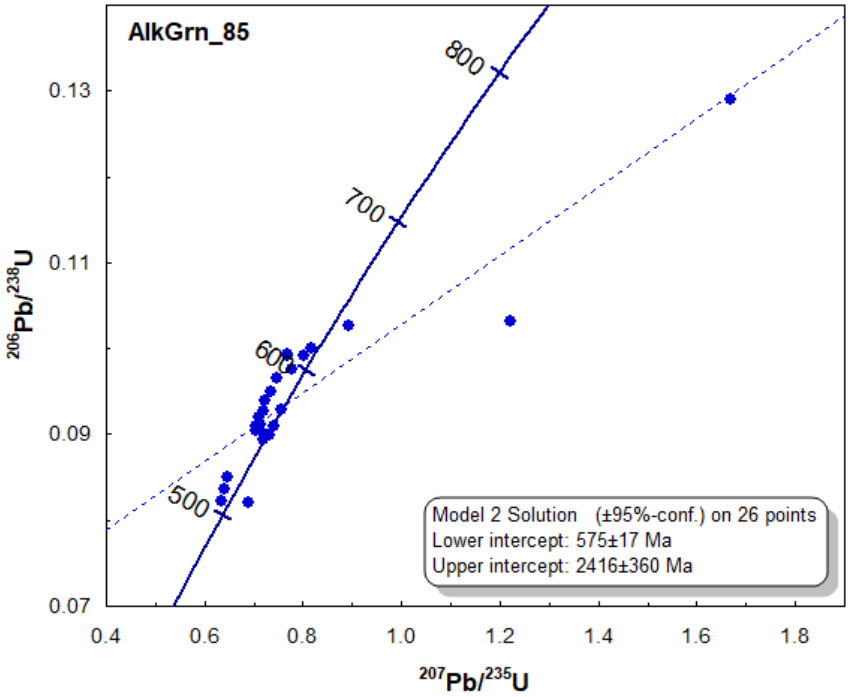


Figure 144: The $^{206}Pb/^{238}U$ versus $^{207}Pb/^{235}U$ Concordia diagram for zircons in syeno-granite.

CHAPTER 6

DISCUSSION AND CONCLUSION

6.1 Discussion

The structure of the Alagbede gold-bearing vein quartz and its mode of occurrence suggest that the mineralization was structurally-controlled and from the observed similarities in orientation and shear movement directions within the quartz vein and in the surrounding granites and gneisses, the vein mineralization may perhaps be linked to the thermotectonic events that affected the basement complex rocks particularly in the western part of Nigeria in the Pan African time (600Ma). The composition of the igneous rocks of Alagbede falls within the continental arc array suggesting their formation from magma similar to that found in modern-day continental arcs. This suggest that the Alagbede gold-sulphide-quartz vein mineralization was, perhaps, related to magmatic emplacement of the syeno-granite which triggered off metamorphic dewatering of the surrounding rocks, including quartzite and talc schist, producing the hydrothermal fluid of continental arc origin that precipitated the gold. Mineralogical and geochemical evidence shows that the Alagbede vein deposit is similar to other orogenic vein-type gold deposits.

The REE pattern of the igneous rocks of Alagbede area is controlled by the REE chemistry of its source and the crystal-melt equilibria which have taken place during its evolution. The roles of individual major rock forming-minerals identified during magmatic evolution, either during partial melting in the source region or in subsequent crystal fractionation is helpful in this regard (Rollinson, 1983). For instance, Eu anomalies, particularly in felsic rocks, are mainly controlled by

feldspars, as Eu (present in divalent state) is compatible in plagioclase and potassium feldspars compared to the trivalent REE which are incompatible. Thus the removal of feldspar from the felsic melt by crustal fractionation or the partial melting of rocks in which feldspar is retained in the source led to the observed negative Eu anomalies in the melt.

Extreme pressure buildup from evolving fluids in areas of partial melting of the psammitic rock initiated at the roof of ascending syenitic melt exceeds the yield strength of the overlying wall rock and eventually fractures the quartzitic and schistose host rocks. Hydrothermal fluids formed as a result of metamorphic dewatering of the surrounding gold-bearing rocks by the syenitic dikes then simultaneously remobilized the gold, propagate and ascend along these fractures, precipitating and deposited the sulfide-gold vein quartz at appropriate P–T conditions as the hot hydrothermal fluids cool. The metasedimentary rock present in Alagede area, which is partially melted and remobilized by the crustal-derived felsic rocks (syeno-granite) and the talc schist are perhaps the potential source for Au in the quartz-sulfide-gold deposits in Alagbede area. This suggests that the Alagbede gold mineralization is metamorphic hydrothermal in origin.

This is consistent with the work of Zhou *et al*. (2017) who proposed that the fluids triggering gold mineralization were probably exsolved from the syenite porphyry based on the observed (1) similar REE patterns between primary igneous perthite, secondary K-feldspar (potassic alteration zone), and pyrite from the ores (Bi *et al*., 2002, 2004); (2) a magmatic signature of pyrite S isotopes and calcite C isotopes (Bi *et al*., 2004); and (3) a mantle contribution indicated by pyrite noble gas

isotopes (Hu *et al.*, 2004), which are all indicative of a genetic connection between the syenite and the sulfide mineralization.

Alagbede gold-bearing quartz veins are associated with disseminated pyrite, arsenopyrite, chalcopyrite, pyrrhotite, galena, and iron ores which are contemporaneous to retrogressive metamorphism and the rejuvenation along the shear zones during D_2 deformation. The auriferous quartz reefs are variable in colour, size, and are preferably hosted in the quartzites and syenogranite, suggesting that gold mineralization is both structurally and lithologically controlled. The work of Zhou *et al.*, 2017a shows that some of the gold inclusions in sulfides were remobilized and precipitated along microfractures due to late brittle deformation or superimposed alteration related to sulfide-stage mineralization, suggesting that some sulfide-hosted gold inclusions were released from sulfides through sulfidation.

Exploration for gold in the study area shows minor gold occurrence in residual soils around the contact between the quartzite ridge hosting the mineralized vein and the surrounding rocks. These rocks are highly fractured and brecciated with vugs and occasional sulphide mineralization comprising pyrites, chalcopyrite, arsenopyrite and galena which are noticeable in some of the hand specimen. Analytical results of panned concentrates of soil samples from the C-horizon gave an average of 0.4g of gold per 50kg of soil. A higher result of between 1.2 to 2g per 50kg of crushed mineralized vein quartz which is far less than a threshold value of 3.7g/kg of gold obtained from geochemical assay result.

These results suggest that Alagbede gold mineralization is not just a mineral occurrence but a primary hydrothermal gold deposit of economic value hosted in vein quartz that cut through the quartzitic portion of the curvilinear trans-crustal fractures of the Anka-Yauri-Iseyin schist belt which are known to be associated with gold mineralization in Nigeria. Gold mineralization in Nigeria appears to be the orogenic type which is controlled by deep seated curvilinear trans-crustal fracture system. These deep seated fracture systems of Anka-Yauri-Iseyin (AYI) and Kalangai-Zuru-Ifewara (KZI) are believed to serve as conduits to the subsidiary fractures which are linked to these major fractures and form sites of gold deposition.

The similarity between the LA-ICPMS U-Pb zircon crystallization ages of the gold-bearing quartz vein and the immediate felsic volcanic rock (vein quartz and syeno-granite) suggests that there is a genetic connection between hydrothermal activity and granitic plutonism as previously suggested by regional relationship. The chronological data obtained are absolutely in consonance with the models previously proposed by other workers, which suggest a temporal link between plutonism and gold metallogeny in the basement complex based on close spatial relationship between the host granitoids.

Igneous zircon (as indicated by its morphology, oscillatory zoning, and Th/U ratios > 0.1 as suggested by Hoskin and Schaltegger (2003); Wu and Zheng (2004), yielded an age 596$\pm$28 Ma (figure 138), representing the age of the syeno-granite emplacement which triggered off metamorphic dewatering of the gold-bearing surrounding rocks and deposited the sulfide-gold bearing vein quartz at 590$\pm$27 Ma (figure 137). This new zircon ages suggest that the gold

mineralization is coeval with the syeno-granite in Alagbede, consistent with the work of Zhou *et al*. (2017a and b).

6.2 Conclusion

A reconnaissance geological investigation of Alagbede area led to the production of a detailed geological map which revealed that the study area is underlain by the basement complex rocks comprising early metamorphic tectonites such as migmatitic gneiss and biotite gneiss on which was deposited the older metasediments including quartzite and talc schist, all of which were intruded by the granitoids and late stage pegmatite and vein quartz in the Pan African time. The evolution and local controls of gold mineralization in the Nigeria Pan African Basement are linked to primary and structural factors.

Alagbede gold is found to be hosted in vein quartz and fine-grained syeno-granite. The primary deposits are being exploited by artisanal miners mainly in the southern segment of the main quartz vein which forms a NNE-SSW-striking belt, extending locally for 500m with a width ranging from 20 to 50m. The concentration of gold in the mineralized vein (VQtz 78) shows a positive correlation with the concentrations of Cu, Pb and Zn which implies a close association between gold and sulfide ores of chalcopyrite, arsenopyrite, pyrite, galena and sphalerite. Petrology and geochemical assay results revealed that gold occurs as discrete primary ore in rocks such as quartzite, syeno-granite, gabbro and talc schist from where gold ore was leached, remobilized and emplaced in fractures within the gold-sulfide-rich vein quartz by hydrothermal fluids during the Pan African thermotectonic event.

The composition of the igneous rocks of Alagbede, from petrogenetic evidence, falls within the continental arc array suggesting their formation from magma similar to that found in modern-day continental arcs. The concave upward REE fractionation pattern of the Alagbede quartz-sulfide-gold ore, presence of strong negative Eu anomalies with progressive enrichment in LREE in most of the rocks analyzed is found to be consistent with the work of Graf (1977) and Hanson (1980) which suggest that aqueous fluids in equilibrium with greenstone belt volcanics would have light REE-enriched, heavy REE-depleted patterns with a negative Eu anomaly and with abundances of all REE lower than that of the parent rocks. This suggest that the Alagbede gold-bearing vein quartz was, perhaps, precipitated from hydrothermal solution of continental arc origin. The Pan African thermotectonic orogeny might have generated heat to establish a thermal gradient for the migration of solutions in veins (Garba, 1993).

This close association between gold and sulfide ores shows that Alagbede gold deposit occurs initially as small free gold in quartzite, syeno-granite, gabbro and talc schist, and mainly as microfracture-fillings or as inclusions in chalcopyrite, arsenopyrite, pyrite, galena and sphalerite in the vein quartz. This suggest that gold mineralization in the Alagbede is coeval with the precipitation of the sulfide phases which is consistent with the work of Morey et al. (2008) and Large et al. (2009) whose studies have shown that gold is primarily hosted in chalcopyrite, arsenopyrite, pyrrhotite and pyrite in most hydrothermal gold deposits, and that its concentration in sulfide varies to a great extent, and can vary from 0.07 to 1.96 ppm within a single sulfide grain.

The U-Th-Pb chronological data shows that the gold deposit in Alagbede area is spatially related to vein quartz (formed at 590±27 Ma) and fine grained syeno-granite (575±17 Ma) which are sinistrally shear by a NW-SE trending fault linked to the transcurrent fault line of the Anka-Yauri-Iseyin schist belt. This suggests that the timing of the gold mineralization in Alagbede is perhaps related to the formation of structural lineaments linked to the period of felsic magmatism in the study area. The fluids that triggered the gold mineralization were probably exsolved from the syeno-granite with little contribution from metamorphic dewatering of the quartzite. A Pan African age of 590+27 Ma is hereby proposed as the age of gold mineralization in Alagbede.

The concordance between the zircon crystallization ages of the gold-bearing quartz vein and the surrounding felsic volcanic rock (syeno-granite) suggests a genetic connection between hydrothermal activity and granitic plutonism as previously suggested by other researchers based on regional relationship. These chronological data are absolutely in consonance with the models previously proposed by other workers, which suggest a temporal link between plutonism and gold metallogeny in Nigeria based on close spatial relationship between the host granitoids.

6.3 Recommendations

In view of the prime and strategic place occupied by precious metals such as gold in the world economy and their potential contributions to Nation's wealth in terms of contributing to the gross domestic product (GDP) of host localities where such commodities are found in economic quantity, further study is recommended to be carried out on Alagbede gold deposit for better understanding

of its prospectivity, development and exploitation. In the light of this, further study in the following areas is therefore recommended:

(i) Carry out fluid inclusion studies to determine the nature, composition and thermometry of the mineralizing fluid that deposited the gold;

(ii) Perform Hafnium (Hf) isotopic studies to establish the petrogenetic origin of rocks and gold deposit in Alagbede.

(iii) Carry out a systematic geochronological study on other gold deposits in Nigeria, as it has been done for Alagbede gold deposit, to determine their respective absolute ages of mineralization and petrogenetic association with a view to assigning to the Nigerian gold deposits its proper genetic model.

REFERENCES

Ajibade, A.C and Fitches W.R. (1988). The Nigerian Precambrian an d the Pan–African Orogeny, Precambrian Geology of Nigeria, 45-53.

Akande, S. O. and Fakorede, O. (1988). Gold mineralization in the Nigerian schist belts. Bicentennial Gold 88, Melbourne, 140-142.

Akande, S. O. (1991). Geological setting and evolution of gold bearing quartz veins in the Nigerian schist belts. In Proc. Symp. Brazil Gold, (E.A. Ladeira Ed.), 257-260.

Akande, S. O., Fakorede, O. and Mucke, A. (1988). Geology and genesis of gold-bearing quartz veins at Bini Yauri and Okolom in the Pan-African domain of western Nigeria. Geol. Mijnbouw, 67, 41-51.

Andersen, T. (2002). Correction of common lead in U–Pb analyses that do not report 204Pb. Chemical Geology 192, 59-79.

Bancroft, G. M., and Hyland, M. M. (1990). Spectroscopic studies of adsorption/reduction reactions of aqueous metal complexes on sulphide surfaces: Mineralogical Society of America, Reviews in Mineralogy, v.23, 511–558.

Bernet, M. and Bassett, K. (2005). Provenance analysis by single-quartz-grain SEM-CL/optical microscopy. J. Sediment. ‘75, 492-500.

Bertrand, J.M.L. and Caby, R. (1978). Geodynamic evolution of the Pa-African orogenic belt: a new interpretation of the Hoggar shield (Algerian Sahara) Geol. Rundsch, 67, 357-388.

Bi, X. W., Cornell, D. H. and Hu, R. Z. (2002). REE composition of primary and altered feldspar from the mineralized alteration zone of alkaline intrusive rocks, western Yunnan Province, China: Ore Geology Reviews, v.19, 69-78.

Bi, X. W., Hu, R. Z. and Cornell, D. H. (2004). The alkaline porphyry associated Yao'an gold deposit, Yunnan, China: Rare earth element and stable isotope evidence for magmatic-hydrothermal ore formation: Mineralium Deposita, v.39, 21–30.

Black, R., Caby, R., Pouhine, A., Boulier, A. M., Fabre, J., Lesquare, R. (1979). Evidence for Late Precambrian plate tectonics in West Africa. Nature, 278p.

Boesse, T.N. and Ocan, O.O. (1988). Geology and evolution of the Ife-Ilesha Schist belt southwestern Nigeria. Symposium on Benin-Nigeria geo-traverse of Proterozoic geology and tectonics of high grade terrains, 87-107.

Bogomolov Ye. S. (1991). Migration of lead in non-metamict zircon. Earth Planet. Sci. Lett. 107, 625-633.

Bruguier, O.; Dada, S.; and Lancelot, J. R. (1994). Early Archaean component (13.5 Ga) within a 3.05 Ga orthogneiss from northern Nigeria: U-Pb zircon evidence. Earth Planet. Sci. Lett. 125, 89-103.

Burke, K.C. Dewey, J.F (1972). Orogeny in Africa . In African Geology A.J. Dessauragie, T.F.J. Whiteman (eds), 583-608, University of Ibadan Press, Nigeria.

Burke, K.C., Freeth S.J. and Grant, N.K. (1976). The structure and sequence of geological events in the basement complex of Ibadan area Western Nigeria Precamb. Res.3, 537-545.

Caby, R. (1989). Precambrian terranes of Benin-Nigeria and northeast Brazil and the Late Proterozoic south Atlantic fit. Geol. Soc. Am., Spec. Pap., 230, 145-158.

Caby, R., Betrand, J. M. L. and Black, R., (1981). Pan-African ocean closure and continental collision in the Hogger-Iforas segment, central sahara. In: Kroner, A. (ed) Precambrian plate tectonics, *Elsevier Amsterdam*. 407-437.

Cherniak, D. J., Lanford, W. A., and Ryerson, F. J. (1991). Lead diffusion in apatite and zircon using ion implantation and Rutherford Backscattering techniques. *Geochim. Cosmochim. Acta.* 55, 1663-1673.

Ciobanu, C. L., Cook, N. J., Utsunomiya, S., Kogagwa, M., Green, L., Gilbert, S., and Wade, B. (2012). Gold-telluride nanoparticles revealed in arsenic-free pyrite: American Mineralogist, v. 97, 1515-1518.

Compston W., Williams I. S., and Meyer C. (1984). U-Pb geochronology of zircons from the lunar breccia 73217 using a sensitive high mass-resolution ion microprobe. Proceedings of the 14th Lunar and Planetary Science Conference, part 2. *J.Geophys. Res.*89, sup.B, 525-534.

Cook, N. J., and Chryssoulis, S. L. (1990). Concentrations of invisible gold in the common sulfides: Canadian Mineralogist, v.28, 1–16.

Cooray P.G (1972). Note on the charnockites of the Ado-Ekiti area, Western State Nigeria. In Africa Geology Ibadan 1970. Eds. Dessauvagie and Whiteman Geol. Dept. Univ. Ibadan, Nigeria, 45-54.

Corfu F., Hanchar J.M., Hoskin P.W.O. and Kinny P. (2003). Atlas of zircon textures. Rev. Mineral Geochem. 53, 469-500.

Cox, K. J., Bell J. D. and R. J. Pankhurst (1979). The Interpretation of Igneous Rocks, 450 pp, Allen and Unwin, St Leonards, NSW, Australia.

Cygan, G. L. and Candela, P. A. (1995). Preliminary study of gold partitioning among pyrrhotite, pyrite, magnetite and chalcopyrite in gold-saturated chloride solutions at 600 to 700^{o}C, 140 MPa (1400 bars). Mineralogical Association of Canada Short Course Series 23. 129-137.

Dada, S. S. (1989). Evolution de la croute continental au Nord Nigeria: apport de la geochemie, de la geochronogy U-Pb et. des traceurs isotopiques Sr, Nd et. Pb. Ph.D Thesis university of Science and Technology Languedoc, Montpellier, France.

Dada, S. S. (1998). Crust-forming ages and Proterozoic crustal evolution in Nigeria: a reappraisal of current interpretations. Precambrian Research, v.87, 65-74.

Dada, S. S. (1999). Geochemistry of U-Pb, Rb-Sr and accessory mineralogical characteristics of the Sarkin Pawa Migmatite-Gneiss, North-Central Nigeria. Spectrum Journal (1 and 2), 126-136.

Dada, S. S. (2006). Proterozoic evolution of Nigeria. In: Oshin O. (ed). The basement complex of Nigeria and its mineral resources, (A Tribute to Prof. M. A. O. Rahaman). Akin Jinad & Co. Ibadan, 29-44.

Drake M. J. and Weill D. F. (1975). Partition of Sr, Ba, Ca, Y, Eu^{2+}, Eu^{3+} and other REE between plagioclase feldspar and magmatic liquids: an experimental study. Geochim. Cosmochim. Acta, 39, 689-712.

Egbuniwe, I. G. (1982). Geotectonic evolution n of Maru Belt, northwestern Nigeria, unpublished Ph.D thesis of the University of Wales, U.K.

Elueze, A. A. (1981). Petrographic studies of metabasic rocks and meta-ultramafites in relation to mineralization in Nigerian schist belts. J Mining Geol 18, 31-36.

Eskola, P., (1920). The mineral facies of rocks. Norsk. Geol. Tidsskr. 6 (1922), 143-194.

Falconer J.D (1911). The geology and geography of Northern Nigeria. Macmillan, London.

Ferre´, E., Gleizes, G., Caby, R., (2002). Obliquely convergent tectonics and granite emplacement in the Trans-Saharan belt of Eastern Nigeria: a synthesis. Precambrian Research 114, 119-219.

Fitches WR, Ajibade AC, Egbuniwe IG, Holt RW, Wright JB (1985). Late Proterozoic SchistBelts Plutonism in North Western Nigeria. Geol. Sec. London 142, 319-337.

Flinter, B. H. (1959). The magnetic separation of some alluvial minerals in Malaya. American Mineralogist, v.44, 738-751.

Frei, D. and Gerdes, A. (2009). Precise and accurate in situ U-Pb dating of zircon with high sample throughput by automated LA-SF-ICP-MS. Elsevier, Chemical Geology 261, 261-270.

Frelinger, S. N., Ledvina, M. D., Kyle, J. R. and Zhao, D. (2014). Scanning electron microscopy cathodoluminescence of quartz: Principles, techniques and applications in ore geology. Elsevier Ore Geology Reviews 65, 840-852.

Garba, I. (2000). Origin of Pan-African mesothermal gold mineralization of Bin Yauri, Nigeria. Journal of African Earth Sciences 31 (2), 433-449.

Garba, I. (2002). Late Pan-African Tectonics and Origin of Gold Mineralization and Rare-Metal Pegmatites in the Kushaka Schist Belt, Northcentral Nigeria. Jour. Min. Geol., 38 (1), 1-12.

Gerdes, A. and Zeh, A. (2006). Combined U–Pb and Hf isotope LA-(MC)-ICP-MS analyses of detrital zircons: comparison with SHRIMP and new constraints for the provenance and age of an Armorican metasediment in Central Germany. Earth and Planetary Science Letters, 249, 47-61.

Götze J., Plötze M., and Habermann D. (2001). Origin, spectral characteristics, and practical applications of the cathodoluminescence (CL) of quartz—A review. Mineralogy and Petrology 71: 225-250.

Graf, J. L., Jr. (1977). Rare earth elements as hydrothermal tracers during the formation of massive sulfide deposits in volcanic rocks: ECON. GEOL., v. 72, 527-548.

Grant, N.K. 1969. The late Precambrian to early Paleozoic Pan Africa Orogeny in Ghana, Togo, Dahomey and Nigeria. Bull. Geol. Soc. Amer. Vol 80, 45-46.

Grant NK (1970). Geochronology of Precambrian Basement Rocks from Ibadan, South-Western Nigeria. Earth plant Sci. Lett., 10, 29-38.

GSN (1994). The Schist belts of Nigeria: a publication of the Geological Survey of Nigeria.

Hagemann S.G. and Brown P.E. (2000). Gold in 2000: an introduction, in Society of Economic Geologists Reviews in Economic Geology 13, 1-7.

Hanson, G. N. (1980). Rare earth elements in petrogenetic studies of igneous rocks: Ann. Rev. Earth Planet. Sci., v. 8, 371-406.

Haskin, L. A., M. A. Haskin, F. A. Frey, and T. R. Wildman (1968). Relative and absolute terrestrial abundances of the rare earths, in Origin and Distribution of the Elements, vol. 1, edited by L. H. Ahrens, 889-911, Elsevier, New York.

Hockey, R.D. Sacchi, R., Degraff, W.P. & Muotoh, E.D.G. (1986). The Geology of Lokoja – Auchi area, GSN Bulletin, 31 -72.

Horn, I., Rudnick, R. L., McDonough, W. F. (2000). Precise elemental and isotope ratio determination by simultaneous solution nebulization and laser ablation-ICP-MS: application to U-Pb geochronology. Chemical Geology 164, 281-301.

Hoskin, P. W. O. and Schaltegger, U. (2003). The composition of zircon and igneous and metamorphic petrogenesis: Reviews in Mineralogy and Geochemistry, v.53, 27-62.

Hu, R. Z., Burnard, P. G., Bi, X. W., Zhou, M. F., Pen, J. T., Su, W. C. and Wu, K. X. (2004). Helium and argon isotope geochemistry of alkaline intrusion associated gold and copper deposits along the Red River-Jinshajiang fault belt, southwest China: Chemical Geology, v.203, 305-317.

Irvine, T.N., and Baragar, W.R.A. (1971). A guide to the chemical classification of the common volcanic rocks: Canadian Journal of Earth Sciences, v.8, 523-548.

Jackson, S., Pearson, N.J., Griffin, W.L., Belousova, E.A., (2004). The application of laser ablation – inductively coupled plasma – mass spectrometry to in situ U–Pb zircon geochronology. Chemical Geology 211, 47-69.

Janoušek, V., Gerdes, A., Vrána, S., Finger, F., Erban, V., Friedl, G., Braithwaite, C. J. R. (2006). Low-pressure granulites of the Lišov Massif, Southern Bohemia: Viséan Metamorphism of Late Devonian Plutonic Arc Rocks. Journal of Petrology 47, 705–744.

Jugo, P. J. (1997). Experimental study of the behavior of Copper and Gold in the system: Haplogranite-$CuFeS_2$-FeS-Au-H_2O-HCl-O_2-S_2 at 850^oC and 100 MPa. MS Thesis, University of Maryland, College Park.

Kinnaird J.A. (1981). Geology of the Nigerian anorogenic ring complexes. Geological map, scale 1:500,000, St. Andrews University Younger Granite Research Group.

Košler, J., Fonneland, H., Sylvester, P., Tubrett, M., Pedersen, R. B. (2002). U–Pb dating of detrital zircons for sediment provenance studies—a comparison of laser ablation ICPMS and SIMS techniques. Chemical Geology 182, 605–618.

Krogh T. E. (1973). A low-contamination method for hydrothermal decomposition of zircon and extraction of U and Pb for isotope age determinations. *Geochim. Cosmochim. Acta.* 37, 485-494.

Krogh T. E. (1982). Improved accuracy of U-Pb zircon ages using an air abrasion technique. *Geochim. Cosmochim. Acta.* 46, 637-649.

Kuno, H. (1968). Differentiation of basalt magmas, in Basalts: The Poldervaart Treatise on Rocks of Basaltic Composition, vol. 2, edited by H. H. Hess and A. Poldervaart, 623–688, Wiley-Interscience, Hoboken, N. J.

Lang, J.R., Baker, T., Hart, C., and Mortensen, J.K., (2000). An exploration model for intrusion-related gold systems: Society of Economic Geologists Newsletter, No. 40 (1), 6-14.

Large, R. R., Ranyushevsky, L., Hollit, C., Maslennikov, V., Meffre, S., Gilbert, S., Bull, S., Scott, R., Emsbo, P., Thomas, H., Singh, B., and Foster, J. (2009). Gold and trace element zonation in pyrite using a laser imaging technique: Implications for the timing of gold in orogenic and Carlin-style sediment-hosted deposits: Economic Geology and the Bulletin of the Society of Economic Geologists, V. 104, 635-668.

Le Bas, M. J., R. W. Le Maitre, A. Streckeisen, and B. Zanettin (1986). A chemical classification of volcanic rocks based on the total alkali-silica diagram, J. Petrol., 27, 745–750.

Lee J. K., Williams I. S., and Ellis D. J. (1997). Pb, U and Th diffusion in natural zircon. *Nature.* 390, 159-162.

Leeman W. P., MacRae, C. M., Wilson, N. C., Torpy, A., Lee, C. A., Student, J. J., Thomas, J. B., Vicenzi, E. (2012). A Study of Cathodoluminiscence and Trace Element Compositional Zoning in Natural Quartz from Volcanic Rocks: Mapping Titanium Content in Quartz. Microscopy and Microanalysis 18, 1322-1341.

Liu, W., Etschmann, B., Testemale, D., Hazemann, J., Rempel, K., Müller, H. and Brugger, J., (2014). Gold transport in hydrothermal fluids: Competition among the Cl−, Br−, HS− and NH_3(aq) ligands: Chemical Geology, v. 376, 11–19.

Ludwig, K.R. (2003). User's Manual for Isoplot 3.0: a geochronological toolkit for Microsoft Excel. Berkeley Geochronology Center, Special publication, 4, 1–71.

McCurry, P. (1976). The Geology of the Precambrian to Lower Paleozoic Rocks of Northern Nigeria. A Review. In Kogbe, C.A., Ed., Geology of Nigeria, Elizabeth Pub. Co., Ibadan, Nigeria, 15-38.

Mehnert, K.R., (1968). Migmatites and the origin of granitic rocks: Elsevier scientific publishing co., Amsterdam, 405p.

Meschede, M. (1986). A method of discriminating between different type of mid-ocean ridge basalts and continental tholeiites with the Nb-Zr-Y diagram, Chem. Geol., 56, 207–218.

Mezger, K. and Krogstad E. J. (1997). Interpretation of discordant U-Pb zircon ages: An evaluation. J. Metamorphic Geol. 15, 127-140.

Middlemost, E. A. K. (1975). The basalt clan, Earth Sci. Rev., 11, 337–364.

Mikhlin, Y. L., and Romanchenko, A. S. (2007). Gold deposition on pyrite and the common sulfide minerals: An STM/STS and SR-XPS study of surface reactions and Au nanoparticles: Geochimica et Cosmochimica Acta, v. 71, 5985–6001.

Morey, A. A., Tomkins A. G., Bierlein, F. P., Weinberg, R. F. Davidson, G. J. (2008). Bimodal distribution of gold in pyrite and arsenopyrite. Examples from the Archean Boorara and Bardoc shear systems, Yilgarn craton, Western Australia. Econ. Geol., 103, 599-614.

Müller, A., René, M., Behr, H. J., Kronz, A. (2003a). Trace elements and cathodoluminescence of igneous quartz in topaz granites from the Hub Stock. Mineral. Petrol. 79, 167-191.

Obaje, N.G. (2009). Geology and mineral resources of Nigeria. Springer Dordrect Heldelberg London New York, 221p. http://dx.doi.org/10.1007/978-3-540-92685-6.

Obiora, S. C. (2005). Mineralogical Compositions and Metamorphic Intensities of Contact Aureoles of Igneous Intrusives from the Lower Benue Rift. Africa Geoscience Review, v. 12, Nos. 1 and 2. 37-48.

Odeyemi, I., (1981). A review of the orogenic events in the Precambrian basement of Nigeria, West Africa. Geologische Rundschau, 70: 897-909.

Ofoegbu, C.O. (1985). "A Review of the Geology of the Benue Trough of Nigeria". J. Afri. Earth Sci. 3: 283-291.

Okonkwo C. T. (2001). Structural Evolution *of* Bode Saadu Area*,* Southwestern Nigeria*.* Science *and Engineering Series Vol. 2, (2), 17-24.*

Okonkwo C.T. (1992). Structural geology of basement rocks of Jebba area, Nigeria. Journal of Mining and Geology, 35 (1), 9-21.

Oluyide, P.O., Nwajide, C.S. and Oni, A.O. (1998). The Geology of Ilorin Area: Explanation of the 1:250,000 series, sheet 50 (Ilorin). Geological Survey of Nigeria bulletin 42, 1-84.

Oyawoye, M.O. (1965). Bauchite: a new variety in the quartz monzonite series. Nature, 205, 689p.

Oyawoye M.O (1972). The basement complex of Nigeria. In: Dessauvagie TFJ, Whiteman AJ (eds) African geology. Ibadan University Press, 66-102.

Oyinloye A. O. (2006b) Metalogenesis of the lode gold deposit in Ilesha area of southwestern Nigeria: inferences from lead isotope systematics. Pakistan Journal of Scientific & Industrial Research 9 (1) 1-11.

Oyinloye A. O. (1992). Application of kaolinitic clays in industrial Clay Technology, TERRA, Jour. Env. Concern (1), (1). 68-72.

Oyinloye, A. O. (1998). Geology, Geochemistry and origin of granite gneisses in the basement complex of the Ilesha area Southwest Nigeria. Journal of African Earth Sciences, 26(4), 633-641.

Oyinloye, O. A. (2011). Geology and Geotectonic Setting of the Basement Complex Rocks in Southwestern Nigeria: Implications on Provenance and Evolution, Earth and Environmental Sciences, http://www.intechopen.com/books/earthand-environmental-sciences.

Pearce, Julian A., Nigel B.W. Harris, and Andrew G. Tindle (1984). Trace element discrimination diagrams for the tectonic interpretation of granitic rocks. Journal of petrology 25 (4): 956-983.

Pearce, J. A. (1982). Trace element characteristics of lavas from destructive plate boundaries, in Andesites: Orogenic Andesites and Related Rocks, edited by R. S. Thorpe, 525–548, John Wiley, Hoboken, N. J.

Pearce, J. A., and J. R. Cann (1973). Tectonic setting of basic volcanic rocks determined using trace element analyses, Earth Planet. Sci. Lett., 19, 290-300.

Peccerillo, A., and S. R. Taylor (1976). Geochemistry of Eocene calc-alkaline rocks from Kastamonu area, Northern Turkey, Contrib. Mineral. Petrol., 58, 63–81.

Pokrovski, G. S., Akinfiev, N. N., Borisova, A. Y., Zotov, A. V., and Kouzmanov, K. (2014). Gold speciation and transport in geological fluids: Insights from experiments and physical-chemical modelling: Geological Society, London, Special Publications, v. 402, 9-70.

Rahaman, M.A (1976). “Review of the Basement Geology of SouthWestern Nigeria”. In: C.A. Kogbe (editor). *Geology of Nigeria*. Elizabethan Publ. Co.: Lagos, Nigeria, 41-58.

Rahaman M.A. (1988). Recent advances in the study of the basement complex of Nigeria Symposium on the Geology of Nigeria, Obafemi Awolowo University, Nigeria.

Rahaman, M.A. and *Ocan*, O. (*1978*). On Relationship in the Precambrian Migmatite-Gneiss of Nigeria. Journal of Mining and Geology, 15, 23-30.

Rahaman, M. A., Emofureta, W. O. and Cean Vacheta, M. (1983). The Potassic of the granites of the Igbetti area: Further Evidence of the Polycyclic Evolution of the pan-Africa Belt in Southwestern Nigeria, Proc. Res. 22, 25-92.

Rahaman MA (2006). Nigeria’s solid minerals endowment and sustainable development. In O. Oshin (Ed), The Basement Complex of Nigeria and its mineral resources: A tribute to Prof. M.A.O. Rahaman, 190p.

Robert, F., Brommecker, R., Bourne, B. T., Dobak, P. J., McEwan, C. J. Rowe, R. R., and Zhou, X. (2007). Models and Exploration Methods for Major Gold Deposit Types. In "Proceedings of Exploration 07: Fifth Decennial International Conference on Mineral Exploration" edited by B. Milkereit, 691-711.

Rollinson H. R. (1993). Using Geochemical Data: Evaluation, Presentation, and Interpretation. Longman Group UK Limited, 1st Ed. 380p.

Rosenblum, S. (1958). Magnetic susceptibilities of minerals in the Frantz Isodynamic magnetic separator. American Mineralogist 47, 170-173.

Rusk, B.G., (2012). Cathodoluminescence and trace elements in hydrothermal quartz. In: Götze, J., Möckel, R. (Eds.), Quartz: Deposits, Mineralogy and Analytics. Springer, Berlin, 307-329.

Russ*, W. (*1957*). The geology* of parts of Niger, Zaria and Sokoto Provinces, with special reference to the occurrence of gold. Bull. 27, Geol. Surv. Nigeria, 42p.

Schwartz, G.M., (1944). The host minerals of native gold: Economic Geology, v. 39, 371-411.

Seward, T.M., (1973). Thio complexes of gold and the transport of gold in hydrothermal ore solutions: Geochimica et Cosmochimica Acta, v. 37, 379-399.

Siddaiah N.S. and Rajamani V. (1989). The Geologic Setting, Mineralogy, Geochemistry, and Genesis of Gold Deposits of the Archean Kolar Schist Belt, India. Economic Geology vol. 84, 2155-2172.

Stern C. R, Futa K. and Muehlenbachs K. (1984). Isotope and trace element data for orogenic andesites from the austral Andes. In: Harmon RS, Barreiro BA (eds) Andean magmatism; chemical and isotopic constraints. Shiva Pub., UK, 31-46.

Spry, Alan (1969). Metamorphic Textures. Oxford*;* New York: Pergamon Press. vol. 8, 350p.

Streckeisen, A., and R. W. Le Maitre (1979). A chemical approximation to the modal QAPF classification of igneous rocks, Neues Jahrb. Mineral. Abh., 136, 169–206.

Thompson, J.F.H. and Newberry, R.J. (2000). Gold deposits related to reduced granitic intrusions. In Society of Economic Geologists Reviews in Economic Geology 13, 377-400.

Turner, D.C. (1983). Upper Proterozoic schist belts in the Nigerian sector of the Pan-African Province of. West Africa. Prec. Res. 21, 5-79.

Whiteman, A. (1982*)*. Nigeria: its Petroleum Geology, Resources and Potential. Published by Springer Netherlands, vol. 8. 394p.

Wiedenbeck, M., Alle, P., Corfu, F., Griffin, W.L., Meier, M., Oberli, F., Vonquadt, A., Roddick, J.C. and Speigel, W. (1995). Three natural zircon standards for U-Th-Pb, Lu-Hf, trace element and REE analyses. Geostandards Newsletter 19, 1-23.

Williams-Jones, A. E., Bowell, R. J., and Migdisov, A. A. (2009). Gold in solution: Elements, v. 5, 281-287.

Winkler, H. G. F. *(*1979*)*. Petrogenesis of metamorphic rocks*.* Springer*,* Heidelberg*,* 348p.

Woakes, M. and Bafor, B.E. (1984). Primary gold mineralization in Nigeria. Foster (Ed.), In gold '82: The geology, geochemistry and genesis of gold deposits, Geology Soc. Zambia Spec. Pub. (1984), 666-671.

Woakes, *M* and Bafor*, B.E. (1982*): Primary Gold Mineralization in Nigeria. In Gold 82: Geochemical Exploration 1982. J. Geochem. Explor., 19: 243-254.

Woakes M, Ajibade C.A, Rahaman M.A (1987). Some metallogenic features of the Nigerian Basement. J. Afr. Sci. 5, 655-664.

Wood, D. A., J. Tarney, J. Varet, A. D. Saunders, Y. Bougault, J. L. Joron, M. Treuil, and J. R. Cann (1979b), Geochemistry of basalts drilled in the North Atlantic by IPOD Leg 49: Implications for mantle heterogeneity, Earth Planet. Sci. Lett., 42, 77–97.

Wu, Y. B. and Zheng, Y. F. (2004). Genesis of zircon and its constraints on interpretation of U-Pb age: Chinese Science Bulletin, v. 49, 1554-1569.

Zeh, A., Gerdes, A., Klemd, R., Barton Jr., J.M., (2007). Archean to Proterozoic crustal evolution in the Central Zone of the Limpopo Belt (South Africa/Botswana): constraints from combined U–Pb and Lu–Hf isotope analyses of zircon. Journal of Petrology 48, 1605–1639.

Zhong, R. C., Brugger, J., Chen, Y. J., and Li, W. B. (2015a). Contrasting regimes of Cu, Zn and Pb transport in ore-forming hydrothermal fluids: Chemical Geology, v. 395, 154–164.

Zhou, H., Sun, X., Cook, N. J, Lin H., Fu, Y., Zhong, R. and Brugger, J. (2017a). Nano- to micron-scale particulate gold hosted by magnetite: A product of gold scavenging by bismuth melts. Economic Geology, vol. 112, 993-1010.

Zhou, H., Sun, X., Wu, Z., Liao, J., Fu, Y., Li, D., Hollings, P., Liu, Y., Lin, H., and Lin, Z. (2017b). Hematite U-Pb geochronometer: insights from monazite and hematite integrated chronology of the yaoan gold deposit, southwest china. Economic Geology, vol. 112, 2023-2039.

Appendix 1a: Geochemical data of some rock samples (Samples 3 – 55)																					
ID	AJ3	AJ16	AJ20	AJ34	AJ35	AJ36	AJ39B	AJ39C	AJ40	AJ40B	AJ42A	AJ43B	AJ44a	AJ44	AJ46	AJ46B	AJ50	AJ51	AJ52	AJ53	AJ55
SiO2	73.40	96.83	82.69	72.47	73.11	71.41	96.10	98.16	71.13	58.64	63.98	64.48	72.37	70.99	72.40	66.58	71.57	72.41	58.14	73.03	72.48
Al2O3	14.21	0.93	4.80	13.82	13.01	15.05	0.43	0.17	14.64	12.48	15.79	15.74	14.93	15.08	15.02	14.77	14.27	14.51	12.31	13.93	14.27
Fe2O3	1.72	1.20	5.60	2.33	2.24	2.32	1.19	1.31	2.67	5.00	6.52	6.59	2.28	3.06	1.38	5.61	2.79	2.09	5.72	2.07	2.06
MnO	0.03	0.01	0.06	0.03	0.04	0.03	0.01	0.02	0.04	0.24	0.14	0.12	0.03	0.04	0.03	0.11	0.04	0.03	0.27	0.04	0.03
MgO	0.32	0.02	1.61	0.31	0.28	0.52	0.02	0.02	0.46	2.10	1.10	1.00	0.47	0.50	0.52	2.02	0.45	0.29	2.08	0.26	0.27
CaO	0.73	0.03	2.17	0.83	0.90	1.42	0.05	0.05	1.35	18.36	2.54	2.58	1.16	1.23	1.50	2.68	1.36	1.55	17.98	1.61	1.56
Na2O	2.82	0.00	1.15	3.25	3.80	3.51	0.03	0.01	3.40	0.26	3.67	3.83	2.81	3.11	4.11	4.54	3.34	3.72	0.29	3.60	3.53
K2O	5.97	0.56	0.98	5.51	6.02	5.10	0.12	0.03	5.24	0.04	4.25	4.66	5.29	5.60	4.24	2.30	5.62	4.43	0.03	4.72	4.94
TiO2	0.32	0.06	0.38	0.21	0.18	0.31	0.03	0.01	0.32	0.53	0.93	0.88	0.23	0.31	0.25	0.69	0.30	0.15	0.55	0.17	0.16
P2O5	0.08	0.01	0.05	0.07	0.06	0.09	0.02	0.01	0.10	0.12	0.29	0.28	0.09	0.10	0.06	0.28	0.11	0.06	0.14	0.05	0.06
Cr2O3	0.01	0.01	0.01	0.01	0.01	0.01	0.01	0.01	0.01	0.02	0.02	0.01	0.02	0.02	0.01	0.02	0.01	0.01	0.02	0.01	0.01
NiO	0.00	0.00	0.01	0.00	0.00	0.00	0.00	0.01	0.00	0.00	0.02	0.00	0.00	0.00	0.00	0.00	0.00	0.00	0.01	0.00	0.00
LOI	0.40	0.17	0.23	0.36	0.34	0.21	-0.10	-0.20	0.50	1.89	0.71	0.36	0.28	0.51	0.49	0.25	0.12	0.68	1.99	0.53	0.67
Total	100.01	99.83	99.74	99.20	99.99	99.98	97.91	99.61	99.86	99.68	99.96	100.53	99.96	100.55	100.01	99.85	99.98	99.93	99.53	100.02	100.04
Ba	20.80	115.83	181.00	610.08	78.60	18.50	22.93	58.50	654.21	49.79	165.40	1053.32	102.60	932.85	75.20	142.97	87.90	21.00	361.10	43.60	495.08
Be	<0.1	0.40	0.30	0.50	0.30	0.30	0.30	0.20	0.20	0.80	0.40	0.50	0.20	0.20	0.20	0.60	0.70	<0.1	1.00	<0.1	0.10
Co	0.60	0.49	18.90	2.14	2.70	1.00	0.75	1.90	3.41	13.94	13.40	8.67	3.70	2.64	8.00	13.12	4.60	0.70	5.30	2.20	1.88
Cs	0.13	0.05	13.19	3.14	2.11	0.57	0.41	1.22	5.53	1.03	3.99	5.87	2.20	2.33	6.84	11.66	4.14	1.67	0.19	3.92	9.91
Ga	0.60	1.30	8.60	17.83	4.00	1.60	0.84	2.00	21.78	16.33	7.70	27.12	4.80	16.61	6.60	24.35	5.40	1.80	7.40	4.00	21.32
Hf	0.10	0.31	0.29	5.90	0.34	0.09	2.90	0.26	8.53	1.58	0.16	6.56	0.05	7.08	0.27	4.21	0.29	0.32	0.04	0.34	3.69
Nb	0.35	1.14	0.11	12.78	0.88	1.53	0.69	0.10	17.65	11.42	0.43	45.78	0.50	15.72	0.84	34.28	0.89	0.56	0.18	2.03	12.51
Rb	3.70	12.10	104.30	180.27	42.90	9.00	5.57	15.70	165.31	2.41	105.10	228.65	67.10	146.36	123.00	210.21	88.60	25.70	0.50	72.30	179.34
Sn	0.30	0.47	2.60	1.85	2.00	1.00	0.44	0.70	2.30	1.40	2.10	1.34	3.20	2.80	3.30	0.80	3.00	1.50	0.90	3.40	3.04
Sr	2.80	21.70	9.00	126.55	15.70	5.60	3.36	8.00	112.14	110.20	12.20	241.42	5.80	181.60	5.50	164.05	12.20	4.10	161.00	7.00	103.33
Ta	<0.05	0.08	<0.05	0.58	<0.05	<0.05	0.06	<0.05	1.41	1.52	<0.05	4.39	<0.05	1.24	<0.05	3.39	<0.05	<0.05	<0.05	<0.05	1.15
Th	3.00	0.55	10.70	32.70	39.20	11.10	2.51	5.30	29.73	2.27	13.80	16.51	32.20	24.54	22.40	17.40	40.20	28.00	5.40	23.70	18.91
U	0.10	0.26	0.60	4.32	3.40	4.40	1.52	1.30	2.28	1.73	2.10	6.57	2.00	2.82	2.00	5.14	2.90	3.50	0.60	4.00	4.46
V	<2	7.75	66.00	10.18	9.00	3.00	2.10	2.00	17.36	44.79	45.00	17.44	14.00	16.80	22.00	54.55	16.00	<2	3.00	7.00	4.99
W	0.40	2.91	1.50	0.38	1.40	0.60	0.31	<0.1	0.26	21.13	0.10	0.48	0.10	0.33	0.40	0.33	0.60	0.30	0.50	0.40	0.37
Zr	3.00	10.78	11.20	238.04	12.30	2.20	91.06	6.40	363.78	58.56	3.60	334.21	3.00	288.74	9.60	157.14	9.00	8.60	1.20	10.10	142.85
Y	2.19	0.73	4.84	6.12	12.85	7.25	1.06	7.40	16.72	10.98	18.50	23.20	18.27	16.28	9.88	23.35	12.77	3.94	15.14	6.74	5.86
Mo	0.56	1.17	1.63	1.81	1.46	1.23	1.24	0.72	1.83	1.89	0.93	0.79	0.34	0.41	1.01	0.61	0.71	0.66	1.53	1.74	1.80
Cu	5.67	19.05	40.04	7.50	10.65	10.02	10.68	8.67	8.15	8.21	19.97	30.98	4.10	7.43	8.97	8.45	11.06	4.76	31.59	6.57	5.48
Pb	7.28	18.94	5.54	37.11	13.99	12.59	2.33	6.12	34.22	1.89	4.13	38.29	8.49	22.94	6.63	14.67	10.72	14.01	20.82	7.61	32.58
Zn	13.10	3.36	79.30	45.24	38.30	12.10	3.40	20.60	53.16	135.87	72.20	133.05	54.10	44.22	79.50	137.66	61.50	19.90	19.20	43.70	57.98

Appendix 1a: Geochemical data of some rock samples (Samples 3 – 55) – Continued																					
Sc	0.20	1.64	4.90	1.53	1.40	0.50	0.95	0.40	2.03	5.28	7.10	6.01	2.30	2.71	4.00	6.36	2.10	1.00	1.20	1.70	1.69
As	4.20	732.10	0.90	1.10	0.90	1.40	42.30	0.60	0.65	10.70	0.60	0.70	0.60	0.80	0.50	5.30	0.50	3.30	13.20	1.10	2.14
Cd	0.02	0.12	<0.01	0.02	0.03	<0.01	0.08	<0.01	0.10	0.26	0.02	0.03	<0.01	0.01	0.03	0.05	0.04	<0.01	0.15	<0.01	<0.01
Sb	1.20	2.31	0.07	0.08	0.09	0.09	1.70	0.10	0.05	0.13	0.04	0.03	0.03	0.05	0.07	0.06	0.07	0.06	0.15	0.06	0.04
Bi	0.04	1.72	0.05	0.09	0.10	0.06	2.11	0.40	0.08	1.11	0.05	0.09	0.04	0.05	0.05	0.03	0.04	0.05	0.07	0.22	0.31
Ag	8.00	51.00	16.00	31.00	28.00	21.00	76.00	13.00	112.00	56.00	18.00	89.00	8.00	31.00	24.00	141.00	23.00	17.00	60.00	21.00	17.00
Au	0.80	0.70	1.50	0.52	0.60	3.70	1.20	<0.2	51.10	17.00	1.20	2.90	0.70	0.90	1.00	0.50	0.70	7.60	24.10	1.60	2.30
Hg	<5	<5	<5	<5	<5	<5	23.00	11.00	5.00	<5	6.00	7.00	<5	<5	<5	<5	<5	10.00	<5	<5	<5
Tl	<0.02	0.08	0.51	0.21	0.24	0.05	0.05	0.08	0.04	<0.02	0.55	0.61	0.37	0.40	0.67	0.51	0.54	0.16	<0.02	0.45	0.37
Se	<0.1	0.23	<0.1	<0.1	<0.1	<0.1	0.10	<0.1	<0.1	<0.1	<0.1	0.10	<0.1	<0.1	<0.1	0.30	<0.1	<0.1	<0.1	<0.1	<0.1
B	<20	<20	<20	<20	<20	<20	<20	<20	<20	<20	<20	<20	<20	<20	<20	<20	<20	<20	<20	<20	<20
S	<0.02	0.30	<0.02	<0.02	<0.02	<0.02	0.50	<0.02	<0.02	<0.02	<0.02	<0.02	<0.02	<0.02	<0.02	<0.02	0.34	<0.02	0.02	<0.02	<0.02
Te	<0.02	0.02	<0.02	<0.02	<0.02	<0.02	0.02	<0.02	<0.02	0.03	<0.02	<0.02	<0.02	<0.02	<0.02	<0.02	<0.02	<0.02	0.04	<0.02	<0.02
Ge	<0.1	<0.1	0.10	<0.1	<0.1	<0.1	<0.1	<0.1	<0.1	0.10	0.20	0.30	<0.1	<0.1	0.20	<0.1	0.20	<0.1	<0.1	<0.1	<0.1
In	<0.02	0.02	0.03	<0.02	<0.02	<0.02	0.03	<0.02	<0.02	<0.02	0.05	<0.02	0.03	0.02	0.05	<0.02	<0.02	<0.02	<0.02	0.03	0.04
Re	<1	1.00	<1	<1	<1	<1	<1	<1	1.00	<1	<1	<1	<1	<1	<1	<1	1.00	<1	<1	<1	<1
Li	1.20	0.62	32.40	24.53	23.60	6.50	2.25	5.10	38.84	4.07	29.70	77.96	17.80	16.85	76.30	181.24	49.40	12.70	1.00	53.30	51.22
Pd	<10	<10	<10	<10	<10	<10	<10	<10	<10	<10	<10	<10	<10	<10	<10	<10	<10	<10	<10	<10	<10
Pt	<2	2.00	<2	<2	<2	<2	2.00	2.00	<2	<2	3.00	2.00	<2	<2	<2	<2	<2	<2	<2	<2	<2
La	7.20	1.34	26.30	70.23	102.70	20.30	4.70	30.00	91.88	16.66	47.00	54.87	88.50	51.97	49.70	24.61	104.10	20.90	26.00	42.50	28.84
Ce	11.90	2.40	48.60	137.32	159.80	35.20	9.64	26.80	182.55	45.81	81.80	105.48	189.50	114.90	87.20	60.04	172.60	36.30	35.70	75.30	66.36
Pr	4.17	0.26	6.77	12.00	13.31	8.58	1.00	0.13	18.30	3.97	17.80	9.79	8.78	11.38	6.56	5.87	7.98	5.91	4.19	6.01	6.17
Nd	13.25	0.93	23.90	36.73	37.54	25.90	3.64	0.37	59.45	14.58	61.00	34.07	25.90	37.22	23.62	22.51	24.50	20.09	12.84	22.30	21.10
Sm	2.38	0.16	5.72	4.63	5.90	5.10	0.62	0.16	8.14	2.72	8.30	5.43	4.42	5.57	4.22	4.89	4.30	3.26	2.19	3.91	3.57
Eu	0.40	0.08	0.86	0.83	1.27	0.79	0.07	0.08	1.12	0.56	2.16	2.62	0.98	1.18	0.52	1.01	0.75	0.42	0.61	0.83	0.66
Gd	1.31	0.17	6.03	4.82	4.13	3.37	0.59	0.17	7.99	2.72	5.15	5.73	3.74	5.57	3.29	5.12	3.43	4.08	2.14	3.42	3.31
Tb	0.23	0.02	1.53	0.41	0.68	0.68	0.07	0.03	0.81	0.37	0.58	0.68	0.58	0.62	0.29	0.76	0.58	0.29	0.32	0.37	0.35
Dy	1.16	0.13	7.69	1.44	4.09	3.14	0.27	0.34	3.35	1.92	2.67	3.40	2.85	2.92	2.07	4.04	3.57	1.34	1.73	1.70	1.40
Ho	0.15	0.03	1.64	0.25	0.60	0.63	0.04	0.04	0.60	0.38	0.37	0.68	0.64	0.56	0.34	0.75	0.54	0.21	0.32	0.37	0.23
Er	0.54	0.10	4.89	0.82	1.72	1.73	0.13	0.21	1.93	1.16	1.19	2.22	1.93	1.81	0.57	2.15	1.93	0.72	1.10	0.71	0.65
Tm	0.06	0.02	0.76	0.10	0.26	0.22	0.02	0.03	0.25	0.16	0.11	0.33	0.32	0.25	0.09	0.28	0.31	0.08	0.18	0.03	0.07
Yb	0.29	0.11	4.42	0.67	1.31	1.61	0.14	0.23	1.70	1.16	1.03	2.51	1.71	1.75	0.35	1.83	1.52	0.38	1.14	0.57	0.50
Lu	0.05	0.02	0.69	0.11	0.28	0.25	0.03	0.02	0.25	0.17	0.12	0.38	0.27	0.26	0.05	0.25	0.24	0.06	0.19	0.06	0.07

Appendix 1b: Geochemical data of some rock samples (Samples 57 - 85)																					
ID	AJ57	AJ60	AJ61	AJ62	AJ64	AJ66	AJ67	AJ77	AJ78	AJ79	AJ80	AJ80A	AJ80A1	AJ80B	AJ80C	AJ80D	AJ80E	AJ80F	AJ81	AJ82	AJ85
SiO2	66.51	72.58	75.53	87.16	97.78	98.20	73.66	96.26	96.52	61.75	96.09	94.79	55.30	59.73	75.70	96.47	97.17	60.53	95.20	72.11	69.64
Al2O3	14.98	14.67	12.12	6.80	0.16	0.19	14.06	0.77	0.89	0.58	0.75	1.02	2.22	1.63	14.00	0.96	0.72	0.95	1.15	14.61	14.92
Fe2O3	5.75	1.87	2.68	0.99	1.63	0.89	1.88	1.46	1.41	3.94	1.33	1.52	12.23	4.20	0.75	2.05	0.94	4.14	1.37	1.73	3.09
MnO	0.09	0.04	0.03	0.01	0.02	0.01	0.03	0.01	0.01	0.05	0.01	0.01	0.42	0.07	0.01	0.02	0.01	0.06	0.01	0.04	0.04
MgO	1.29	0.43	0.91	0.08	0.01	0.01	0.39	0.04	0.03	29.01	0.05	0.04	21.11	27.57	0.12	0.03	0.03	28.39	0.07	0.47	0.98
CaO	2.13	1.53	1.67	0.60	0.05	0.03	1.61	0.04	0.04	0.21	0.05	0.04	2.05	0.17	0.28	0.05	0.03	0.44	0.03	1.56	1.92
Na2O	3.71	3.99	3.35	2.01	-0.01	-0.01	3.93	0.02	0.02	0.05	0.03	0.03	0.10	0.07	4.22	0.02	0.00	0.07	0.02	3.86	3.58
K2O	4.35	4.01	1.92	1.51	0.03	0.05	3.95	0.27	0.31	0.03	0.24	0.29	0.10	0.07	3.95	0.31	0.22	0.07	0.37	4.11	5.16
TiO2	0.73	0.23	0.33	0.03	0.01	0.01	0.24	0.05	0.04	0.01	0.06	0.04	0.05	0.04	0.03	0.05	0.02	0.03	0.05	0.23	0.51
P2O5	0.19	0.07	0.12	0.03	0.01	0.01	0.07	0.02	0.02	0.01	0.02	0.02	0.02	0.01	0.02	0.03	0.01	0.01	0.02	0.06	0.15
Cr2O3	0.01	0.01	0.00	0.01	0.01	0.01	0.01	0.01	0.01	0.18	0.02	0.01	0.31	0.27	0.01	0.01	0.01	0.26	0.01	0.01	0.02
NiO	0.01	0.00	0.01	0.00	0.00	0.00	0.00	0.00	0.00	0.14	0.00	0.01	0.06	0.14	0.00	0.00	0.00	0.14	0.00	0.00	0.00
LOI	0.22	0.41	0.98	0.13	-0.23	-0.08	0.12	0.26	0.93	4.70	0.98	1.71	6.40	5.89	0.77	0.38	0.23	5.22	0.42	1.19	0.51
Total	99.97	99.84	99.65	100.36	99.47	99.32	99.95	99.21	100.23	100.66	99.63	99.53	100.37	99.86	99.86	100.38	99.40	100.29	98.73	99.98	100.53
Ba	197.70	584.08	255.60	398.24	6.16	18.25	43.00	149.93	18.50	3.40	69.9	174.7	118.5	36.15	168.71	69.40	33.24	25.16	54.63	55.50	706.68
Be	0.60	0.10	0.20	0.10	0.10	0.10	0.10	0.10	<0.1	0.30	<0.1	0.60	0.40	0.30	0.50	0.20	0.30	0.30	0.40	<0.1	0.10
Co	15.10	2.23	15.00	0.84	1.09	0.52	2.60	1.52	1.90	29.18	0.90	30.5	57.21	34.24	0.68	17.70	0.42	30.71	0.63	2.10	5.62
Cs	4.21	3.17	10.66	0.64	0.03	0.06	2.96	0.06	<0.02	0.11	0.03	0.91	0.86	0.16	0.32	0.35	0.03	0.21	0.05	0.10	3.47
Ga	9.40	22.47	12.50	6.26	0.29	0.30	4.40	1.14	0.40	0.82	0.90	3.90	3.79	2.14	19.39	2.30	0.97	1.34	1.77	1.60	18.93
Hf	0.11	3.24	0.09	3.05	0.01	0.04	0.12	0.25	<0.02	0.16	0.05	0.07	0.20	0.03	1.31	0.05	0.24	0.03	0.38	0.07	7.37
Nb	0.20	6.08	0.43	0.77	4.09	0.07	0.37	0.63	0.03	1.28	0.03	0.02	1.64	1.68	25.47	0.02	0.43	1.11	0.86	0.08	20.86
Rb	130.80	132.97	194.30	26.78	0.90	2.05	61.70	8.01	0.50	1.61	3.70	8.10	7.89	3.08	86.99	5.60	5.34	3.51	9.97	20.60	157.95
Sn	1.10	3.18	2.10	3.11	0.83	1.13	1.20	0.56	0.50	1.81	0.60	3.30	1.97	1.83	2.82	2.60	1.71	1.98	2.14	0.50	2.94
Sr	18.70	237.05	10.80	109.97	1.23	1.72	2.90	14.72	3.70	1.83	41.60	12.8	11.74	7.44	62.99	12.60	4.97	4.80	16.95	10.00	331.21
Ta	<0.05	0.64	<0.05	0.10	2.72	0.04	<0.05	0.06	<0.05	0.12	<0.05	<0.05	0.19	1.23	1.75	<0.05	0.04	0.10	0.07	<0.05	1.72
Th	25.40	21.69	9.40	0.47	0.03	0.16	8.90	0.34	0.20	0.17	0.50	0.70	0.42	0.40	6.42	3.10	0.28	0.75	0.45	0.60	15.53
U	2.10	3.05	3.00	0.75	0.01	0.03	1.10	0.17	0.10	0.08	0.50	0.50	0.53	0.20	0.94	0.50	0.18	0.19	0.30	<0.1	5.39
V	59.00	17.77	80.00	2.47	1.94	2.00	14.00	5.48	<2	5.47	3.00	27	40.68	15.41	1.41	8.00	5.56	8.57	8.74	10.00	36.51
W	0.40	0.10	0.80	0.34	0.38	0.13	0.20	3.25	1.20	0.12	0.40	0.30	0.71	1.54	1.46	0.20	1.64	0.12	3.30	0.30	0.39
Zr	3.20	122.92	4.20	108.12	0.45	1.50	2.60	8.68	0.20	5.05	1.30	1.90	5.54	1.02	29.07	1.10	8.07	0.89	13.43	2.70	294.21
Y	7.14	6.40	14.62	2.35	0.11	0.15	3.65	0.63	0.19	0.64	0.57	2.90	2.73	1.69	4.12	1.22	0.55	1.11	0.72	2.78	12.98
Mo	0.83	0.44	1.23	0.40	0.93	1.04	0.38	1.25	1.10	1.83	1.27	0.26	2.10	1.96	0.10	0.05	0.09	1.88	0.12	0.73	1.76
Cu	29.39	5.74	24.16	9.31	16.63	7.91	3.90	13.01	394.60	4.03	23.85	16.17	25.65	42.34	7.48	6.63	24.38	5.08	40.55	8.26	59.78
Pb	5.58	29.34	3.05	16.23	0.72	2.77	2.07	7.80	3190.2	1.11	693.22	3.75	1.99	0.79	25.20	2.00	481.58	1.95	1736.24	3.30	31.44
Zn	95.20	47.04	141.70	5.06	2.29	2.16	45.40	3.27	4589.3	70.93	16.00	68.7	190.03	245.82	6.98	39.90	11.55	135.07	25.52	11.80	41.02

Appendix 1b: Geochemical data of some rock samples (Samples 57 - 85) – Continued																					
Sc	3.50	2.48	13.60	1.20	0.69	0.59	1.80	1.30	0.10	2.03	0.40	12.7	16.59	2.20	3.25	7.10	1.06	2.06	1.29	0.70	3.59
As	0.70	0.30	3.10	0.91	0.40	0.20	0.20	1131.2	1622.6	527.3	383.8	144.9	8.30	12.20	30.50	27.20	73.10	9.30	11.70	0.50	3.20
ID	AJ57	AJ60	AJ61	AJ62	AJ64	AJ66	AJ67	AJ77	AJ78	AJ79	AJ80	AJ80A	AJ80A1	AJ80B	AJ80C	AJ80D	AJ80E	AJ80F	AJ81	AJ82	AJ85
ID	AJ57	AJ60	AJ61	AJ62	AJ64	AJ66	AJ67	AJ77	AJ78	AJ79	AJ80	AJ80A	AJ80A1	AJ80B	AJ80C	AJ80D	AJ80E	AJ80F	AJ81	AJ82	AJ85
Cd	<0.01	0.02	0.01	<0.01	<0.01	<0.01	<0.01	0.17	26.68	0.24	0.11	0.31	0.19	0.20	0.03	0.05	0.02	0.23	0.05	<0.01	<0.01
Sb	0.04	0.02	0.06	0.04	0.11	0.09	0.03	2.63	6.85	0.05	1.90	0.29	0.07	0.05	0.03	0.04	0.16	0.06	0.09	0.07	0.05
Bi	0.04	0.09	0.09	0.03	0.40	0.50	0.07	1.50	1.63	0.30	3.70	0.05	0.20	0.30	0.06	0.04	0.05	0.40	0.30	<0.02	0.40
Ag	30.00	5.00	31.00	8.00	15.00	21.00	7.00	2116	8662	1827	543	50	762	293.00	51.00	22.00	19.00	9.00	27.00	8.00	16.00
Au	2.00	0.90	0.70	0.50	<0.2	<0.2	0.80	961	3723	662.0	1179.6	8.30	113	217.0	82.00	62.70	122.00	91.00	27.00	0.70	4.60
Hg	5.00	<5	7.00	5.00	9.00	6.00	<5	328.00	863.00	<5	64.00	12.00	<5	<5	21.00	13.00	10.00	<5	6.00	8.00	<5
Tl	0.69	0.31	0.98	0.06	0.09	0.11	0.35	0.10	0.09	0.50	0.02	0.14	0.38	0.33	0.12	0.08	0.06	0.15	0.07	0.10	0.29
Se	<0.1	0.10	<0.1	<0.1	<0.1	<0.1	<0.1	0.30	0.60	0.10	0.20	<0.1	0.10	0.08	0.50	<0.1	0.30	<0.1	0.70	<0.1	0.10
B	<20	<20	<20	<20	<20	<20	<20	<20	<20	<20	<20	<20	<20	<20	<20	<20	<20	<20	<20	<20	<20
S	<0.02	<0.02	<0.02	<0.02	<0.02	<0.02	<0.02	0.47	0.68	<0.02	0.20	<0.02	<0.02	<0.02	0.40	0.90	0.50	<0.02	0.30	<0.02	0.09
Te	<0.02	<0.02	<0.02	<0.02	<0.02	<0.02	<0.02	0.03	0.04	<0.02	0.08	0.03	<0.02	<0.02	0.03	0.02	0.04	<0.02	0.03	0.03	<0.02
Ge	0.20	<0.1	0.20	<0.1	<0.1	<0.1	<0.1	<0.1	<0.1	0.10	<0.1	<0.1	0.10	0.10	<0.1	<0.1	<0.1	0.10	<0.1	<0.1	<0.1
In	<0.02	<0.02	0.09	<0.02	<0.02	<0.02	<0.02	0.03	0.05	<0.02	0.02	0.06	<0.02	<0.02	0.05	0.03	0.02	<0.02	0.03	<0.02	<0.02
Re	<1	1.00	<1	<1	<1	<1	<1	1.00	1.00	<1	<1	<1	1.00	1.00	<1	<1	<1	<1	<1	<1	<1
Li	51.70	34.70	80.90	1.53	1.09	1.47	26.20	0.75	0.10	0.75	0.20	2.80	0.93	1.55	1.67	3.50	0.68	1.42	1.24	3.90	28.66
Pd	<10	<10	<10	<10	<10	<10	<10	<10	<10	<10	<10	<10	<10	<10	<10	<10	<10	<10	<10	<10	<10
Pt	<2	<2	<2	<2	<2	<2	<2	2.00	<2	<2	<2	8.00	<2	<2	3.00	2.00	3.00	<2	2.00	<2	<2
La	92.50	33.30	22.10	5.12	0.24	0.70	17.00	1.83	<0.5	2.06	3.60	6.70	4.12	6.07	7.22	2.50	2.40	2.42	2.75	6.30	38.44
Ce	150.60	65.18	54.20	5.31	0.35	1.00	29.40	2.73	0.90	2.64	5.70	11.10	8.80	12.41	18.83	5.80	3.24	4.96	4.87	9.80	82.70
Pr	14.43	7.06	0.81	0.90	0.03	0.11	4.96	0.26	0.17	0.46	0.22	0.34	0.92	1.06	2.01	0.52	0.39	0.52	0.70	5.86	8.09
Nd	51.70	24.46	2.71	3.23	0.12	0.40	20.76	0.89	0.56	1.67	0.68	0.75	3.52	3.84	7.88	1.43	1.25	2.03	2.70	25.13	27.19
Sm	11.40	4.12	0.53	0.59	0.02	0.07	4.37	0.16	0.06	0.30	0.17	0.19	0.78	0.58	2.00	0.21	0.20	0.44	0.41	3.17	4.13
Eu	1.56	0.75	0.25	0.79	0.01	0.02	0.61	0.08	0.05	0.11	0.06	0.05	0.24	0.15	0.24	0.07	0.05	0.07	0.10	0.75	1.00
Gd	8.31	3.80	0.57	0.60	0.03	0.07	3.47	0.16	0.15	0.28	0.26	0.19	0.83	0.65	1.58	0.45	0.20	0.44	0.36	3.91	4.09
Tb	1.44	0.42	0.11	0.08	0.00	0.01	0.31	0.02	0.01	0.04	0.02	0.01	0.13	0.07	0.20	0.07	0.02	0.06	0.04	0.17	0.49
Dy	6.98	1.62	0.79	0.40	0.02	0.04	2.13	0.12	0.10	0.17	0.22	0.35	0.67	0.29	0.90	0.12	0.13	0.27	0.19	2.13	2.32
Ho	1.29	0.24	0.21	0.08	0.00	0.01	0.41	0.03	0.01	0.03	0.01	0.05	0.12	0.05	0.16	0.05	0.03	0.04	0.03	0.31	0.44
Er	3.83	0.64	0.78	0.27	0.01	0.02	0.49	0.09	0.01	0.08	0.02	0.04	0.31	0.15	0.53	0.07	0.08	0.11	0.11	0.61	1.38
Tm	0.51	0.06	0.09	0.04	0.00	0.00	0.11	0.01	0.01	0.01	0.03	0.05	0.04	0.02	0.08	0.03	0.01	0.01	0.01	0.07	0.19
Yb	3.12	0.40	0.81	0.36	0.01	0.01	0.28	0.09	0.05	0.06	0.07	0.05	0.26	0.09	0.61	0.05	0.08	0.08	0.11	0.27	1.24
Lu	0.49	0.05	0.08	0.07	0.00	0.00	0.05	0.01	0.01	0.01	0.03	0.05	0.04	0.01	0.10	0.03	0.01	0.01	0.02	0.03	0.18

Appendix 2: U-Th-Pb Isotopic data for Alkali Granite																	
Zircon ID no.	207Pb /235U	% Error	206Pb /238U	% Error	Error Correl. (rho)	208Pb /232Th	% Error	207Pb /206Pb	% Error	207Pb/ 235U Age	% Error	206Pb/ 238U Age	% Error	208Pb/ 232Th Age	% Error	207Pb/ 206Pb Age	% Error
34_15_1	0.993	0.064	0.1157	0.0087	0.62571	0.0342	0.0034	0.0615	0.0021	696	27	706	19	679	67	637	76
34_9_2	0.2419	0.012	0.03494	0.0025	0.96758	0.0191	0.0065	0.0498	0.00035	220.3	5.1	221.3	4.4	390	130	184	17
34_29_1	0.744	0.028	0.09034	0.0065	0.98479	0.0187	0.0012	0.0596	0.00025	565.4	6.1	557.5	5.8	375	24	586.9	9.1
34_2_3	1.332	0.059	0.1436	0.010	0.70838	0.0433	0.0083	0.0671	0.0014	855	18	865	15	840	160	820	47
34_24_1	1.360	0.097	0.1402	0.014	0.86521	0.111	0.018	0.0694	0.002	852	36	843	35	2050	310	871	64
34_23_1	1.34	0.15	0.1336	0.013	0.97643	0.051	0.024	0.0681	0.0026	815	54	803	48	1050	380	814	76
34_39_1	0.692	0.017	0.0874	0.0040	0.84912	0.0234	0.0013	0.0569	0.00091	532.6	9.1	540.1	6.7	467	26	474	39
34_39_2	0.635	0.049	0.0792	0.0068	0.98192	0.0194	0.0014	0.0582	0.00073	496	21	491	19	389	29	532	27
34_41_2	1.493	0.11	0.1537	0.012	0.9007	0.0448	0.0024	0.0692	0.0019	910	33	920	29	891	46	870	60
34_50_1	1.165	0.068	0.1311	0.010	0.87259	0.0790	0.0091	0.0641	0.0013	777	22	793	20	1520	170	724	47
34_60_2	1.518	0.086	0.1626	0.012	0.67507	0.0583	0.0043	0.0674	0.0018	931	22	971	16	1140	81	818	59
34_53_2	1.223	0.062	0.1396	0.011	0.62242	0.0581	0.0041	0.0638	0.0015	810	16	842	11	1136	77	707	53
34_45_1	2.11	0.49	0.130	0.018	0.89893	0.0492	0.0060	0.106	0.012	988	97	774	76	960	120	1480	170
34_18_2	2.07	0.22	0.1925	0.017	0.8515	0.0608	0.0030	0.0758	0.0031	1105	46	1132	36	1190	57	1018	86
34_8_2	2.55	0.23	0.2264	0.020	0.73501	0.0685	0.0023	0.0807	0.0031	1265	37	1314	24	1337	43	1151	82
34_11_2	2.55	0.23	0.216	0.018	0.92182	0.0646	0.0068	0.0820	0.0031	1238	59	1254	54	1250	130	1195	81
34_21_1	3.41	0.29	0.2518	0.020	0.94524	0.0693	0.0021	0.0953	0.0033	1462	57	1441	51	1352	39	1494	72
34_21_2	3.05	0.26	0.2334	0.018	0.92827	0.0655	0.0018	0.0928	0.0030	1393	43	1350	32	1286	33	1461	63
34_26_2	3.27	0.25	0.2498	0.020	0.80279	0.0708	0.0022	0.0947	0.0033	1457	40	1436	27	1382	42	1507	62
34_14_2	3.09	0.21	0.2333	0.017	0.74601	0.0654	0.0017	0.0957	0.0022	1423	25	1351	18	1279	32	1527	44
34_32_1	2.66	0.20	0.2242	0.018	0.32996	0.0651	0.0019	0.0855	0.0027	1309	31	1303	18	1274	36	1316	59
34_32_2	2.02	0.18	0.1838	0.015	0.94065	0.0547	0.0024	0.0769	0.0026	1089	47	1084	40	1074	47	1070	70
34_56_1	3.13	0.29	0.230	0.020	0.94425	0.051	0.018	0.0931	0.0039	1366	73	1326	66	1140	270	1413	91
34_33_1	2.68	0.20	0.2203	0.017	0.77938	0.0588	0.0023	0.0887	0.0021	1314	27	1283	18	1154	44	1378	46
34_33_2	1.763	0.084	0.1699	0.013	0.71935	0.0426	0.0019	0.0756	0.0013	1027	18	1011	13	843	36	1080	34
34_12_2	3.57	0.26	0.272	0.022	0.66441	0.0899	0.0052	0.0952	0.0037	1522	43	1549	29	1734	95	1491	80
34_2_2	2.09	0.18	0.1917	0.015	0.89874	0.0586	0.0041	0.0768	0.0027	1110	47	1126	43	1145	79	1062	74
34_59_1	1.699	0.070	0.1614	0.011	0.77366	0.136	0.014	0.0766	0.0015	1004	21	964	16	2570	250	1117	36
34_4_2	1.98	0.12	0.1816	0.0085	0.75652	0.087	0.011	0.0789	0.0033	1098	40	1074	26	1650	200	1110	87
34_24_2	2.66	0.25	0.213	0.018	0.93979	0.0635	0.0048	0.0864	0.0033	1259	64	1236	60	1238	93	1285	79
34_61_1	2.87	0.23	0.2395	0.019	0.61706	0.0713	0.0011	0.0863	0.0029	1359	31	1384	16	1392	21	1318	66
34_61_2	2.55	0.23	0.210	0.018	0.91629	0.0582	0.0045	0.0844	0.0035	1237	62	1224	55	1138	87	1236	87

Appendix 2: U-Th-Pb Isotopic data for Alkali Granite - Continued																	
34_41_1	2.73	0.21	0.2147	0.016	0.94121	0.0556	0.0028	0.0907	0.0023	1316	36	1252	31	1092	55	1418	47
34_38_2	3.349	0.22	0.2390	0.019	0.73464	0.0651	0.0023	0.1013	0.0018	1487	19	1381	11	1280	42	1637	34
34_40_1	3.56	0.29	0.268	0.022	0.87646	0.0707	0.0044	0.0933	0.0032	1492	60	1520	59	1399	77	1465	70
34_3_1	3.54	0.29	0.2646	0.022	0.76724	0.1165	0.0082	0.0962	0.0041	1510	48	1511	29	2210	150	1466	98
34_37_2	2.32	0.18	0.1980	0.015	0.91106	0.0520	0.0033	0.0833	0.0025	1195	38	1162	31	1021	64	1240	60
34_X_1	2.15	0.39	0.1098	0.0094	0.88572	0.195	0.095	0.133	0.016	1050	110	668	40	3380	690	1720	200
34_38_1	2.928	0.19	0.2244	0.017	0.70158	0.0599	0.0028	0.0944	0.0019	1383	20	1304	14	1173	53	1501	39
34_13_1	4.32	0.24	0.3088	0.022	0.57209	0.0836	0.0024	0.1029	0.0019	1694	27	1734	22	1621	45	1683	34
34_13_2	4.24	0.21	0.3002	0.021	0.43506	0.0826	0.0022	0.1043	0.0019	1681	22	1692	18	1603	40	1696	33
34_12_1	4.76	0.26	0.3251	0.022	0.27336	0.0837	0.0020	0.1078	0.0023	1774	24	1814	21	1623	37	1748	37
34_10_1	3.74	0.21	0.2783	0.02	0.60303	0.0799	0.0025	0.0987	0.0017	1572	23	1585	23	1562	44	1593	33
34_10_2	4.409	0.21	0.3112	0.019	0.15292	0.0786	0.0011	0.1036	0.0011	1711	13	1749	11	1529	20	1690	18
34_19_1	3.95	0.25	0.2866	0.021	0.72627	0.0807	0.0013	0.1013	0.0021	1613	29	1623	23	1568	24	1638	38
34_19_2	4.370	0.21	0.3065	0.020	0.28297	0.0786	0.0014	0.1046	0.0017	1711	18	1723	15	1528	27	1704	26
34_17_1	4.411	0.21	0.3093	0.021	0.26769	0.0789	0.0017	0.1040	0.0012	1711	15	1739	15	1533	32	1695	22
34_18_1	3.648	0.18	0.2667	0.019	0.4811	0.0744	0.0023	0.1001	0.0020	1554	21	1523	16	1449	43	1617	38
34_16_1	4.005	0.26	0.2760	0.019	0.44072	0.07590	0.00095	0.1063	0.0018	1633	16	1570.9	8.5	1478	18	1728	30
34_9_1	4.07	0.24	0.2929	0.021	0.42337	0.0821	0.0023	0.1018	0.0027	1639	29	1655	21	1594	42	1655	49
34_8_1	4.60	0.23	0.3136	0.022	0.29905	0.0810	0.0022	0.1063	0.0018	1743	20	1758	19	1580	40	1728	30
34_20_1	4.70	0.26	0.3172	0.023	0.34046	0.0840	0.0026	0.1074	0.0022	1758	24	1775	21	1640	45	1748	36
34_20_2	4.58	0.26	0.3200	0.023	0.53033	0.0839	0.0031	0.1040	0.0019	1742	28	1788	23	1626	57	1696	35
34_22_1	3.66	0.22	0.2681	0.021	0.70425	0.0754	0.0024	0.0990	0.0023	1552	27	1533	22	1468	45	1594	44
34_22_2	4.41	0.30	0.3023	0.023	0.70779	0.0834	0.0028	0.1058	0.0030	1694	38	1701	31	1617	52	1700	54
34_14_1	3.73	0.24	0.2685	0.020	0.85882	0.0736	0.0020	0.1008	0.0025	1572	37	1531	31	1434	39	1637	48
34_56_2	4.662	0.24	0.3129	0.021	0.23972	0.0784	0.0011	0.1070	0.0016	1759	16	1755	11	1524	21	1752	27
34_31_1	3.91	0.27	0.2690	0.020	0.64983	0.0735	0.0015	0.1053	0.0022	1611	22	1535	16	1433	27	1705	37
34_30_1	4.12	0.28	0.2787	0.022	0.66016	0.0726	0.0021	0.1067	0.0023	1650	23	1584	17	1415	39	1729	38
34_35_1	4.52	0.27	0.3152	0.024	0.56077	0.0816	0.0037	0.1031	0.0024	1719	31	1765	28	1582	69	1688	42
34_35_2	3.57	0.23	0.2636	0.020	0.63863	0.0725	0.0019	0.0977	0.0023	1535	26	1508	20	1414	36	1573	44
34_34_1	4.59	0.25	0.3134	0.022	0.40145	0.0822	0.0024	0.1054	0.0027	1738	30	1759	30	1602	46	1713	44
34_34_2	3.60	0.26	0.2607	0.020	0.84676	0.0694	0.0024	0.0987	0.0028	1526	41	1491	34	1354	46	1579	53
34_28_1	3.93	0.24	0.2744	0.020	0.70936	0.0756	0.0023	0.1038	0.0024	1607	28	1562	27	1472	43	1675	43
34_27_1	3.92	0.23	0.2804	0.022	0.5891	0.0719	0.0028	0.1013	0.0022	1614	27	1592	22	1401	53	1639	39
34_26_1	4.52	0.32	0.2942	0.021	0.4722	0.0748	0.0018	0.1106	0.0023	1728	20	1662	12	1462	33	1795	35
34_3_2	3.67	0.27	0.2553	0.016	0.88081	0.129	0.014	0.1021	0.0045	1529	53	1463	35	2430	260	1580	96

Appendix 2: U-Th-Pb Isotopic data for Alkali Granite - Continued																	
34_1_1	4.57	0.24	0.3060	0.021	0.40256	0.0749	0.0020	0.1072	0.0018	1737	21	1720	16	1459	38	1755	32
34_1_2	4.79	0.28	0.3161	0.024	0.37393	0.0758	0.0025	0.1104	0.0025	1780	27	1770	20	1475	47	1801	42
34_2_1	4.39	0.23	0.2964	0.021	0.57752	0.0757	0.0020	0.1087	0.0024	1707	24	1672	22	1473	37	1767	40
34_4_1	3.70	0.26	0.2706	0.022	0.70664	0.0698	0.0033	0.0992	0.0030	1555	33	1542	23	1361	63	1584	56
34_5_1	4.82	0.25	0.3139	0.023	0.33678	0.0806	0.0025	0.1118	0.0025	1784	23	1759	22	1565	47	1825	40
34_5_2	4.75	0.25	0.3177	0.022	0.37179	0.0786	0.0029	0.1070	0.0017	1771	23	1778	19	1527	54	1751	30
34_25_1	3.98	0.30	0.2653	0.021	0.74304	0.0695	0.0021	0.1083	0.0024	1622	23	1516	12	1363	40	1753	40
34_23_2	4.41	0.21	0.3030	0.021	0.58276	0.0696	0.0018	0.1056	0.0015	1709	20	1705	20	1359	34	1718	26
34_37_1	4.448	0.33	0.2833	0.020	0.35827	0.0753	0.0017	0.1139	0.0021	1717	17	1608	10	1467	32	1850	33
34_42_1	4.57	0.29	0.3020	0.022	0.49478	0.0735	0.0020	0.1093	0.0023	1739	21	1701	14	1432	39	1773	36
34_42_2	4.61	0.30	0.3006	0.023	0.59742	0.0737	0.0020	0.1111	0.0026	1745	25	1694	17	1436	38	1805	40
34_42_3	4.85	0.39	0.3170	0.028	0.75667	0.0920	0.0030	0.1097	0.0045	1768	45	1773	32	1776	56	1759	73
34_42_4	3.57	0.22	0.2532	0.020	0.76754	0.0697	0.0022	0.1022	0.0022	1538	23	1454	14	1362	43	1650	40
34_43_1	4.85	0.25	0.3228	0.023	0.35502	0.0833	0.0021	0.1088	0.0019	1786	22	1802	23	1617	40	1769	31
34_43_2	4.63	0.29	0.3065	0.023	0.58261	0.0781	0.0030	0.1094	0.0030	1744	30	1722	23	1525	59	1766	49
34_46_1	4.41	0.24	0.3027	0.022	0.63354	0.0852	0.0015	0.1043	0.0017	1708	23	1704	21	1651	27	1703	29
34_46_2	3.46	0.24	0.2607	0.022	0.68375	0.0682	0.0027	0.0961	0.0027	1505	31	1492	22	1331	51	1521	55
34_47_1	4.27	0.28	0.2832	0.021	0.58022	0.0793	0.0010	0.1087	0.0021	1683	20	1607	16	1543	19	1765	35
34_50_2	3.77	0.29	0.2673	0.021	0.74424	0.0759	0.0017	0.1017	0.0029	1571	31	1526	21	1477	31	1640	53
34_36_1	4.10	0.22	0.2794	0.020	0.50775	0.0769	0.0015	0.1066	0.0021	1650	21	1588	13	1497	28	1730	35
34_60_1	3.80	0.25	0.2772	0.022	0.63043	0.0748	0.0016	0.1008	0.0026	1590	28	1576	19	1457	31	1629	47
34_53_1	3.53	0.26	0.2703	0.021	0.73045	0.0805	0.0028	0.0942	0.0032	1513	37	1541	25	1562	53	1476	65
34_54_1	4.02	0.27	0.2904	0.021	0.80759	0.0822	0.0030	0.1027	0.0030	1624	42	1647	31	1603	58	1653	53
34_54_2	4.50	0.22	0.3142	0.022	0.41439	0.0890	0.0023	0.1043	0.0016	1726	21	1763	21	1723	43	1706	31
34_57_1	4.599	0.26	0.3150	0.021	0.23299	0.0822	0.0011	0.1078	0.0018	1750	18	1765	11	1596	20	1754	28
34_58_1	3.54	0.34	0.2555	0.021	0.88902	0.0723	0.0012	0.1004	0.0025	1521	33	1466	22	1410	23	1607	49
34_49_1	4.56	0.27	0.3221	0.021	0.78201	0.0845	0.0020	0.1052	0.0021	1732	33	1798	27	1639	37	1709	39
34_48_1	4.30	0.22	0.3085	0.023	0.54985	0.0826	0.0021	0.1041	0.0017	1692	24	1732	23	1602	40	1694	32
34_51_1	3.80	0.27	0.2706	0.020	0.62347	0.0756	0.0012	0.1017	0.0022	1584	22	1544	14	1472	22	1643	39
34_52_1	9.4	2.0	0.216	0.034	0.92028	0.0818	0.0079	0.291	0.026	2170	200	1300	170	1580	150	3320	180
34_6_1	16.6	5.2	0.38	0.10	0.91977	0.219	0.057	0.381	0.061	2830	370	2000	430	3870	930	3750	270

Appendix 3: U-Th-Pb isotopic data for Porphyritic Granite																	
Zircon ID no.	207Pb /235U	% Error	206Pb /238U	% Error	Error Correl. (rho)	208Pb /232Th	% Error	207Pb /206Pb	% Error	207Pb/ 235U Age	% Error	206Pb/ 238U Age	% Error	208Pb/ 232Th Age	% Error	207Pb/ 206Pb Age	% Error
44_44_2	0.689	0.027	0.0885	0.0012	0.71209	0.02400	0.00062	0.0017	0.0017	531	16	546.5	7.3	479	12	443	74
44_41_1	0.703	0.022	0.09007	0.00085	0.45179	0.02738	0.00084	0.0016	0.0016	539	13	556.0	5.0	546	17	458	64
44_41_2	0.646	0.021	0.0829	0.0010	0.47892	0.02454	0.00054	0.0017	0.0017	505	13	513.3	6.2	490	11	458	70
44_42_2	0.655	0.026	0.0837	0.0013	0.67296	0.02473	0.00063	0.0018	0.0018	510	16	518.1	7.7	494	12	462	76
44_30_1	0.703	0.013	0.09028	0.00069	0.41826	0.02453	0.00037	0.00073	0.00073	540.8	7.7	557.1	4.1	489.8	7.2	463	31
44_42_1	0.684	0.027	0.0871	0.0012	0.72749	0.02606	0.00061	0.0017	0.0017	528	16	538.1	7.0	520	12	470	72
44_31_1	0.422	0.012	0.0544	0.0014	0.85161	0.076	0.011	0.00047	0.00047	356.8	8.5	341.1	8.6	1480	200	482	18
44_44_1	0.717	0.024	0.09076	0.00096	0.55199	0.02774	0.00044	0.0017	0.0017	547	14	560.0	5.7	553.1	8.7	483	67
44_39_1	0.675	0.020	0.08575	0.00089	0.67762	0.02597	0.00035	0.0014	0.0014	523	12	530.3	5.3	518.1	6.9	483	57
44_17_1	0.727	0.025	0.0920	0.0014	0.35524	0.02600	0.00069	0.0011	0.0011	553	15	567.4	8.3	519	14	488	38
44_15_1	0.740	0.025	0.0933	0.0010	0.35629	0.0296	0.0021	0.0012	0.0012	561	15	575.2	6.2	589	42	489	48
44_4_1	0.766	0.029	0.0958	0.0015	0.74147	0.0261	0.0010	0.0015	0.0015	576	16	589.5	8.9	520	20	521	58
44_34_1	0.664	0.024	0.0830	0.0016	0.84512	0.02562	0.00045	0.0012	0.0012	516	14	513.9	9.5	511.3	8.9	528	45
44_15_2	0.701	0.015	0.0870	0.0012	0.62117	0.0282	0.0013	0.00085	0.00085	538.7	9.2	537.8	7.1	561	25	544	29
44_47_1	0.654	0.023	0.0809	0.0017	0.82684	0.02442	0.00069	0.0012	0.0012	510	14	501	10	488	14	564	38
44_43_1	0.737	0.022	0.0907	0.0010	0.77744	0.02538	0.00084	0.00082	0.00082	563	12	559.7	6.2	506	17	571	29
44_19_1	0.823	0.044	0.1005	0.0025	0.51121	0.0277	0.0019	0.0013	0.0013	606	25	617	15	551	37	576	39
44_35_1	0.792	0.020	0.0962	0.0011	0.49441	0.02634	0.00072	0.00094	0.00094	591	12	592.2	6.3	525	14	580	33
44_43_2	0.758	0.014	0.09222	0.00098	0.70351	0.0245	0.0013	0.00070	0.00070	572.2	8.3	568.6	5.8	488	27	590	25
44_40_1	0.753	0.013	0.09123	0.00079	0.66232	0.02519	0.00067	0.00069	0.00069	569.5	7.4	562.8	4.6	503	13	599	24
44_6_1	1.18	0.14	0.134	0.013	0.92223	0.024	0.045	0.0025	0.0025	776	69	806	71	550	800	690	82
44_7_1	0.692	0.072	0.0755	0.0055	0.57745	0.0421	0.0090	0.0061	0.0061	523	42	468	33	820	170	730	140
44_38c_1	1.28	0.15	0.133	0.011	0.97982	0.0200	0.0044	0.0024	0.0024	815	66	799	62	398	87	851	78
44_38b_1	0.758	0.074	0.0806	0.0051	0.46657	0.0480	0.0071	0.0076	0.0076	584	50	499	30	940	140	870	170
44_23_1	0.817	0.085	0.0778	0.0064	0.47171	0.0501	0.0071	0.0091	0.0091	593	47	482	38	980	140	1010	180
44_A1_2	1.678	0.078	0.1582	0.0042	0.87526	0.0387	0.0061	0.0021	0.0021	995	29	946	23	760	120	1111	51
44_10_2	2.126	0.081	0.1879	0.0023	0.59122	0.0526	0.0024	0.0027	0.0027	1153	26	1110	12	1035	46	1226	66
44_A1_1	2.60	0.21	0.2191	0.0078	0.86953	0.0646	0.0023	0.0046	0.0046	1278	60	1275	41	1264	43	1260	110

Appendix 3: U-Th-Pb isotopic data for Porphyritic Granite - Continued																	
44_38a_1	1.07	0.15	0.0830	0.0056	0.34765	0.0564	0.0095	0.013	0.013	710	72	513	33	1100	180	1290	230
44_27_1	2.87	0.20	0.2432	0.0056	0.72801	0.0733	0.0022	0.0047	0.0047	1359	53	1403	29	1429	41	1310	100
44_6a_1	1.06	0.16	0.0798	0.0072	0.42571	0.061	0.010	0.014	0.014	706	75	494	43	1190	200	1440	260
44_16_1	3.46	0.30	0.2655	0.0087	0.72757	0.0805	0.0073	0.0058	0.0058	1493	70	1516	44	1560	130	1450	120
44_9_1	1.27	0.20	0.0867	0.0078	0.56427	0.070	0.012	0.014	0.014	799	93	534	46	1360	230	1470	250
44_51_1	3.19	0.18	0.2394	0.0060	0.82733	0.0677	0.0033	0.0038	0.0038	1452	42	1382	32	1338	56	1538	70
44_1_1	3.88	0.15	0.2740	0.0041	0.68588	0.0786	0.0020	0.0029	0.0029	1594	32	1560	21	1534	39	1641	53
44_13_1	4.13	0.15	0.2875	0.0041	0.59126	0.0783	0.0033	0.0028	0.0028	1651	29	1628	20	1520	61	1699	47
44_12_2	4.57	0.15	0.3050	0.0043	0.11117	0.0853	0.0020	0.0029	0.0029	1739	28	1716	21	1654	37	1718	50
44_50_1	3.96	0.10	0.2713	0.0025	0.44424	0.0779	0.0010	0.0024	0.0024	1624	21	1547	12	1516	19	1719	42
44_27_2	3.95	0.14	0.2661	0.0039	0.62382	0.0770	0.0022	0.0031	0.0031	1619	29	1525	21	1499	43	1735	54
44_14_1	4.58	0.11	0.3066	0.0029	0.039586	0.0834	0.0019	0.0018	0.0018	1743	20	1724	14	1619	35	1760	30
44_22_2	4.55	0.15	0.2981	0.0035	0.55781	0.0818	0.0023	0.0022	0.0022	1736	28	1682	18	1590	43	1761	37
44_13_2	4.44	0.20	0.2957	0.0053	0.6731	0.0837	0.0023	0.0030	0.0030	1712	36	1669	26	1625	42	1771	50
44_36_1	4.23	0.20	0.2838	0.0043	0.70897	0.0806	0.0012	0.0040	0.0040	1672	40	1610	21	1566	22	1777	61
44_8_1	4.50	0.15	0.2966	0.0044	0.75399	0.0773	0.0015	0.0027	0.0027	1722	29	1673	22	1505	28	1779	42
44_11_1	4.63	0.10	0.3072	0.0029	0.32021	0.0829	0.0013	0.0021	0.0021	1750	18	1726	14	1609	25	1782	32
44_28_1	4.41	0.16	0.2939	0.0049	0.57522	0.0819	0.0011	0.0034	0.0034	1716	33	1660	24	1590	21	1788	55
44_10_1	4.48	0.19	0.2918	0.0045	0.5238	0.0836	0.0016	0.0040	0.0040	1720	34	1650	22	1622	29	1793	65
44_28_2	4.55	0.18	0.2966	0.0035	0.5397	0.0834	0.0014	0.0036	0.0036	1734	34	1674	17	1618	26	1799	57
44_12_1	4.88	0.18	0.3187	0.0055	0.46215	0.0881	0.0026	0.0026	0.0026	1792	32	1783	27	1706	48	1800	46
44_37_1	4.80	0.19	0.3116	0.0041	0.44677	0.0853	0.0018	0.0035	0.0035	1778	33	1748	20	1654	33	1818	59
44_26_1	4.96	0.21	0.3062	0.0035	0.48308	0.0821	0.0021	0.0043	0.0043	1806	34	1722	17	1595	39	1891	63
44_20_1	1.66	0.27	0.0887	0.0089	0.66689	0.066	0.010	0.018	0.018	950	110	545	53	1280	190	2000	270
44_5_1	2.21	0.72	0.1026	0.0096	0.64171	0.086	0.018	0.022	0.022	1070	120	627	55	1720	290	2010	250
44_3_1	1.63	0.22	0.0864	0.0072	0.25484	0.068	0.012	0.017	0.017	946	82	533	43	1310	230	2060	250
44_8a_1	4.82	0.87	0.162	0.023	0.74611	0.261	0.080	0.025	0.025	1660	180	960	130	4430	990	2790	240
44_2_1	4.63	0.86	0.133	0.020	0.7797	0.42	0.23	0.023	0.023	1640	160	790	110	-	-	3130	170
44_21_1	20.7	8.6	0.39	0.12	0.95435	-1.6	2.3	0.068	0.068	2990	370	2020	540	-	-	3780	260

Appendix 4: U-Th-Pb isotopic data for Syenite																	
Zircon ID no.	207Pb /235U	% Error	206Pb /238U	% Error	Error Correl. (rho)	208Pb /232Th	% Error	207Pb /206Pb	% Error	207Pb/ 235U Age	% Error	206Pb/ 238U Age	% Error	208Pb/ 232Th Age	% Error	207Pb/ 206Pb Age	% Error
55_16_1	0.723	0.025	0.0938	0.0019	0.50117	-0.006	0.029	0.05623	0.00093	551	15	578	11	-90	700	456	37
55_36_1	0.742	0.026	0.0924	0.0013	0.41508	0.0283	0.0034	0.0577	0.0015	562	15	569.4	7.7	563	66	506	60
55_15_1	0.610	0.041	0.0777	0.0045	0.70885	0.001	0.064	0.05744	0.00080	480	26	482	27	-100	1400	515	26
55_17_1	0.663	0.027	0.0800	0.0025	0.92927	0.0372	0.0034	0.0597	0.0010	512	16	496	15	734	66	578	41
55_18_1	0.635	0.049	0.0761	0.0044	0.90375	0.0332	0.0047	0.0601	0.0020	494	30	472	26	658	91	583	81
55_43_1	0.772	0.014	0.09320	0.00080	0.66909	0.02748	0.00063	0.05994	0.00086	580.7	8.1	574.4	4.7	548	12	598	31
55_19_1	0.659	0.062	0.0781	0.0066	0.90276	0.0336	0.0036	0.0611	0.0022	516	41	483	39	667	71	621	88
55_40_1	0.678	0.056	0.0761	0.0047	0.78439	0.0374	0.0046	0.0619	0.0018	518	33	472	28	739	89	650	72
55_22_1	0.788	0.086	0.0861	0.0074	0.73824	0.0413	0.0064	0.0643	0.0025	592	52	531	44	820	120	726	96
55_X_1	0.883	0.085	0.0927	0.0075	0.84778	0.34	0.19	0.0657	0.0016	632	46	570	44	-	-	788	53
55_45_1	1.49	0.52	0.128	0.034	0.85858	-0.08	0.26	0.0799	0.0096	810	180	820	220	2600	1800	1150	220
55_7_1	2.08	0.12	0.1840	0.0071	0.99816	0.0147	0.0014	0.0815	0.0014	1134	38	1087	39	294	28	1228	34
55_35_2	2.82	0.19	0.2355	0.0051	0.51424	0.091	0.010	0.0865	0.0052	1343	54	1362	27	1760	190	1280	140
55_12_1	3.00	0.12	0.2313	0.0044	0.74122	0.0636	0.0045	0.0941	0.0027	1402	31	1341	23	1244	86	1498	53
55_3_1	3.96	0.29	0.301	0.013	0.64989	0.0849	0.0091	0.0973	0.0031	1605	57	1694	62	1640	170	1573	57
55_9_1	3.78	0.20	0.2718	0.0071	0.86493	0.0731	0.0018	0.0993	0.0034	1558	46	1547	36	1426	33	1574	69
55_42_1	3.94	0.24	0.2794	0.0093	0.83139	0.0770	0.0021	0.1012	0.0037	1606	52	1586	47	1498	40	1626	68
55_29_1	3.83	0.22	0.2707	0.0056	0.71461	0.0665	0.0050	0.1023	0.0044	1586	45	1544	28	1299	95	1641	78
55_11_1	4.21	0.16	0.3018	0.0043	0.44502	0.0793	0.0020	0.1019	0.0020	1685	25	1700	21	1543	37	1675	36
55_41_1	1.42	0.20	0.0910	0.0078	0.42857	0.0574	0.0076	0.115	0.015	879	85	560	46	1120	140	1710	240
55_32_1	4.42	0.12	0.2971	0.0036	0.1993	0.0768	0.0020	0.1051	0.0025	1713	22	1676	18	1494	37	1710	41
55_35_1	4.43	0.25	0.3071	0.0086	0.62969	0.0830	0.0044	0.1046	0.0040	1732	38	1725	43	1610	83	1715	58
55_12_2	4.51	0.18	0.3099	0.0047	0.3616	0.0800	0.0026	0.1042	0.0022	1728	33	1740	23	1554	48	1717	49
55_37_1	4.32	0.13	0.2915	0.0037	0.14895	0.0761	0.0020	0.1057	0.0032	1693	25	1649	19	1482	37	1717	51
55_38_1	4.41	0.20	0.2950	0.0045	0.45093	0.0818	0.0098	0.1075	0.0042	1706	37	1666	22	1503	77	1739	68
55_26_1	4.23	0.14	0.2835	0.0035	0.66095	0.0744	0.0025	0.1075	0.0028	1674	28	1609	18	1449	47	1748	46
55_31_1	4.16	0.15	0.2784	0.0037	0.52096	0.0744	0.0026	0.1076	0.0034	1661	29	1583	18	1449	50	1748	57
55_13_1	4.55	0.16	0.3099	0.0046	0.20766	0.0850	0.0034	0.1075	0.0030	1735	29	1740	23	1648	63	1748	49
55_34_1	4.090	0.074	0.2728	0.0026	0.55785	0.0743	0.0012	0.1077	0.0017	1649	15	1555	13	1449	23	1753	28
55_5_1	4.71	0.19	0.3094	0.0035	0.22375	0.0825	0.0024	0.1114	0.0038	1763	33	1737	17	1602	44	1808	57
55_23_1	2.70	0.43	0.132	0.011	0.703	0.089	0.010	0.150	0.020	1270	120	812	65	1710	190	2100	260
55_20_1	9.6	1.9	0.202	0.024	0.94125	0.63	0.18	0.319	0.022	2240	160	1200	140	-	1500	3520	98

Appendix 5: U-Th-Pb isotopic data for Granodiorite																	
Zircon ID no.	207Pb /235U	% Error	206Pb /238U	% Error	Error Correl. (rho)	208Pb /232Th	% Error	207Pb /206Pb	% Error	207Pb/ 235U Age	% Error	206Pb/ 238U Age	% Error	208Pb/ 232Th Age	% Error	207Pb/ 206Pb Age	% Error
57_5_1	0.780	0.019	0.0985	0.0013	0.52655	0.0256	0.0012	0.05842	0.00076	555	11	586.2	6.7	591	55	421	48
57_35_2	0.786	0.015	0.09826	0.00082	0.31772	0.0248	0.0013	0.05847	0.00068	516.9	9.0	536.0	4.7	453.2	8.5	438	37
57_20_1	0.782	0.016	0.09733	0.00088	0.50893	0.02583	0.00058	0.05895	0.00048	536.6	9.4	558.0	4.4	457.5	4.3	440	38
57_17_1	0.745	0.015	0.09332	0.00091	0.59751	0.02401	0.00039	0.05785	0.00081	526.9	9.0	544.3	4.7	460.3	6.1	444	39
57_16_1	0.757	0.014	0.09469	0.00076	0.64792	0.02427	0.00029	0.05879	0.00029	554.9	9.6	574.0	4.2	504.4	8.0	463	41
57_51_2	0.741	0.023	0.0938	0.0012	0.46165	0.02632	0.00078	0.05680	0.00092	562	14	577.7	7.1	525	15	470	38
57_29_1	0.770	0.019	0.0967	0.0013	0.63157	0.02516	0.00054	0.05770	0.00072	535.3	8.8	547.1	4.6	442.4	6.0	470	36
57_33_1	0.705	0.013	0.08932	0.00072	0.6343	0.02322	0.00051	0.05723	0.00066	559.1	8.6	576.3	4.6	478.5	5.3	483	37
57_36_2	0.699	0.015	0.09043	0.00075	0.65531	0.02290	0.00022	0.05603	0.00087	556.6	8.0	573.9	3.5	481.6	4.4	483	35
57_32_1	0.696	0.011	0.08893	0.00068	0.67537	0.02248	0.00036	0.05785	0.00031	564.1	9.0	583.6	4.5	479.4	7.5	488	32
57_35_1	0.730	0.016	0.09313	0.00072	0.64605	0.02527	0.00040	0.05667	0.00097	571.7	8.8	590.6	4.7	502.1	5.6	490	33
57_45_1	0.682	0.015	0.08810	0.00080	0.70671	0.02304	0.00031	0.05615	0.00090	563.2	8.6	580.3	3.9	471.4	6.3	491	30
57_7_1	0.711	0.013	0.09033	0.00081	0.40736	0.0271	0.0016	0.05749	0.00073	558.1	8.4	571.1	4.9	524	15	493	39
57_24_1	0.734	0.014	0.09265	0.00083	0.49445	0.02627	0.00075	0.05741	0.00094	586	12	604.5	5.1	504	10	503	31
57_50_1	0.731	0.019	0.0952	0.0011	0.60479	0.0298	0.0028	0.0558	0.0012	580	11	594.7	7.7	502	11	510	30
57_52_2	0.744	0.016	0.0929	0.0010	0.65429	0.0247	0.0017	0.05821	0.00080	564.2	8.6	575.1	5.4	479.5	7.7	513	35
57_21_1	0.828	0.023	0.1021	0.0015	0.70845	0.02610	0.00077	0.05952	0.00062	537.7	6.2	549.2	4.0	449.4	7.2	523	12
57_15_1	0.756	0.011	0.09363	0.00071	0.50152	0.0263	0.0010	0.05862	0.00057	544.5	7.9	557.4	4.8	539	31	523	24
57_41_1	0.7685	0.0093	0.09561	0.00061	0.46647	0.02400	0.00020	0.05859	0.00026	563.6	8.6	581.2	4.3	490.7	5.9	525	16
57_34_1	0.749	0.016	0.09471	0.00096	0.56405	0.02447	0.00057	0.05779	0.00073	562.1	8.5	572.3	4.5	492	28	531	25
57_1_1	0.777	0.012	0.09666	0.00080	0.48939	0.02467	0.00028	0.05876	0.00034	564.9	9.0	572.8	6.1	492	33	537	29
57_47_1	0.759	0.014	0.09362	0.00085	0.738	0.02405	0.00052	0.05959	0.00041	566.6	9.3	583.2	5.6	489	11	538	23
57_28_1	0.741	0.014	0.09420	0.00067	0.43912	0.02360	0.00032	0.05721	0.00071	575.3	7.6	585.9	4.3	532	11	538	18
57_19_1	0.743	0.015	0.09477	0.00076	0.52878	0.02400	0.00038	0.05716	0.00075	541.6	8.0	551.5	4.3	464	10	539	11
57_18_2	0.768	0.018	0.0961	0.0013	0.62217	0.0256	0.0012	0.05835	0.00076	587.4	8.8	604.1	4.8	494	26	541	25
57_37_1	0.736	0.014	0.09352	0.00077	0.64316	0.02396	0.00027	0.05711	0.00084	569.5	7.9	579.2	4.5	483.6	8.5	543	17
57_3_1	0.771	0.016	0.0956	0.0011	0.76527	0.02527	0.00072	0.05948	0.00043	571.8	6.3	577.0	4.2	524	20	549	21

Appendix 5: U-Th-Pb isotopic data for Granodiorite - Continued																	
57_39_1	0.760	0.014	0.09502	0.00082	0.46888	0.02435	0.00047	0.05856	0.00038	573.1	8.2	585.1	4.8	486.2	9.3	549	14
57_18_1	0.741	0.015	0.09285	0.00076	0.516	0.0247	0.0014	0.05810	0.00067	584	11	605.2	7.8	510	23	550	26
57_10_1	0.756	0.015	0.09595	0.00079	0.50729	0.02515	0.00028	0.05722	0.00078	578.5	5.4	588.6	3.6	479.3	4.0	551	10
57_32_2	0.666	0.014	0.08670	0.00080	0.65364	0.02268	0.00043	0.05596	0.00085	577	10	591.6	7.4	514	25	556	24
57_48_1	0.744	0.015	0.09436	0.00074	0.52698	0.02458	0.00030	0.05707	0.00067	583.2	7.0	594.7	4.7	492.6	5.6	557	13
57_51_1	0.809	0.025	0.0968	0.0014	0.80498	0.02811	0.00081	0.0605	0.0014	571.3	8.2	583.1	4.5	484.6	5.7	558	11
57_52_1	0.732	0.013	0.09312	0.00060	0.59869	0.02411	0.00022	0.05706	0.00080	585.2	9.2	598.7	5.2	515	12	562	18
57_2_1	0.752	0.013	0.09402	0.00077	0.42519	0.02422	0.00043	0.05842	0.00045	610	13	626.6	8.5	521	15	581	24
57_27_1	0.763	0.014	0.09415	0.00086	0.70223	0.02405	0.00049	0.05951	0.00035	600.3	8.4	610.6	4.6	510.8	4.9	583	10
57_43_1	0.815	0.017	0.0994	0.0011	0.58201	0.02719	0.00069	0.05960	0.00063	575.6	8.2	580.0	5.1	480.4	9.6	584	12
57_31_1	0.784	0.020	0.09831	0.00088	0.53169	0.02524	0.00052	0.05752	0.00073	579.3	9.1	588.2	6.6	504	14	586	17
57_44_1	0.806	0.015	0.09936	0.00079	0.56705	0.02560	0.00025	0.05946	0.00027	574.6	7.4	576.9	5.0	480	10	587	15
57_38_1	0.764	0.013	0.09516	0.00073	0.45848	0.02668	0.00055	0.05821	0.00045	604.0	9.5	610.6	6.4	542	14	592	22
57_36_1	0.696	0.014	0.08858	0.00078	0.74564	0.02213	0.00030	0.05675	0.00082	599	14	595.7	8.3	560	16	594	54
57_26_1	0.857	0.055	0.0913	0.0050	0.79359	0.0257	0.0037	0.0646	0.0019	616	29	561	29	509	73	802	81
57_22_1	1.13	0.11	0.1004	0.0076	0.78893	0.045	0.012	0.0811	0.0059	743	50	612	44	840	230	1100	110
57_42_1	1.46	0.28	0.1021	0.0088	0.75551	0.127	0.071	0.0902	0.0087	801	78	621	50	1870	690	1250	150
57_49_1	3.001	0.074	0.2231	0.0025	0.82943	0.0630	0.0014	0.0972	0.0017	1533	39	1534	28	1432	88	1541	65
57_53_1	1.96	0.23	0.137	0.012	0.78636	0.057	0.023	0.1047	0.0086	1402	19	1300	13	1234	27	1560	33
57_23_1	3.63	0.17	0.2690	0.0055	0.69585	0.0737	0.0047	0.0977	0.0032	1031	66	817	66	1130	270	1560	130
57_8_2	4.27	0.14	0.2796	0.0036	0.67252	0.0812	0.0011	0.1102	0.0026	1502	60	1450	54	1301	99	1607	69
57_9_1	4.57	0.14	0.2997	0.0038	0.62392	0.0792	0.0023	0.1110	0.0026	1743	29	1728	28	1606	39	1776	36
57_53_2	4.86	0.13	0.3163	0.0039	0.39311	0.0850	0.0020	0.1117	0.0024	1681	26	1589	18	1578	20	1784	45
57_4_1	4.61	0.15	0.3077	0.0056	0.71045	0.0828	0.0021	0.1094	0.0022	1734	25	1689	19	1539	44	1799	40
57_53_3	4.77	0.11	0.3113	0.0029	0.47465	0.0822	0.0016	0.1113	0.0021	1790	22	1771	19	1648	38	1812	37
57_8_1	3.63	0.24	0.254	0.010	0.94321	0.0669	0.0050	0.1002	0.0036	1774	20	1747	14	1595	30	1814	33
57_40_1	3.07	0.57	0.145	0.016	0.7896	0.137	0.070	0.139	0.014	1240	110	855	86	2700	1100	2010	170

Appendix 6: U-Th-Pb isotopic data for Pegmatite																	
Zircon ID no.	207Pb /235U	% Error	206Pb /238U	% Error	Error Correl. (rho)	208Pb /232Th	% Error	207Pb/ 206Pb Age	% Error	207Pb/ 235U Age	% Error	206Pb/ 238U Age	% Error	208Pb/ 232Th Age	% Error	207Pb/ 206Pb Age	% Error
62_52_2	0.3565	0.0059	0.04778	0.00069	0.98786	-0.0030	0.0017	378	34	438.6	9.9	453.2	9.0	506	87	378	34
62_47_2	0.542	0.015	0.0729	0.0015	0.82264	0.0256	0.0045	439	28	465.4	7.0	470.8	5.6	362	24	439	28
62_47_1	0.631	0.013	0.0810	0.0010	0.69303	0.0184	0.0028	464	32	495.9	7.9	502.2	6.0	367	56	464	32
62_51_2	0.583	0.011	0.07578	0.00093	0.81921	0.0181	0.0012	542	34	578	11	588.9	6.6	543	16	542	34
62_7_1	0.770	0.019	0.0957	0.0011	0.71046	0.02724	0.00080	564	22	512	12	499	11	283	49	564	22
62_51_1	0.659	0.020	0.0806	0.0018	0.96729	0.0142	0.0024	576	23	628.3	9.6	641.5	5.5	604	16	576	23
62_21_1	0.859	0.017	0.10464	0.00095	0.53858	0.03036	0.00083	576	24	616.0	8.7	629.9	6.8	557	16	576	24
62_20_2	0.8457	0.0088	0.10103	0.00080	0.53778	0.0286	0.0020	617	49	669	26	683	24	700	220	617	49
62_21_2	0.836	0.016	0.1025	0.0011	0.50771	0.02796	0.00084	631	16	621.9	4.8	620.4	4.7	568	41	631	16
62_14_2	0.951	0.049	0.1120	0.0041	0.91101	0.037	0.011	766	59	752	29	741	24	1740	580	766	59
62_3_2	1.124	0.063	0.1220	0.0042	0.90202	0.093	0.028	787	75	795	54	791	49	-10	480	787	75
62_24_1	1.440	0.043	0.1467	0.0024	0.86491	0.0397	0.0014	852	74	916	54	937	52	990	250	852	74
62_25_1	1.25	0.12	0.1313	0.0086	0.96212	0.005	0.022	945	37	901	18	882	13	786	27	945	37
62_32_1	1.58	0.15	0.1576	0.0094	0.94529	0.053	0.012	970	100	1013	78	1018	70	870	280	970	100
62_44_2	4.59	0.12	0.2945	0.0031	0.40397	0.0747	0.0023	1048	69	1032	43	1017	37	950	100	1048	69
62_45_2	1.969	0.063	0.1818	0.0027	0.78447	0.0503	0.0019	1133	22	1089	14	1071	12	772	36	1133	22
62_6_2	1.94	0.24	0.173	0.013	0.95356	0.066	0.038	1142	88	1143	69	1139	64	1000	160	1142	88
62_50_1	1.84	0.12	0.1714	0.0067	0.93442	0.0511	0.0079	1152	44	1101	22	1076	14	992	36	1152	44
62_23_2	1.924	0.038	0.1808	0.0022	0.77387	0.0390	0.0019	1176	66	1210	40	1224	37	1218	69	1176	66
62_2_1	2.37	0.13	0.2096	0.0068	0.83128	0.0623	0.0037	1191	43	1119	26	1085	20	926	41	1191	43
62_35_2	2.039	0.078	0.1835	0.0037	0.86992	0.0469	0.0021	1256	81	1176	63	1118	55	430	420	1256	81
62_41_2	2.24	0.20	0.195	0.012	0.92075	0.0517	0.0080	1286	51	1249	26	1226	18	1116	40	1286	51
62_55_2	2.36	0.19	0.191	0.010	0.97177	0.032	0.014	1295	63	1240	42	1199	33	1088	55	1295	63
62_55_1	2.443	0.087	0.2097	0.0033	0.7626	0.0568	0.0021	1306	93	1323	73	1327	68	1279	69	1306	93
62_10_1	2.48	0.14	0.2049	0.0062	0.94423	0.0554	0.0028	1418	56	1383	34	1357	23	1277	51	1418	56
62_28_1	2.97	0.28	0.231	0.013	0.94744	0.0655	0.0036	1459	44	1397	24	1368	19	1198	59	1459	44
62_30_2	2.97	0.10	0.2366	0.0037	0.55564	0.0612	0.0031	1496	85	1514	73	1534	71	1529	91	1496	85
62_52_1	4.81	0.10	0.3145	0.0032	0.37514	0.0880	0.0016	1515	82	1489	59	1459	49	1435	46	1515	82
62_3_1	4.64	0.21	0.3207	0.0072	0.65931	0.0959	0.0040	1531	42	1432	23	1365	15	1200	50	1531	42
62_28_2	4.81	0.12	0.3209	0.0040	0.51426	0.0918	0.0023	1555	43	1467	33	1419	26	1330	80	1555	43
62_31_2	4.78	0.13	0.3237	0.0043	0.25987	0.0953	0.0022	1583	75	1588	70	1616	68	1544	78	1583	75
62_44_1	4.38	0.12	0.2915	0.0028	0.66116	0.08340	0.00081	1595	34	1459	21	1368	16	1247	42	1595	34
62_38_2	3.81	0.14	0.2722	0.0044	0.84262	0.0795	0.0012	1599	44	1513	30	1450	21	1149	71	1599	44

Appendix 6: U-Th-Pb isotopic data for Pegmatite - Continued																	
62_60_2	3.53	0.22	0.2550	0.0093	0.93394	0.0737	0.0024	1623	48	1582	30	1551	22	1545	22	1623	48
62_14_1	4.70	0.10	0.3145	0.0032	0.42148	0.0844	0.0012	1634	39	1556	23	1508	15	1375	43	1634	39
62_15_2	4.109	0.078	0.2824	0.0030	0.67122	0.0809	0.0012	1651	26	1572	19	1528	19	1480	21	1651	26
62_5_2	3.223	0.086	0.2365	0.0031	0.76904	0.0637	0.0022	1653	70	1575	57	1524	49	1457	50	1653	70
62_38_1	4.76	0.16	0.3249	0.0059	0.45053	0.0872	0.0030	1664	42	1536	25	1449	16	1269	60	1664	42
62_30_1	5.01	0.12	0.3188	0.0031	0.12008	0.0812	0.0015	1665	46	1538	30	1446	21	1220	72	1665	46
62_17_1	4.86	0.11	0.3129	0.0030	0.31075	0.0803	0.0017	1685	41	1703	28	1717	27	1595	33	1685	41
62_12_1	4.90	0.12	0.3197	0.0034	0.30373	0.0789	0.0016	1691	46	1804	47	1947	45	1720	80	1691	46
62_2_2	4.74	0.11	0.3112	0.0032	0.44166	0.0794	0.0013	1692	51	1615	33	1550	28	1452	80	1692	51
62_22_2	4.56	0.16	0.2948	0.0048	0.81366	0.0763	0.0018	1692	44	1600	32	1542	24	1436	41	1692	44
62_5_1	4.61	0.11	0.3043	0.0028	0.45778	0.0758	0.0015	1694	75	1640	63	1599	59	1540	120	1694	75
62_35_1	4.92	0.11	0.3184	0.0030	0.2446	0.0802	0.0016	1699	28	1719	25	1741	23	1600	53	1699	28
62_23_1	4.36	0.11	0.2851	0.0029	0.64483	0.0781	0.0015	1700	48	1735	38	1790	35	1847	74	1700	48
62_19_1	4.11	0.13	0.2838	0.0036	0.59171	0.0778	0.0024	1700	34	1714	24	1742	24	1427	57	1700	34
62_41_1	4.045	0.077	0.2699	0.0020	0.61199	0.07707	0.00087	1715	43	1650	26	1610	18	1513	44	1715	43
62_53_2	4.132	0.092	0.2689	0.0023	0.62675	0.0735	0.0022	1721	23	1657	15	1603	15	1571	23	1721	23
62_42_1	4.65	0.17	0.3118	0.0050	0.4351	0.0774	0.0022	1730	36	1746	24	1768	20	1563	37	1730	36
62_29_2	4.79	0.14	0.3148	0.0037	0.43459	0.0777	0.0023	1734	35	1694	22	1679	20	1600	87	1734	35
62_54_1	4.69	0.13	0.3204	0.0044	0.46034	0.0791	0.0027	1736	29	1760	24	1791	22	1538	50	1736	29
62_1_1	4.497	0.089	0.3020	0.0032	0.39594	0.0788	0.0015	1736	38	1629	24	1545	19	1319	64	1736	38
62_45_1	4.61	0.13	0.3158	0.0042	0.35566	0.0804	0.0020	1748	42	1775	29	1812	29	1688	56	1748	42
62_58_1	3.58	0.11	0.2521	0.0032	0.73291	0.0650	0.0031	1757	44	1749	30	1748	25	1505	42	1757	44
62_17_2	3.50	0.13	0.2525	0.0041	0.77583	0.0587	0.0037	1761	29	1754	19	1744	21	1619	34	1761	29
62_27_2	4.76	0.11	0.3096	0.0027	0.27715	0.0767	0.0017	1762	25	1635	13	1534	12	1478	18	1762	25
62_15_1	4.129	0.095	0.2706	0.0023	0.60678	0.0743	0.0014	1763	27	1767	16	1779	16	1535	27	1763	27
62_54_2	4.46	0.13	0.3103	0.0046	0.46858	0.0825	0.0029	1764	26	1727	16	1701	16	1533	28	1764	26
62_53_1	3.30	0.14	0.2465	0.0051	0.78288	0.0683	0.0042	1768	26	1763	18	1762	16	1637	22	1768	26
62_6_1	4.32	0.10	0.2851	0.0022	0.34138	0.0755	0.0014	1770	36	1777	24	1790	19	1576	51	1770	36
62_16_1	4.34	0.12	0.2977	0.0041	0.4335	0.0804	0.0022	1771	32	1717	19	1673	15	1591	22	1771	32
62_40_1	3.61	0.13	0.2517	0.0041	0.8337	0.0624	0.0037	1773	28	1642	15	1540	10	1500	16	1773	28
62_60_1	3.78	0.32	0.271	0.014	0.89448	0.0789	0.0048	1780	39	1705	23	1648	14	1619	15	1780	39
62_36_2	4.734	0.089	0.3149	0.0028	0.35593	0.0824	0.0012	1782	32	1702	18	1636	14	1560	22	1782	32
62_59_2	4.08	0.29	0.287	0.013	0.86893	0.0796	0.0041	1783	36	1780	23	1807	21	1844	42	1783	36
62_29_1	5.11	0.15	0.3235	0.0048	0.57931	0.0856	0.0026	1783	37	1692	19	1617	11	1470	26	1783	37
62_12_2	4.720	0.093	0.3107	0.0026	0.32007	0.0816	0.0013	1785	41	1734	28	1722	28	1475	51	1785	41

Appendix 6: U-Th-Pb isotopic data for Pegmatite - Continued																	
62_31_1	4.342	0.086	0.2890	0.0028	0.42082	0.0802	0.0012	1786	26	1770	15	1764	14	1600	22	1786	26
62_8_2	4.20	0.26	0.281	0.012	0.90712	0.0795	0.0066	1787	40	1709	24	1651	17	1519	42	1787	40
62_34_2	3.88	0.22	0.2664	0.0096	0.89431	0.0712	0.0083	1792	33	1745	20	1712	14	1476	28	1792	33
62_59_1	4.80	0.14	0.3203	0.0039	0.34322	0.0812	0.0027	1794	29	1784	20	1793	20	1775	43	1794	29
62_37_2	4.651	0.098	0.3017	0.0027	0.39436	0.0802	0.0015	1797	33	1655	19	1544	12	1448	27	1797	33
62_9_1	4.666	0.089	0.3031	0.0025	0.19527	0.0791	0.0017	1803	38	1715	26	1644	23	1556	31	1803	38
62_36_1	3.96	0.16	0.2721	0.0055	0.78314	0.0747	0.0042	1806	28	1767	17	1744	13	1586	25	1806	28
62_48_2	3.115	0.091	0.2359	0.0029	0.33713	0.0613	0.0026	1809	31	1771	19	1746	16	1544	24	1809	31
62_49_2	4.02	0.12	0.2704	0.0038	0.70382	0.0676	0.0033	1809	34	1702	20	1617	15	1526	25	1809	34
62_39_1	4.58	0.13	0.2878	0.0032	0.59743	0.0738	0.0022	1811	33	1656	19	1535	12	1432	43	1811	33
62_57_1	4.752	0.097	0.2982	0.0030	0.38061	0.0791	0.0015	1814	36	1775	24	1764	18	1511	44	1814	36
62_18_1	4.43	0.13	0.2920	0.0034	0.53468	0.0778	0.0023	1816	36	1744	23	1703	18	1457	49	1816	36
62_48_1	4.45	0.14	0.2908	0.0045	0.76596	0.0801	0.0017	1818	34	1797	20	1787	16	1534	31	1818	34
62_26_1	2.93	0.12	0.2346	0.0045	0.7762	0.0653	0.0026	1821	34	1804	19	1795	15	1484	33	1821	34
62_34_1	4.87	0.12	0.3126	0.0038	0.3888	0.0762	0.0022	1822	43	1735	29	1664	24	1485	34	1822	43
62_24_2	5.10	0.28	0.3522	0.0092	0.56862	0.0891	0.0043	1823	29	1782	18	1762	16	1703	30	1823	29
62_37_1	4.55	0.15	0.3065	0.0056	0.64355	0.0758	0.0027	1823	37	1772	20	1739	13	1492	33	1823	37
62_49_1	5.05	0.13	0.3237	0.0033	0.40953	0.0754	0.0020	1824	33	1801	19	1782	14	1559	29	1824	33
62_22_1	4.008	0.068	0.2687	0.0023	0.56726	0.07590	0.00094	1825	30	1775	17	1736	17	1540	22	1825	30
62_4_1	4.93	0.11	0.3211	0.0032	0.1817	0.0762	0.0018	1826	30	1754	17	1699	13	1559	27	1826	30
62_18_2	4.61	0.12	0.3026	0.0037	0.44529	0.0748	0.0026	1836	41	1803	24	1781	21	1560	38	1836	41
62_4_2	4.95	0.14	0.3185	0.0043	0.3614	0.0803	0.0020	1837	28	1757	16	1706	12	1538	31	1837	28
62_13_1	4.44	0.12	0.3106	0.0050	0.46611	0.0733	0.0030	1842	35	1790	21	1752	19	1482	42	1842	35
62_46_2	3.66	0.10	0.2636	0.0030	0.53901	0.0705	0.0023	1846	33	1792	20	1755	15	1560	32	1846	33
62_20_1	4.722	0.088	0.3180	0.0033	0.19094	0.0789	0.0014	1849	36	1741	21	1663	15	1455	44	1849	36
62_27_1	3.719	0.090	0.2676	0.0038	0.7254	0.0760	0.0011	1851	36	1821	22	1807	16	1469	38	1851	36
62_46_1	4.37	0.16	0.3056	0.0055	0.66635	0.0822	0.0018	1856	36	1815	20	1783	15	1577	29	1856	36
62_33_1	4.62	0.11	0.3108	0.0042	0.47655	0.0834	0.0018	1865	38	1828	25	1805	23	1659	49	1865	38
62_1_2	4.45	0.10	0.2963	0.0029	0.53296	0.0819	0.0012	1869	40	1737	23	1630	16	1437	41	1869	40
62_8_1	4.770	0.098	0.3092	0.0034	0.36018	0.0792	0.0012	1884	31	1775	17	1682	15	1538	28	1884	31
62_11_1	3.89	0.15	0.2704	0.0047	0.78848	0.0737	0.0022	2250	250	907	97	455	50	1020	250	2250	250
62_7_2	1.50	0.21	0.0736	0.0083	0.72049	0.053	0.013	374	7.0	309.3	4.4	300.8	4.3	-62	34	374.0	7.0

Appendix 7: U-Th-Pb isotopic data for vein quartz																	
Zircon ID no.	207Pb /235U	% Error	206Pb /238U	% Error	Error Correl. (rho)	208Pb /232Th	% Error	207Pb /206Pb	% Error	207Pb/ 235U Age	% Error	206Pb/ 238U Age	% Error	208Pb/ 232Th Age	% Error	207Pb/ 206Pb Age	% Error
81_18_1	0.665	0.023	0.0864	0.0018	0.78169	0.0244	0.0012	0.05563	0.00097	515	14	534	11	486	24	420	41
81-12_1	0.780	0.013	.09720	0.00059	0.41564	0.0313	0.0021	0.05866	0.00062	584.3	7.2	597.9	3.5	622	42	552	22
81-14_2	0.7829	0.0092	.09541	0.00057	0.32769	0.0281	0.0032	0.05952	0.00046	587.4	5.1	587.4	3.3	556	64	583	17
81_9_1	0.7338	0.0080	.08948	0.00085	0.9937	0.0061	0.0012	0.05945	0.00011	558.4	4.7	552.4	5.0	122	23	583.5	4.1
81_14_1	0.7945	0.0096	.09730	0.00059	0.57566	0.02470	0.00025	0.05968	0.00017	593.2	5.5	598.5	3.5	493.1	4.9	591.7	6.2
81_11_2	0.805	0.012	.09773	0.00056	0.29052	0.0291	0.0023	0.05995	0.00065	599.1	6.7	601.0	3.3	578	45	596	24
81_23_1	0.856	0.026	0.1011	0.0015	0.87698	0.068	0.018	0.0613	0.0013	625	14	620.6	8.7	1240	310	628	47

Appendix 8: U-Th-Pb isotopic data for Alkali Granite (Syeno-granite)																	
Zircon ID no.	207Pb /235U	% Error	206Pb /238U	% Error	Error Correl. (rho)	208Pb /232Th	% Error	207Pb /206Pb	% Error	207Pb/ 235U Age	% Error	206Pb/ 238U Age	% Error	208Pb/ 232Th Age	% Error	207Pb/ 206Pb Age	% Error
85_36_1	0.646	0.017	0.0850	0.0012	0.80723	0.02429	0.00076	0.05550	0.00092	506	11	526.0	7.2	485	15	418	39
85_4_1	0.641	0.013	0.08367	0.00076	0.5336	0.02504	0.00082	0.05550	0.00089	501.7	8.3	518.0	4.5	500	16	419	38
85_8_2	0.721	0.027	0.0940	0.0015	0.45688	0.02325	0.00082	0.05556	0.00091	548	16	578.9	9.1	464	16	421	38
85_51_1	0.703	0.021	0.0909	0.0015	0.76174	0.0289	0.0015	0.0558	0.0011	538	12	560.4	8.7	576	29	423	47
85_5_2	0.633	0.025	0.0822	0.0026	0.91733	0.0314	0.0022	0.05576	0.00098	494	16	509	15	623	42	427	41
85_49_1	0.768	0.033	0.0994	0.0022	0.55831	0.0257	0.0011	0.0561	0.0010	573	19	610	13	512	22	439	42
85_37_1	0.709	0.021	0.0920	0.0011	0.4943	0.02304	0.00062	0.05617	0.00069	543	13	567.1	6.7	460	12	451	29
85_33_1	0.735	0.019	0.0950	0.0011	0.53328	0.02539	0.00064	0.05640	0.00089	559	12	586.0	6.5	507	13	455	37
85_38_2	0.718	0.019	0.0927	0.0012	0.45705	0.02378	0.00090	0.05656	0.00089	548	11	572.3	7.1	478	19	462	37
85_3_1	0.777	0.032	0.0975	0.0018	0.43731	0.0262	0.0012	0.05677	0.00097	578	19	599	10	523	24	468	40
85_42_2	0.705	0.012	0.09034	0.00071	0.19575	0.0251	0.0014	0.05660	0.00066	540.7	7.2	557.5	4.2	501	28	469	26
85_8_1	0.736	0.023	0.0949	0.0013	0.39033	0.02351	0.00067	0.05672	0.00077	560	14	584.6	7.7	470	13	472	31
85_48_1	0.712	0.014	0.09104	0.00079	0.34925	0.0256	0.0018	0.05669	0.00071	544.7	8.5	561.6	4.7	511	36	472	28
85_10_1	0.769	0.025	0.0991	0.0014	0.52905	0.02493	0.00077	0.05698	0.00089	576	15	608.7	8.5	497	15	478	37
85_47_1	0.746	0.023	0.0965	0.0019	0.60093	0.0269	0.0012	0.05732	0.00096	563	14	594	11	537	23	490	39
85_5_1	0.801	0.026	0.0992	0.0013	0.38647	0.02420	0.00083	0.05781	0.00077	596	15	609.4	7.6	483	16	514	31
85_42_1	0.720	0.011	0.08940	0.00071	0.61273	0.02714	0.00083	0.05832	0.00051	550.2	6.3	551.9	4.2	541	16	541	19
85_6_1	0.719	0.016	0.0900	0.0011	0.82402	0.02356	0.00057	0.05857	0.00044	548.5	9.6	555.4	6.6	471	11	549	17
85_34_1	0.732	0.011	0.08984	0.00070	0.60054	0.02671	0.00072	0.05878	0.00063	557.0	6.5	554.6	4.1	533	14	553	24
85_41_2	0.756	0.011	0.09285	0.00060	0.5606	0.0285	0.0013	0.05877	0.00056	570.9	6.3	572.4	3.5	567	26	554	21
85_39_1	0.740	0.012	0.09090	0.00084	0.57754	0.02624	0.00071	0.05922	0.00058	561.6	7.3	560.8	4.9	523	14	574	21
85_46_1	0.689	0.034	0.0821	0.0030	0.88665	0.0352	0.0030	0.0601	0.0013	526	20	508	18	697	58	583	52
85_7_1	0.817	0.014	0.1000	0.0011	0.85152	0.02646	0.00046	0.05948	0.00039	605.2	7.8	614.5	6.5	527.8	9.0	585	15
85_41_1	0.894	0.056	0.1027	0.0043	0.92849	0.048	0.011	0.0615	0.0015	647	30	629	25	840	180	639	54
85_9_1	1.221	0.097	0.1031	0.0061	0.69279	0.0382	0.0036	0.0875	0.0064	783	42	630	35	754	69	1220	110
85_9_2	1.67	0.22	0.129	0.011	0.43763	0.0456	0.0069	0.096	0.013	986	88	781	65	900	130	1400	260